

Jets, Mixing, and Topography in the Southern Ocean

Emma J. D. Boland

Department of Applied Mathematics and Theoretical Physics
University of Cambridge

A thesis submitted for the degree of Doctor of Philosophy

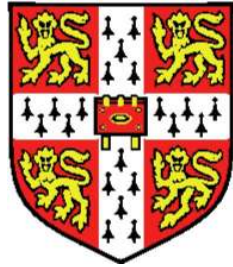
May 2013

The Southern Ocean holds a unique place in our planet. It is home to the world's longest and strongest ocean current, the Antarctic Circumpolar Current (or ACC), which is formed of jets (alternating velocity structures), thought to be significant surface transport barriers. The dynamical processes (particularly mixing processes) in the Southern Ocean are crucial to driving the global overturning circulation, which is in turn responsible for the global transport of heat, CO₂, and nutrients. Despite the evident importance of the Southern Ocean to current and future climate, the important dynamical processes that occur there are poorly understood.

This thesis attempts to contribute towards the understanding of some of the open questions in Southern Ocean dynamics. In particular, we investigate the effect that topography might have on the jets that form the ACC, with regards to their formation and in particular, their transport properties. Through a quasi-geostrophic model we investigate the properties of jets that form over a zonal slope in bottom topography, and find that the jets become tilted, aligning perpendicular to the large-scale barotropic potential vorticity gradient. As the jets tilt more, they become significantly more energetic, corresponding with an increase in across-jet transport. We compare various theories regarding the formation of such jets, involving linear analysis of the system. It is found that the analytical form of the Rossby wave frequencies correctly predicts the anisotropy of the energy spectra of simulations, and so the jet direction.

Additionally, there is a need to characterise accurately the isopycnal mixing occurring throughout the Southern Ocean. We utilise satellite measurements to estimate isopycnal diffusivities in the Southern Ocean in two different studies. Using an effective diffusivity diagnostic to extend a previous study, we find reduced surface horizontal mixing at the latitudes of the ACC core. By comparing a tracer advection simulation with measurements from an experiment in the Southern Ocean, we find that simulations with a vertically averaged horizontal diffusivity of $\sim 20 \text{ m}^2\text{s}^{-1}$ best match observations in the Pacific sector of the ACC.

Jets, Mixing, and Topography in the Southern Ocean



Emma J. D. Boland

Department of Applied Mathematics and Theoretical Physics

University of Cambridge

A thesis submitted for the degree of

Doctor of Philosophy

May 2013

Acknowledgements

I owe a great many people thanks for their help, both indirectly and directly, for completing this thesis.

Firstly, I would like to thank both my supervisors, Peter and Emily, who were always generous with their time, and provided guidance, encouragement, and insight every step of the way. It has been a pleasure to work with them, I have learnt an immeasurable amount, and hope to continue to collaborate with them in the future.

Andrew Thompson also deserves my gratitude, for giving so much of his time in the first year of my PhD, reading endless re-writes of my work, and always willingly contributing, whether it be looking at a line of code or discussing potential vorticity.

I have also had the pleasure to work along side many colleagues at DAMTP and BAS who I would now count as friends. Both groups have helped make the last 3+ years much easier, by providing a supportive atmosphere in which there was always someone willing to lend a hand with a particular problem, have a cup of tea with, or buy me a pint.

I would like to thank my family and my parents, Catharine and Henry, in particular, for their love and support. My parents taught me to live my life independently, and both have demonstrated the value of hard work. Knowing that they believe in me and support me unconditionally has always given me confidence.

Finally, and most importantly, I owe the biggest thanks to my husband Rob. Without you, I'm sure I would not have managed to stay sane. You are always there to listen to me talk about work, or distract me completely, which ever is called for. Countless times over the past years you have cooked, handed me a large drink and provided encouragement. Your tireless belief in me has kept me going at my lowest ebb, and I am eternally grateful for your love.

Summary

The Southern Ocean holds a unique place in our planet. It is home to the world's longest and strongest ocean current, the Antarctic Circumpolar Current (or ACC), which is formed of jets (alternating velocity structures), thought to be significant surface transport barriers. The dynamical processes (particularly mixing processes) in the Southern Ocean are crucial to driving the global overturning circulation, which is in turn responsible for the global transport of heat, CO₂, and nutrients. Despite the evident importance of the Southern Ocean to current and future climate, the important dynamical processes that occur there are poorly understood.

This thesis attempts to contribute towards the understanding of some of the open questions in Southern Ocean dynamics. In particular, we investigate the effect that topography might have on the jets that form the ACC, with regards to their formation and in particular, their transport properties. Through a quasi-geostrophic model we investigate the properties of jets that form over a zonal slope in bottom topography, and find that the jets become tilted, aligning perpendicular to the large-scale barotropic potential vorticity gradient. As the jets tilt more, they become significantly more energetic, corresponding with an increase in across-jet transport. We compare various theories regarding the formation of such jets, involving linear analysis of the system. It is found that the analytical form of the Rossby wave frequencies correctly predicts the anisotropy of the energy spectra of simulations, and so the jet direction.

Additionally, there is a need to accurately characterise the isopycnal mixing occurring throughout the Southern Ocean. We utilise satellite measurements to estimate isopycnal diffusivities in the Southern Ocean in two different studies. Using an effective diffusivity diagnostic to extend a previous study, we find reduced surface horizontal mixing at the latitudes of the ACC core. By comparing a tracer advection simulation with measurements from an experiment in the Southern Ocean, we find that simulations with a vertically averaged horizontal diffusivity of $\sim 20 \text{ m}^2\text{s}^{-1}$ best match observations in the Pacific sector of the ACC.

This dissertation is the result of my own work and includes nothing which is the outcome of work done in collaboration except where specifically indicated in the text. This dissertation is not substantially the same as any submitted for a degree or diploma or other qualification at the University of Cambridge or any other university or similar institution and no part, has already been, or is concurrently being, submitted for any degree, diploma, or other qualification at the University of Cambridge or any other university or similar institution.

Contents

Contents	iv
1 Introduction	1
1.1 The Southern Ocean and the Climate System	1
1.2 Southern Ocean dynamics	3
1.2.1 Eddies	5
1.2.2 Jets	7
1.3 The Southern Ocean in models	9
1.4 Open questions in the Southern Ocean	12
2 Jet Formation in a Quasi-Geostrophic Model of the Southern Ocean	14
2.1 Introduction	14
2.1.1 Rossby wave theories	15
2.1.2 Zonostrophic instability theory	17
2.1.3 Noodle mode theory	18
2.1.4 PV theories	19
2.2 Rossby wave frequencies	21
2.2.1 Beta Plane	21
2.2.2 Topographic Slope	29
2.2.3 Systems with background shear and bottom friction	41
2.2.4 Unstable Modes	58
2.3 Conclusions	63
3 Jet Properties in a Quasi-Geostrophic Model of the Southern Ocean	67
3.1 Introduction	67
3.2 Model	73
3.2.1 Equations	73

3.2.2	Example Results	76
3.3	Results	79
3.3.1	Jet Deflection	79
3.3.2	Jet Spacing	84
3.3.3	Eddy Energy Production	85
3.3.4	Jet Drift	90
3.3.5	Transport	93
3.4	Unequal Layer Depths	102
3.5	Ridged topography	105
3.5.1	Barotropic Control: Varying Slope Magnitude	108
3.5.2	Barotropic Control: Varying Ridge Width	112
3.5.3	Large Scale Baroclinic Compensation	113
3.5.4	Jet Drift	123
3.5.5	Summary	127
3.6	Conclusions	130
4	Effective Diffusivity in the Southern Ocean	134
4.1	Introduction	134
4.2	Altimetric Data	137
4.2.1	Comparison with previous generation altimetry	137
4.2.2	Mean-anomaly decompositions	139
4.3	Effective Diffusivity Calculation	148
4.3.1	Numerical Simulation Description	148
4.3.2	Results: Spatial Distribution	154
4.3.3	Results: Temporal Variability	157
4.4	Other mixing parameterisations	160
4.4.1	Comparison with κ_{FN}	162
4.4.2	Spatial distributions	164
4.4.3	Temporal Variability	170
4.5	Conclusions	173
5	DIMES: A tracer experiment in the Southern Ocean	177
5.1	Introduction	177
5.1.1	Results so far	178
5.2	2-D simulations	182
5.2.1	Experiment description	182

5.2.2	Velocity field analysis	185
5.2.3	Varying the velocity fraction	188
5.2.4	Varying the horizontal diffusivity	191
5.2.5	Aside: Roughness calculation	197
5.2.6	Roughness calculation results	201
5.3	Conclusions	211
6	Conclusions	213
References		222

Chapter 1

Introduction

1.1 The Southern Ocean and the Climate System

The Southern Ocean holds a unique place in the climate system of our planet. It is home to the world's longest and strongest ocean current, the Antarctic Circumpolar Current or ACC, which transports ~ 150 Sv ($10^6 \text{ m}^3\text{s}^{-1}$) around a path 24 000 km long. It is also unique in its geographical extent - due to the lack of continental barriers at the latitudes it inhabits, it is circumpolar, i.e. it encircles the globe completely. Its key importance in the climate system is in part due to the fact that it joins all three major ocean basins together: the Atlantic, Pacific and Indian oceans communicate temperature, salinity, CO₂ and other important climate attributes via the Southern Ocean. It is also home to an important limb of the ocean meridional overturning circulation (a.k.a. the ocean conveyor belt or thermohaline circulation) or MOC, as recently reviewed by [Marshall and Speer \(2012\)](#). The Southern Ocean is where mid-depth water is transported to the surface along sloping isopycnals, unique to the Southern Ocean, and then transformed into other water masses before being transported back into other ocean basins at various depths. Figure 1.1 shows a schematic of the MOC with the importance of the Southern Ocean apparent as a region home to many processes, where cooler colours represent denser water masses and reds lighter, warmer waters.

The time-scale of circulation around the MOC is on the order of thousands of years, and given that most of the ocean only interacts with the atmosphere in the polar regions, the properties taken on by water masses in these locations are essentially ‘locked away’ in the ocean interior on short to medium climate time scales. The ocean as a whole currently takes up a significant fraction of emitted CO₂ from the atmosphere [$\sim 30\text{-}50\%$, see for example, [McElroy \(2012\)](#); [Sabine et al. \(2004\)](#)], and the Southern Ocean is responsible

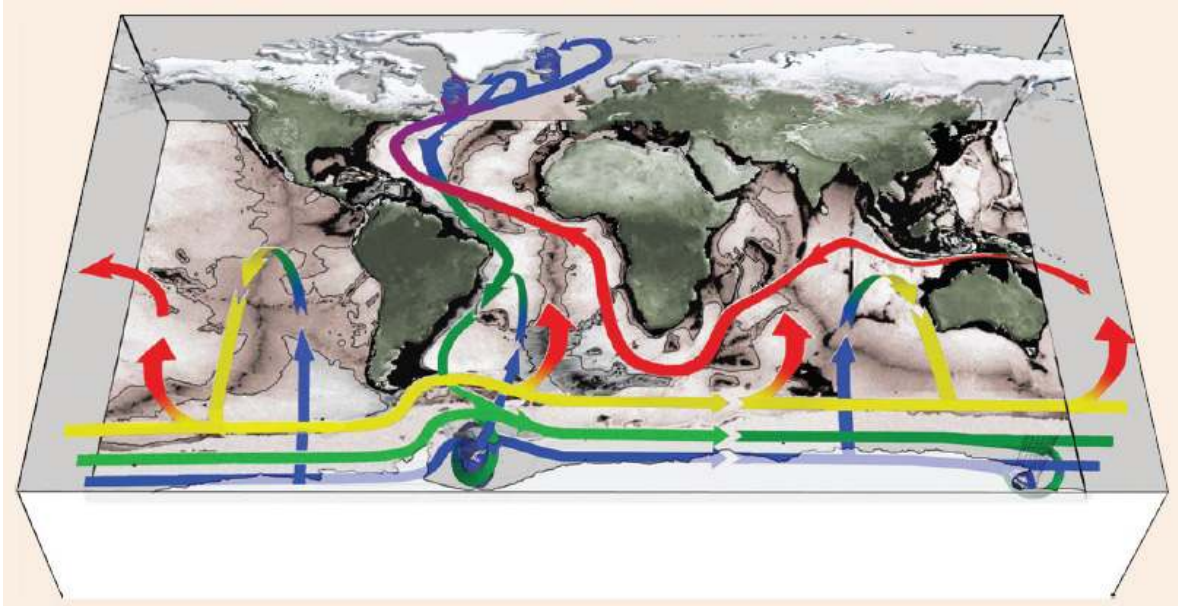


Figure 1.1: Schematic of the meridional overturning circulation, with cooler colours representing more dense water masses and reds less dense water masses. The Southern Ocean is home to a number of important processes, transforming mid-depth water(greens) into upper layer waters (reds and yellows) and deep water (blues). ([Marshall and Speer, 2012](#)).

for a significant proportion of this, so the dynamical properties of the Southern Ocean are extremely important for setting current atmospheric CO₂ levels. In addition, future changes to atmospheric dynamics due to climate change are likely to have a significant impact on carbon and heat sequestration in the Southern Ocean. In fact, [Le Quéré et al. \(2007\)](#) find, using a combination of observations and an inverse model, that the Southern CO₂ sink may in fact be decreasing on decadal time scales due to increasing winds attributed to climate change. [Le Quéré et al. \(2007\)](#) find that this is likely due to increased CO₂ out-gassing due to increased mixing and upwelling driven by the increased winds. This has mainly been observed in a strengthening of the Southern Annular Mode or SAM, the main mode of atmospheric variability in the extra-tropical Southern Hemisphere, see [Thompson et al. \(2011\)](#), who attribute this change to a combination of global warming and ozone depletion.

There is also evidence to suggest that the Southern Ocean may have been important for setting atmospheric CO₂ on glacial-inter-glacial time-scales in the past, see [Sigman and Boyle \(2000\)](#). Although regions of upwelling may well have been in different locations in previous millennia, there is evidence that Southern Ocean upwelling may have played a significant role in glacial cycles through mechanisms such as: air-sea buoyancy flux

variation increasing eddy activity (Watson and Garabato, 2006), increased sea-ice cover reducing CO₂ out-gassing (Stephens and Keeling, 2000), latitudinal shifts in Southern hemisphere westerlies altering the MOC (Toggweiler et al., 2006), and increased heat in the Southern Hemisphere due to the shutting down of the MOC in the northern hemisphere because of freshwater fluxes from melting Arctic ice (Stocker, 1998).

Despite the evident importance of the Southern Ocean to current and future climate as well as its vital role in the dynamics of the MOC, the important dynamical processes that occur there are poorly understood. This is partly due to its remote location making in situ measurements difficult to obtain and therefore sparse in space and time. This has been somewhat ameliorated by the advent of satellite measurements, although these cannot provide detailed information about the interior. It is also due to the unique nature of the Southern Ocean and the ACC, as discussed above, making many processes there unlike those observed elsewhere. The rest of this chapter will focus on describing these dynamical processes, specifying the areas of current uncertainty and which questions this thesis will try to contribute towards answering.

1.2 Southern Ocean dynamics

As mentioned in the previous section, the Southern Ocean plays an important part in the global MOC, bringing up water from mid-depth to the surface, where it is transformed into other water masses. It is this isopycnal transport of water to the surface combined with the circumpolar nature of the Southern Ocean that is thought to provide an answer to the ‘missing mixing’ paradox puzzling oceanographers since the seminal work of Munk (1966). In this work, Munk uses a simple one dimensional model of abyssal vertical transport which predicted that measured upwelling values should be balanced by an average interior diapycnal eddy diffusivity of the order of $10^{-4} \text{ cm}^2\text{s}^{-1}$. In situ measurements consistently find values on average an order of magnitude lower than this, leading to the so-called ‘missing mixing’ paradox. However, the tilted isopycnals of the Southern Ocean allow for isopycnal transport to close the vertical circulation and predicts the correct abyssal stratification, without call for regions of extra mixing to be found, see discussion in, for example, Nikurashin and Vallis (2011).

Several studies have pointed to topography being a leading cause of the spatial variability observed in the eddy field in the Southern Ocean. As mentioned previously, the topography of the Southern Ocean is unique in that it is a circumpolar ocean with no latitudinal continental boundaries. Figure 1.2 shows the bathymetry of the region with

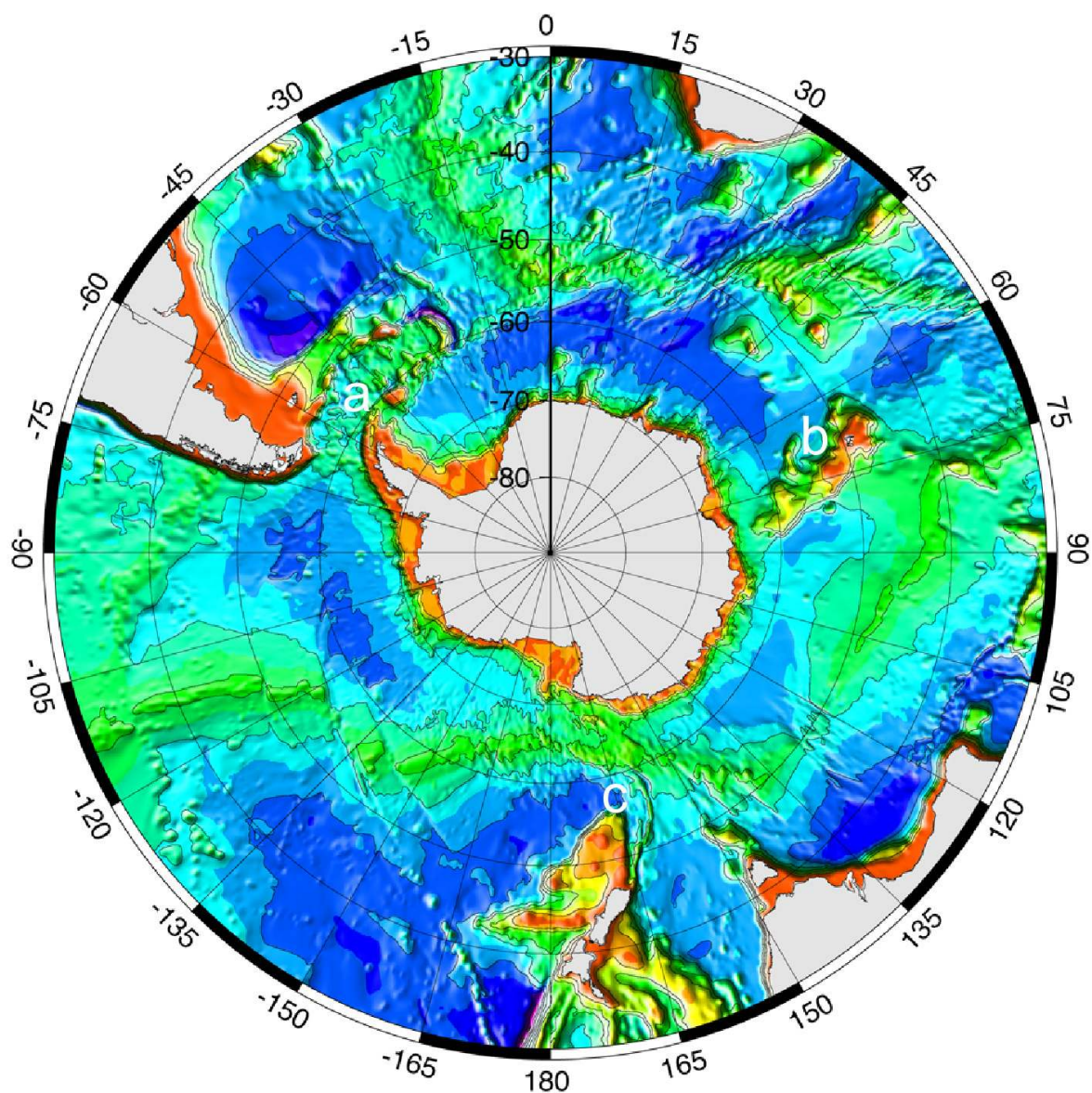


Figure 1.2: a - Drake Passage, b - Kerguelen Plateau, c - Macquarie Ridge. ([Hayes and Weisssel, 2009](#))

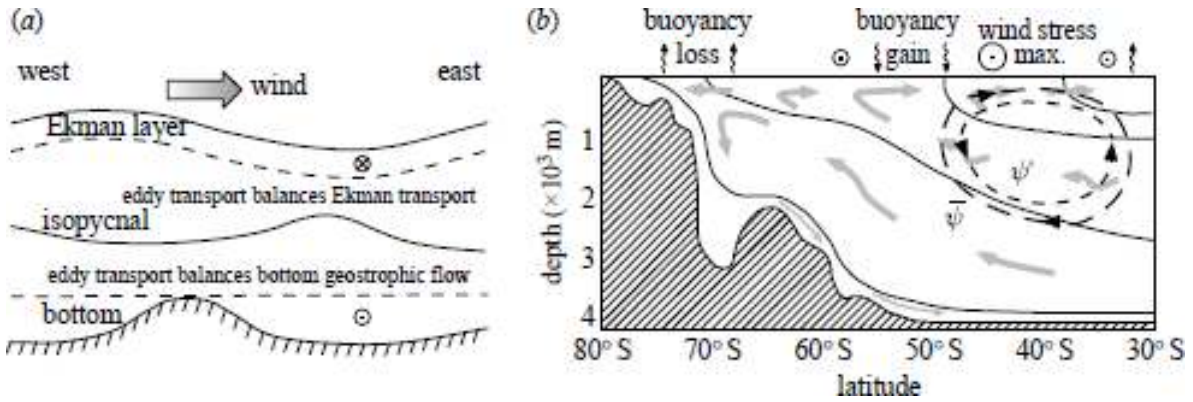


Figure 1.3: ACC schematics showing a) a zonal section and b) a meridional section. a) shows how eddies can transport meridional momentum vertically by displacing isopycnals. b) shows the Eulerian $\bar{\psi}$ and eddy ψ' overturning cells (circular curves), transport (grey arrows) and isopycnal surfaces (black lines). From [Thompson \(2008\)](#).

several important features labelled. The Drake Passage (labelled a) is where the Southern Ocean is squeezed through the narrow gap between South America and the Antarctic Peninsula. The Kerguelen Plateau (labelled b) and the Macquarie Ridge (labelled c) are where large topographic ridges are found due to plate tectonics. Several studies have shown that downstream of these regions are patches of increased EKE ([Williams et al., 2007](#)) and increased across streamline transport ([Thompson and Sallée, 2012](#)).

1.2.1 Eddies

Eddies play a crucial role in setting the tilt of the isopycnals in the Southern Ocean, and so the meridional overturning transport, as well as being vital to the meridional momentum balance of the ACC. These effects are shown schematically in figure 1.3, taken from [Thompson \(2008\)](#). Figure 1.3a shows the necessity for a momentum link between the upper Ekman layer of the Southern Ocean and the bottom topography. Strong westerlies impart eastward momentum into the upper ocean, which has a northward Ekman flow component due to the Coriolis effect. This meridional momentum would be balanced by an east-west pressure gradient in an ocean basin, but due to the unique lack of zonal continental boundaries in the Southern Ocean, the momentum has to be balanced by zonal pressure gradients across large topographic features on the ocean floor. To transport the meridional momentum in the interior, meso-scale eddies are required which communicate the transport by the displacement of isopycnal layer interfaces.

Figure 1.3b shows the role of the eddy-induced overturning, ψ' , in setting the total

meridional overturning. The solid lines represent isopycnals, which are tilted due to a combination of buoyancy forcing and wind stress divergence, also shown. The tilted isopycnals are a source of potential energy, released through baroclinic instability as kinetic energy, creating meso-scale eddies which act to relax the isopycnals. Thus, it is the balance between these forcings that sets the overall tilt of the isopycnals, and so the overall overturning transport. The net overturning streamfunction ψ , is often called the residual overturning, and is decomposed into the Eulerian mean transport $\bar{\psi}$, produced by wind and buoyancy forcing, and the eddy transport ψ' , both of which are depicted in figure 1.3b, i.e. $\psi = \bar{\psi} + \psi'$. This simple residual-mean decomposition allows for the parametrisations of eddies, see, for example, Visbeck et al. (1997). However, these parametrisations assume the ocean interior is purely diabatic, and neglects spatial variations in, for example, buoyancy and wind forcing, due to the averaging inherent.

One of the key open questions facing oceanographers in the Southern Ocean is what the effect of increasing westerlies, which, as discussed earlier, have been observed in the recent past and are predicted to continue as a result of climate change, will have on the transport of the ACC. The ACC is thought to be a primarily wind-driven current (although some recent studies have suggested diapycnal mixing could provide a significant forcing, see Munday et al. (2011)) and so one might expect increasing winds to drive an increasing zonal ACC volume transport. Indeed, this is what is observed in global circulation models which parametrise eddies as discussed previously, see Fyfe and Saenko (2006). However, studies using eddy-resolving models (Hogg et al., 2008) and observations (Böning et al., 2008) suggest that the ACC volume transport is not correlated with wind forcing on inter-annual time-scales. This is thought to be because the ACC is in an ‘eddy saturated’ regime, whereby increasing winds increase eddy activity, and the net result is no large change in transport. The increasing winds will increase the isopycnal tilt, which will initially increase overturning and the zonal transport of the ACC. However, following a short transition period, the increased tilt of the isopycnals will drive stronger baroclinic instability, creating more vigorous eddies, which will ultimately reverse the increased isopycnal tilting and the increase in zonal transport.

Eddy *saturation* is often discussed in conjunction with the concept of eddy *compensation*, which relates to the similar theory that the meridional overturning in the Southern Ocean will be insensitive to wind forcing. The two are often thought to be two parts of the same phenomenon, but recent studies (Morrison and McC. Hogg, 2013; Munday et al., 2013) have argued that they are separate, and found that whilst a large degree of eddy saturation is present in eddy resolving models, there appears to be little eddy com-

pensation, with increasing wind forcing leading to increasing overturning. This will have implications for air-sea exchange processes, giving surface waters less time to equilibrate with the atmosphere before being subducted.

1.2.2 Jets

Large scale flows in the atmosphere and ocean are consistently observed to form jets in measurements and in simulations (Rhines, 1994). Jets are defined as banded velocity structures, often observed to be zonally orientated with narrow, faster, eastward flowing regions and broad, slower, westward flowing regions. Figure 1.4 shows an example of the jets that form the ACC in a snapshot of the observed sea surface height (SSH) gradient field, associated with surface velocity via geostrophic balance, in a patch of the Southern Ocean below Australia and New Zealand. These are formed due to interactions between the turbulent (eddy) part of the flow and the wave-like part of the flow, whereby instabilities of the waves produce eddies which feed back on the waves, strengthening the jets, however the exact mechanism of jet formation is still disputed, see chapter 2.

As discussed in Dritschel and McIntyre (2008), jets can be understood in terms of potential vorticity (PV). In the absence of friction, atmospheric and oceanic flows conserve PV. The PV of a fluid parcel Q depends on its relative vorticity, η , the planetary vorticity f , and the depth of the fluid parcel h , $Q = (\eta + f)/h$. PV conservation results in the wave-like part of the flow, where the restoring force is the apparent gradient in the planetary vorticity $f = 2\omega \sin \theta$, where ω is the Earth's rate of rotation and θ is latitude. PV conservation also results in topographic steering, important in the Southern Ocean, whereby topographic features that alter h can cause fluid parcels to migrate, (meridional motion changing f) or to change their relative vorticity. The relationship between a parcel's relative vorticity and PV leads to the 'invertibility principle' which links the velocity of the parcel with its PV.

Thus strong jets are associated with strong PV gradients, and regions of high eddy activity which mix PV with weak PV gradients, leading to the 'PV staircase' picture of alternating strong and weak gradients discussed in Dritschel and McIntyre (2008). This study explains jets as emerging spontaneously because of a positive feedback mechanism, comparable to the 'Phillips effect' (Phillips, 1972), which describes the spontaneous vertically inhomogeneous mixing of the background buoyancy gradient of a stably stratified fluid. Starting with a large scale planetary PV gradient, baroclinic instability forms eddies, which mix out the large scale gradient, producing locally weak PV gradients adjacent

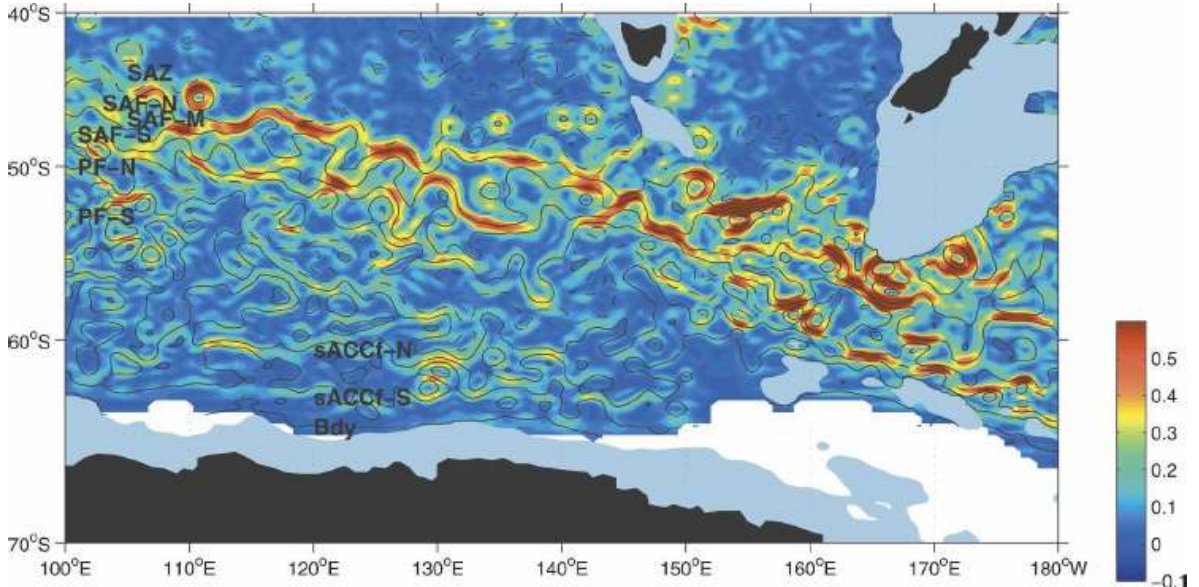


Figure 1.4: Snapshot of the ACC south of Australia and New Zealand on 3 July 2002. Colour shows the instantaneous SSH gradient, and the black lines are mean SSH contours. Shading indicates depths shallower than 2.5km. From [Sokolov and Rintoul \(2007\)](#).

to strong gradients. These strong gradients are associated with jets, which shear the eddies, causing an up-gradient momentum flux, which further sharpens and strengthens the eastward jets.

Until recently, the jets of the ACC had been viewed as zonally orientated circumpolar features, concurrent with fronts, the boundaries between water masses of different properties, see for example figure 1.5a. However, studies using high resolution satellite data such as [Sokolov and Rintoul \(2007\)](#), reveal a richer, more varied, filamentary structure, see figure 1.4. These jets are often non-zonal, and are not zonally consistent - they merge and separate, disappear and reappear as one moves around the pole. However, in other respects they display persistence - the number and position of jets is fairly consistent over time in a particular region. As discussed earlier, eddies play an important role in determining the large scale meridional overturning of the Southern Ocean. It is therefore an area of active interest as to how jets might alter local transport properties, how eddies and jets interact, and how changes in eddy activity might alter jet properties. Studies such as [Greenslade and Haynes \(2008\)](#) have shown that jets can either be ‘barriers’ or ‘blenders’ with respect to meridional transport, with behaviour varying in the vertical. Satellite measurements imply that ACC jets are barriers at the surface, with enhanced mixing on their northern flanks, see [Marshall et al. \(2006\)](#). Measurements of

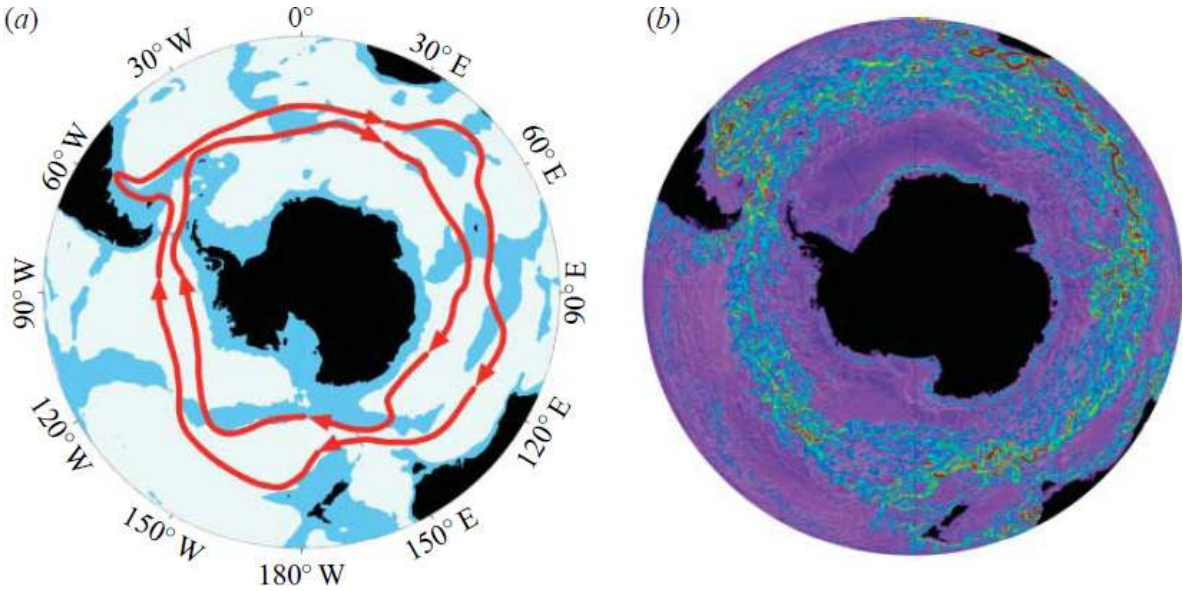


Figure 1.5: a) ACC schematic with bathymetry shallower than 3.5 km shaded blue. b) Snapshot of surface speed from the OCCAM 1/12° ocean model ([Lee and Coward, 2003](#)). The jets of the ACC are clearly visible as bright filaments. Figure from [Thompson \(2008\)](#).

ACC jet structure in the vertical are extremely sparse, but a similar study using model data ([Abernathy et al., 2010](#)) shows the ACC to exhibit enhanced mixing at depth in a zonally averaged picture. However, studies such as [Williams et al. \(2007\)](#) show highly spatially variable eddy activity in the Southern Ocean, suggesting understanding local effects will be crucial to understanding how the large scale circulation might vary in a changing climate.

1.3 The Southern Ocean in models

The Southern Ocean has been represented in models with a range of complexities, from full Earth system models to simple 2D quasi-geostrophic models to 1D flux models. Due to computational restrictions, modern global circulation models and earth system models are eddy-permitting, rather than eddy-resolving. This requires some parametrisation of eddy activity, as previously mentioned. [Lee and Coward \(2003\)](#) studied the Southern Ocean in the OCCAM model at 1/4° (eddy permitting), and showed that at that resolution, the eddy transport is dependent on the choice of co-ordinates. However, running the same model at higher resolution (1/12°) can show the same filamentary structure as observations, see figure 1.5b.

The simplest domain used in models of the ACC is a re-entrant zonal channel, and

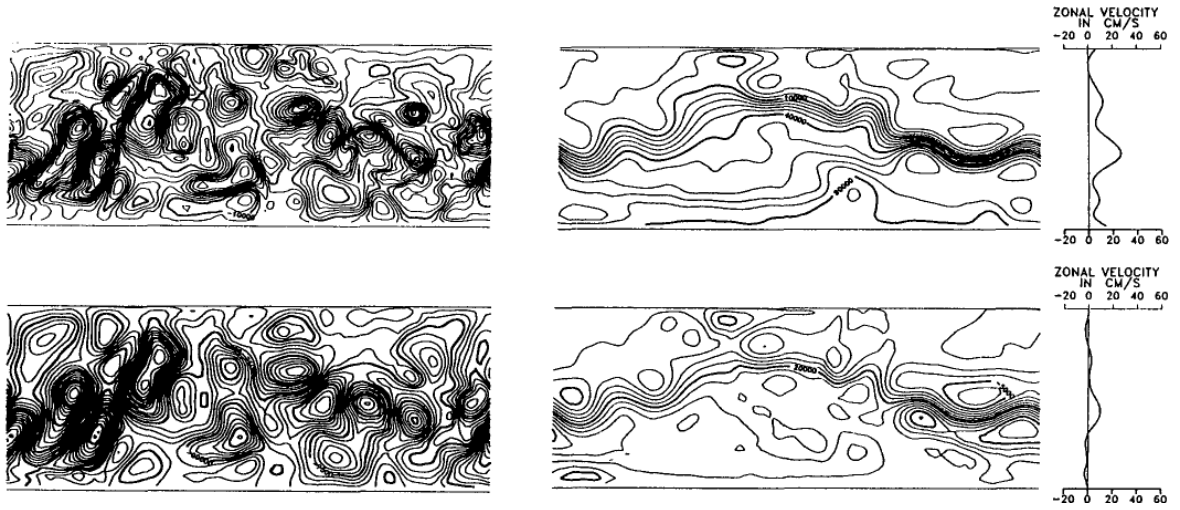


Figure 1.6: Results from Wolff et al. (1991), showing instantaneous eddy streamfunctions (left), time-mean eddy streamfunctions (centre) and zonal mean zonal velocities (right) from upper (top panels) and lower (bottom panels) layers. The topography in these simulations imitates the Macquarie Ridge, and reproduces some of the form of the ACC in this region.

many studies have used 2-layer quasi-geostrophic beta-plane models in this configuration, such as Krupitsky and Cane (1997); Treguier and McWilliams (1990); Treguier and Panetta (1994); Witter and Chelton (1998) and Wolff et al. (1991). These have a range of topography, from flat bottoms to more accurate bathymetry. Figure 1.6 shows results from Wolff et al. (1991) where, in one simulation, the topography imitates the Macquarie Ridge. The upper panels show the upper layer, the lower panels the lower layer, and from left to right are plotted instantaneous eddy streamfunctions, time mean eddy streamfunctions and zonally averaged zonal velocities. This shows that even a simple model such as this can reproduce some of the form of the jets seen in this region. The results from all of these studies have emphasised the importance of topography in altering the dynamics of the ACC.

Primitive equation models have also shown that topographic effects in the ACC are important: Jackson et al. (2006) used the isopycnal 1/12° MICOM model to show that bottom pressure torques significantly steer jets, by transferring vorticity from wind-driven gyres near topographic obstacles or submerged topography. Losch and Heimbach (2007) used the MITgcm adjoint model to show that topography is as important as surface boundary conditions in setting the mean circulation of the ACC. Despite the advancements made in these state-of-the-art models, there are still important insights to be gained from simpler models. This is demonstrated in Venaille et al. (2011), in which

the authors compare the results from a primitive equation model to a quasi-geostrophic model, using averaged fields from the former to force the latter, in six locations throughout the Southern Ocean. They find good agreement for some locations, but in others, particularly those with high eddy activity, the QG model does not equilibrate.

In other recent work, [Ioannou et al. \(2011\)](#) use a quasi-linear model of a wind-forced ACC, in which eddy-eddy interactions are parametrised and the model is forced stochastically. The study found two distinct statistically equilibrated regimes, dependent on wind variance: moderate variance resulted in an ACC transport linearly dependent on wind stress, and high variance resulted in a state similar to the observed eddy saturated regime, with very weak transport dependence on wind stress. This points to wind variance as a possible parameter of interest for more complicated models.

A subset of the modelling literature not often referenced is that of linear models of the Southern Ocean, see a recent review by [LaCasce and Isachsen \(2010\)](#). As mentioned previously, the prevailing view of oceanographers is that meso-scale eddies are of first-order important in determining the transport of the ACC. However, there are indications that many of the features of the Southern Ocean, including realistic sea-surface height fields, can be produced in linear models with no explicit eddy processes.

Linear models assuming barotropic ACC flow, such as those investigated in [Gill \(1968\)](#), [Webb \(1993\)](#) and [Ishida \(1994\)](#), successfully reproduce circumpolar jet structures, but over-estimate the ACC transport without the inclusion of unrealistically high bottom friction. Improved transport estimates come from an equivalent barotropic model, studied in [Krupitsky et al. \(1996\)](#), where the velocity is assumed to be self-similar at all depths, with a vertical structure dependent on a prescribed e -folding scale. To obtain a realistic value of ACC transport, however, [LaCasce and Isachsen \(2010\)](#) add lateral dissipation in the form of a viscosity, assumed to be induced by eddies. This also produces realistic-looking sea-surface height fields.

The success of this simple model is impressive, however the inclusion of the eddy viscosity does indicate that eddies are an important part of the dynamical balance. Additionally, these linear models provide no explanation for the vertical structure of the velocity, determined in reality by the stratification, which must be specified. The model also predicts that the transport will be dependent on the integrated wind stress, but as mentioned previously, most eddy-permitting models consistently show a weak (or no) response in ACC transport to increasing winds. Nonetheless, the simplicity of these models could allow for their use in conjunction with more complicated models and observations in tackling questions about the momentum balance of the Southern Ocean.

1.4 Open questions in the Southern Ocean

As previously discussed, due to the lack of observations, there remain many open questions for oceanographers studying the Southern Ocean, and a few have been mentioned already in this chapter. As mentioned in section 1.2, although it has been recently hypothesised that the tilting of isopycnals in the Southern Ocean solves the ‘missing mixing’ paradox, it has not been universally proven as such, and it still remains to be measured how much interior diapycnal mixing could be taking place in hot-spots throughout the Southern Ocean. In general, there is a need to accurately characterise the diapycnal and isopycnal mixing occurring throughout the Southern Ocean.

Thus, in this thesis, chapters 4 and 5 use observations of the Southern Ocean to investigate how comparisons between a tracer release experiment and offline simulations using satellite altimetry could produce estimates of the isopycnal mixing occurring in the Southern Ocean. A surface effective diffusivity is calculated in chapter 4, and chapter 5 diagnoses a localised interior isopycnal diffusivity by comparing simulations with a tracer release experiment. These results both provide much needed information about the distribution of isopycnal mixing in the Southern Ocean, of use for comparison with models and other observations.

The jets that form the ACC also pose many questions. As discussed, there is evidence that the jets are transport barriers at the surface, and increase mixing at depths, although again this is still not certain. Open questions being studied are what the effects of topography are on the jets - if it can affect jet formation, and how it might alter their transport properties. Topographic steering is thought to play a role in the non-zonality of the observed jets, but the dynamic mechanisms for jet steering are not well determined. While topography is thought to be the leading cause of the zonal variations in jet properties, there are still questions as to what determines the temporal variability of jet formation and transport, and how this might be linked to wind forcing, eddy activity, and internal variability. This understanding is again limited by the lack of time series observations, apart from at the surface.

In response to these questions, chapters 2 and 3 investigate the effect of a generally orientated slope in topography on jets in a simple quasi-geostrophic model. Chapter 2 looks at the linear properties of the system and jet formation theories within quasigeostrophic systems. We believe this work advances the understanding of jet formation, leading to the identification of the barotropic PV gradient as central to determining jet properties. The possible implications of this for the Southern Ocean are discussed in chapter 6. Chapter 3

looks at the properties of the jets that form in this system, including the energetics and transport properties, which has implications for the properties of the jets of the Southern Ocean, suggesting there may be increased cross-jet transport at all depths in the presence of large-scale, gentle, non-meridional topographic slopes. In chapter 3, sections 3.1 to 3.3 have been published in part in [Boland et al. \(2012\)](#), although there is extended discussion in the introduction and of the one-layer barotropic model here.

The thesis finishes with chapter 6, summarising the conclusions of the thesis, and looking to possible future work.

Chapter 2

Jet Formation in a Quasi-Geostrophic Model of the Southern Ocean

2.1 Introduction

The phenomenon of the formation of zonal jets on a β plane is still the subject of a number of competing theories, despite study over the last 35 years. In this chapter, we will test several current theories on the formation of zonal jets, with regards to how they can be adapted to a two-layer baroclinic system with a general slope in bottom topography (the jets that form in this system will be investigated in chapter 3). By examining which theories are consistent with simulations, we hope to further understanding of the jet formation phenomena, by at the very least ruling out some contenders. Whilst all of the jet formation theories explained in the following are describing the same phenomenon, and are not mutually exclusive, we nonetheless broadly categorise and describe some of the main competitors. We note that some of these theories are derived for barotropic systems only, and some for baroclinic systems with two layers. We can either attempt to extend these theories to two layers, or we can view our system as a barotropic ‘mode’ forced by baroclinic instability. This interpretation could be argued to not be strictly applicable, as the normal modes of our system are not the barotropic and baroclinic fields of the system. This is discussed in detail in section 2.2.3, where we see that at scales $k\lambda \ll 1$, the normal modes are, in fact, barotropic- and baroclinic-like.

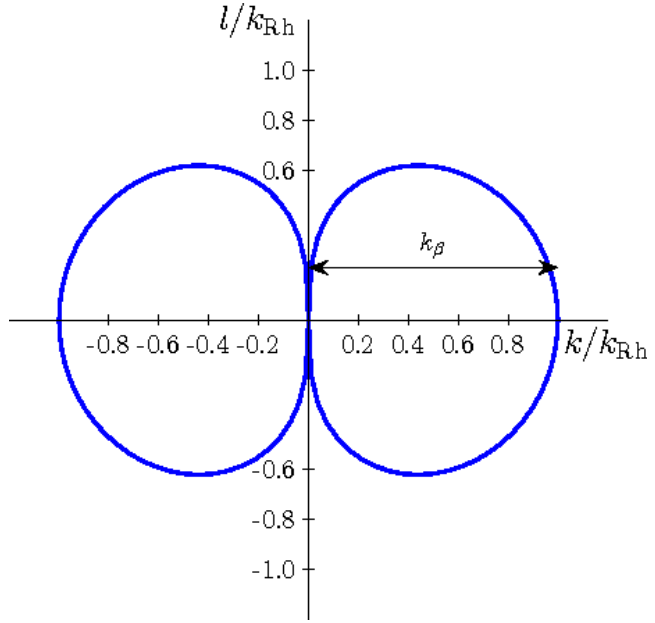


Figure 2.1: Theoretical cascade barrier for 2D barotropic turbulence, derived by equating the Rossby wave frequency $\omega_{\bar{\psi}}$ with the Rhines turbulent frequency ω_t^{Rh} . The cascade barrier scale, k_β , is labelled, and equal to the Rhines scale, k_{Rh} , in this case.

2.1.1 Rossby wave theories

The first study to look in detail at quasi-geostrophic simulations on a β plane was [Rhines \(1975\)](#). In this seminal paper, Rhines sets out a theory for the formation of zonal jets in a barotropic quasi-geostrophic system, and the scale at which they form, known thereafter as the Rhines scale. Energy and enstrophy conservation in 2-D barotropic turbulence implies that the energy of the system will seek the gravest mode, or largest physical scale [see, for example, [Vallis \(2006\)](#)]. If we assume that the frequency of this turbulence is given by $\omega_t^{\text{Rh}}(K) = U_t K$, where U_t is a velocity scale of the turbulence and $K \equiv |\mathbf{k}|$ is the total wavenumber, then it is clear that the turbulent frequency decreases as the ‘inverse cascade’ of energy heads towards the gravest mode. Rhines postulated that when the energy reaches the frequency at which Rossby waves can be supported, the excitation of these waves would, to a large extent, halt the cascade, leaving most of the energy at a finite wavenumber.

The frequency of the Rossby waves supported by the system, $\omega_{\bar{\psi}}$, can be derived by linearising the system equations, see figure 2.2, left panel, for the form of $\omega_{\bar{\psi}}$, and section 2.2 for details of the derivation. Equating $\omega_{\bar{\psi}}$ with ω_t , one can derive the form of the cascade barrier, plotted in figure 2.1, where the cascade barrier scale, $k_\beta = k_{\text{Rh}}$, the

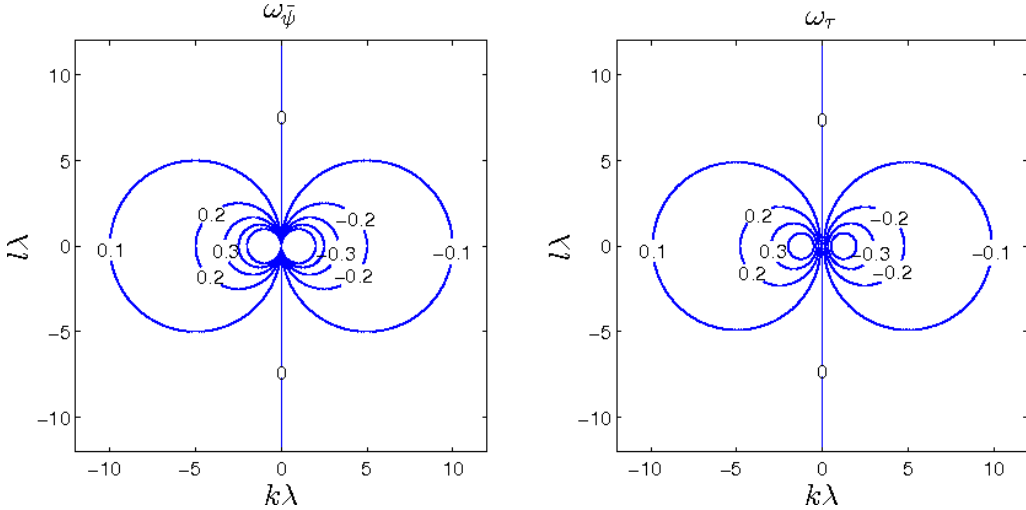


Figure 2.2: Rossby wave frequencies for a two layer unforced quasigeostrophic system with barotropic ($\omega_{\bar{\psi}}/\beta\lambda$) and baroclinic ($\omega_{\tau}/\beta\lambda$) modes, see (2.5) and (2.6).

Rhines scale, is labelled. The anisotropic nature of $\omega_{\bar{\psi}}$ leads to an anisotropic cascade barrier, which theoretically provides a pathway for the continuing inverse cascade for modes with zero zonal-wavenumber k , because $\omega_{\bar{\psi}}(k = 0, l) = 0$. The cascade halts at k_{jet} , close to a scale given by k_{Rh} , albeit on a mode with $k = 0$, such that the resulting form of the system is one with large-scale variation in the meridional direction, i.e. zonal jets. As to why the cascade should halt close to k_{Rh} , [Vallis and Maltrud \(1993\)](#) appeal to resonant triad theory, and the fact that modes with similar wavenumbers cannot efficiently excite further modes with similar wavenumbers. [Smith et al. \(2002\)](#) derive a halting scale, k_{jet} , that is determined by the removal of energy at low wave-numbers by friction. These ideas will be further investigated in section 2.2.

In [Rhines \(1977\)](#), the theory is extended to include baroclinic turbulence, which crucially introduces different possible cascade routes, dependent on initial conditions. Specifically, there is the tendency for barotropization of energy starting in the baroclinic mode, resulting in the same halting as discussed above. Alternately, low energy, high wavenumber baroclinic states will be halted in the baroclinic regime. See section 2.2.1 for further discussion.

Rhines' ideas were extended and tested further in [Vallis and Maltrud \(1993\)](#), which we will refer to as VM93 from now on. They compare k_{Rh} with the measured cascade barrier k_{β} from simulation and with the theoretical form for two other turbulent frequency scalings: a Kolmogorov scaling $\omega_t^{\text{Ko}}(K) = \varepsilon^{1/3} K^{2/3}$, and a vorticity scaling $\omega_t^{\zeta} = \bar{\zeta}$, where

$\bar{\zeta}$ is the r.m.s. vorticity. As can be seen in their figure 3, the choice of turbulent scaling makes very little difference to the form of the cascade barrier, as the anisotropy of $\omega_{\bar{\psi}}$ largely determines the shape. Presenting simulations in which they vary β , they confirm that, as predicted, k_{jet} is consistently of the same magnitude as, but smaller than the cascade barrier scaling, k_{β} . The theoretical scalings are of similar magnitude, but larger than both k_{β} and k_{jet} .

[Smith et al. \(2002\)](#) derive a similar prediction for k_{β} using Kolmogorov turbulent scaling, which only differs from VM93 by constant pre-factors. They also derive a halting scale, k_{jet} , which depends on the assumption that the cascade between k_{β} and k_{jet} should be a function of β only, and that this part of the cascade will contain the majority of the energy of the system. In comparing with simulation, they find the cascade extends beyond their theoretical k_{β} on the k -axis, and find over-prediction by their theoretical k_{jet} , but close to the correct dependence on the simulation parameters at smaller bottom friction values. We extend these theories to our system by deriving the cascade barriers implied by the linear Rossby wave frequencies, and comparing the energy spectra qualitatively and quantitatively to these, see section [2.2.3](#).

2.1.2 Zonostrophic instability theory

VM93 relies on the presence of an inverse cascade to explain the collection of energy close to the cascade barrier k_{β} . However, the work of [Srinivasan and Young \(2012\)](#) and [Farrell and Ioannou \(2008\)](#), amongst others, shows the emergence of jets in simulations where a local inverse cascade is impossible. Specifically, they simulate quasi-linear (QL) systems, derived by first decomposing the QG system into eddy and zonal-mean components, then discarding the eddy-eddy interactions and forcing the system with a rapidly decorrelating, isotropic field and, in baroclinic systems, relaxation to a prescribed background flow. Second order cumulant expansion (CE2), a.k.a. stochastical structural stability theory, shows that such systems are unstable to rapidly growing zonal modes, produced by the interaction between the zonal-mean flow and the eddies, which develop into zonal jets. This is termed ‘zonostrophic instability’, with the most unstable mode being at a non-zero meridional wavenumber, and is different from the negative viscosity instability found in, e.g. [Manfroi and Young \(1999\)](#), which has the most unstable mode at wavenumber zero. Close to the zonostrophic stability boundary, the scale of the jets predicted by CE2 is close to that seen in QL simulations, but more unstable regimes show jets that start at the predicted scale, and then merge until the scales are closer to those found in fully

non-linear systems.

For a barotropic system stochastically forced completely isotropically, as in Srinivasan and Young (2012), the addition of a zonal slope in bottom topography is exactly equivalent to altering β , or rotating the frame of reference of the system. As such, the results of Srinivasan and Young (2012) are completely applicable to any barotropic flow with a constant slope in bottom topography. However, as will be discussed in chapter 3, the complexity of the baroclinic system is required to realise the full implications of a zonal bottom slope. If we consider the zonal-mean decomposition of such a system, we can immediately see that the addition of the h_x term stops the application of CE2 being as simple as previously, when no large x gradients appear in the system equations. An adaption of the CE2 method is beyond the scope of this work¹, however a simple test of the theory would be to carry out numerical QL simulations containing a zonal bottom slope to see if the formation of jets persisted.

2.1.3 Noodle mode theory

Berloff et al. (2009), referred to as BKP09 from now on, also propose a jet formation theory based on the linear stability of the QG system. It is well known that the most unstable mode of baroclinic QG turbulence in the presence of zonal shear is a ‘noodle’ or ‘elevator’ mode, with zero y -wavenumber, see, for example, Pedlosky (1987). The presence of dissipation only modifies this slightly. BKP09 numerically solve the linear stability of the analytically derived noodle mode added to the background flow, and find that the secondary instability takes the form of meridionally periodic modes. They claim that these modes strengthen and persist to form the zonal jets seen at statistical equilibrium in simulations of the same system, and that the meridional scale of these jets is set by the properties of the secondary instability. Although the scales are not directly compared, plotting the form of these secondary instabilities with the final spun-up jets shows similarities in scale.

Whilst the instabilities derived by BKP09 can clearly be seen in the ‘spin-up’ of such simulations, it is unclear to us that these should be representative of processes in the real ocean, given that the ocean has already ‘spun-up’. We test this theory by deriving the most unstable modes of our system and analysing the spin-up of our simulations, see section 2.2.3.

¹The theory relies on simplifications arising from zonal integration of system equations, thus introducing an x -gradient into the system via a zonal topographic slope component means the extension of the theory would not be a trivial mathematical exercise.

2.1.4 PV theories

The view of jets as PV ‘staircases’ or ‘washboards’ goes back to McIntyre (1982) and is reviewed in Dritschel and McIntyre (2008), which we will refer to as DM08 from now on. The theory depends on the material conservation of PV on a given surface, and the tendency of small regions of PV mixing to encourage further mixing through positive feedback effects. This results in the staircase structure, related through invertability to jets, and the horizontal shear on the flank of these jets strengthens them further. The jets are barriers to eddies via Rossby wave ‘elasticity’ (the restoring force due to a PV gradient), and so the jet scale is postulated to be set by the threshold jet-penetration size required for an eddy to pierce the barrier. This derived jet scale depends on the square of a Rhines scale using $U_{\text{vortex}} \sim U_{\text{jet}}$.

Taking the view of our system as a barotropic ‘mode’ forced by baroclinic instability, the DM08 interpretation would be that the barotropic PV produces jets through the staircase formation method as described above. However, the system their theory is derived for is a barotropic one with a finite deformation radius, and their scalings are for a jet where $l_{\text{jet}} > \lambda$ - our system has effectively an infinite deformation radius in the barotropic mode, and so this scaling is not applicable to our system.

We wish to test the extent to which the qualitative behaviour and scalings proposed in VM93, BKP09 apply to a two-layer, baroclinic QG system with generally orientated sloped bottom topography. Because two of the jet formation theories, VM93 and BKP09, rely on the linear behaviour of the system, we first investigate the linear properties of our system. In section 2.2.1 we investigate how VM93 might extend in the addition of a second layer, in a simple decaying β plane baroclinic system. We add bottom topography in section 2.2.2, and then investigate the full closed system with background zonal shear and bottom friction in section 2.2.3. The linear properties of quasi-geostrophic models with zonally varying topography has been investigated in terms of free Rossby waves in, for example, Hallberg (1997); Samelson (1992); Straub (1994), who find regimes of surface/bottom intensified modes in the presence of strong gradients, as well as barotropic regimes in the limit of weak topographic gradients. The strong topographic gradients required to create the trapped modes are not strictly valid in the quasi-geostrophic approximation, however Hallberg (1997) reproduces some of the qualitative behaviour in a primitive equation model. Tailleux and McWilliams (2000) also use a primitive equation model to investigate wind-forced Rossby waves over zonally varying topography, and find that waves over steep topography have enhanced phase speeds, and that the wind-forced

response is enhanced.

Finally, we look at the unstable modes of the shear-dissipative system in section 2.2.4. The unstable modes of the sheared system with a zonal slope in bottom topography were recently investigated in [Chen and Kamenkovich \(2013\)](#), but in the absence of bottom friction, which we include. They find that even a small zonal slope can destabilise an otherwise stable flow, and that the orientation of the fastest growing mode is dependent on the bottom slope. In particular, they find that the fastest growing, or ‘noodle’ mode, is only orientated in the same direction as the barotropic PV gradient, i.e. perpendicular to the jet direction, in a small part of parameter space, which has interesting implications for BKP09, discussed in section 2.2.4. We finish by summarising the comparisons with the various theories in section 2.3.

2.2 Rossby wave frequencies

2.2.1 Beta Plane

We begin by recalling a freely decaying baroclinic system on a β plane, in the absence of any forcing, bottom friction or topography. The system equations can be cast in terms of the normal modes, $\bar{\psi} \equiv \delta_2\psi_1 + \delta_1\psi_2$ and $\tau \equiv \delta_2\psi_1 - \delta_1\psi_2$, the barotropic and baroclinic streamfunctions respectively:

$$\frac{\partial}{\partial t} \nabla^2 \bar{\psi} + \beta \bar{\psi}_x + J(\bar{\psi}, \nabla^2 \bar{\psi}) + J(\tau, (\nabla^2 - 1/\lambda^2)\tau) = 0, \quad (2.1)$$

$$\frac{\partial}{\partial t} (\nabla^2 - 1/\lambda^2)\tau + \beta \tau_x + J(\tau, \nabla^2 \bar{\psi}) + J(\psi, (\nabla^2 - 1/\lambda^2)\tau) = 0. \quad (2.2)$$

$J(\bar{\psi}, \tau)$ is the Jacobian determinant of $\bar{\psi}$ and τ . The layer-wise velocities $(u_i, v_i) = (-\psi_{iy}, \psi_{ix})$, and the internal deformation radius, $\lambda = \sqrt{g^* H}/2f_0$, $g^* = g(\rho_2 - \rho_1)/\rho_0$ is the reduced gravity at the internal interface in terms of the layer densities, ρ_i , and a reference density ρ_0 . H is the overall depth of the system, the layers are of equal depth $H/2$ and the Coriolis parameter f is approximated by $f_0 + \beta y$. If we drop all non-linear terms, we find:

$$\frac{\partial}{\partial t} \nabla^2 \bar{\psi} + \beta \bar{\psi}_x = 0, \quad (2.3)$$

$$\frac{\partial}{\partial t} (\nabla^2 - 1/\lambda^2)\tau + \beta \tau_x = 0. \quad (2.4)$$

We now seek solutions of the form $\hat{\bar{\psi}} = \hat{\bar{\psi}} e^{ikx + i ly - i \omega t}$, $\hat{\tau} = \hat{\tau} e^{ikx + i ly - i \omega t}$, which leads to Rossby wave frequencies:

$$\omega_{\bar{\psi}} = \frac{-\beta k}{k^2 + l^2}, \quad (2.5)$$

$$\omega_{\tau} = \frac{-\beta k}{k^2 + l^2 + 1/\lambda^2}, \quad (2.6)$$

see figure 2.2 for the form of both. At short wavelengths ($K = \sqrt{k^2 + l^2} > 1/\lambda$), they are indistinguishable, but at long wavelengths ($K < 1/\lambda$) the baroclinic mode contours are separated in the k -direction, rather than passing through the origin as in the barotropic mode.

Following VM93, we seek the wave-turbulence boundary of the system by equating these frequencies with turbulent frequency scales. As mentioned in section 2.1, we will

consider two scalings, a Rhines scaling (Rhines, 1975):

$$\omega_t^{\text{Rh}}(K) = U_t K, \quad (2.7)$$

where U_t is a turbulent velocity scale, and a Kolmogorov scaling (Arnold and Meshalkin, 1960):

$$\omega_t^{\text{Ko}}(K) = \varepsilon^{1/3} K^{2/3}, \quad (2.8)$$

where ε is the rate of energy transfer and $K = \sqrt{k^2 + l^2}$ is the total 2D wavenumber. Note that Rhines' turbulent frequency was intended to describe freely-evolving turbulence, and the Kolmogorov scaling assumes a forced flow with constant ε . Given that we are investigating a freely decaying system in this section, we do not expect the Kolmogorov scalings to apply to our simulations, but we derive them nonetheless for completeness, to compare with results in the following sections, and for reference as to expected behaviour in the equivalent forced system.

Equating (2.7,2.8) with the Rossby wave frequencies (2.5,2.6) leads to the following expressions for the wavenumbers of the barotropic wave-turbulence boundary:

$$K_\beta(\theta) = \left(\frac{\beta \cos \theta}{\varepsilon^a U_t^{1-3a}} \right)^{1/(2-a)}, \quad a = \{0, 1/3\}, \quad (2.9)$$

where $\theta = \tan^{-1}(l/k)$ is a polar coordinate, the Rhines scaling is found for $a = 0$ and the Kolmogorov for $a = 1/3$. The Rhines form can be seen in figure 2.1, but the shape is qualitatively similar for the Kolmogorov scaling, see figure 2.3. Generally, the x -wavenumber scale of the boundary $k_\beta = K_\beta(\theta = 0)$ is referred to, where the wave region is largest. For Rhines scaling, this recovers the recognisable $k_\beta = k_{\text{Rh}} = \sqrt{\beta/U_t}$.

The equivalent expression for the baroclinic wave-turbulence boundary can be found by solving the following expression:

$$\frac{K^2 + 1/\lambda^2}{K^a} = \frac{\beta \cos \theta}{\varepsilon^a U_t^{1-3a}}, \quad (2.10)$$

which leads to real solutions for K_β^τ only for certain parameters. For Rhines scaling ($a = 0$) $k_\beta^\tau = \sqrt{\beta/U_t - 1/\lambda^2}$, also found in Smith (2004) for a barotropic system with a finite deformation radius, which leads to the condition $\beta\lambda^2/U_t > 1$ for a real solution. For Kolmogorov scaling ($a = 1/3$), (2.10) becomes a 6th order polynomial in K , and the condition is not as simple, but it can be shown that real solutions exist for $\beta\lambda^{5/3}/\varepsilon^{1/3} \gtrsim 0.75$. Figure 2.3 shows the form of K_β^τ for Kolmogorov scaling and $\beta\lambda^{5/3}/\varepsilon^{1/3} = 1$,

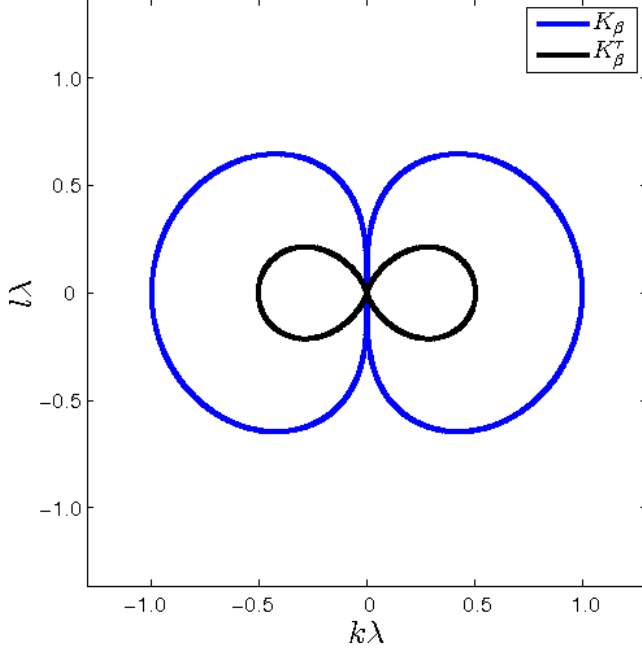


Figure 2.3: Theoretical cascade barrier for 2D turbulence, derived by equating the Rossby wave frequencies $\omega_{\bar{\psi}}$ (blue line) or ω_{τ} (black line) with the Kolmogorov turbulent frequency ω_t^{Ko} , for $\beta\lambda^{5/3}/\varepsilon^{1/3} = 1$.

although the form for Rhines scaling is qualitatively very similar for $\beta\lambda^2/U_t > 1$. If we follow the arguments of VM93, we might expect the inverse cascade to reach smaller wavenumbers in the baroclinic mode, where $k_{\beta}^{\tau} < k_{\beta}$.

It can also be shown that for large $\beta\lambda^2/U_t$ or large $\beta\lambda^{5/3}/\varepsilon^{1/3}$, $K_{\beta}^{\tau} \rightarrow K_{\beta}$. Thus, if we seek to apply VM93 to the barotropic and baroclinic modes separately, we expect to see broadly similar behaviour at large values of $\beta\lambda^2/U_t$ or $\beta\lambda^{5/3}/\varepsilon^{1/3}$, where the planetary vorticity is of a greater magnitude than that of the turbulence: k_{β} increasing with increasing β and decreasing ε/U_t . At smaller values, where $\beta\lambda^2/U_t$ or $\beta\lambda^{5/3}/\varepsilon^{1/3}$ is $\mathcal{O}(1)$, we expect the modes to exhibit different behaviour, as the cascade barriers become significantly different, as discussed above. Finally, at small values of $\beta\lambda^2/U_t$ or $\beta\lambda^{5/3}/\varepsilon^{1/3}$, we expect the baroclinic mode to stop supporting jets, when the cascade barrier disappears, and energy can collect isotropically at the gravest modes.

Given that the derivation of Kolmogorov scaling assumes a quasi-steady state with constant forcing, and (2.1,2.2) represent an unforced system, we can only qualitatively compare these predictions in numerical simulations. However, it has been demonstrated that the form of the turbulent frequency has little effect on the form of the cascade barrier, and whilst a decaying simulation doesn't have constant forcing, it does have

constant energy, and we seek a dependence of the cascade barrier on $\beta\lambda^2/E_K^{1/2}$, where $E_K = \langle|\nabla\bar{\psi}|^2\rangle + \langle|\nabla\tau|^2\rangle$ is the total kinetic energy, where $\langle.\rangle$ represents a domain average.¹ We expect to find, following the previous arguments,

$$k_\beta^{\bar{\psi}} = \sqrt{k_\beta^\tau{}^2 - 1/\lambda^2} = \left(\frac{\beta}{E_K^{1/2}}\right)^{1/2}, \quad (2.11)$$

where $k_\beta^{\bar{\psi}}$ is the cascade barrier in the barotropic mode, and k_β^τ in the baroclinic mode.

Following VM93, we initialise simulations with a ring of energy at a large wavenumber, with a random phase. The advantage of this type of decaying simulation is that we can control the total energy of the system, but the disadvantage is that, if simulated for long enough, the system would reach an isotropic state. For all simulations, the initial ring of energy quickly adjusts to a pattern like those seen in figure 2.4 before extremely slowly adjusting towards isotropy. Thus these snapshots, whilst not representative of a statistical equilibrium, can show the qualitative dependence of the system on $\beta\lambda^2/E_K^{1/2}$. It should also be noted that energy is not strictly conserved due to the inclusion of a high wavenumber filter for numerical stability, although this effect is small over the short time scales considered here (changes to the total energy are on the order of a few %).

Figure 2.4 shows snapshots of baroclinic and barotropic kinetic energy spectra for a range of simulations with various non-dimensional PV gradients $\beta\lambda^2/E_K^{1/2}$ in domains of length $L = 38\lambda$ and grid size 512 by 512 (a resolution of $\sim 0.07\lambda$). The corresponding streamfunction fields can be seen in figure 2.5. In the upper two panels, for large $\beta\lambda^2/E_K^{1/2}$, the predicted ‘dumbbell’ pattern can clearly be seen in both the barotropic and baroclinic spectra, with a concentration of energy in the same shape as that predicted by the cascade barrier, and as well as a large concentration along the l axis. As can be seen in figure 2.5, these spectra correspond to zonal jets of the same scale in both modes. For $\beta\lambda^2/E_K^{1/2} = 4$ the dumbbell shape is still visible in the barotropic spectra, but is very faint in the baroclinic spectra, corresponding to clear jets in the barotropic streamfunction and a more isotropic baroclinic field, albeit with similar scale features visible. For $\beta\lambda^2/E_K^{1/2} = 0.4$, there is no clear dumbbell shape in the baroclinic spectra, which appears isotropic, and corresponds to an isotropic baroclinic streamfunction. Overall, there is a clear relationship between decreasing β , decreasing spectral shape and increasing jet scale, as predicted by VM93.

Figure 2.6 shows the most common values of the cascade barriers over a short period of

¹N.B. equivalent to a Rhines scaling where $U_t = E_K^{1/2}$.

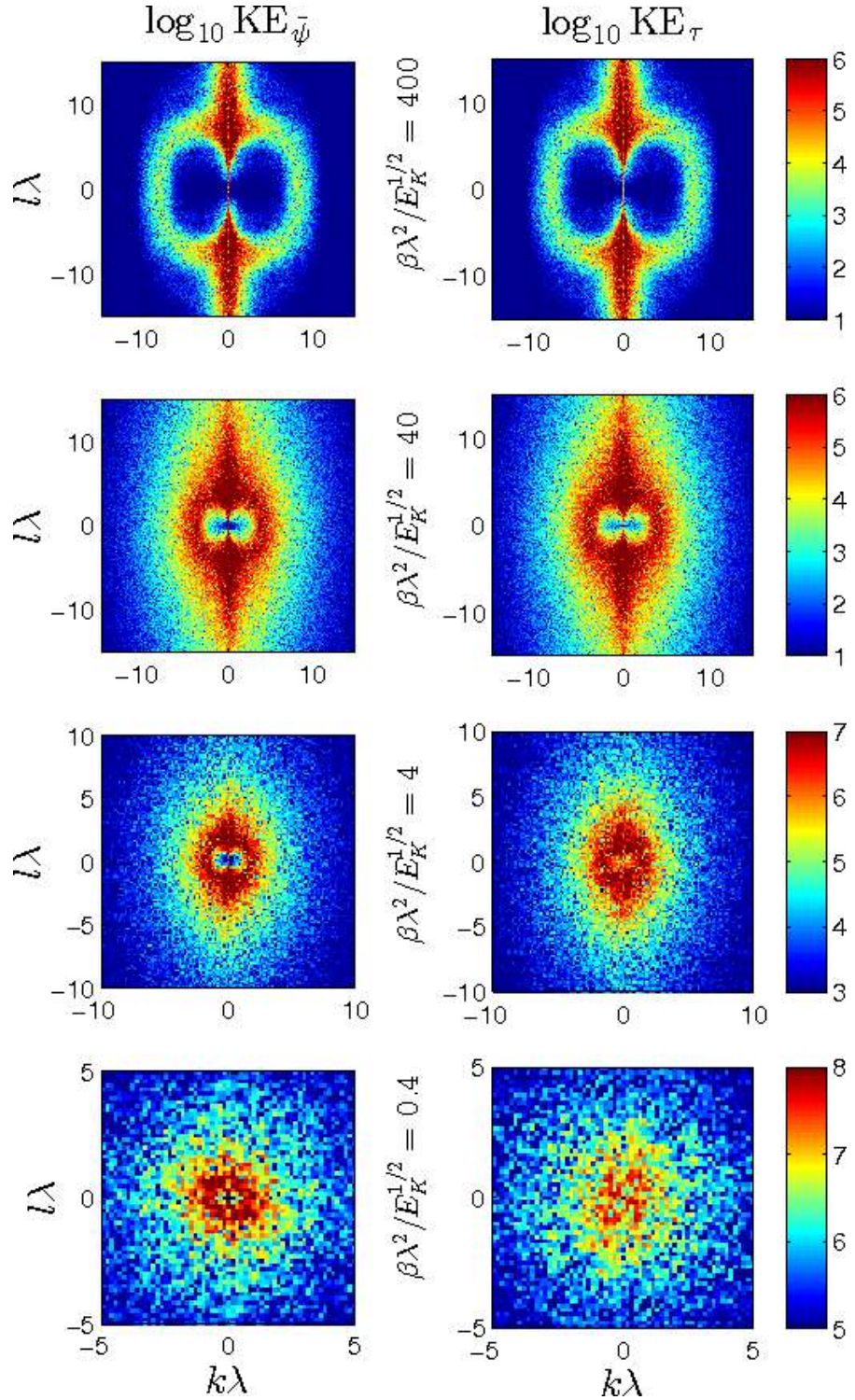


Figure 2.4: Kinetic energy spectra of barotropic and baroclinic field snapshots for simulations with various values of $\beta\lambda^2/E_K^{1/2}$ as indicated. The colour axes (same for both fields) are log-scale in arbitrary units.

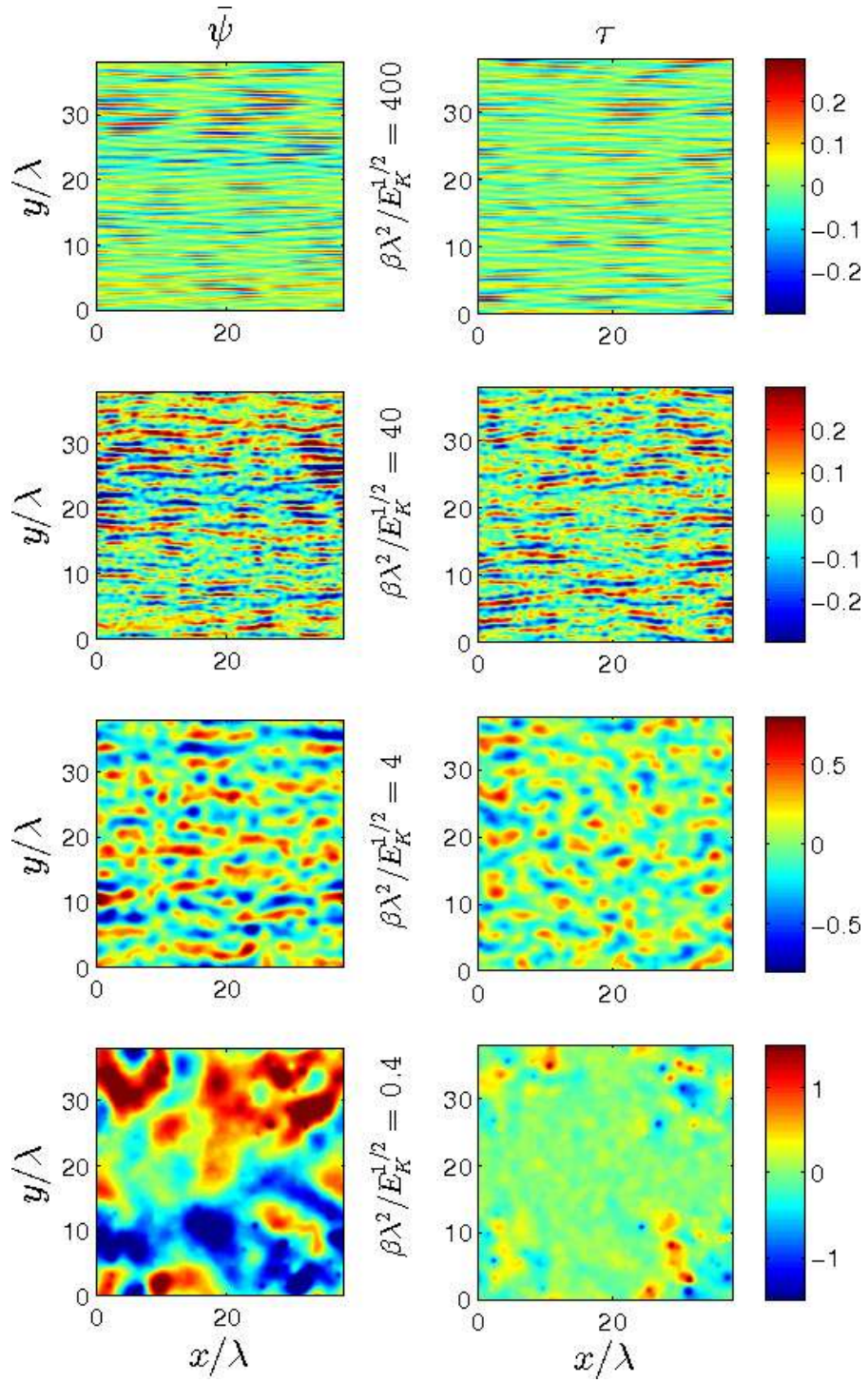


Figure 2.5: Barotropic and baroclinic perturbation streamfunction snapshots for unforced simulations with various values of $\beta\lambda^2/E_K^{1/2}$ as indicated. The colour axes (same for both fields) are in arbitrary units.

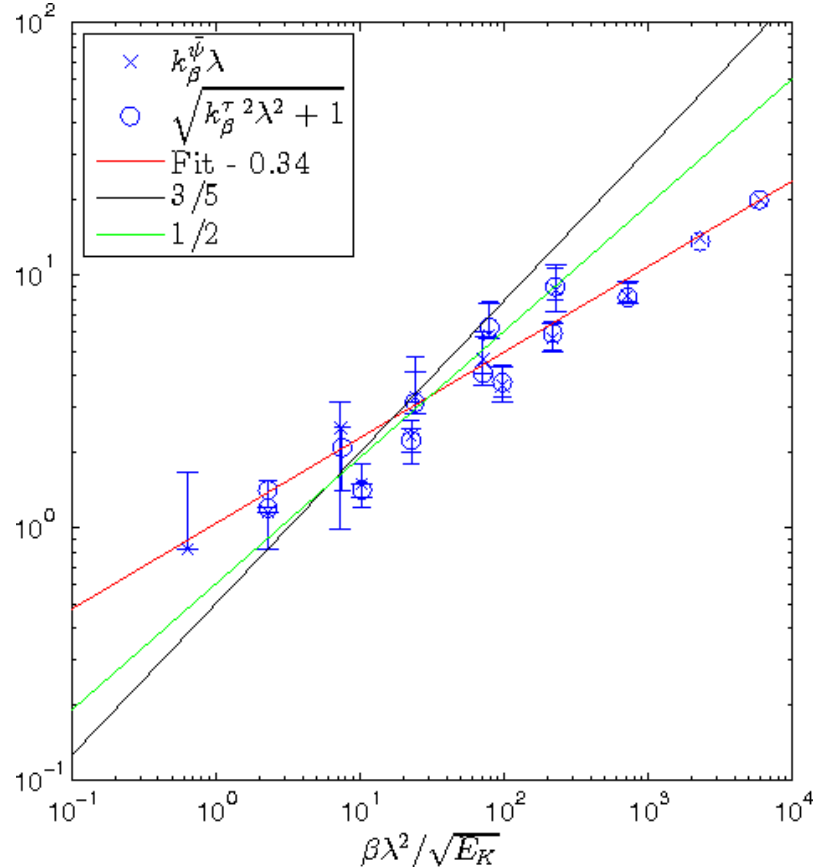


Figure 2.6: Mode or most common values of the cascade barriers in each mode from a variety of simulations plotted against the non-dimensional PV gradient. Error bars denote the max/min cascade barriers measured over a short period ($\sim 300\lambda/E_K^{1/2}$), over which the kinetic energy change is smaller than the markers shown on this scale. Also plotted are a least-squares fit (red), a $3/5$ power law (black) and a $1/2$ power law (green).

time in each mode from a variety of simulations, plotted against mean values of $\beta\lambda^2/E_K^{1/2}$ for that time period. In VM93 k_β is determined by looking at the time evolution of mean kinetic energy slices centred on the $k = 0$ axis, and taking the wavenumber at which the spectra ‘start to steepen’ in sequential snapshots (see their fig. 7a). In [Smith et al. \(2002\)](#) and [Sukoriansky et al. \(2007\)](#), they identify k_β as the wavenumber at which the spectra becomes anisotropic, i.e. where the cascade along the l axis becomes different from that along the k axis. These both depend on an equilibrated state emerging, with a well defined isotropic spectra. As this system is evolving, we take one measure of k_β to be the maxima of the k axis spectra.

Following VM93, we use a mean kinetic energy spectra in a $\pm\pi/30$ slice around the k -axis, and the error bars represent the uncertainty in determining this maximum, which is not a sharp peak as can be seen in figure 2.4. The variations in kinetic energy over the time period are smaller than the marker size on the scale plotted. Also shown in red is a least-squares best fit relationship to the data of the form $A(\beta\lambda^2/E_K^{1/2})^B$, which finds $A = 1.04 \pm 0.03$, $B = 0.339 \pm 0.004$, with an R^2 value of 0.93, where the errors are the 95% confidence intervals of the fit. In green is the theory predicted 1/2 power law, and in black a 3/5 power law that would be expected from the Kolmogorov scaling dependence on β (included for reference, although as noted before we do not expect this scaling to apply for a freely decaying system). The fit suggests a relationship closer to

$$k_\beta^\psi = \sqrt{k_\beta^\tau{}^2 - 1/\lambda^2} \approx \left(\frac{\beta}{\lambda E_K^{1/2}} \right)^{1/3}, \quad (2.12)$$

where the dependence on the deformation radius λ suggests that the linear properties of the two modes is not sufficient to completely predict the cascade barrier in this system, as the deformation radius only affects the non-linear behaviour of the barotropic mode, see (2.1).

These simulations show that, qualitatively at least, the ideas of VM93 are consistent with the behaviour observed in decaying baroclinic turbulence, although non-linear effects may be important for quantitative predictions. We will next see if the ideas remain consistent if we add a topographic slope, and compare quantitative predictions in section 2.2.3.

2.2.2 Topographic Slope

If we now consider the addition of a topographic slope to the baroclinic system discussed in section 2.2.1, we find the following system equations:

$$\frac{\partial q_1}{\partial t} + J(\psi_1, q_1) + \beta\psi_{1x} = 0, \quad (2.13)$$

$$\frac{\partial q_2}{\partial t} + J(\psi_2, q_2) + (\beta + h_y)\psi_{2x} - h_x\psi_{2y} = 0, \quad (2.14)$$

where the topography parameter is defined as:

$$h = \frac{f_0}{H}(\alpha_1 x + \alpha_2 y), \quad \alpha_{1,2} = \text{const.}, \quad (2.15)$$

and we have again assumed equal layer depths. The background layer and background barotropic PV gradients are defined as follows:

$$\mathbf{G}_i = (0, \beta) + \delta_{i2}(h_x, h_y), \quad i = 1, 2, \quad (2.16)$$

$$\mathbf{G}_{\text{BT}} = \left(\frac{h_x}{2}, \beta + \frac{h_y}{2} \right), \quad (2.17)$$

where δ_{ij} is the Kronecker delta function, subscript $i = 1$ represents the upper layer and $i = 2$ the lower layer.

Carrying out the same linear analysis as described in section 2.2.1, we find that the normal modes of the system are no longer the barotropic and baroclinic fields. The Rossby wave dispersion relations are solutions to a quadratic of the form $\omega_{\pm} = A \pm \sqrt{B}$. $B \geq 0$, so there is no instability, however, $\omega_{\pm} = 0$ for some wavenumbers, as seen below, so the roots are not continuous functions of k, l . The form is more complicated than previously, but the solutions have simple approximate forms in the long and short wave limits, as mentioned in Hallberg (1997).

In the short wave limit, $K^2 \gg 1/\lambda^2$, the layers are effectively decoupled, the layer-wise streamfunctions are the normal modes, and the Rossby wave frequencies are equal to the equivalent layer-wise frequencies:

$$\omega_1^s \approx \frac{-\beta k}{k^2 + l^2 + 1/2\lambda^2} = \frac{\mathbf{G}_1 \times \mathbf{k}}{K^2 + 1/2\lambda^2}, \quad (2.18)$$

$$\omega_2^s \approx \frac{-(\beta + h_y)k + h_x l}{k^2 + l^2 + 1/2\lambda^2} = \frac{\mathbf{G}_2 \times \mathbf{k}}{K^2 + 1/2\lambda^2}. \quad (2.19)$$

However, the full numerical solutions, ω_{\pm} , are not consistently associated with a

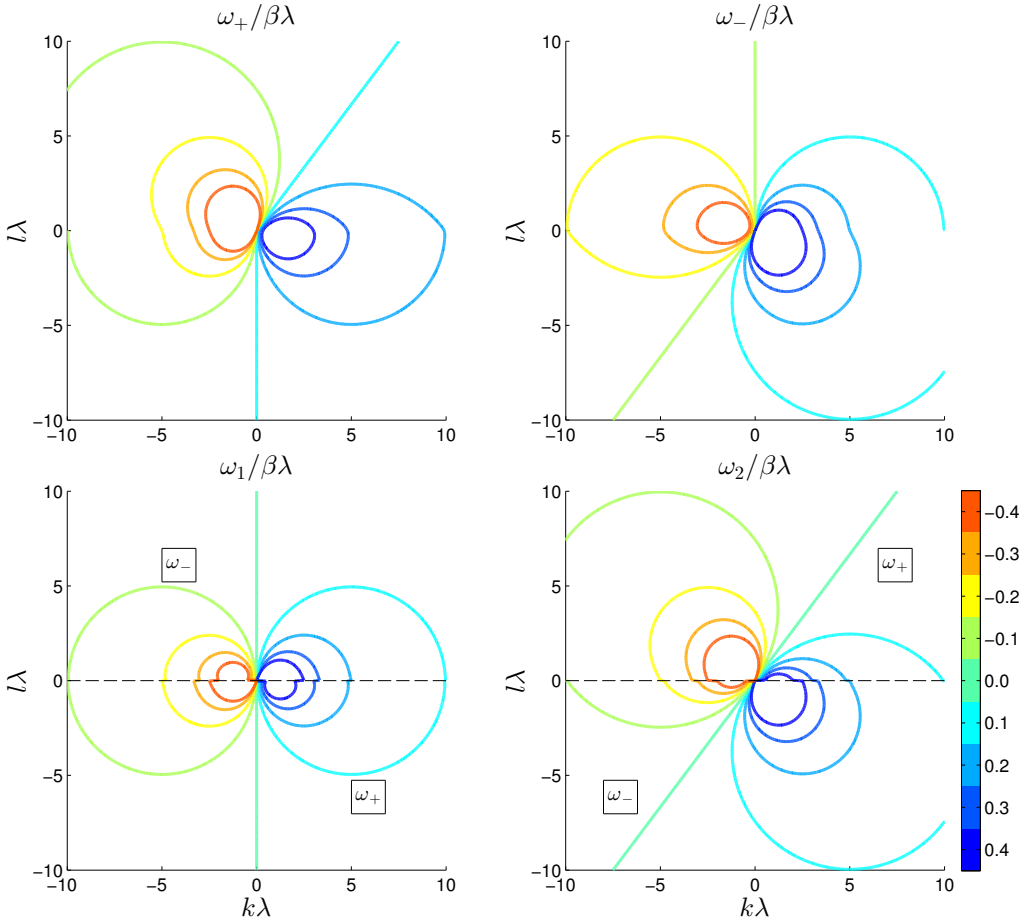


Figure 2.7: Linear Rossby Wave frequencies for a two layer unforced quasigeostrophic system, with $h_x/\beta = 3/4$, $h_y/\beta = 0$. Upper panels show the two full solutions, ω_{\pm} . The lower panels show the same frequencies replotted as indicated, such that each is consistently associated with one dominant mode, so it becomes clear that the frequencies resemble ω_i^s , equivalent layer frequencies, for $K\lambda \gg 1$. The colour scale indicates the contour values for all four plots.

bottom/top mode, but rather approach different modes on either side of the $l = 0$ axis. The upper panels of figure 2.7 show the full form of these frequencies, and the upper panels of figure 2.8 show log scaled contours of the magnitude of the corresponding ratios of streamfunction amplitudes, $|\hat{\psi}_1^\pm/\hat{\psi}_2^\pm|$, on the same axes. Large values (warm colours) correspond to an upper-layer dominated mode, and small values (cold colours) to a lower-layer dominated mode. The black lines show the hyperbolic points where the ratio tends to $\pm\infty$ or to 0, and the shading indicates where $\hat{\psi}_1^\pm/\hat{\psi}_2^\pm < 0$. At large $K\lambda$, the dominant modes are either an upper or lower layer mode, as expected. To see the full form of the modes expected in each layer, we therefore re-plot w_\pm such that the upper/lower layer dominated mode frequencies are plotted on the same axes, see figure 2.7 lower panels. The dotted line indicates the boundary between the two numerical solutions. These plots make it apparent that the upper layer dominant mode has a dispersion relation similar to the barotropic mode derived in the previous section, symmetric about the $k = 0$ axis, where, as predicted by ω_1^s , $\omega_1 = 0$. Conversely, the lower layer dominant mode resembles a similar mode, but rotated such that the axis of symmetry is now determined by the lower layer PV gradient, and $\omega_2 = 0$ for $\mathbf{G}_2 \times \mathbf{k} = 0$. In the short wave limit, the anisotropy of both appears to indeed be determined by the layer equivalent Rossby waves, ω_i^s .

In the long wavenumber limit, $K^2 \ll 1/\lambda^2$, the layers are strongly coupled and the Rossby wave frequencies are barotropic and baroclinic-like:

$$\omega_1^l \approx \frac{-(\beta + h_y/2)k + h_x l/2}{k^2 + l^2} = \frac{\mathbf{G}_{\text{BT}} \times \mathbf{k}}{K^2}, \quad (2.20)$$

$$\omega_2^l \approx \frac{-(\beta + h_y/2)k + h_x l/2}{k^2 + l^2 + 1/\lambda^2} = \frac{\mathbf{G}_{\text{BT}} \times \mathbf{k}}{K^2 + 1/\lambda^2}, \quad (2.21)$$

which have the same form as the barotropic and baroclinic frequencies derived in section 2.2.1, where \mathbf{G}_{BT} is the background barotropic PV gradient. See figure 2.9 for the full form of the frequencies in this limit, where as before, the numerical solutions ω_\pm , are not consistently associated with one of the long wave limit modes. The lower panels of figure 2.8 show the ratios between the linear mode amplitudes in this limit, on a log scale with large values in warm colours and small in cold. As before, the black lines show where this ratio tends to $\pm\infty$ or 0, and the shading indicates where $\hat{\psi}_1^\pm/\hat{\psi}_2^\pm < 0$. The dash-dotted line is $\mathbf{G}_{\text{BT}} \times \mathbf{k} = 0$, i.e. the axis of symmetry expected for the long wave limit frequencies ω_i^l . It can be seen that, in this limit, on one side of this line $\hat{\psi}_1^\pm/\hat{\psi}_2^\pm \approx 1$, i.e. a barotropic dominant mode, and on the other a bottom/top trapped baroclinic mode is found. This is discussed in Hallberg (1997), who also finds that the normal modes in

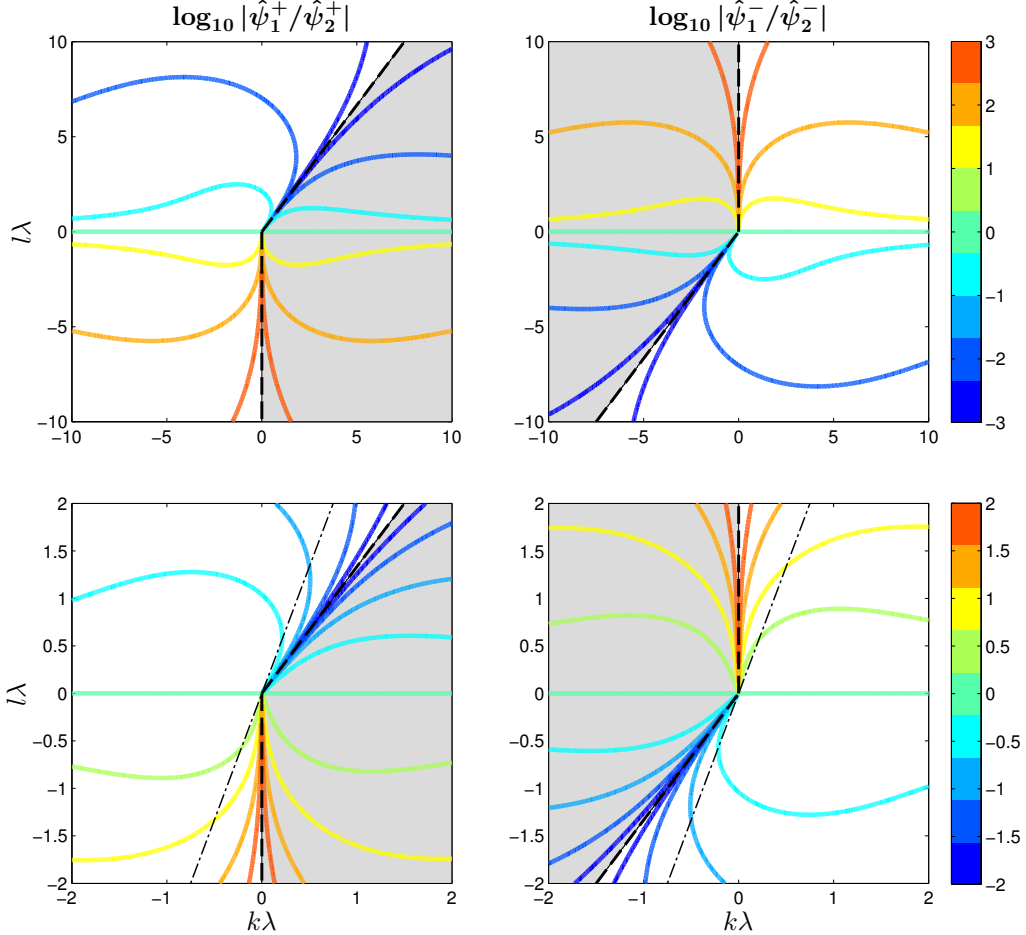


Figure 2.8: Ratio of linear mode amplitudes, $|\hat{\psi}_1^\pm/\hat{\psi}_2^\pm|$, on a log scale, for $h_x/\beta = 3/4$, $h_y/\beta = 0$. The black lines show the hyperbolic points where the ratio tends to $\pm\infty$ or to 0. The shaded indicate $\hat{\psi}_1^\pm/\hat{\psi}_2^\pm < 0$. The upper panels show the ratios for large wavenumbers, and the lower the same quantities but on a small wavenumber scale. The dash-dotted lines in the lower panels indicate the boundary between the frequencies plotted in figure 2.9, lower panel. These provide the motivation for reorganising the Rossby wave frequencies in figures 2.7 and 2.9 in terms of the dominant modes. The colour scales on the RHS refer to both plots on that row.

this limit are a barotropic mode and a surface/bottom intensified baroclinic wave, dependent on wavenumber. Correspondingly, we again replot ω_{\pm} to show the dispersion relation associated with these two dominant modes, which can be seen in figure 2.9, lower panels, where the dotted line indicates the boundary between the two solutions. Again, these figures make it clear that the barotropic dominated mode has a dispersion relation resembling that predicted by the short wave limit, i.e. with anisotropy determined by the barotropic PV gradient. The baroclinic bottom/top trapped mode somewhat resembles a rotated form of the baroclinic mode found in the previous section for a beta plane, but the complicated mode structure means there is not a good quantitative agreement with ω_2^l . However, qualitatively, we expect these limits to predict the anisotropy of the cascade barrier in this limit as before.

Following VM93, and the results of the previous section, the anisotropy of these dispersion relations determine the shape of the theoretical cascade barrier in each limit. The general solution for the cascade barrier becomes:

$$\frac{K^2 + \Lambda^2}{K^a} = \frac{\mathbf{G} \times \hat{\mathbf{k}}}{\varepsilon^a U_t^{1-3a}}, \quad a = \{0, 1/3\}, \quad (2.22)$$

where $\hat{\mathbf{k}} = (\cos \theta, \sin \theta)$, $\Lambda^2 = 1/2\lambda^2$, 0 or $1/\lambda^2$ in the short, barotropic long or baroclinic long wave limits respectively, \mathbf{G} is the relevant PV gradient, and $a = 0$ or $1/3$ for Rhines or Kolmogorov scaling respectively, as before. If we define k_{β} as where the pattern is largest, we find that this is when $\theta = -\phi$, where ϕ is perpendicular to the relevant PV gradient angle. This leads to, for example for Rhines scaling:

$$k_{\beta} = \sqrt{\frac{|\mathbf{G}|}{U_t} - \Lambda^2}, \quad (2.23)$$

which recovers the previous definitions derived in section 2.2.1 if we set $h_y = h_x = 0$. Note that this only has real solutions for $|\mathbf{G}|/U_t \Lambda^2 > 1$, i.e. the cascade will not be halted and jets will not form if $|\mathbf{G}|/U_t \Lambda^2 < 1$. [LaCasce and Brink \(2000\)](#) find similar dependence on this factor in their investigation of vortex formation over a meridional slope in a two-layer quasigeostrophic system, finding that unstable growth is inhibited for $|\mathbf{G}|/U_t \Lambda^2 > 1$.

Thus these dispersion relations predict two distinct regimes - one in which the cascade barriers are in the short wave limit i.e. $k_{\beta}\lambda \gg 1$, where we expect, given the form of ω_i^s , to see uncoupled jets in each layer, orientated perpendicular to their layer-wise potential

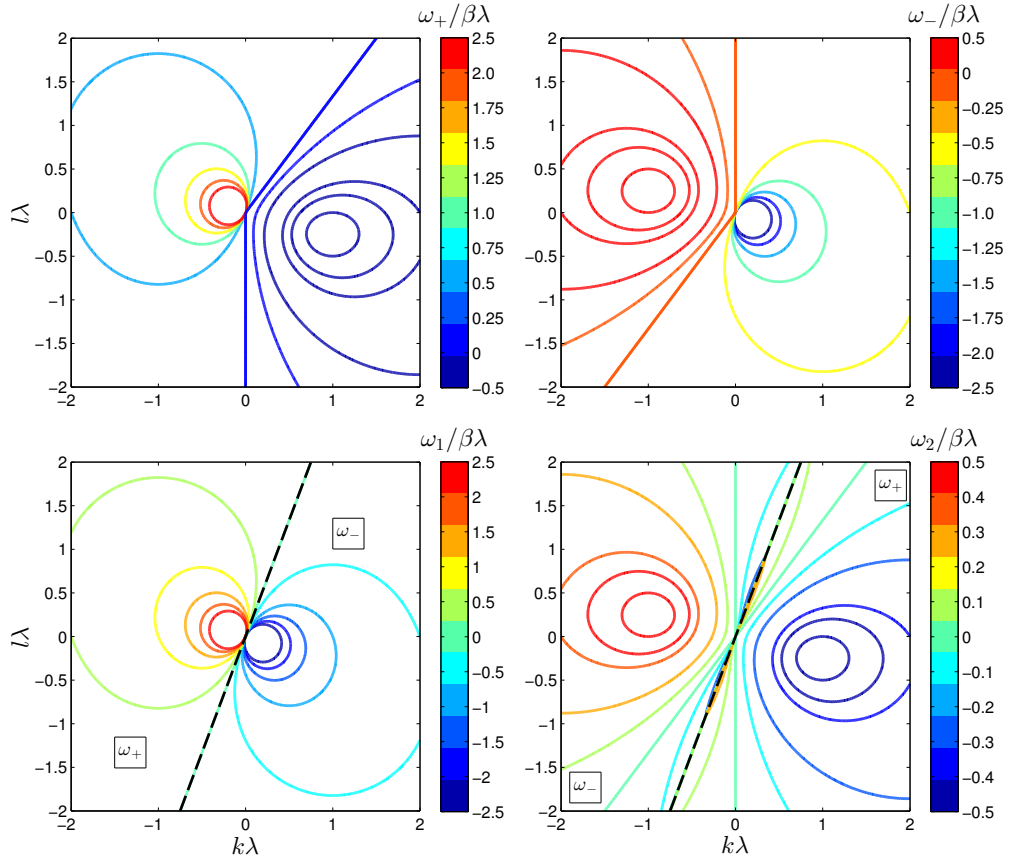


Figure 2.9: Linear Rossby Wave frequencies for a two layer unforced quasigeostrophic system, with $\beta\lambda^2/E_K^{1/2} = 2$, $h_x\lambda^2/E_K^{1/2} = 1.5$. The lower panels show the same frequencies replotted as indicated, such that each is consistently associated with one dominant mode, so it becomes clear that the frequencies resemble ω_i^l , rotated barotropic and baroclinic frequencies, for $K\lambda \ll 1$. The dashed line indicates the boundary between the two frequencies.

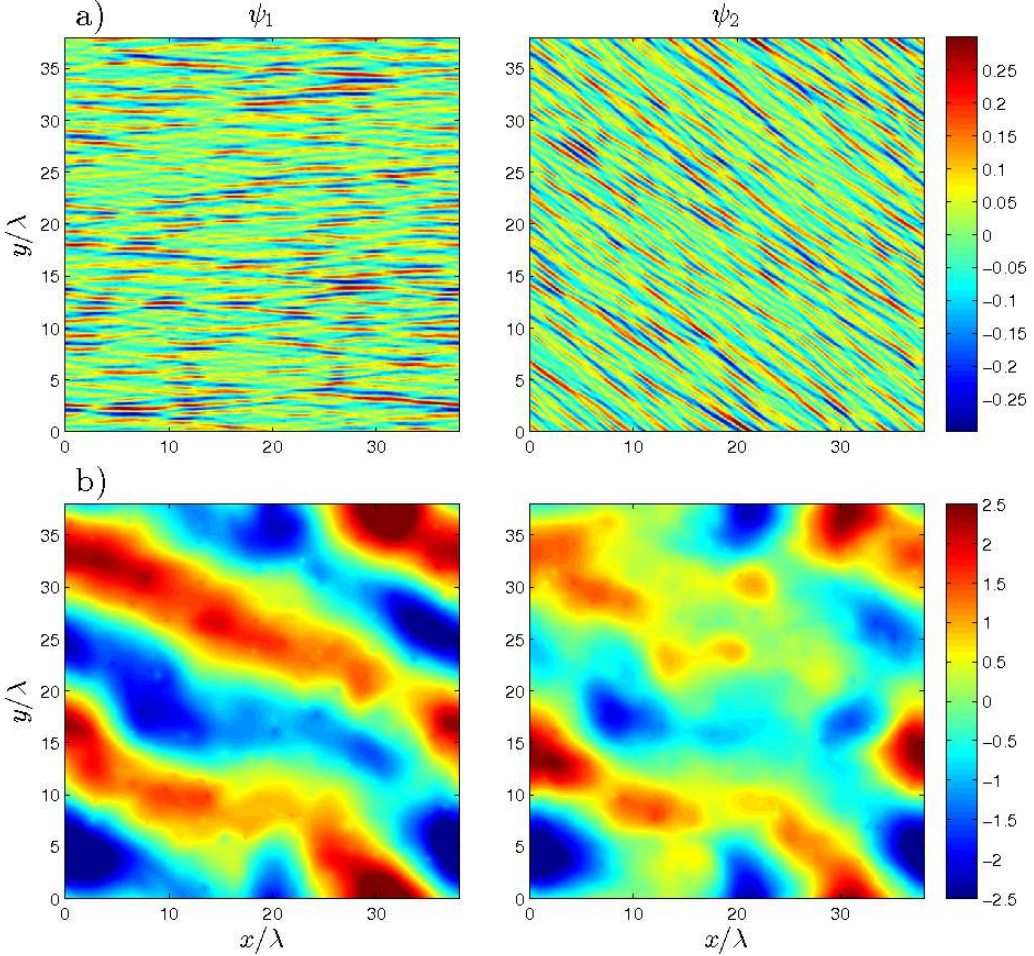


Figure 2.10: Snapshots of upper and lower layer perturbation streamfunctions from two simulations with a) $\beta\lambda^2/\sqrt{E_K} = 400$, $h_x\lambda^2/\sqrt{E_K}$ b) $\beta\lambda^2/\sqrt{E_K} = 0.2$, $h_x\lambda^2/\sqrt{E_K} = 0.15$. Spectra for these snapshots can be seen in figure 2.11.

vorticity gradients. In the other regime, where $k_\beta\lambda \ll 1$, the long wave limit, the two layers are strongly coupled and are a mixture of the two normal modes. We expect to see jets in both layers perpendicular to the barotropic PV gradient, as both modes' dispersion relations (ω_i^l) are aligned in this direction, see figure 2.9.

Again, we test these predictions qualitatively by numerical simulation, initialising the fields with a ring of energy at a large wavenumber and random phase, as in section 2.2.1. Simulations are on domains of length 38λ , 76λ or 128λ with grids of length 512 or 1024 (resolutions 0.07–0.25 λ). We choose to set $h_y\lambda^2/\sqrt{E_K} = 0$, where E_K is the total kinetic energy of the system, and fix the ratio $\beta : h_x = 4 : 3$, such that the angles of the PV gradients remain fixed, and are the same as for figures 2.7 and 2.9. As predicted, we

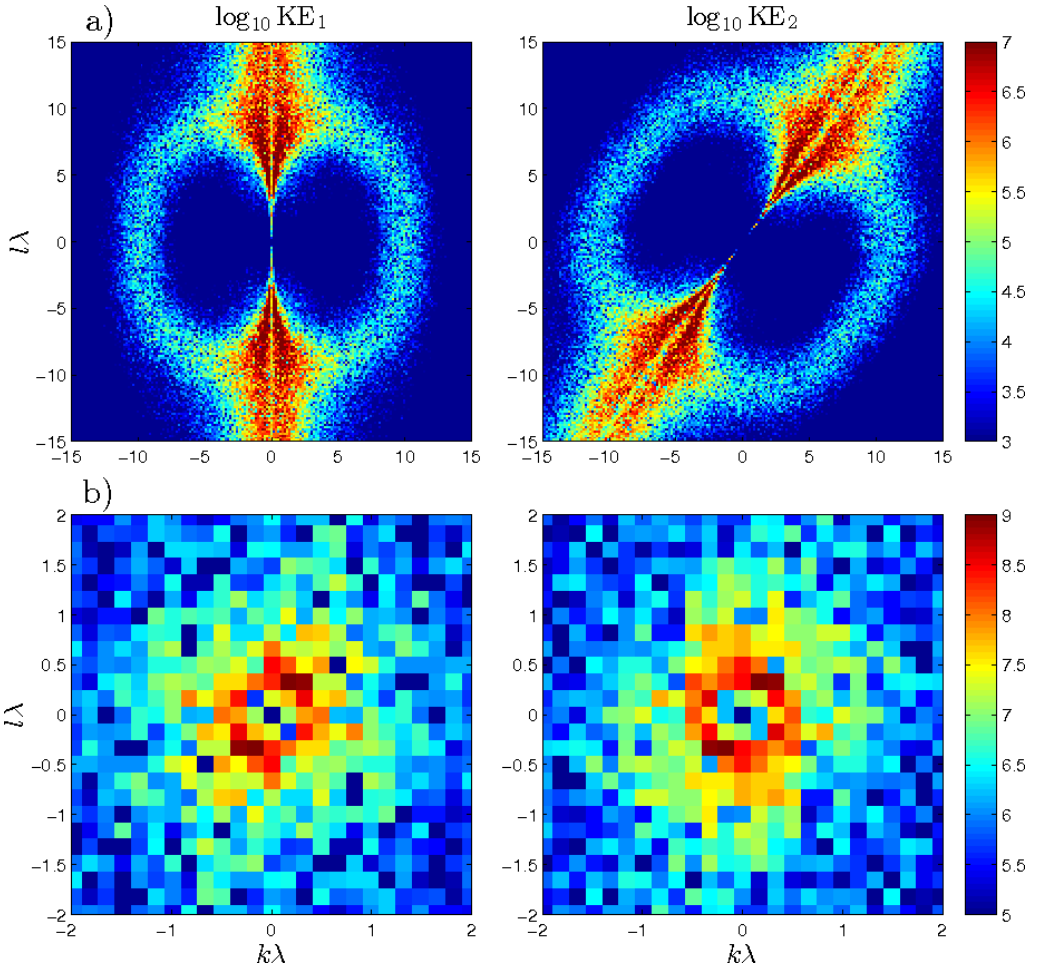


Figure 2.11: Snapshots of upper and lower layer perturbation kinetic energy spectra from the two simulations in figure 2.10. The snapshots have cascade barriers of a) $k_\beta^1 \lambda \approx k_\beta^2 \lambda \approx 10$, b) $k_\beta^1 \lambda \approx k_\beta^2 \lambda \approx 0.4$. The colour axis is on a log-scale in arbitrary units.

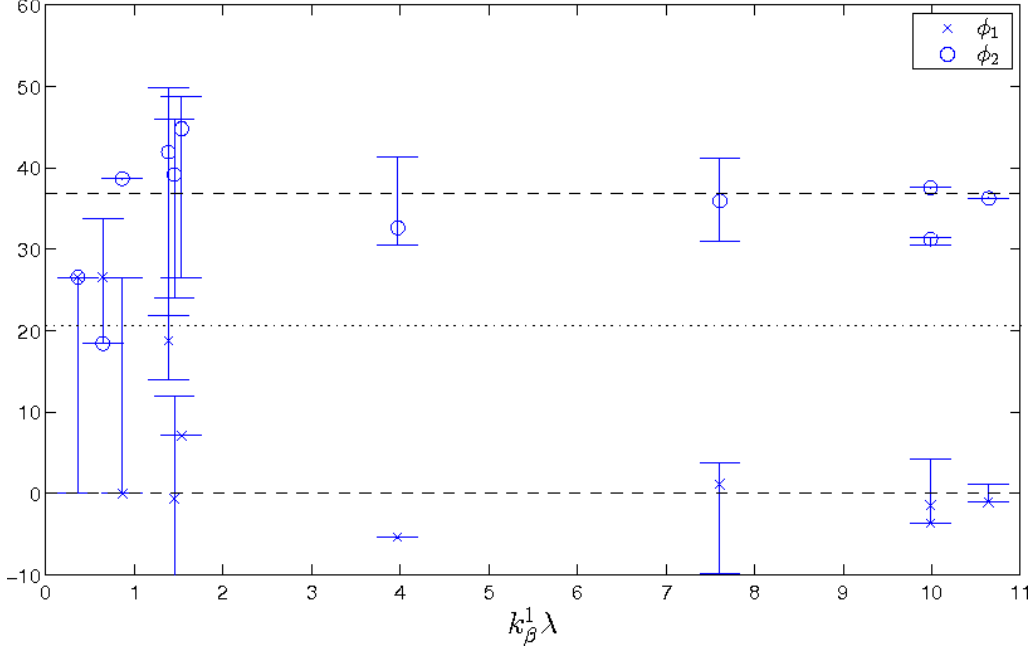


Figure 2.12: Variation of measured jet angles in upper and lower layers, ϕ_1 and ϕ_2 respectively, with the cascade barrier in the upper layer, k_β^1 , for a range of unforced simulations. Each point is placed at mean values over a short time period, and the y -errorbars indicate the max/min angles in that period. The dashed lines indicate the direction perpendicular to the layer-wise PV gradients, and the dotted line ϕ_{BT} .

find coupled and uncoupled regimes, dependent on the magnitude of the PV gradients. Figure 2.10 shows perturbation streamfunction snapshots for two simulations, one in each regime. Figure 2.10a shows clear jets in both layers, which are uncoupled from one another and are orientated zonally in the upper layer and strongly tilted in the lower layer. Figure 2.10b again shows clear jets, but these are coupled, with jets in both layers strongly tilted and in the same direction. The corresponding spectra can be seen in figure 2.11, where a clear relationship between the orientation of the spectra and the jet orientation can be seen - figure 2.11a shows clear ‘dumbbell’ shapes which are orientated similarly to the dispersion relations in figure 2.7. The ‘dumbbells’ are harder to see in figure 2.11b, as the spectral resolution is close to the magnitude of the pattern, but minima in energy are still visible close to the origin, and maxima on an axis orientated similarly to the dispersion relations in figure 2.9.

We measure the instantaneous cascade barrier scales in each layer by first determining the jet tilt ϕ_{jet} and jet wavenumber k_{jet} from the absolute maxima of the kinetic energy spectra. We then find k_β^i , as before, by finding the maxima of $\pm\pi/30$ slices of the spectra

at right angles to ϕ_{jet} . Figure 2.12 shows mean jet angles over a short time period ϕ_{jet} for each layer against mean k_β^1 for a range of simulations. k_β^2 is of similar magnitude for these simulations. Also shown are the angles perpendicular to the layer and barotropic PV gradients. Clearly seen is the coupled regime, for $k_\beta^1 \lambda \ll 1$ where jet angles in both layers are close to ϕ_{BT} , and the uncoupled regime, for $k_\beta^1 \lambda \gg 1$ where jet angles in both layers are close to ϕ_i , perpendicular to the layer-wise PV gradients. The transition region, where $k_\beta^1 \lambda \approx 1$, shows highly variable angles, and the streamfunction fields for these simulations show no clear jets.

As before, although there is no constant forcing present, we seek a relationship between the cascade barrier in each layer and the non-dimensional PV gradients $|\mathbf{G}| \lambda^2 / \sqrt{E_K}$. Following the arguments above, we expect to find:

$$\sqrt{k_\beta^i{}^2 + 1/2\lambda^2} = \left(\frac{|\mathbf{G}_i|}{E_K^{i \ 1/2}} \right)^{1/2}, \quad K\lambda \gg 1, \quad (2.24)$$

$$k_\beta^i = \left(\frac{|\mathbf{G}_{\text{BT}}|}{E_K^{\text{BT} \ 1/2}} \right)^{1/2}, \quad K\lambda \ll 1, \quad (2.25)$$

where $E_K^i = \langle |\nabla \psi_i|^2 \rangle$ is the layer kinetic energy, $E_K^{\text{BT}} = \langle |\nabla \bar{\psi}|^2 \rangle$ is the barotropic kinetic energy.

The upper panel of figure 2.13 shows mode layer cascade barriers from a variety of simulations against $|\mathbf{G}_i| \lambda^2 / \sqrt{E_K^i}$ where $k_\beta^i \lambda \gg 1$. The measurements were made over a short period of time, where the variation in E_K was relatively constant on the scale plotted. Once again, the errorbars indicate the uncertainty in determining the maximum of the energy spectra. Also plotted in red is a least-squares fit to the data of the form $A(|\mathbf{G}_i| \lambda^2 / \sqrt{E_K^i})^B$, which produces the result $A = 0.81 \pm 0.01$, $B = 0.385 \pm 0.003$, with an R^2 value of 0.99, where the errors indicate the 95% confidence level of the fit. Power laws of 1/2 and 3/5 are also shown for reference. The lower panel of the figure shows the layer cascade barriers for a variety of simulations where $k_\beta^i \lambda \lesssim 1$ against $|\mathbf{G}_{\text{BT}}| \lambda^2 / \sqrt{E_K^{\text{BT}}}$. Here the spectral resolution of the simulations will be relevant, which is different for different simulations but of the order 10^{-1} , and there is a greater spread of results. Also plotted in red is a least-squares fit to the data of the form $A(|\mathbf{G}_{\text{BT}}| \lambda^2 / \sqrt{E_K^{\text{BT}}})^B$, which produces the result $A = 0.589 \pm 0.009$, $B = 0.27 \pm 0.03$, where the errors indicate the 95% confidence level of the fit, but the R^2 value is only 0.21. Also shown are 1/2 and 3/5 power laws for reference, and both can be seen to be consistent within the spread of the data, but the 1/2 law is closer. Although the fit to the long-wave data is not well determined, the power law for the short-wave data suggests a $\sim 2/5$ scaling, i.e. somewhere between the

$1/3$ scaling found in section 2.2.1 and the $1/2$ expected. Figure 2.13 shows us that the qualitative relationship between k_β and the system parameters exists as expected, but that a Rhines-like quantitative scaling is not a good match.

As in section 2.2.1, the form of the Rossby wave dispersion relations allows for the qualitative prediction of the behaviour of a decaying baroclinic system in the presence of a topographic slope. In particular, the existence of two distinct regimes, coupled and uncoupled, is predicted, and the angles of the jets in both. The cascade barrier also shows the same qualitative dependence on the magnitudes of the PV gradients and the energy of the system as predicted by VM93. The quantitative predictions show some success in predicting the power law of the dependence of the cascade barrier on PV gradient magnitude in the long wave limit, although the short wave limit again seems to imply the importance of non-linear effects. It should be noted, however, that the constantly evolving nature of the decaying simulations is likely to make their behaviour different to those with forcing present, and we would not assume that these results would hold in such situations. However, notable is the emergence of $\mathbf{G} \times \mathbf{k}$, a vector perpendicular to the relevant PV gradient, as the element of the dispersion relations that controls their anisotropy, and thus, it seems, the jet direction. Section 2.2.3 will investigate the stability of a baroclinic system forced by background shear and containing bottom friction, to investigate if these elements alter the qualitative predictions, and to test the quantitative predictions of VM93 and BKP09.

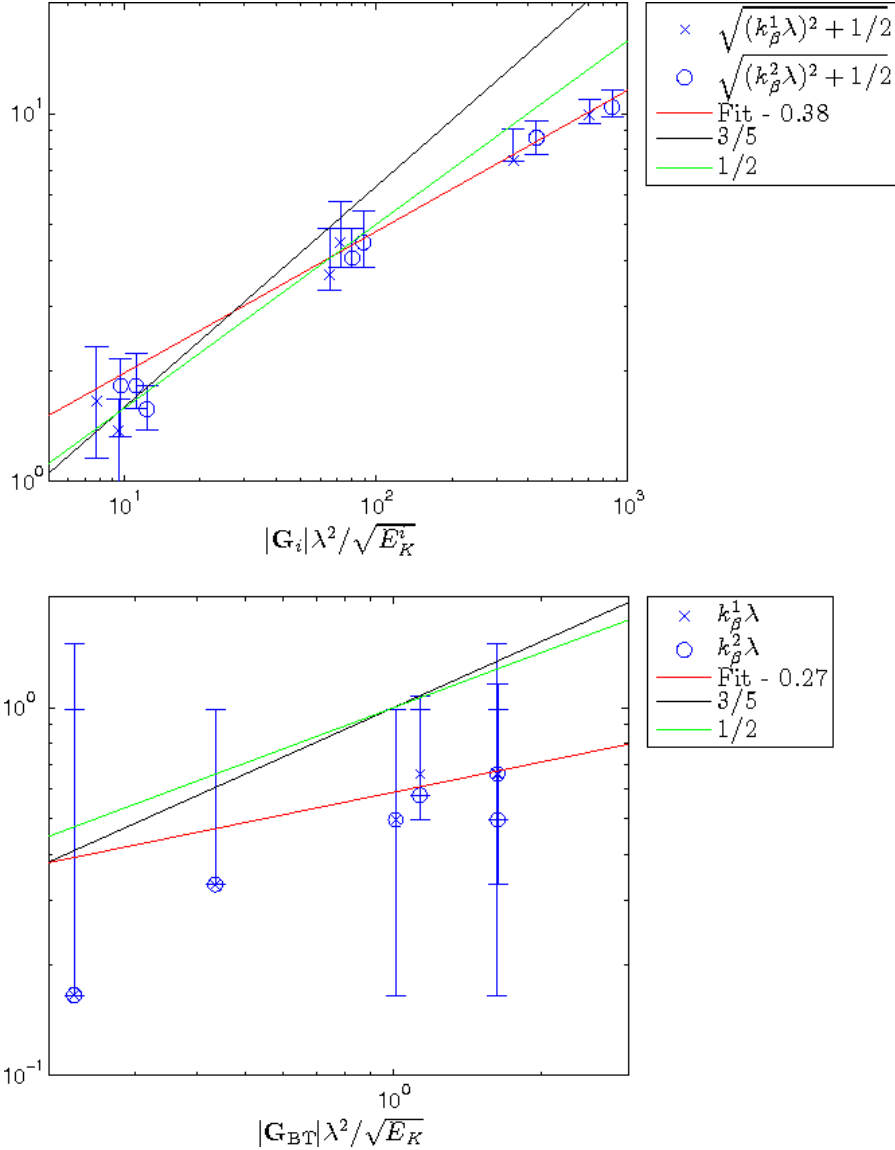


Figure 2.13: Mode (most common) cascade barriers over a short time period in each layer from a variety of simulations plotted against the mean non-dimensional vorticity gradient. The errorbars indicate the max/min cascade barrier measured over that period, indicative of the uncertainty in determining the maximum in the energy spectra. The upper panel shows the short wave (uncoupled) simulations and the lower the long wave (coupled) simulations. Also plotted are a least-squares fit (red), a $3/5$ power law (black) and a $1/2$ power law (green).

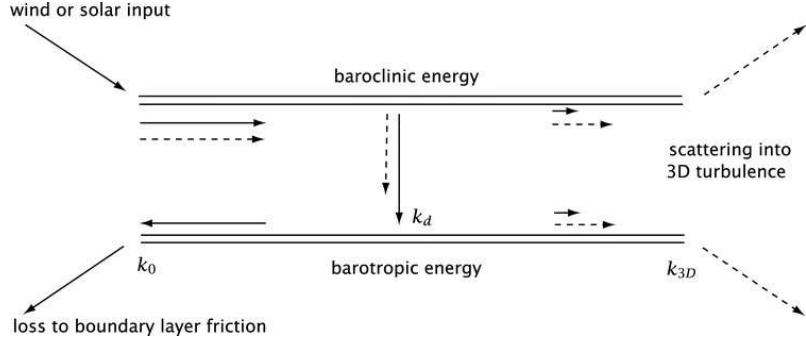


Figure 2.14: Idealised baroclinic turbulence, with the horizontal axis representing horizontal wavenumber and the barotropic and first baroclinic modes separated in the vertical. Solid lines represent energy transfer, and dashed enstrophy transfer. $k_d = 1/\lambda$ is the deformation wavenumber, k_0 is the halting scale and k_{3D} the scale at which enstrophy and energy scatter into 3D turbulence. From [Zurita-Gotor and Vallis \(2010\)](#), adapted from [Salmon \(1980\)](#).

2.2.3 Systems with background shear and bottom friction

We now consider a system where energy is provided by a global domain-averaged shear between the two layers, $\mathbf{S} = \mathbf{U}_1 - \mathbf{U}_2$, and is then released through dynamic baroclinic instability. The domain-averaged layer-wise velocities $\mathbf{U}_1 = (2U, 0), \mathbf{U}_2 = (0, 0)$, provide basis states that are solutions to the quasi-geostrophic equations in each layer. We define two streamfunctions for each layer, Ψ_i and ψ_i , related by $\Psi_i = \psi_i + \mathbf{U}_i \cdot (-y, x)$. Note that this velocity structure is a solution of the equations:

$$\frac{\partial Q_i}{\partial t} + J(\Psi_i, Q_i) = -\delta_{i2}\kappa\nabla^2\Psi_i + d, \quad i = 1, 2 \quad (2.26)$$

where κ is the bottom friction, and d is the small scale dissipation included for numerical stability. The small scale dissipation is implemented using a wave-number filter, as described in the appendix of [Smith et al. \(2002\)](#). The potential vorticities are given by

$$Q_i = q_i + \mathbf{G}_i \cdot \mathbf{x}, \quad i = 1, 2 \quad (2.27)$$

$$q_i = \nabla^2\psi_i + \frac{1}{2\lambda^2}[\psi_{(3-i)} - \psi_i], \quad i = 1, 2 \quad (2.28)$$

and the background layer gradients are now defined as follows:

$$\mathbf{G}_i = \left(0, \beta + (-1)^{i-1} \frac{U}{\lambda^2}\right) + \delta_{i2} (h_x, h_y), \quad i = 1, 2, \quad (2.29)$$

$$(2.30)$$

with the barotropic PV gradient \mathbf{G}_{BT} as defined previously in (2.17).

Unlike the previous systems discussed in this chapter, this system generates baroclinic instability through the background shear between the two layers, and the sink of energy provided by bottom friction allows the system to reach statistical equilibrium. As will be discussed in section 3.3, this balance sets the value of ε , the eddy energy production, which is not known a priori. An idealised picture of baroclinic turbulence can be seen in figure 2.14, which derives from ideas first mentioned in [Salmon \(1978\)](#). Energy is created at large scales in the baroclinic mode, and energy conservation considerations, derived in detail in [Vallis \(2006\)](#), imply transfer to the barotropic mode at the deformation scale. Also implied is an inverse cascade of energy to the halting scale k_0 , and a forward cascade of energy and enstrophy to the scale at which scattering into 3D turbulence occurs, $k_{3\text{D}}$. In our simulations, $k_{3\text{D}}$ is determined by the high wave number filter which mimics this effect. This picture has been shown to be incomplete in simple quasi-geostrophic models before, in particular there have been studies showing significant transfer of energy to the barotropic mode at larger scales than the deformation radius. Other studies such as [Sukoriansky et al. \(2007\)](#) show significant non-local transfer of energy within the barotropic mode, thus showing that a local ‘cascade’ is not necessarily present, confirmed by the work of [Srinivasan and Young \(2012\)](#) and others that show the characteristics of QG turbulence in QL models that have no local interactions. If these non-local processes are important in QG turbulence, then we would not expect to see Kolmogorov-like spectra, which, as discussed previously, explicitly require a local inverse cascade.

Thus, the most direct way of testing this picture is to compare the quantitative predictions with simulations. We now derive the predictions for the shapes of the energy spectra, and the implied jet and cascade barrier scales, before comparing these to our simulations.

Spectral scaling predictions

Assuming that the form of the inverse cascade of energy is proportional only to the constant energy flux ε and wavenumber K , leads, by dimensional considerations, to the

Kolmogorov scaling for the region between the forcing and cascade halting scales:

$$\mathcal{E}^{\text{Kol}}(K) = \mathcal{C}_{\varepsilon} \varepsilon^{2/3} K^{-5/3}, \quad K_{\beta} < K < 1/\lambda, \quad (2.31)$$

where $\mathcal{C}_{\varepsilon}$ is known as the Kolmogorov constant and is normally taken to be 6 ([Maltrud and Vallis, 1991](#)). To derive the equivalent spectra for the Rhines scaling, we note by dimensional considerations that $\omega_t \propto \sqrt{K^3 \mathcal{E}(K)}$, which gives:

$$\mathcal{E}^{\text{Rh}}(K) = U^2 K^{-1}, \quad K_{\beta} < K < 1/\lambda. \quad (2.32)$$

Assuming similarly that the forward cascade of entropy will be proportional to a constant enstrophy flux, ε_z , leads to the following form of the energy spectrum in this region:

$$\mathcal{E}^{\text{Kol}}(K) = \mathcal{C}_z \varepsilon_z^{2/3} K^{-3}, \quad 1/\lambda < K < K_d, \quad (2.33)$$

where \mathcal{C}_z is a constant, again assumed universal, and K_d is the small scale dissipation scale.

These scalings assume an isotropic cascade up until the cascade barrier, and an anisotropic cascade is expected to continue along the axis allowed by the form of the Rossby wave frequencies (discussed shortly), until it reaches the stopping or jet scale k_{jet} . As argued in [Vallis \(2006\)](#), if we assume that $k_{\text{jet}} \ll 1/\lambda$, then most of the energy in this region is in the barotropic mode. A theoretical spectral shape for this region was derived in [Rhines \(1975\)](#) by assuming that the spectra should now only depend on β . If we adapt this by using $|\mathbf{G}_{\text{BT}}|$ instead, this leads to, again by dimensional considerations:

$$\mathcal{E}_{\bar{\psi}}(l') = \mathcal{C}_{\beta} |\mathbf{G}_{\text{BT}}|^2 k'^{-5}, \quad k_{\text{jet}} < l' < K_{\beta}, \quad (2.34)$$

where l' is the wavenumber along the allowed axis, dependent on the shape of the Rossby wave frequency, $\mathcal{E}_{\bar{\psi}}$ is the barotropic energy spectra, and \mathcal{C}_{β} is sometimes called the Rhines constant. This assumption of β dependence has no clear justification, as discussed in [Smith et al. \(2002\)](#), and [Danilov and Gryankin \(2004\)](#) find no universal \mathcal{C}_{β} exists, but an approximate -5 spectra is seen to join peaks in the spectra in both studies as well as others. We can derive a prediction for the jet scale if we assume that the majority of the system energy will be collected in this region, i.e. the total system energy $E \approx \int_{k_{\text{jet}}}^{\infty} \mathcal{E}_{\bar{\psi}}(k') dk'$. The total barotropic energy $E_{\bar{\psi}} = 1/2(\langle |\nabla \psi_1|^2 \rangle + \langle |\nabla \psi_2|^2 \rangle)$. By manipulating the system equations, we know that, at statistical equilibrium $\langle |\nabla \psi_2|^2 \rangle = \varepsilon/\kappa$ [see (3.13)], but we have no way of estimating $\langle |\nabla \psi_1|^2 \rangle$ in terms of other parameters. We

assume proportionality to $\langle |\nabla \psi_2|^2 \rangle$ (valid as we expect both $E_{\bar{\psi}}$ and ε to be constant at statistical equilibrium) and so find $E_{\bar{\psi}} \propto \varepsilon/\kappa$, which, combined with (2.34), gives:

$$k_{jet} = \left(\frac{\mathcal{C}|\mathbf{G}_{BT}|^2 \kappa}{\varepsilon} \right)^{1/4}, \quad (2.35)$$

where \mathcal{C} may not be universal. Note that substituting $\varepsilon/\kappa = U_{rms}^2$ retrieves a Rhines scaling based on U_{rms} if the constant is dropped, where $U_{rms} \gg V_{rms}$ is the rms velocity scale in the jet direction.

Cascade barrier derivation

We will make qualitative and quantitative predictions for the cascade barrier based on the properties of the linearly derived dispersion relations. The introduction of a background velocity to the upper layer has two main effects on the linear behaviour. Firstly, the velocity directly alters the Rossby wave frequencies, however we will show that this does not affect the anisotropy of these relations in the long-wave limit, which we will see is most relevant to the jets found in this system. Secondly, along with the bottom friction (which doesn't alter the real part of the frequencies), the background shear allows for the presence of unstable modes, i.e. $\text{Im}(\omega(K)) \neq 0$ for certain parameters. This aspect will be investigated in section 2.2.4, and here we will concentrate on the behaviour of the real, wave frequencies. The frequencies are again solutions to a quadratic of the form $\omega_{\pm} = A \pm \sqrt{B}$, and $B = 0$ for some parts of wavenumber space, and so ω_{\pm} are not continuous functions of k, l .

As in section 2.2.2, the real parts of the dispersion relations have two simple limits, short- and long-wave. Interpreting the system as a barotropic mode forced by the baroclinic field, as discussed above, we expect the forcing to excite the barotropic mode around the deformation scale. Thus we expect the inverse energy cascade to begin from near the deformation scale and that the cascade barrier will be found at scales $k_{\beta} \lesssim 1/\lambda$, and so the long-wave limit could be relevant in some cases, but the short-wave limit is not expected to be relevant. This is consistent with the further results that will be presented in chapter 3, in which no de-coupled jets are observed across a range of parameters. Nonetheless, for completeness and for comparison with the previous results we derive both limits. The short-wave limits ($K\lambda \gg 1$) are again the equivalent layer-wise

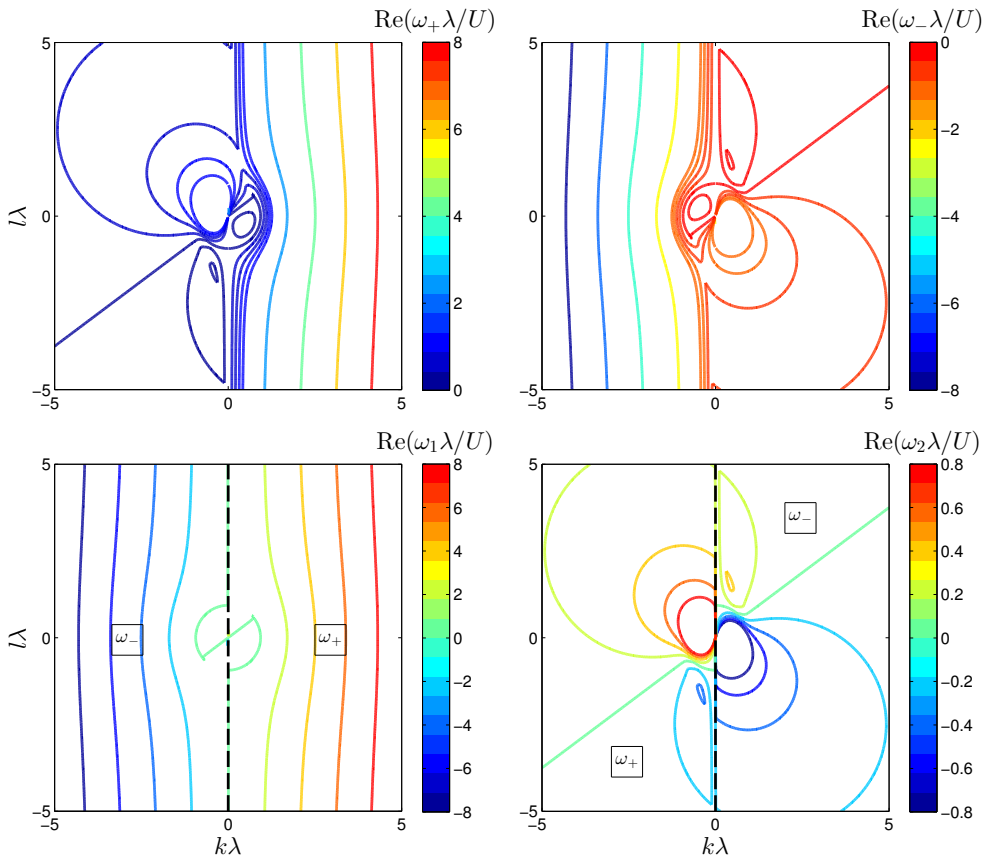


Figure 2.15: Linear Rossby wave frequencies for a two layer forced quasigeostrophic system, with $\beta\lambda^2/U = 1.75$, $h_x\lambda^2/U = 1$, $h_y\lambda^2/U = 0$. Upper panels show the full solutions ω_{\pm} , replotted in the lower panels as indicated, such that each panel relates to one of the dominant modes. The dashed line is the boundary between the two solutions, which resemble ω_s^i for $K\lambda \gg 1$.

frequencies:

$$\text{Re}(\omega_1^s) \approx \frac{-(\beta + U/\lambda^2)k}{k^2 + l^2 + 1/2\lambda^2} + 2Uk/\lambda^2 = \frac{\mathbf{G}_1 \times \mathbf{k}}{K^2 + 1/2\lambda^2} + \mathbf{U}_1 \cdot \mathbf{k}/\lambda^2, \quad (2.36)$$

$$\text{Re}(\omega_2^s) \approx \frac{-(\beta + h_y - U/\lambda^2)k + h_xl}{k^2 + l^2 + 1/2\lambda^2} = \frac{\mathbf{G}_2 \times \mathbf{k}}{K^2 + 1/2\lambda^2}, \quad (2.37)$$

where $\mathbf{U}_1 = (2U, 0)$. The real parts of frequencies in this limit can be seen in figure 2.15, where as before the upper panels show the full numerical solutions, ω_{\pm} , and we have replotted them in the lower panels according to the dominant modes. The ratio of the linear mode amplitudes on the same axes can be seen in figure 2.16, upper panels, on a log scale, where as before the warm colours are high values and the cold colours low values. The modes are dominant in the upper/lower layer at large $K\lambda$, and the dominant mode swaps near the $k = 0$ axis. Thus the lower panels of figure 2.15 show ω_i replotted as indicated, with the boundary between the two shown by the dashed line. The upper mode is dominated by the contribution from the background velocity, whereas the lower layer shows a similar form as in section 2.2.2, and both show good qualitative agreement with ω_i^s .

In the long-wave limit ($K\lambda \ll 1$), the frequencies again resemble barotropic and baroclinic modes, but modified by the background shear vector \mathbf{S} :

$$\text{Re}(\omega_1^l) \approx \frac{-(\beta + h_y/2)k + h_xl/2}{k^2 + l^2} + Uk/\lambda^2 = \frac{\mathbf{G}_{\text{BT}} \times \mathbf{k}}{K^2} + \mathbf{S} \cdot \mathbf{k}/\lambda^2, \quad (2.38)$$

$$\text{Re}(\omega_2^l) \approx \frac{-(\beta + h_y/2)k + h_xl/2}{k^2 + l^2 + 1/\lambda^2} + Uk/\lambda^2 = \frac{\mathbf{G}_{\text{BT}} \times \mathbf{k}}{K^2 + 1/\lambda^2} + \mathbf{S} \cdot \mathbf{k}/\lambda^2, \quad (2.39)$$

where $\mathbf{S} = (U, 0)$ as before. $\text{Re}(\omega_{\pm})$ in this limit can be seen in the upper panels of figure 2.17, and are replotted in the lower panels as before. Similarly to section 2.2.2, the modes in the long-wave limit resemble a barotropic and upper/lower trapped baroclinic mode, as can be seen in figure 2.16, lower panels. The area on one side of the line $\mathbf{G}_{\text{BT}} \times \mathbf{k} = 0$, indicated by the dash-dotted line, has $\hat{\psi}_1^{\pm}/\hat{\psi}_2^{\pm} \approx 1$, a dominant barotropic mode, and the other side a top/bottom trapped baroclinic mode. The black lines again show where $\hat{\psi}_1^{\pm}/\hat{\psi}_2^{\pm} = \pm\infty$ or 0, and the shading where the ratio is negative. The replotted frequencies, shown in the lower panels of figure 2.17, broadly qualitatively resemble the long-wave limits of the system without shear or bottom friction, see figure 2.9, which indicates that in this limit, the addition of the background shear has not affected the qualitative form of the dispersion relations, and the anisotropy is well approximated by ω_i^l .

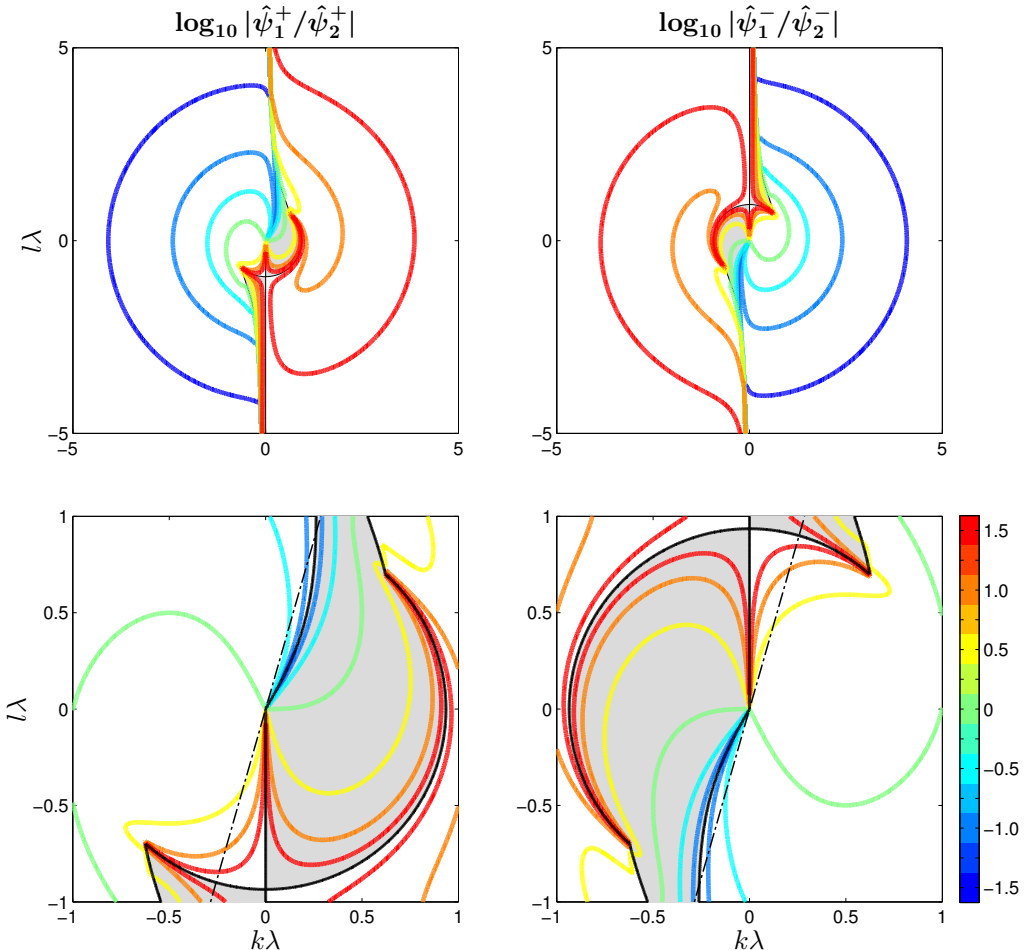


Figure 2.16: Ratio of linear mode amplitudes, $|\hat{\psi}_1^\pm/\hat{\psi}_2^\pm|$, on a log scale, for $\beta\lambda^2/U = 1.75$, $h_x\lambda^2/U = 1$, $h_y\lambda^2/U = 0$. The black lines show the hyperbolic points where the ratio tends to $\pm\infty$ or to 0. The shading indicates $\hat{\psi}_1^\pm/\hat{\psi}_2^\pm < 0$. The upper panels show the ratios for large wavenumbers, and the lower the same quantities but on a small wavenumber scale. The dash-dotted lines in the lower panels indicates the boundary between the frequencies plotted in figure 2.17, lower panel. The colour scale shows the contour values for all four plots.

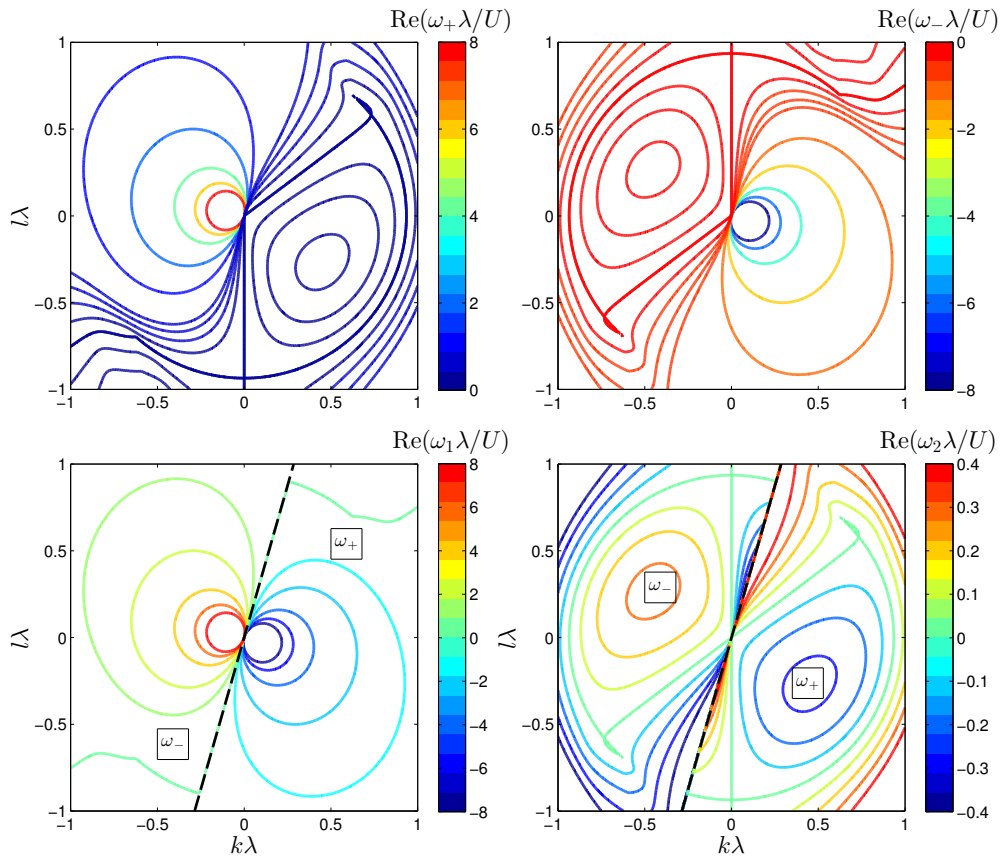


Figure 2.17: Linear Rossby Wave frequencies for a two layer forced quasigeostrophic system, with $\beta\lambda^2/U = 1.75$, $h_x\lambda^2/U = 1$, $h_y\lambda^2/U = 0$. Upper panels show the full solutions ω_{\pm} , replotted in the lower panels as indicated, such that each panel relates to one of the dominant modes. The dashed line is the boundary between the two solutions, which resemble ω_l^i for $K\lambda \ll 1$.

If we again equate the Rossby wave frequencies $\text{Re}(\omega_i)$ with the turbulent frequency, the wave-turbulent boundary is found by the solution to the following:

$$\frac{\mathbf{G} \times \hat{\mathbf{k}}}{K^2 + \Lambda^2} + \mathbf{S} \cdot \hat{\mathbf{k}} = \frac{\varepsilon^a U_t^{1-3a}}{K^a}, \quad a = \{0, 1/3\}, \quad (2.40)$$

where again $\Lambda^2 = 1/2\lambda^2$, 0 or $1/\lambda^2$ in the short-, barotropic long- or baroclinic long-wave limits respectively, \mathbf{G} is the relevant PV gradient, and \mathbf{S} the relevant velocity vector. We similarly define the cascade barrier scale as the barrier size at $\theta = -\phi$, where ϕ is the angle perpendicular to the PV gradient \mathbf{G} . For Rhines scaling, this leads to

$$k_\beta = \sqrt{\frac{|\mathbf{G}|}{U_t - \mathbf{S} \cdot \hat{\mathbf{k}}|_{-\phi}} - \Lambda^2}, \quad (2.41)$$

where the turbulent velocity scale is altered by the component of the background velocity perpendicular to the PV gradient. We expect the Kolmogorov scaling to be relevant here as the system will experience constant forcing from the baroclinic instability of the mean flow at statistical equilibrium.

We can test these predictions quantitatively against our simulations in two ways: firstly, as before, we can calculate the cascade barrier from the kinetic energy spectra and compare it directly with the predictions from solving (2.40). Secondly, since the cascade barrier theory is based on assumptions about the dependence of the energy spectra on wavenumber, as discussed above, we can compare the spectral slopes from simulation to theory.

The dependence of spectral shape on the non-dimensional topographic slope, h_x , can be seen in figure 2.18, which shows KE spectra for simulations with $\kappa\lambda/U = 0.1$, $\beta\lambda^2/U = 0.75$, $h_y\lambda^2/U = 0$, and increasing $h_x\lambda^2/U$. The corresponding streamfunctions are seen in figure 2.19. As with the previous sections, the spectra show anisotropy and minima close to the wavenumber origin, although the minima is not a clear dumbbell shape in all cases. As h_x increases, top to bottom, the spectra tilt more and the shape shrinks, consistent with the increased energy in the systems (see chapter 3 for plots of eddy energy production versus jet tilt). Also shown in figure 2.18 are the solutions to (2.40) for k_β given the parameters of the simulations (green contours on top of the lower layer spectra). For $h_x = 0$, the contour lies along the high energy bands at $k \sim 0.5\lambda$, but doesn't match the dumbbell shape of the energy minima well. However, for $h_x = 0.2 - 0.4$ the contours appear to match the dumbbell shapes very well.

For the $h_x = 0$ simulation, the majority of the energy is collected in bands either

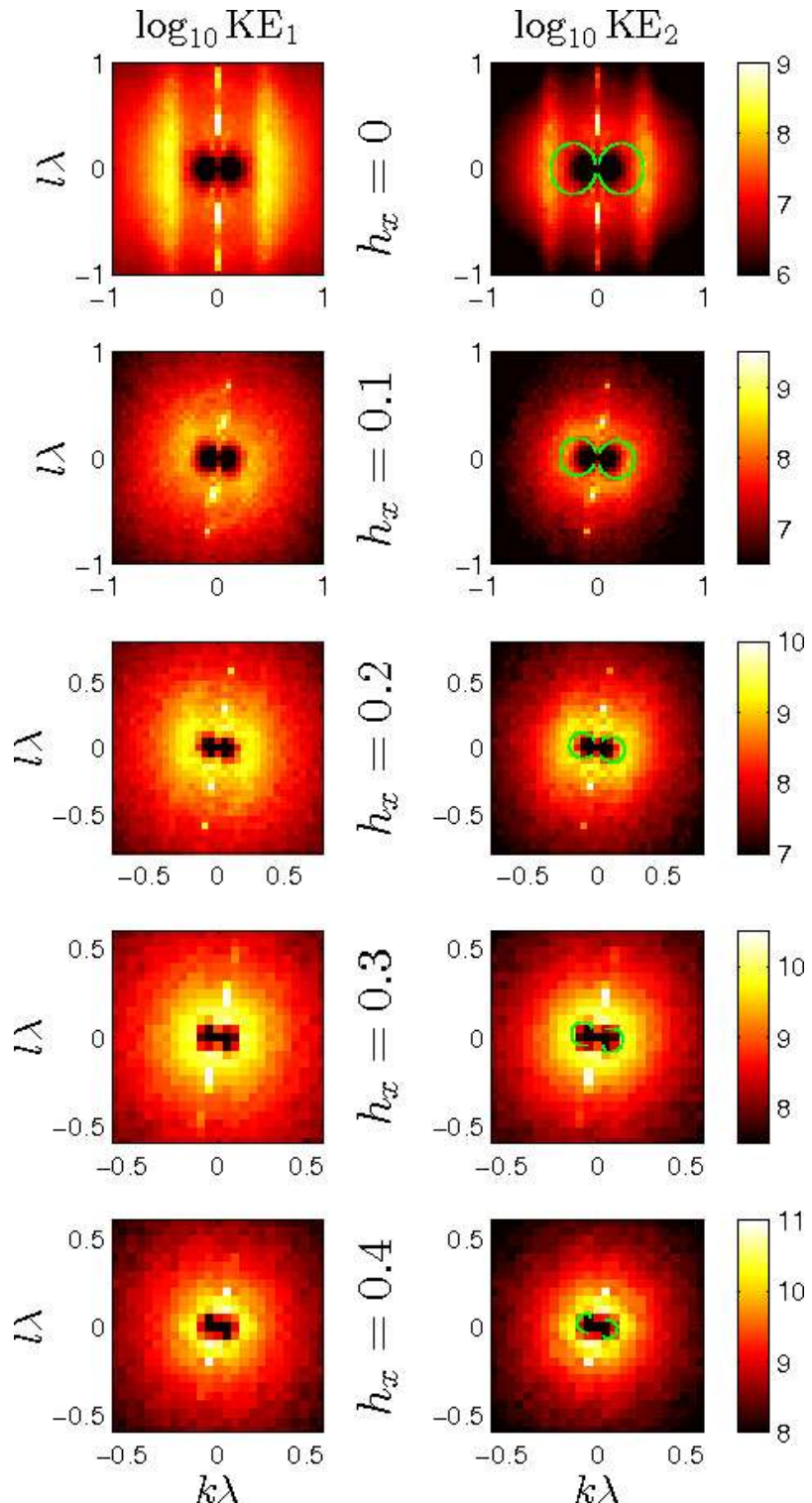


Figure 2.18: Upper and lower layer time-mean KE from full simulations with $\kappa\lambda/U = 0.1$, $\beta\lambda^2/U = 0.75$, $h_y\lambda^2/U = 0$ and $h_x\lambda^2/U$ from 0 to 0.4, top to bottom. Theoretical k_β indicated by the green contours over lower layer plots. The colour axis is a log-scale with arbitrary units, and is the same for both layers.

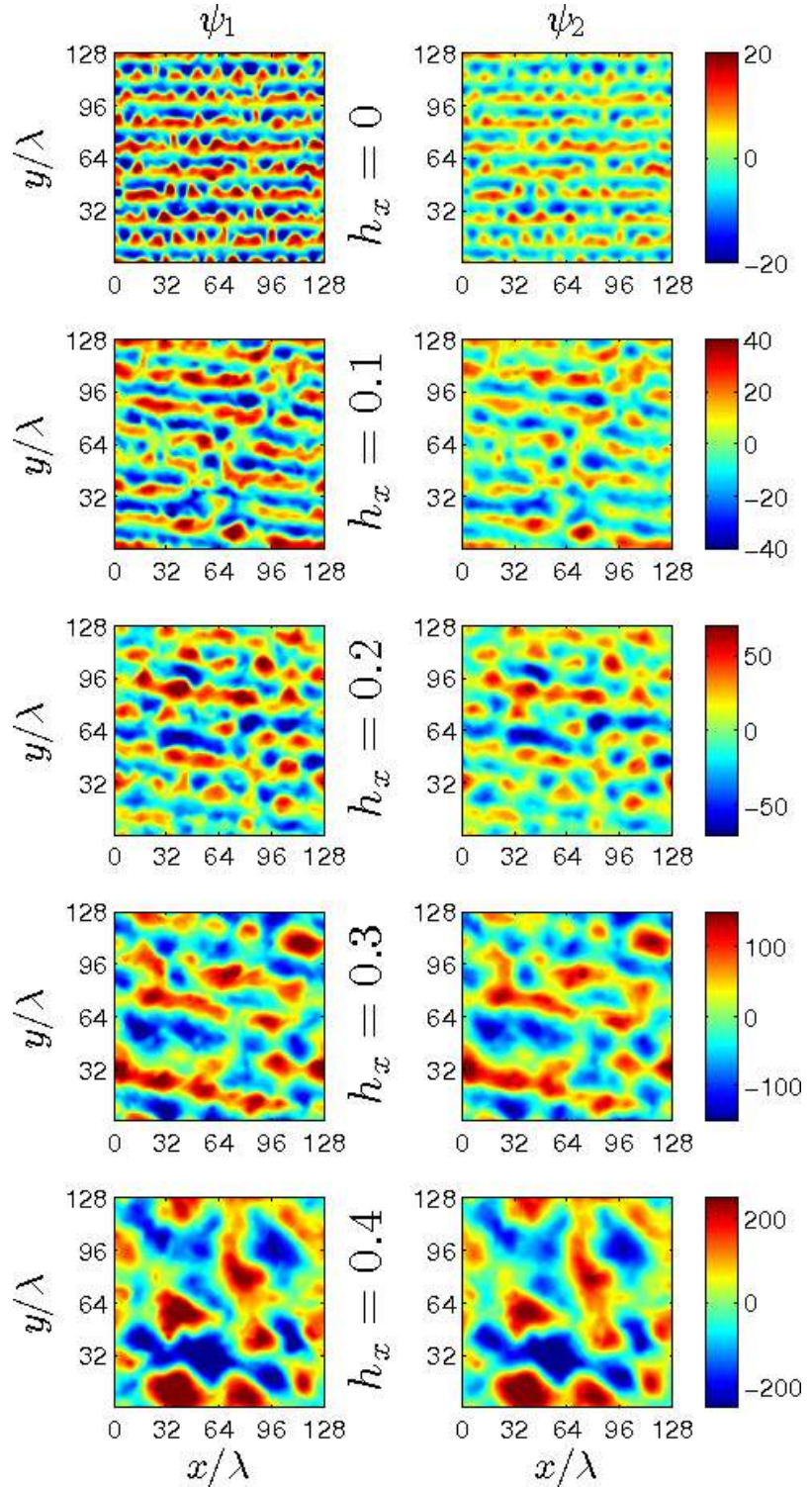


Figure 2.19: Snapshots of upper and lower layer perturbation streamfunctions from the forced-dissipative simulations shown in figure 2.18. The colour axis has arbitrary units and is the same for both layers

side of the l -axis, rather than uniformly around the dumbbell region as seen in the other spectra. This is also seen in other simulations where the cascade barrier scale is similarly relatively large, and so we postulate this is due to the cascade halting close to the scale at which energy is entering the system, $K \approx 1/\lambda$, which stops a fully developed inverse cascade from developing.

This is confirmed by looking at the spectral shape in more detail. Figure 2.20 shows time mean barotropic energy spectra, $\mathcal{E}_{\bar{\psi}}$, with slices of the full 2D spectra in the upper panel, and the full integrated 1D spectra in the lower panel. In the upper panel we have taken slices along the k' and l' axes, which are aligned with the spectra, i.e. rotated by $-\phi_{\text{jet}}$. The solid blue lines are the spectra along the k' axis from four simulations with increasing eddy energy production values, see lower panel. These have been artificially separated vertically so the axes are not accurate. The dashed black lines are the spectra along the l' axis, for the same simulations and separated identically. Thus it can be seen that all four are approximately isotropic for $k > 1/\lambda$, and then the l' spectra separates from the k' , and rises to the peak at k_{jet} .

A change in slope is seen at around $k \sim \lambda$, as expected by the scaling theory mentioned previously. The red dash-dotted line shows a k^{-4} slope, which is what would be expected from the isotropic Kolmogorov K^{-3} slope for the forward enstrophy cascade region, $1/\lambda < k < k_D$. Shown in the red and green dashed lines are the expected Kolmogorov and Rhines scaling slopes, respectively, for the inverse energy cascade region, $k_\beta < k < 1/\lambda$, which have also been scaled by a factor of k^{-1} . The light blue dashed line is the expected k^{-6} slope, which has been observed to join peaks in the region $k_{\text{jet}} < k < k_\beta$ in previous studies (see previous discussion). As noted previously, the lower energy spectra, which have spectral peaks close to $1/\lambda$, show steeper spectra than expected in both the enstrophy and energy cascade regions, and are less isotropic in the enstrophy cascade region. However, the spectra which are more fully developed below $1/\lambda$ show good approximate agreement with the Kolmogorov scalings, although the multiple peaks along the l' axis are not apparent in these simulations, and so the -6 slope is not apparent.

Following Smith et al. (2002), we define $k_\beta^{\bar{\psi}}$ as the wavenumber at which the k' and l' spectra separate, which is marked by the black circles in the upper and lower panels. As can be seen, this is harder to specify in the cases where the spectral peak is close to $1/\lambda$, and so we have in these cases (e.g. in the lower two spectra in fig. 2.20) used the 1D spectra to choose the wavenumber at which spectral steepening is seen. As also seen in Smith et al. (2002), the spectra continue on past this scale along the k' axis, indicating some continuation of the inverse cascade. The lower panel shows the same scalings on

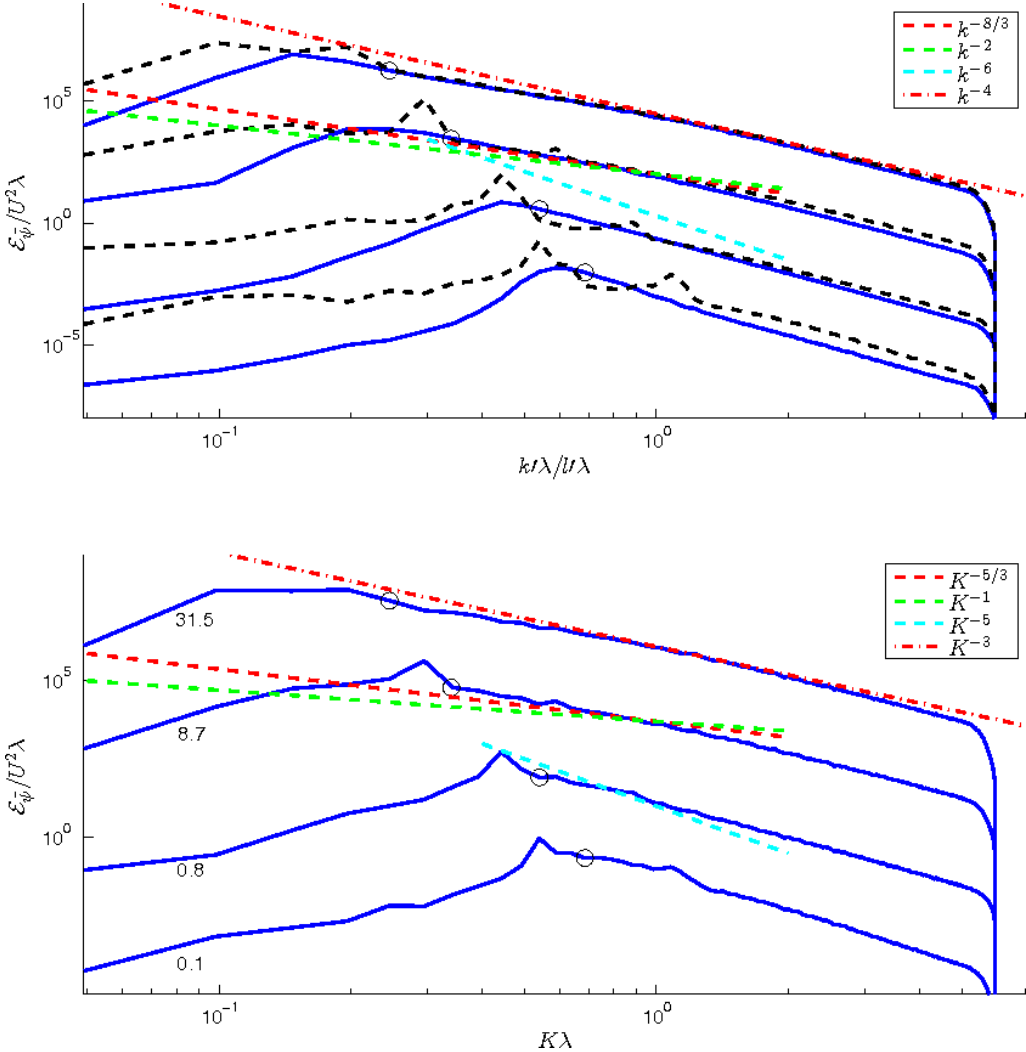


Figure 2.20: Time mean barotropic energy spectra, $\mathcal{E}_{\bar{\psi}}$ for four simulations, with $\varepsilon\lambda/U^3$ as indicated by the numbers in the lower panel. The black circles in both panels indicate the cascade barrier scale derived from these spectra. Upper panel: Solid blue lines are spectral slices along the $k\lambda$ axis, dashed black along the $l\lambda$ axis, where the primes indicate the axes have been rotated by $-\phi_{jet}$. Lower panel: integrated 1D spectra against total wavenumber K . Also shown are theoretical scalings (dashed lines) as labelled: -3 (-4) and $-5/3$ ($-8/3$) based on Kolmogorov scalings for the forward enstrophy and inverse energy cascade regions, -1 (-2) based on Rhines scaling for the inverse energy cascade region, and -5 (-6) based on PV gradient scaling in 1D (2D) spectra.

the 1D spectra, which have the same qualitative behaviour as the k' spectra, but with the peak at the jet scale visible. The numbers shown are the equilibrated eddy energy production values, ε . Unlike previous barotropic studies, we do not see a significant K^{-5} slope region, and k_{jet} is only a few wavenumbers below $k_{\beta}^{\bar{\psi}}$.

To more accurately assess the agreement with the Kolmogorov spectral slope scalings, we make a linear least-squares fit of the spectral slopes in the enstrophy and energy cascade regions, using the time-mean barotropic energy spectra as plotted in figure 2.20. The results can be seen in figure 2.21, where the upper panel shows the slopes fit in the enstrophy cascade region, $1/\lambda < k < k_D$, and the lower shows the energy cascade region, $k_{\beta}^{\bar{\psi}} < k < 1/\lambda$, for a range of simulations. The calculation was carried out for the 2D slices along the k' and l' axes as well as for the full 1D spectra, but the slopes calculated along the former are adjusted by a factor of k to compare directly with the latter. We omit the calculation for the energy cascade region along the l' axis as this is not a clear constant slope for some of the simulations, as seen in figure 2.20, but it is close to the other values shown for $k_{\beta}^{\bar{\psi}} < 0.5$. In the enstrophy cascade region (upper panel), the slope along the l' axis (black circles) is consistently slightly shallower than the k' and K slopes, which are similar for most simulations. The black dashed line indicates the expected -3 Kolmogorov scaling for this region, see (2.33). For $k_{\beta}^{\bar{\psi}} < 0.5$, the slopes are fairly consistent between simulations and show a K slope of ~ -0.33 to -0.35 . However, for $k_{\beta}^{\bar{\psi}} > 0.5$, the slopes consistently steepen as the cascade barrier approaches $1/\lambda$. In the energy cascade region (lower panel), the slopes along the k' axis are shallower than the Kolmogorov scaling for this region, shown by the black dashed line ($-5/3$, see (2.31)). Again, for $k_{\beta}^{\bar{\psi}} < 0.5$, we see a fairly consistent K and k' slope, of around -2.0 to -2.2 . However, the K slopes show a shallowing and then reversal of sign for $k_{\beta}^{\bar{\psi}} > 0.5$. The slopes in this region are less well defined, indicated by the error bars, which are larger when the spectral region is shorter, i.e. for larger $k_{\beta}^{\bar{\psi}}$, which is due to the irregular shape of the cascade along the l' axis, see figure 2.20.

If we interpret these results as indicating that the simulations with $k_{\beta}^{\bar{\psi}} < 0.5$ are close to the theoretical Kolmogorov cascades, then we might expect that the Kolmogorov predicted cascade barrier, k_{β}^{Kol} , to be closest to the measured values for these simulations. It appears that if $k_{\beta}^{\bar{\psi}}$ is closer to the scale at which energy is transferred to the barotropic mode, thought to be $\sim 1/\lambda$, then the cascades do not fully develop, and the energy/enstrophy remains collected around these scales, as indicated by the steeper slopes in both regions, see figure 2.21. Figure 2.22 shows the measured cascade barriers $k_{\beta}^{\bar{\psi}}$ and jet scales k_{jet} , calculated from time-mean barotropic energy spectra, against the

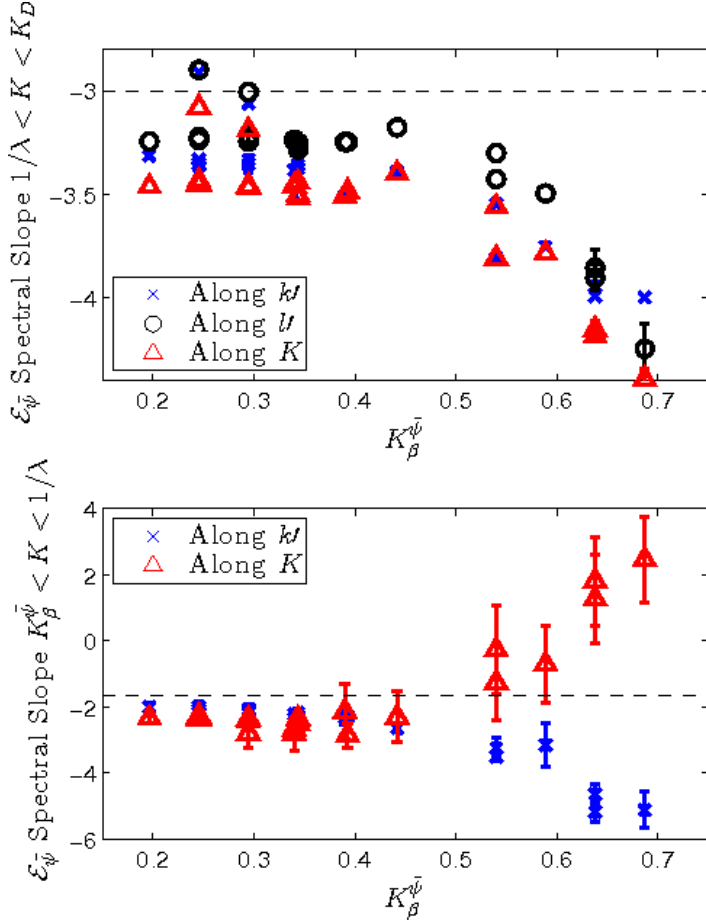


Figure 2.21: Barotropic energy spectral slopes determined by a linear least squares fit for various simulations. The symbols indicate the part of the spectra fitted: slices of the 2D spectra along the k' and l' axis as well as the full 1D spectra along K . Error bars indicate the 95% confidence intervals, and are not shown where these are smaller than the plotted symbols. Upper panel: calculated in the enstrophy cascade region $1/\lambda < k < k_D$. Black dashed line at the Kolmogorov scaling -3. Lower panel: calculated in the energy cascade region $k_{\beta}^{\bar{\psi}} < k < 1/\lambda$. Black dashed line at the Kolmogorov scaling $-5/3$. See text for more details.

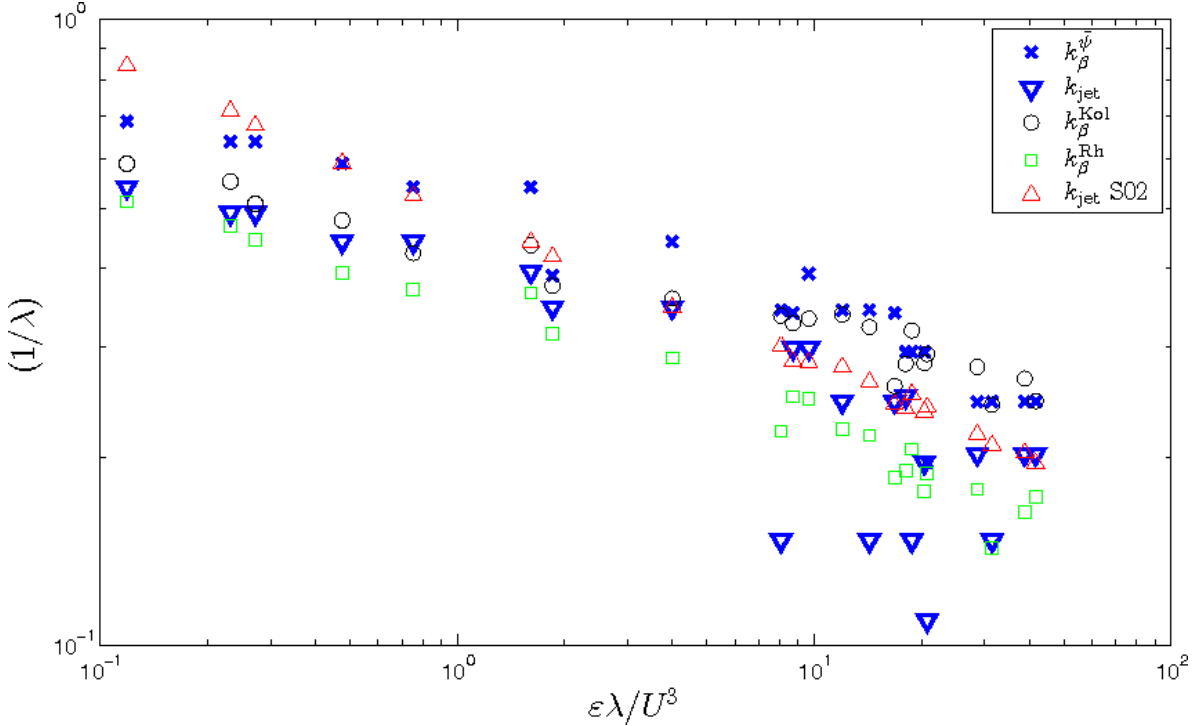


Figure 2.22: Measured cascade barriers $k_{\beta}^{\bar{\psi}}$ and jet scales k_{jet} in units of λ , calculated from time-mean barotropic energy spectra, denoted by blue crosses and triangles respectively, plotted against the non-dimensional eddy energy production ε . Also shown are various theoretical estimates: Predictions of $k_{\beta}^{\bar{\psi}}$, $k_{\beta}^{\text{Kol/Rh}}$, based on Kolmogorov/Rhines scalings, and a prediction of k_{jet} , $k_{\text{jet}} \text{ SO2}$, defined in (2.35).

time mean energy production ε for various simulations, shown by the blue crosses and triangles respectively. We have *not* plotted errors on the quantities measured, which all show a degree of time variability, in order to be able to clearly compare the values. As observed in [Vallis and Maltrud \(1993\)](#), [Smith et al. \(2002\)](#) and others, we find k_{jet} to be consistently below $k_{\beta}^{\bar{\psi}}$. $k_{\beta}^{\bar{\psi}}$ shows a clear inverse relationship with ε , and whilst k_{jet} also shows a general decrease with increasing ε , there is some variability between simulations at high ε . The simulations that appear to have k_{jet} below the curve suggested by the other simulations all have $\phi_{\text{jet}} = 26.6^\circ$, and we believe these simulations are affected by the geometrical effects discussed in chapter 3, see especially figure 3.6.

Also shown are the theoretical cascade barrier scales, taken by directly solving (2.40) for $\phi = \phi_{\text{jet}}$, where we have included the Kolmogorov constant, $\mathcal{C}_{\varepsilon} = 6$, in the derivation of k_{β}^{Kol} . k_{β}^{Kol} (black circles) shows good agreement with the measured values for lower values of $k_{\beta}^{\bar{\psi}}$, as expected, but under-predict at higher values, where the spectra do not

scale as expected, and in fact is closer to the jet scale in this region. It should be noted that, as previously mentioned, $k_\beta^{\bar{\psi}}$ is not well defined for these simulations. k_β^{Rh} (green squares) comes out consistently below $k_\beta^{\bar{\psi}}$ for all values, but remains relatively close to k_{jet} across both regions. The relative similarity of both scales with the jet scale for higher values of $k_\beta^{\bar{\psi}}$ suggests that, when the jet scale is close to the energy input scale, the energy collects near this scale, as seen in the spectra in figure 2.20, and then scalings dependent on the energetics of the system (U_T or ε) are a good approximation to the jet scale.

Also plotted (red triangles) is the theoretical jet scale used in [Smith et al. \(2002\)](#) from (2.35) (labelled k_{jet} S02), where we take $\mathcal{C} = 1$. This shows good agreement with the higher jet scales at large ε , but over-predicts at small ε . This is surprising as the K^{-5} spectra that this theory relies on is not seen in the high ε spectra, but may be present between the peaks in the low ε spectra. This suggests that, although there is no good justification for the spectra, as previously discussed, and indeed it is not observed, a dimensionally consistent scaling dependent on the magnitude of the PV gradient and the equilibrated kinetic energy ε/κ shows good agreement with the jet scale when there is a well developed inverse cascade between this scale and the forcing. Given $\mathcal{C} = 1$ fits the data well, and taking $\mathcal{C}_\beta = 0.5$, as is standard ([Sukoriansky et al., 2007](#)), implies that $\mathcal{E}_{\bar{\psi}} \approx 2\varepsilon/\kappa$, i.e. $\langle |\nabla\psi_1|^2 \rangle \approx \langle |\nabla\psi_2|^2 \rangle$, as could be expected in a barotropic dominated regime.

In this section we have seen that, in simulations containing shear and bottom friction, the anisotropy of the kinetic energy spectra observed in the unsteady simulations persists, and seems again to be well described by the anisotropy of the Rossby wave dispersion relations. Additionally, there is some agreement between the Kolmogorov scalings and the spectral slopes for simulations with higher eddy energy production values, which also have cascade barriers and jet scales in good agreement with theory. However, for simulations with lower energy production, the spectra are steeper than theory, and Rhines scalings based on eddy velocity scales give a better estimate of the jet scale.

2.2.4 Unstable Modes

As mentioned in section 2.2.3, the introduction of shear and bottom friction to the two-layer system allows for unstable linear modes. As discussed in section 2.1, BKP09 rely on the form of these instabilities as the basis for their theory of the formation of zonal jets in baroclinic QG systems with a β plane. [Chen and Kamenkovich \(2013\)](#) investigate the behaviour of the most unstable modes in an similar system to ours, in the presence of shear and meridional and zonal slopes in bottom topography, but in the absence of bottom friction. In the absence of topography, the stability of a system with background shear is dependent on the value of $\beta\lambda^2/U$ (see, for example, [Vallis \(2006\)](#)). [Chen and Kamenkovich \(2013\)](#) find that a meridional slope in bottom topography acts only to alter the instability as would be expected due to the moderation of the magnitude of the lower layer PV gradient in the y -direction, but that a zonal bottom slope can destabilise otherwise stable flows in the absence of topography. In our system, all parameters have some instability introduced by the bottom friction, but this is small in magnitude compared to that introduced by U and the topographic slopes.

An example of the form of the unstable modes can be seen in figure 2.23, which shows the Rossby wave frequencies and the unstable growth rates for ω_- from two simulations, without (upper panels) and with (lower panels) a zonal slope in bottom topography. The upper panels show that the most unstable mode is at $l = 0$, a wave-vector perpendicular to the meridional PV gradient. This is the classic noodle mode. In the lower layer, the most unstable mode is not at $l \neq 0$, and crucially is no longer perpendicular to the PV gradient direction, as can be seen from the tilt of the dispersion relation. The relationship between the PV gradient angle and the direction of the most unstable mode wave-vector was investigated for a range of parameters in [Chen and Kamenkovich \(2013\)](#), who find that, for $h_x \neq 0$, these two quantities are not perpendicular, and in fact are aligned for some parts of parameter space.

BKP09 calculate the successive instabilities of a baroclinic system on a β plane and in the presence of shear, calculating numerically the instability of the background shear superimposed with the most unstable noodle mode of the shear itself. They find this to be dominated by a $k = 0$ mode, which produces a gridded pattern when superimposed on the primary instability. BKP09 propose that the scale of this secondary instability sets the scale of the jets, by efficiently projecting energy onto the zonal linear eigenmodes of the system, which contribute to jet formation by interactions with the primary and secondary instabilities. They find good agreement between the form of the instabilities they calculate and full non-linear simulations of the system. They argue that these instabilities directly

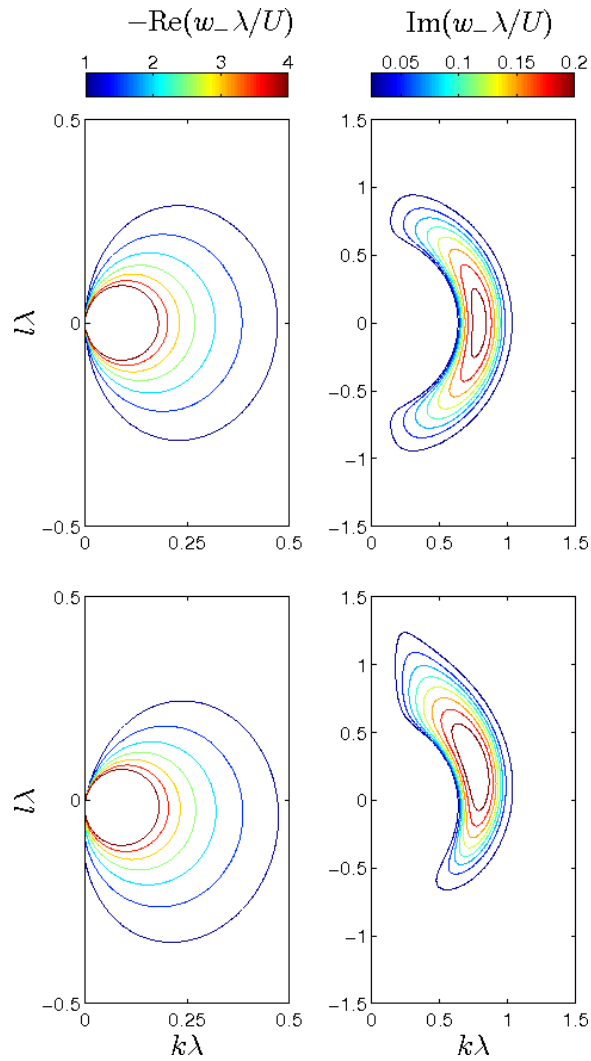


Figure 2.23: Contours of Rossby wave frequency (left panels) and growth rate of unstable modes (right panels) for two simulations with $\beta \lambda^2 / U = 0.75$, $\kappa \lambda / U = 0.1$ and $h_x \lambda^2 / U = 0$ (upper panels) and $h_x \lambda^2 / U = 0.3$ (lower panels).

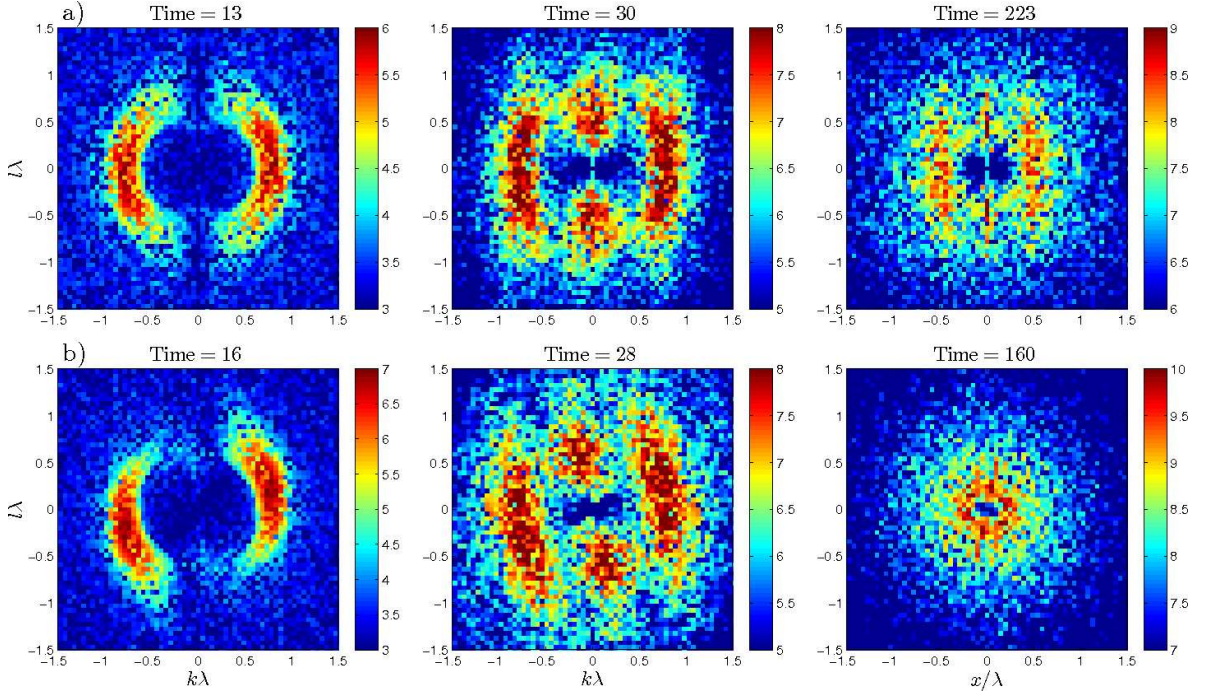


Figure 2.24: Snapshots of upper layer kinetic energy during the spin-up phase and statistical equilibrium of two simulations with $\beta\lambda^2/U = 0.75$, $\kappa\lambda/U = 0.1$ and a) $h_x\lambda^2/U = 0$ b) $h_x\lambda^2/U = 0.3$. Time is in units of λ/U and the energy is plotted on a log scale. The left panels can be compared with the right panels of figure 2.23.

localise the energy without the need for a Rossby wave halting mechanism. Could these ideas provide an alternative explanation for the non-zonal jets seen in our simulations?

The form of instabilities can readily be observed in the spin-up of simulations, and so figures 2.24 and 2.25 show successive spectra (on a log scale) and streamfunction snapshots from the spin-up of two representative simulations, with and without zonal slopes in bottom topography. Both simulations have $\beta\lambda^2/U = 0.75$, $h_y\lambda^2/U = 0$, $\kappa\lambda/U = 0.1$, and a) $h_x\lambda^2/U = 0$, b) $h_x\lambda^2/U = 0.3$. These can be directly compared to the linear Rossby wave frequencies and growth rates shown in figure 2.23, which are calculated with the same values. All simulations are initialised with an isotropic kinetic energy field with fixed amplitude and random phase at each wavenumber. A short period of time later, the left hand panels in figure 2.24 clearly show the form of instability predicted by the linearly unstable growth rates in the right hand panels of figure 2.23. These correspond to the noodle modes seen in the left panels in figure 2.25. The fastest growing secondary instability can be seen in the middle panels, a short time after the left hand panels, which appears to be a $k = 0$ mode for the $h_x\lambda^2/U = 0$ case, as in BKP09, and is similarly a

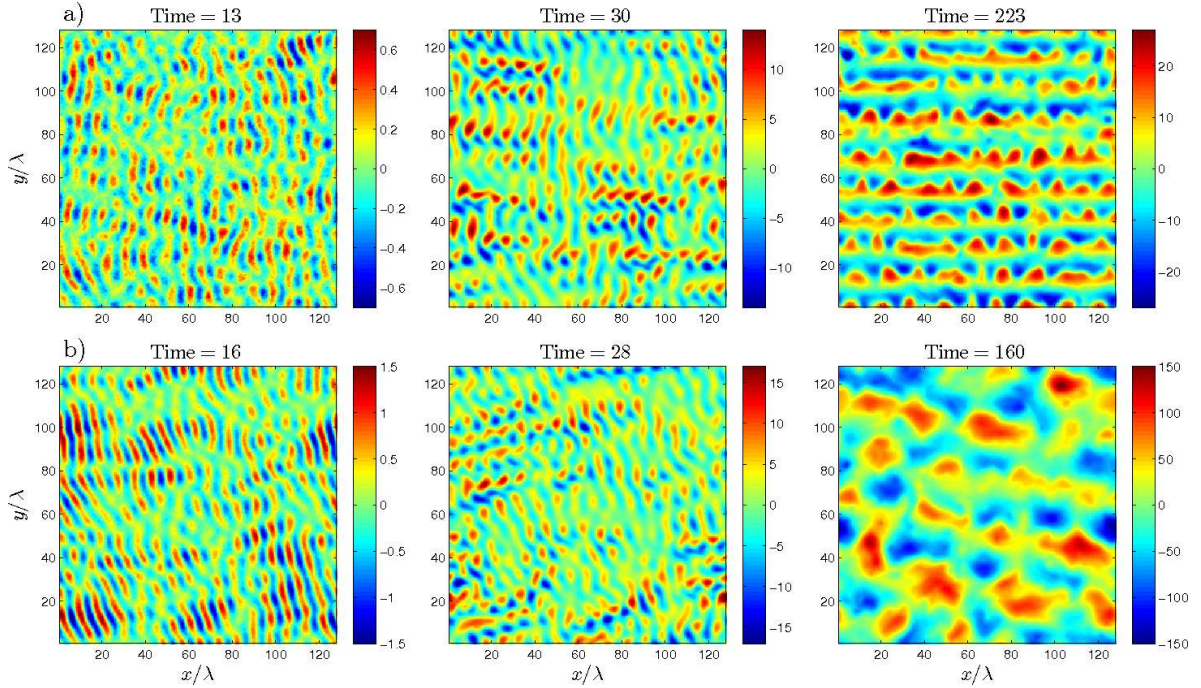


Figure 2.25: The upper-layer perturbation streamfunctions, ψ_1 , corresponding to the spectra plotted in figure 2.24.

mode perpendicular to the fastest growing primary instability for the $h_x\lambda^2/U = 0.3$ case. This results in the ‘gridded’ structure in the streamfunctions seen in figure 2.25.

Finally, the right hand panels show the fully equilibrated quasi-steady states. For the $h_x\lambda^2/U = 0$ case, the final spectral shape and streamfunctions show similarities with the form of the instabilities, although the energy has been concentrated further along the $k = 0$ axis, resulting in the jets seen in the streamfunction field, which do show a similar scale to the secondary instability. However, for the $h_x\lambda^2/U = 0.3$ case, there does not appear to be any similarity between the form of the secondary instabilities and the equilibrated state. Indeed, the orientation of the secondary instability is not the same direction as the jets that emerge, and the scales are not similar. At intermediate times (not shown), the structure seen in the streamfunction fields in the central panels breaks down before the emergence of the jets which then remain the quasi-steady state. This agrees with the idea that for numerical simulations of non-linear systems such as this, the statistically equilibrated state should not depend on the structure of the initial condition.

Although we have not carried out a full calculation of the secondary instabilities of our system, the observed secondary instabilities in the spin-up of our simulations

appears to be consistently perpendicular to the primary, noodle instability, as is seen in figure 2.24. As the results of [Chen and Kamenkovich \(2013\)](#) show, the direction of the primary instability wave-vector does not have a consistent relation with the direction of the barotropic PV gradient over a wide range of parameters in systems with a zonal slope in bottom topography. If indeed the secondary instability is always perpendicular to the primary instability, then this implies that the secondary instability will not result in flow aligned with the direction of the jets that form. Even if this is not true, and there is not a consistent relationship between the directions of the primary and secondary instability wave-vectors, it seems clear that for simulations with a zonal slope in bottom topography, linear instability cannot predict the form of the jets present in these simulations. This does not mean that the process outlined in BKP09 is not part of the formation of zonal jets in the absence of bottom topography, but that once the symmetry of the system is broken by the introduction of a zonal slope in bottom topography then the instabilities no longer efficiently put energy into the wavenumbers favourable for jet formation.

2.3 Conclusions

In this chapter we have sought to investigate the mechanism of jet formation in quasi-geostrophic systems. A survey of the literature found a wide range of theories describing the formation of zonal jets on a β plane, dating back to Rhines (1975). The oldest theory is one that has developed from the ideas of this seminal work, is based on the form of the linear barotropic Rossby wave frequency, and which has been updated in Vallis and Maltrud (1993). More recent theories include ‘zonostrophic’ instability, derived from the analysis of quasi-linear systems (Srinivasan and Young, 2012); ‘noodle mode’ theory, in which linear instabilities are proposed to produce and shape the jets (Berloff et al., 2009); and PV theories which explain jet formation by the tendency for mixing of PV to form ‘staircases’ (Dritschel and McIntyre, 2008).

In order to attempt to apply the theory of VM93 to a baroclinic system with a general slope in bottom topography, we first attempted to extend it to a simple baroclinic system on a β plane, in the absence of forcing or dissipation, in order to see whether any qualitative predictability was possible. The normal modes of such a system are the barotropic and baroclinic modes, both with associated Rossby wave dispersion relations. Comparing the form of kinetic energy spectra from decaying simulations of the same system with the form of these frequencies, it was found that, as in VM93, the anisotropy of the frequencies corresponded with the anisotropy of the spectra, and so with the form of the jets. The introduction of a second layer to the theory lead to dependence on the deformation radius, and so to the presence of two limiting regimes - a longwave limit ($K \ll 1/\lambda$) in which the two frequencies were distinctly different, and a shortwave limit ($K \gg 1/\lambda$) in which the two frequencies were approximately equal. The theory of VM93 dictates that the scale of the jets is determined by the scale of the cascade barrier, k_β , the wavenumber at which the turbulent frequency equals the Rossby wave frequency. This cascade barrier should be proportional to the PV gradient and inversely proportional to the energy of the system. Thus, in simulations with low $\beta/\sqrt{E_K}$, where E_K is the kinetic energy of the system, we find jets at short wavelengths, and both layers support jets of the same scale. In simulations with high $\beta/\sqrt{E_K}$, we see jets at long wavelengths in the barotropic mode but none in the baroclinic mode. Thus, qualitative agreement with the theoretical dependence of the cascade barrier on the magnitude of $\beta/\sqrt{E_K}$ is found, although a quantitative scaling derived from dimensional considerations does not agree well with the simulations - in fact it was found that k_β , as determined by the maxima of the kinetic energy spectra along the k -axis, also depends on λ , indicating that nonlinear

effects may be relevant to setting the spectral shape in these cases. It should be noted, however, that these were unsteady simulations, and the scalings found may not relate to the behaviour of a similar steady system.

We then attempted to extend VM93 to a baroclinic system in the presence of bottom topography (though again in the absence of forcing or dissipation). In this case, the shortwave limit corresponds to an uncoupled regime in which the eigenmodes of the system were the individual layers, and the frequencies are the layer-wise Rossby wave frequencies. The longwave limit is a coupled regime in which the eigenmodes resemble a barotropic and baroclinic mode, and the frequencies resemble rotated barotropic and baroclinic frequencies, dependent on the barotropic PV gradient. Similarly to the β plane case, the cascade barrier k_β is predicted to depend on the magnitude of the PV gradients and the system energy. Comparison with simulation again showed good qualitative agreement: simulations with low $|\mathbf{G}_{\text{BT}}| \lambda^2 / \sqrt{E_K}$ showed uncoupled shortwave jets, following their individual layer PV gradients, and simulations with high $|\mathbf{G}_{\text{BT}}| \lambda^2 / \sqrt{E_K}$ showed coupled longwave jets of identical scale in both layers, following the barotropic PV gradient. Quantitative scaling of k_β again did not agree well with the measured values from simulation, but the theory was again successful at predicting the anisotropy of the spectra observed and the qualitative scaling of k_β .

Returning to the system of chapter 3, the introduction of background shear was shown to affect the shortwave linear Rossby wave frequencies, but not significantly alter the longwave. The shortwave limit again corresponded to layer-wise modes with layer-wise wave frequencies, and the longwave to barotropic and baroclinic like modes, with frequencies dependent on the barotropic PV gradient. The longwave limit has the same qualitative form as the unsteady case, without background shear, such that the anisotropy is again dependent on the direction of the barotropic PV gradient, and the frequencies are close to the wavenumber origin perpendicular to this gradient. The predicted scaling of k_β depended on the parameterisation of the turbulent frequency, of which two were investigated - a Rhines scaling [$\omega(K) = U_T K$, where U_T is a turbulent velocity scale] and a Kolmogorov scaling [$\omega(K) = C_\varepsilon \varepsilon^{1/3} K^{2/3}$, where ε is the eddy energy production]. These predict that k_β should be dependent on $|\mathbf{G}_{\text{BT}}| \lambda^2 / U_T$ or $|\mathbf{G}_{\text{BT}}| \lambda^{5/3} / \varepsilon^{1/3}$, respectively. Both turbulent frequency scalings correspond to turbulent energy scalings, and thus both were tested by their resemblance to the spectra of full simulations as well as the cascade barriers predicted. Whilst the decaying simulations were initialised with a ring of energy at large wavenumbers, the simulations of the full system produce energy through baroclinic instability, which is then thought to transfer to the barotropic mode at $k \approx 1/\lambda$. Thus,

the shortwave limit is not relevant, as is borne out by the absence of any coupled jets in the simulations carried out over a wide range of parameters. The control of the jet angle by the barotropic PV gradient is explained by the longwave limit, in which the layers are dominated by the barotropic mode, and the anisotropy of their spectra determined by the barotropic PV gradient.

Comparing the shape of the energy spectra with the predicted scalings, we find that the Kolmogorov scalings in the energy and enstrophy cascade regions show good approximate agreement for simulations with $k_\beta^\psi \lambda < 0.5$, but simulations with $k_\beta^\psi \lambda > 0.5$ show progressively steeper spectra for larger cascade barriers in both regions. We interpret this as demonstrating that a full inverse cascade cannot develop if the cascade barrier is too close to the forcing scale, and that energy therefore remains more collected in the region around the cascade barrier. Consequently, we find that the Kolmogorov scalings for k_β^ψ agree well for $k_\beta^\psi \lambda < 0.5$, but not otherwise.

We also compared various derived jet scales k_{jet} with that measured in simulations. The ideas of VM93 predict this to be close to, but lower in value, than k_β^ψ . We find good agreement with a scale dependent on the magnitude of the barotropic PV gradient and the equilibrated kinetic energy, ε/κ , for simulations with $k_\beta^\psi \lambda < 0.5$. However, there are some simulations for which the jet scale appears to not be following a consistent relationship with ε , which we postulate is due to the geometric effects discussed in chapter 3. For $k_\beta^\psi \lambda > 0.5$, the Kolmogorov and Rhines scalings for k_β^ψ show good approximate agreement with k_{jet} , suggesting that when the energy remains collected around the cascade scale, that this provides a good estimation of the jet scale.

Along with bottom friction, the background shear also introduces unstable modes to the system - although these are concentrated around $K \sim 1/\lambda$ and so do not affect the longwave linear behaviour. We demonstrated how the form of the instabilities depends on the introduction of a zonal bottom slope in topography. As with [Chen and Kamenkovich \(2013\)](#), we find that the most unstable ‘noodle’ mode wave-vector does not remain consistently perpendicular to the barotropic PV gradient. Analysing the spectra and streamfunction of the system as it spins up shows that the primary and secondary instabilities do not appear to be related to the quasi-steady jets that emerge in cases of zonal bottom topography, as the orientation and scale of the instabilities do not match. This suggests that the ideas of [Berloff et al. \(2009\)](#) do not explain the formation of the jets in these cases.

The success of the linear Rossby wave frequencies at predicting the anisotropy of the spectra, and so the jet orientation, lends support to the ideas of VM93. The good

approximate agreement with Kolmogorov spectral scalings and the resultant cascade barrier and jet scales for some of the simulations also suggest that the ideas of an inverse cascade halted by Rossby wave excitation may be able to explain the formation of jets in this and other quasi-geostrophic simulations. However, the cases without a developed inverse cascade also show jets forming, and the work of Srinivasan and Young (2012) and others have shown categorically that an inverse cascade is not necessary to form jets. This suggests that jet formation is a richer picture, and indeed it may be that the ideas of BKP09 are relevant at low energies, when the baroclinic instability transfers energy directly to scales close to the cascade barrier, such that Rossby waves are directly excited and the jets are formed close to this scale. However, at higher energies an inverse cascade can develop, which is rendered anisotropic by the excitation of Rossby waves, and eventually halted by a balance with bottom friction. In both cases, the Rossby wave frequencies produce a barrier to the system energy, whether it cascades towards it or not, and so it might be better termed the Rossby wave barrier. This would explain the replication of jet formation in quasi-linear models without a mechanism for a direct small scale cascade - if the energy is instead transferred via non-local interactions, the Rossby wave barrier still remains which sets anisotropy of the system.

We do not claim that the current work constitutes proof of this picture, however it does provide a consistent explanation for the results found in this and other studies. Further work to assess its viability could include carrying out two layer QL simulations in the presence of zonal bottom topography to see whether tilted jets can be produced and if their behaviour is similar to the full system. Additionally, the full calculation of the secondary instabilities of the system, as in BKP09, could show categorically whether they can or cannot be linked to jet formation.

Chapter 3

Jet Properties in a Quasi-Geostrophic Model of the Southern Ocean

3.1 Introduction

A number of studies have identified and noted the potential impact of zonal jet structure (alternating eastward and westward velocities) on ocean circulation (Berloff et al., 2009; Maximenko et al., 2005), yet many instances of non-zonal jet orientation are also evident. Observations of sea surface height indicate jet cores at topographic gradient maxima (Hughes and Ash, 2001), and also reveal increased eddy forcing of jets near topographically complex regions (Hughes, 2005; Maximenko et al., 2005). Jets are known to be effective barriers to meridional transport near the surface from studies of the Southern Ocean (Marshall et al., 2006; Shuckburgh et al., 2009a,b). However, at mid-depths, diagnostics have shown enhanced mixing by eddies, (Abernathay et al., 2010), strongly linked to the interaction between topography and jets (Lu and Speer, 2010).

Understanding the processes involved in topography feedback on jet properties is of particular importance in the Southern Ocean: the flow of the ACC is known to be composed of several strong jets, as can be seen from observations of sea surface height through satellite altimetry (Sokolov and Rintoul, 2007) and eddy-resolving numerical models [e.g. the OCCAM model, Lee and Coward (2003); the MESO project, Hallberg and Gnanadesikan (2006)]. The ACC also passes through several topographically complex regions, such as the Drake Passage, the Macquarie Ridge and the Campbell Plateau (see

figure 1.2, which have been observed to introduce significant meridional perturbations to the flow (Gordon et al., 1978), resulting in many occurrences of non-zonal flows.

The ACC plays an important role in determining the Earth's climate. It is important for the mixing of properties such as carbon dioxide (Le Quéré et al., 2007) and heat (Gille, 2008; Hogg et al., 2008) between ocean basins and between ocean and atmosphere. It is critical to the exchange of water masses between the Southern Ocean and elsewhere (e.g. Orsi et al. (2001)). Thus, determining how the widely varying topography in the Southern Ocean affects the transport and meridional overturning of the ACC would contribute to our overall understanding of ocean circulation, and its effect on the Earth's climate.

One mechanism for the generation of non-zonal flow is topographic steering. This refers to the tendency of ocean currents to follow contours of f/h , where f is the Coriolis parameter and h is depth, which are the mean potential vorticity (PV) contours for a purely barotropic system (Marshall, 1995). However, topographic steering may also impact more general barotropic and baroclinic stability properties of the flow. These processes are still not well understood in terms of their influence on transport and eddy-mean flow interactions. Several authors have investigated the dynamical effects of various types of bottom topography in numerical models, ranging from sinusoidal ridges (Thompson, 2010) to an idealised Southern Ocean (Jackson et al., 2006), as well as simple quasi-geostrophic models of the ACC [see also Treguier and McWilliams (1990); Treguier and Panetta (1994); Witter and Chelton (1998); Wolff et al. (1991)].

Historically, simplified models have provided insight into the dynamical processes that govern turbulent flows in the atmosphere and ocean. For example, previous investigations into both one- and two-layer models, such as Panetta (1993); Vallis and Maltrud (1993), have shown the development of zonal jets as a result of the β effect. This chapter extends the previous work by considering a suite of doubly periodic barotropic and two-layer baroclinic turbulence simulations in which non-zonal jets form. Having investigated the process of jet formation in this system in 2, we now look at the properties of the jets generated by the introduction of a bottom slope with both zonal and meridional components. Importantly, topographic steering in these simulations allows for a meridional component in the jets without the addition of any artificial forcing (c.f. Arbic and Flierl (2004b); Smith (2007); Spall (2000)). Our choice of a QG model is motivated by the key insight this system of equations has provided in similar flows. We acknowledge that in certain regions of the ocean, in particular the Southern Ocean, topographic slopes may be larger than formal QG scalings. The impact of steeper slopes is addressed briefly in the conclusion, section 3.6.

The introduction of a linear bottom slope into a baroclinically forced two-layer model was first investigated by Hart (1975) and Steinsaltz (1987), who analysed the linear stability. LaCasce and Brink (2000) investigated the role of meridional slopes on wave and jet formation in a two-layer, f-plane model. They considered decaying turbulence whereas we focus on a forced-dissipative model. Thompson (2010) investigated the introduction of a meridional bottom slope in the presence of the β effect as one of a range of bottom topographies for forced-dissipative turbulence – here we consider zonal components of a sloping bottom as well.

Our present model, in an effort to isolate key dynamics, is a significant simplification over real oceanographic situations. Yet sloped bottom topography has long been used in experimental fluid dynamics to introduce PV gradients, see, for example, Mason (1975); Tamaki and Ukaji (2003); Whitehead et al. (1990), in which baroclinic effects in rotating tanks are investigated using applied density gradients. More recent experiments have also seen the formation of zonal jets in the presence of meridional slopes in such tanks (Bastin and Read, 1998; Wordsworth et al., 2008), therefore aligning with the barotropic PV contours, suggesting that the results of this study may apply to a broad range of flows.

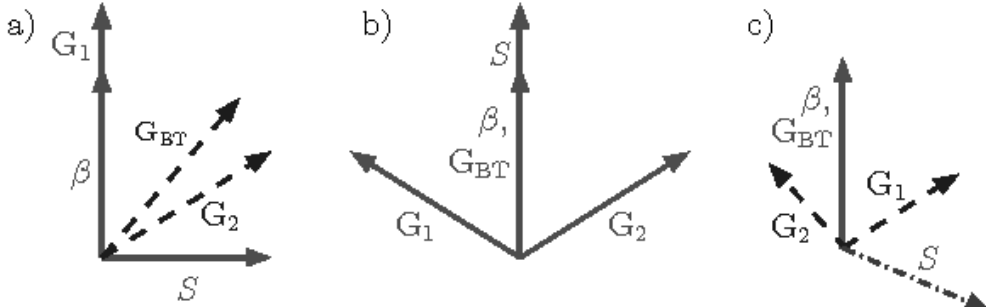


Figure 3.1: Depiction, in the x - y plane, of the configuration of the two-layer, doubly periodic, quasi-geostrophic models used in a) this paper, b) Smith (2007), and c) Arbic and Flierl (2004b). Thick lines denote that the quantity is fixed in direction, whereas dashed lines denote a quantity varied in direction, and the arrows point in the direction of the vector. \mathbf{S} denotes the overall shear of the background velocities driving the baroclinic instability, β denotes planetary vorticity, $\mathbf{G}_{1,2}$ represent the individual layer potential vorticity gradients and \mathbf{G}_{BT} the background barotropic potential vorticity gradient, as defined in (2.29) and (2.17) respectively for a). In c), the dash-dot line for the shear indicates that while Arbic and Flierl could vary their shear direction, for most of the paper it was kept in one of two fixed directions. Note that in both b) and c), \mathbf{G}_{BT} and β are fixed in the same direction.

We will now discuss our model configuration and compare it with other doubly-periodic studies that have investigated non-zonal jets. Our barotropic simulations have a single PV gradient that rotates with the magnitude and orientation of the bottom slope. Our baroclinic, two-layer model, is more subtle, and the governing PV gradients are shown in figure 3.1a. The upper layer background PV gradient, \mathbf{G}_1 , is fixed in the y -direction, defined by the planetary vorticity, β , and the background velocity shear, U , which provides the source of potential energy from which baroclinic turbulence is generated. The lower layer background PV gradient, \mathbf{G}_2 , varies with the magnitude and orientation of the slope in the bottom topography. This is not inconsistent with the doubly periodic nature of the domain as it is the depth gradient, not the absolute depth, that alters the PV gradient. The doubly periodic domain can be thought of as representing a patch of the ocean far from boundaries, or a patch that is smaller than any externally enforced scale.

The background layer and background barotropic PV gradients are defined in (2.29) and (2.17). The evolution equations, the bottom gradients, h_x, h_y , and the other parameters, are defined in chapter 2. We find through our investigation that the introduction of a zonal (x -) gradient in bottom slope leads to the production of tilted jets, steered as expected by PV conservation, but with the consequence that these jets flow across layer-wise PV gradients. Whilst we keep the shear vector in our model purely zonal, others (Smith (2007) and Arbic and Flierl (2004b)) have investigated applying a non-zonal mean flow through a β field in two-layer models, motivated by observation of such flows in the ocean.

Smith (2007) investigates forcing a doubly periodic two-layer quasi-geostrophic model with a purely meridional mean flow. This configuration is illustrated in figure 3.1b for comparison with ours, where the fixed directions of the shear velocity, planetary vorticity and layer-wise potential vorticities are shown in the x - y plane. Smith's configuration produces what he describes as the ‘shear dispersion of potential vorticity’; the planetary PV acts to elongate zonally the eddies produced in the mean flow, leading to jet-like structure in cases with relatively strong β and low bottom friction. He also notes an increase in barotropic kinetic energy with increasing β whilst holding other variables fixed.

Arbic and Flierl (2004b) investigate a different parameter space again, once more in a doubly periodic two-layer quasi-geostrophic model. By allowing arbitrary background velocities in either layer, they vary both the direction of the shear vector, \mathbf{S} , and the angle between the layer PV gradients, \mathbf{G}_1 and \mathbf{G}_2 , as illustrated in figure 3.1c. Their results

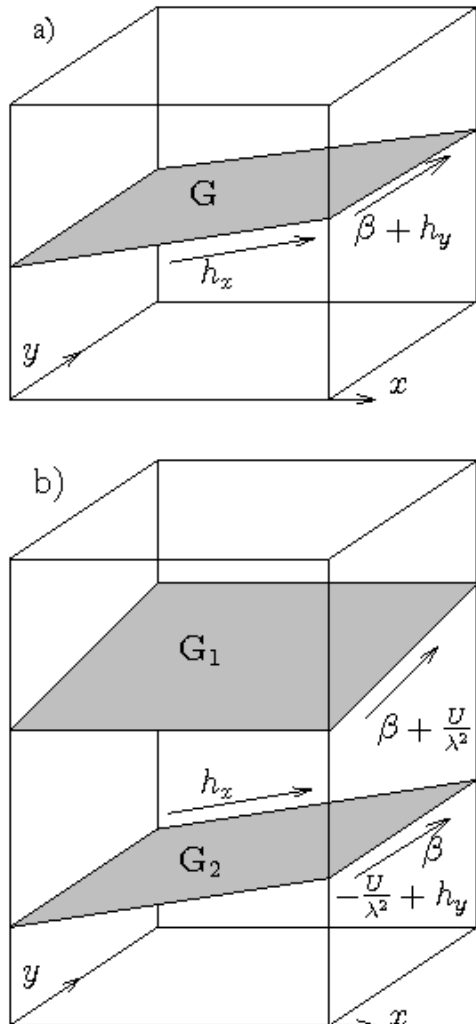


Figure 3.2: Depiction of the background (as opposed to perturbation) PV structure of the a) one- and b) two-layer models. The labels refer to the quantities defined in a) equation (3.3) and b) equation (2.29).

show clear zonal jets in setups with large values of β and small angles between the layer PV gradients, and like-signed vortices in those with smaller values of β and larger angles between PV gradients. There are also notably some anisotropic structures, see especially their figures 6c and 7c. Significantly, whilst the individual layer PV gradients can be varied (by varying the background shear velocities), shear components cancel such that the barotropic PV gradient is always only determined by β , and so is fixed in direction.

A significant difference between the configuration we present (shown in figure 3.1a) and those in [Smith \(2007\)](#) and [Arbic and Flierl \(2004b\)](#), is that whilst their configurations require a *prescribed* non-zonal mean flow to try to imitate observed features, non-zonal jets arise in our configuration more naturally, we would argue, through the introduction of zonal gradients in topography. Furthermore, a non-zonal mean flow is not a solution to the quasi-geostrophic equations in [Smith \(2007\)](#), although [Arbic and Flierl \(2004b\)](#) ensure their shear vectors are solutions to their evolution equations. See section 3.2.1 for an aside on background flow solutions.

In addition, our configuration allows for variation in the directions of the barotropic and layer-wise PV gradients. We find that the anisotropic jets produced in the presence of a zonal slope in bottom topography align perpendicular to the direction of the barotropic PV gradient, rather than the individual layer gradients. [Arbic and Flierl \(2004b\)](#) find a maximum in eddy energy production when their overall shear is southward, or anti-aligned with the planetary PV gradient, which is similar to the configuration used by [Smith \(2007\)](#). Whilst holding the shear fixed at two separate values and varying β they similarly find an increase in eddy energy production with increasing β .

In section 3.2.1 we summarise the results of the one-layer model, and then in section 3.2.1 set out the details of the two-layer model, and show some example results that demonstrate the formation of non-zonal jets. Section 3.3 contains analysis of the impact of the slope magnitude and orientation on the flow structure and statistical characteristics. We investigate the effect of variations in layer depths in section 3.4, and briefly consider zonal slopes in more complicated topographies in section 3.5. We then compare and contrast the two-layer model results with previous papers, and comment on these in section 3.6.

3.2 Model

3.2.1 Equations

One-Layer Model

We consider a one-layer fluid, taking quasi-geostrophic approximations: small Rossby number, and small variations in the Coriolis parameter and depth. The system is described by the following equation:

$$\frac{\partial Q}{\partial t} + J(\Psi, Q) = F_0^2 \cos(k_0 x) - \kappa \nabla^2 \Psi + d. \quad (3.1)$$

$J(\Psi, Q)$ is the Jacobian determinant of Ψ and Q , the streamfunction and PV fields respectively, where the velocity $(u, v) = (-\Psi_y, \Psi_x)$. F_0^2 is the amplitude of the forcing, which has a single zonal wave number k_0 , κ is the bottom friction, and d is the small scale dissipation included for numerical stability as before. We force the system via sinusoidal forcing in the y -direction at a single x -wavenumber. This was first suggested by Kolmogorov (Arnold and Meshalkin, 1960), as linear stability analysis shows that the fastest growing mode in baroclinic instability is at a constant x -wavenumber and zero y -wavenumber (see 2.2.4). A one-layer model can be thought of as representing the barotropic mode of a multi-layer system, and so we wish to try to mimic the forcing of such a system by baroclinic instability. Note that whilst baroclinic instability is responsible for the excitation of the barotropic mode in multi-layer systems in the absence of topography, the vertical structure may vary over topography.

The PV, Q , is defined in terms of the perturbation PV, $q = \nabla^2 \Psi$, and the background PV gradient \mathbf{G} :

$$Q = q + \mathbf{G} \cdot \mathbf{x}, \quad (3.2)$$

$$\mathbf{G} = (h_x, \beta + h_y). \quad (3.3)$$

The background PV depends on the latitudinal variation of the Coriolis parameter, $f = f_0 + \beta y$, and the linear gradients of the bottom surface, h_x, h_y , which have the same meanings as in chapter 2.

From now on we will refer to $\beta^* = \beta + h_y$ for brevity. The resulting background PV structure can be seen in figure 3.2a. The effect of adding a topographic slope in the x -direction, h_x , is equivalent to rotating the domain (and modifying the magnitude of β). Still, this is not a trivial transformation since the forcing has a highly anisotropic

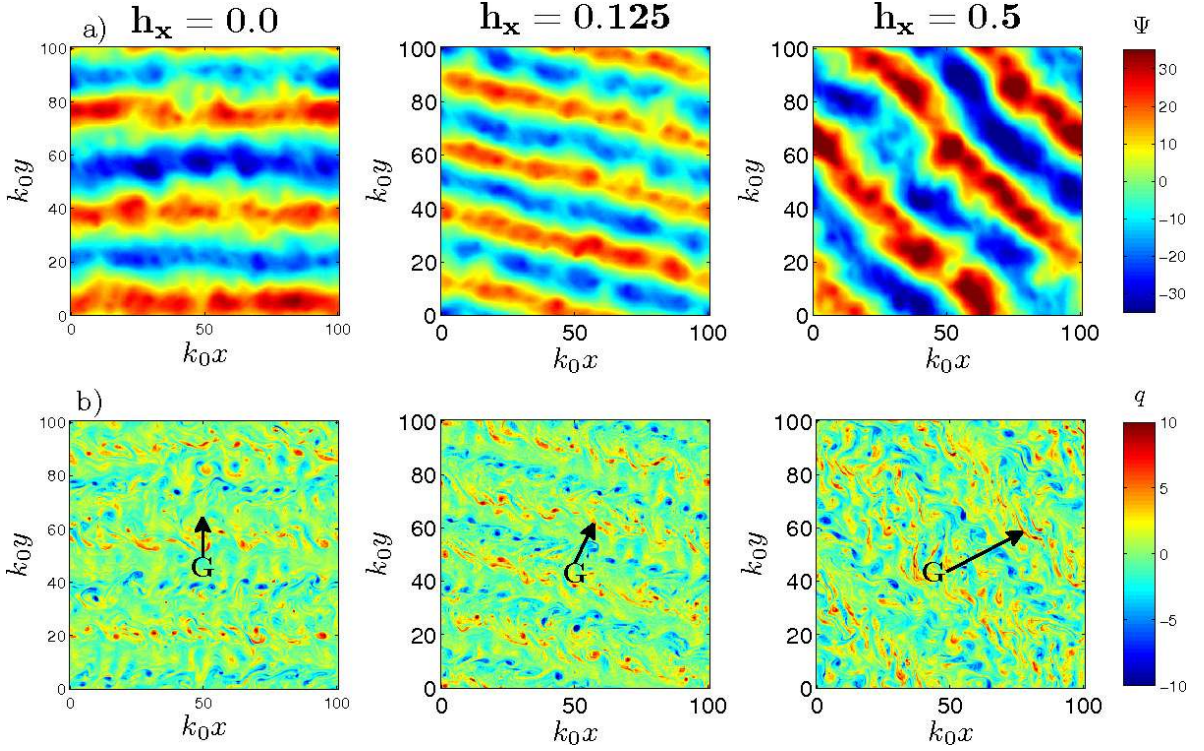


Figure 3.3: Snapshots of one-layer a) streamfunctions (Ψ) and b) PV perturbations (q) during statistical equilibrium, for three values of h_x : 0.0, 0.125 and 0.5. In these simulations $\beta^* = 0.5$. The tilting of the jets is associated with the changes in the PV structure caused by the introduction of a zonal gradient in bottom slope, h_x . The direction of the background PV gradient, \mathbf{G} , is depicted for each run by the black arrow in the lower panels.

horizontal structure and the alignment of this structure relative to the barotropic PV gradient changes. The system is non-dimensionalised using F_0 and k_0 as follows: $\Psi' = k_0^2 \Psi / F_0$, $q' = q / F_0$, $\kappa' = \kappa / F_0$, $\beta' = \beta / k_0 F_0$, $h' = h / k_0 F_0$. From now on we will drop the 's. For all the simulations presented, the domain is a square of length $32\pi/k_0$ and calculations are made on a square grid of size 256×256 [Higher resolution simulations were tested and showed similar results]. This corresponds to a resolution of $\sim 0.4/k_0$, which, if we assume the forcing is imitating baroclinic instability (i.e. k_0 is the deformation radius), resolves below the scale of the deformation radius. We hold the bottom friction fixed throughout, $\kappa = 0.01$.

Two-layer Model

While the two-layer model represents a moderate increase in complexity, the potential for baroclinic instability to be active produces a dramatic difference from the barotropic

simulations, and as mentioned previously, topography may alter the types of modes that are excited. No explicit small scale forcing is required, and following the work of Haidvogel and Held (1980), Panetta (1993), and Held and Larichev (1996), we constrain the system to a global domain-averaged shear between the two layers, \mathbf{S} , as previously defined. All symbols and the system equations are defined in section 2.2.3. The resulting background PV structure can be seen in figure 3.2b. The equations are non-dimensionalised using λ and U : $\psi'_i = \psi_i/U\lambda$, $q'_i = \lambda q_i/U$, $\kappa' = \lambda\kappa/U$, $\beta' = \lambda^2\beta/U$, resulting in the following system of equations, where we have dropped the 's and d:

$$q_{1t} + (\beta + 1)\psi_{1x} + 2q_{1x} + J(\psi_1, q_1) = 0, \quad (3.4)$$

$$q_{2t} + (\beta - 1 + h_y)\psi_{2x} - h_x\psi_{2y} + J(\psi_2, q_2) = -\kappa\nabla^2\psi_2. \quad (3.5)$$

The perturbations, ψ_i , about the background flow are stepped in time using a 3rd order Adams-Bashforth scheme. For all the simulations presented, unless otherwise specified, the domain is a square of length 128λ and calculations are made on a square grid of size 256×256 [Higher resolution simulations were tested and showed similar results]. We hold the bottom friction fixed throughout, $\kappa = 0.1$, chosen to be small enough to allow the generation of clear jets, but large enough to statistically equilibrate the system. See, for example, Arbic and Flierl (2004a).

An aside on background flow solutions

We chose our background flow configuration, $\mathbf{U}_1 = (2U, 0)$, $\mathbf{U}_2 = (0, 0)$, for two reasons. Firstly, the shear between the two layers produces baroclinic instability that drives the system. Secondly, as mentioned previously, this state is a solution to the system equations. These are not the only solutions to the system equations. Let us define the layer-wise PV gradients in terms of those due to the background flow and those applied:

$$\mathbf{G}_i = \frac{\mathbf{S}^\perp}{2} + \hat{\mathbf{G}}_i, \quad (3.6)$$

where $\mathbf{S}^\perp = (\mathbf{S}^x, -\mathbf{S}^y)$ and for our study $\hat{\mathbf{G}}_i = (0, \beta) + \delta_{i2}(h_x, h_y)$. If we rewrite (2.26) in terms of velocities rather than streamfunctions, then assuming we are seeking constant flow solutions (i.e. $\nabla^2\psi_i = 0$) we find:

$$\frac{(-1)^{i-1}}{2} \mathbf{U}_1 \cdot \mathbf{U}_2^\perp + \mathbf{U}_i \cdot \hat{\mathbf{G}}_i = 0. \quad (3.7)$$

The simplest solutions to these equations are those where the layer-wise flows are perpendicular to the applied layer-wise PV gradients ($\mathbf{U}_i \propto \hat{\mathbf{G}}_i^\perp$), and parallel to each other ($\mathbf{U}_1 \cdot \mathbf{U}_2^\perp = 0$). If $\hat{\mathbf{G}}_1$ and $\hat{\mathbf{G}}_2$ are parallel (though not necessarily equal), then any \mathbf{U}_i aligned perpendicular to these gradients satisfies these conditions. For example, in the case of a β plane with no topography, any constant zonal flows are solutions, and equal but opposite flows are often chosen to produce a shear between the layers. Alternatively, (3.7) can be satisfied by choosing $\mathbf{U}_i = \alpha \hat{\mathbf{G}}_i^\perp + \frac{(-1)^{i-1}}{2} \mathbf{S}$ where α is a constant, as in [Arbic and Flierl \(2004b\)](#). This results in the overall layer-wise gradients \mathbf{G}_i being unaligned with each other and $\hat{\mathbf{G}}_i$ in general, but the barotropic PV gradient remains aligned with $\hat{\mathbf{G}}_i$, see figure 3.1.

However, if the layer-wise applied gradients $\hat{\mathbf{G}}_i$ are not aligned, then both conditions cannot be satisfied individually unless one of the layer-wise flows is zero. If the flow in one layer is perpendicular to the layer-wise PV gradient, then the other layer's flow is required to be zero. This is the configuration in our study, where we choose a zonal flow in the upper layer and no flow in the lower layer in order to mimic the predominantly zonal flows seen in the ACC.

3.2.2 Example Results

Example fields from the one-layer model can be seen in figure 3.3, which shows snapshots of the streamfunction, Ψ , and the perturbed PV, q , respectively, at a time after statistical equilibrium has been reached, for three different values of h_x . In these runs, $\beta^* = 0.5$. Coherent jets are observed in all three snapshots, although the jets are not purely zonal in nature when h_x is non-zero. Due to the presence of the slope in the zonal direction, h_x , the background PV gradient controlling the flow rotates, and so the jets tilt in order to align perpendicular to the gradient, since this is the only PV gradient in the system. However, the forcing still imposes directionality on the flow, since it has a fixed orientation, see (3.1). The direction of the jets is further discussed in section 3.3.

Example fields from the two-layer model can be seen in figure 3.4, which shows snapshots of the perturbed upper and lower layer PV, q_1 and q_2 respectively, at a time after statistical equilibrium has been reached, for three values of h_x , alongside histograms of the total PVs, Q_1 and Q_2 respectively. In this run the parameters are set at $\beta = 0.75$ and $h_y = 0.0$. Again, non-zonal jet structure is observed. Despite the differing background PV structure in both layers (see (2.27) and figure 3.2), the upper and lower layer perturbed PV fields are identical in the orientation of their jets.

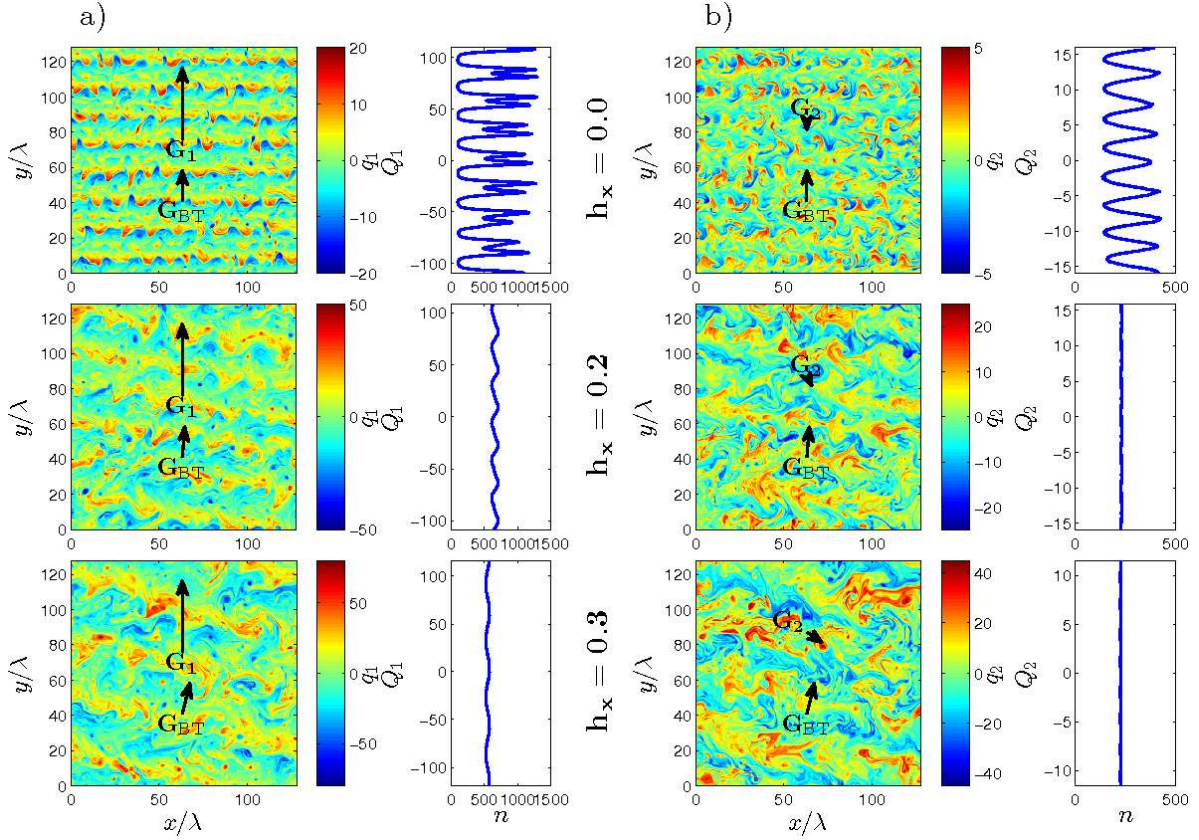


Figure 3.4: Snapshots of two-layer a) upper and b) lower layer PV perturbations, q_1 and q_2 , during statistical equilibrium, for various values of h_x , alongside time-mean histograms of the total PV, Q_1 and Q_2 , respectively, see equation (2.27). In these simulations, $h_y = 0.0$ and $\beta = 0.75$. The tilting of the jets is associated with the changes in the lower layer PV structure, q_2 , caused by the introduction of a zonal gradient in bottom slope, h_x . The sharp minima in the total PV histograms for the $h_x = 0.0$ case is associated with steep PV gradients at the core of the jets. The relative homogenisation shown in the other histograms shows that the jets cross layer-wise PV contours in these cases. In the cases where $h_x \neq 0$, we take advantage of the PV mapping technique described in section 3.2.2 to produce the histograms. The magnitude and direction of the layer-wise background PV gradients, \mathbf{G}_1 and \mathbf{G}_2 are shown along with the background barotropic PV gradient, \mathbf{GBT} , by black arrows.

Probability density functions (PDFs) of PV have been used in previous work, such as Marshall et al. (1993) and Thompson et al. (2010), to identify regions of high and low mixing. Intense mixing leads to PV homogenisation, resulting in a high probability at the PV associated with that region, and conversely transport barriers are associated with sharp gradients in PV, and so low probability at the relevant PV value. Throughout this paper we use time-mean histograms (un-normalised PDFs) of total PV to gain insight into the transport properties of the numerical simulations. As discussed in section 3.3.1, in some simulations with tilted jets, the doubly-periodic domain means that there is only one unique jet in the domain. In these cases, we take advantage of this feature by remapping all PV values into the unique range of PV covered by one pair of east-west jets before producing the histogram. When plotting these, we repeat the histogram to reproduce the number of jets and the full range of PV in one domain, for purposes of comparison.

In the case where $h_x = 0.0$ (the upper row plots in figure 3.4), classic zonal jets can clearly be seen in both layers, though they are stronger in the upper layer, which has a stronger background PV gradient. The PV histogram shows minima in both layers associated with the sharp PV gradients present at the core of the jets. In the top layer, weaker transport barriers associated with the westward jets are also present – these can be seen in the total PV histogram and are correlated with the features that can just be seen between the jet structures in the snapshot. Westward jets are a robust feature in two layer quasi-geostrophic simulations that are also observed to be transport barriers by, for example, Beron-Vera et al. (2008).

Whilst the relationship between the direction of the flow and the PV gradients will be investigated in section 3.3, it is immediately apparent that, in the top layer at least, the jets are crossing the local PV contours in cases where h_x is non-zero, as the top layer PV gradient is always in the meridional direction (see figure 3.1). The total PV histograms confirm that for these cases, the PV is rather homogeneous, i.e. with no strong spatial structure, in both layers, without the sharp minima seen in the $h_x = 0.0$ case, implying more strongly homogenised PV, despite the clearly inhomogeneous perturbation PV fields q_i .

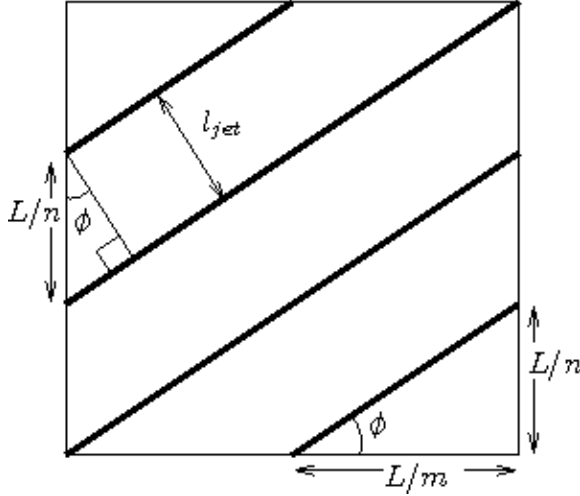


Figure 3.5: Example geometry for a simulation in a domain of size L by L with $n = 3$ jets crossing the y -axis and $m = 2$ jets crossing the x -axis. We can see that $\cos \phi = l_{jet}n/L = n/\sqrt{n^2 + m^2}$, and therefore that the jet spacing, $l_{jet} = L/\sqrt{n^2 + m^2}$.

3.3 Results

3.3.1 Jet Deflection

When analysing the angle of jet deflection, it is important to recognise that the doubly periodic nature of the domain results in some restrictions on the possible deflection angles, ϕ_{jet} , for a given number of jets, in both the one- and two-layer cases. For a given number of jets, there are set angles at which re-entry at the beginning of the domain is possible. In fact, for n jets crossing the y -axis in one domain, the tangent of the angle must be equal to m/n , where m is the number of jets crossing the x -axis, see figure 3.5. While this applies to both models, this can be seen most clearly in the stepped nature of the two-layer results in figure 3.7a, partly because the two-layer runs cover a smaller range of angles, and so the effect appears larger. We do not believe that this angle quantisation affects our results, given that figure 3.7a clearly shows that our simulations cover a range of alignments with their preferred direction.

Taking m and n to be in the range 0 to 16, as is found for the two-layer runs investigated, the allowed values of ϕ_{jet} and the separation between the jets, $l_{jet} = L/\sqrt{n^2 + m^2}$, where L is the length of the domain, can be seen in figure 3.6, with the actual points for the two-layer results highlighted. See figure 3.5 for the geometry of these quantities. A purely zonal jet would have $m = 0$ and so $\phi = 0^\circ$. A purely meridional jet would have $n = 0$ and so $\phi = 90^\circ$. Note that for a given value of m and n , there are n unique jets only

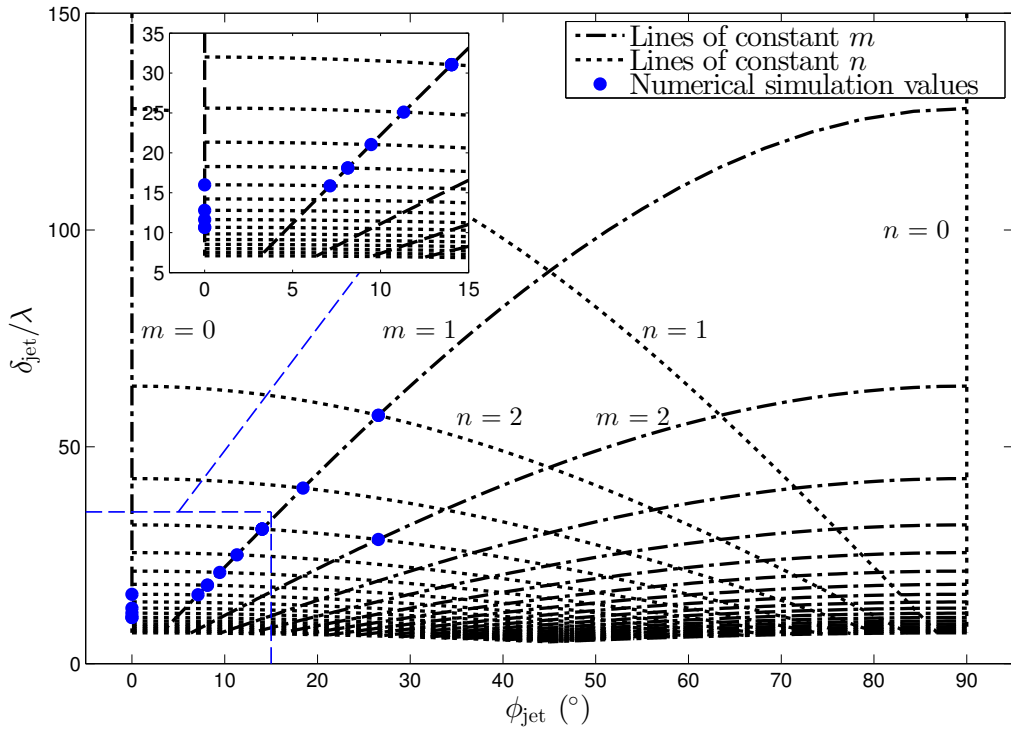


Figure 3.6: Allowed jet separations, δ_{jet}/λ , vs jet angle, ϕ_{jet} , where $\tan \phi_{jet} = m/n$, where m and n are in the range 0 to 18, for a doubly periodic domain. Dotted lines indicate constant n , and dash-dot lines constant m : these lines cross at integer pairs of m and n . The dots highlight the values for our two-layer numerical simulations. The finite size of the domain provides fewer and fewer options at large separations and large angles. This shows that the system appears to increase δ_{jet} (l_{jet}) with increasing h_x , which corresponds to increasing ϕ_{jet} , associated with increased eddy energy production, see 3.3.3.

if m is a multiple of n , or vice versa (m unique jets if n is a multiple of m). Otherwise, there is only one unique jet, as the doubly periodic nature of the domain means that what might appear to be distinct jets are in fact all parts of a single jet that wraps around the domain.

One-Layer Case

The jet deflection in the barotropic, one-layer case, as seen in figure 3.3, is largely a geometric result of changing the orientation of the background PV gradient, \mathbf{G} . We present these results primarily to contrast them with the response in the two-layer, baroclinic simulations.

The definition of the PV gradient, \mathbf{G} , in section 3.2, shows that the introduction of the zonal bottom slope, h_x , alters its orientation. The perturbations to the streamfunction then align perpendicular to this gradient, resulting in the non-zonal structure observed. Figure 3.7a shows the observed angle of jet tilt from the numerical simulation, ϕ_{jet} , calculated by taking the ratio of the meridional to zonal wavenumbers corresponding to the maximum amplitude of the power spectrum of the PV perturbation, q , time averaged after statistical equilibrium had been reached, against the theoretical angle, ϕ_{BT} , defined as perpendicular to the PV gradient:

$$\phi_{BT} = \tan^{-1} \left(\frac{h_x}{\beta^*} \right). \quad (3.8)$$

Both angles are defined such that $\phi = 0$ is equivalent to purely zonal flow. The excellent fit confirms that the jets align perpendicular to the PV gradient in order to conserve PV. Note that the introduction of the bottom slopes does not act to rotate the entire problem, as the sinusoidal forcing still varies only in the zonal direction, however, this effect is apparently small compared to the system's organisation into coherent jets.

Two-Layer Case

In the two-layer case, the jets also deflect from purely zonal when a zonal bottom slope, h_x , is introduced. Motivated by the one-layer model, which can be interpreted as the barotropic mode of a multi-layered model in the limit of relatively weak slopes, we look for a relationship between the gradient of the mean *barotropic* potential vorticity, \mathbf{G}_{BT} , defined in (2.17), and the angle of deflection, ϕ_{jet} , calculated as previously from the power spectrum of the upper layer PV perturbation field, q_1 . Calculations using the equivalent

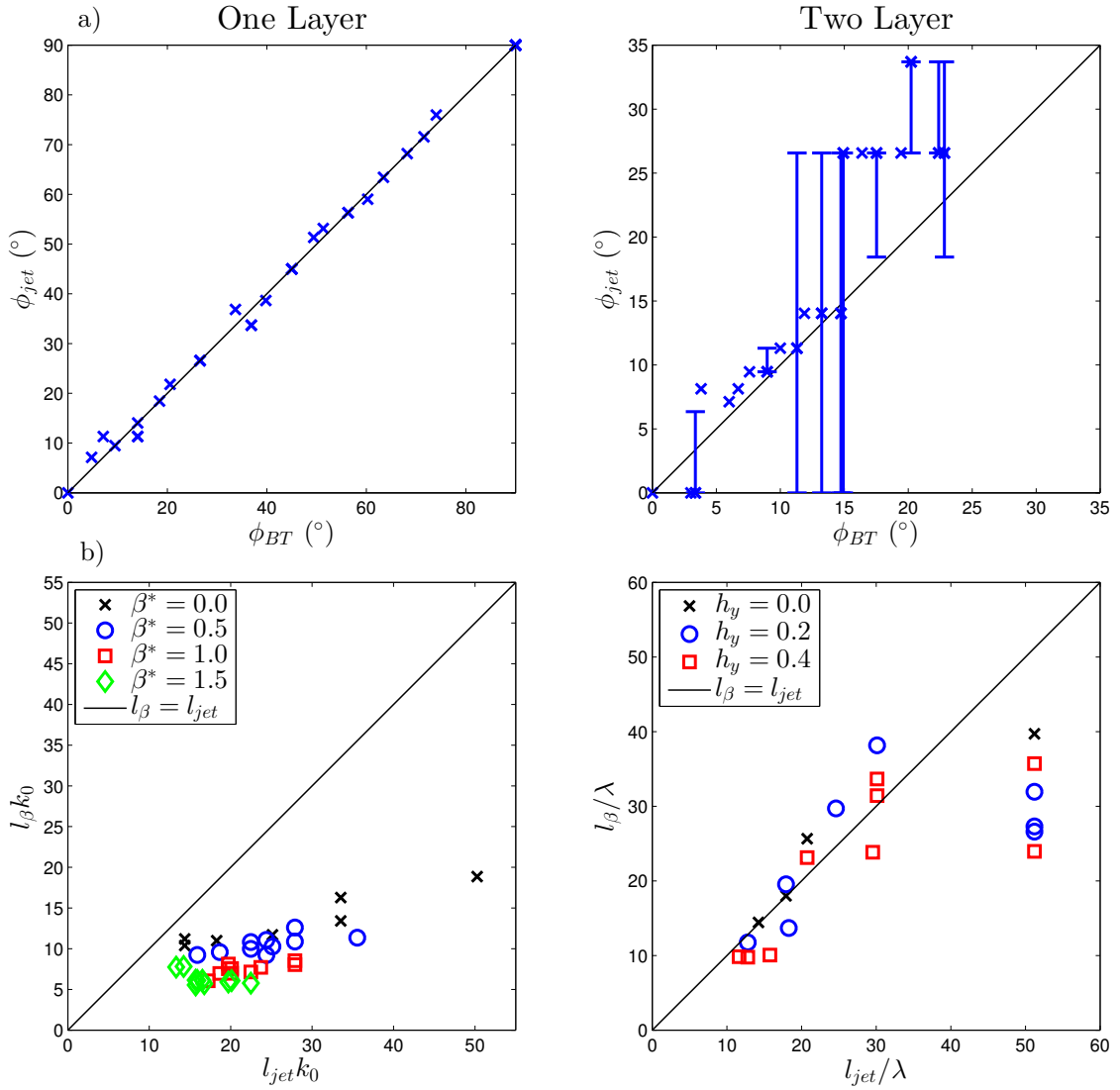


Figure 3.7: a) A comparison between observed jet tilt, ϕ_{jet} , and the predicted tilted, ϕ_{BT} , for one- and two-layer cases. ϕ_{jet} is found from the power spectrum of the PV field, q , and the upper-layer PV field, q_1 , for the one- and two-layer simulations, respectively; ϕ_{BT} is defined in (3.8) and (3.9). Symbols indicate the modes of the measured angle, ϕ_{jet} , and the error bars indicate maxima and minima, after statistical equilibrium – the angles in the one-layer simulations, and many two-layer simulations, remained constant in time so have no error bars. b) A comparison between observed jet spacing, l_{jet} and the Rhines scale, l_β . $l_{jet} = L \cos(\phi_{jet})/n_{jet}$, where L is the length of the domain, and n_{jet} is the number of jets crossing the y -axis; l_β is defined in equation (3.10). The different symbols indicate simulations with different values of β^* or h_y .

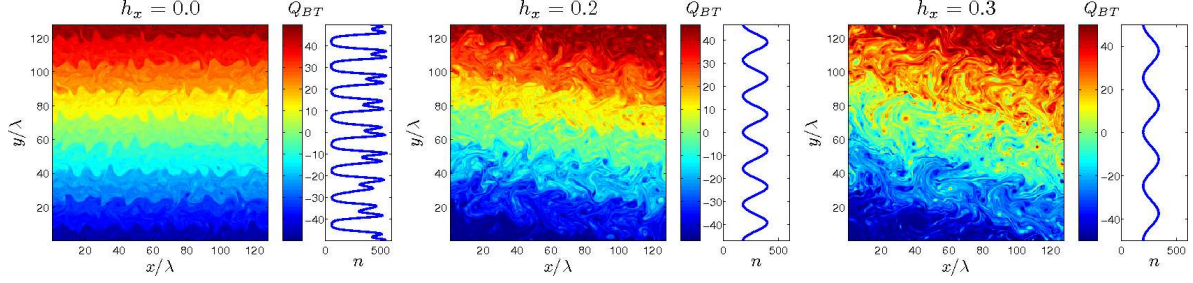


Figure 3.8: Snapshots and mean histograms of total barotropic potential vorticity, Q_{BT} , for two-layer runs with $h_x = 0.0, 0.2$ and 0.3 . Minima in the histograms correspond to the sharp gradients in PV at the centre of jets. These plots confirm that the jets are aligning perpendicular to the barotropic PV gradient rather than local layer gradients.

lower layer field, q_2 produce identical results. Once again, a strong linear fit is found, which can be seen in figure 3.7a, where the theoretical angle,

$$\phi_{BT} = \tan^{-1} \left(\frac{h_x/2}{\beta + h_y/2} \right), \quad (3.9)$$

is perpendicular to \mathbf{G}_{BT} . The error bars indicate the minimum and maximum values of ϕ_{jet} measured after statistical equilibrium. The large deviations seen, for example for simulations with mode $\phi_{jet} \sim 15^\circ$, are due to the fact that the larger angle simulations are at larger energies and so k_{jet} is relatively small, see figure 3.10 and chapter 2. This means that k_{jet} , the maximum of the energy spectrum, from which the jet angle is computed, is relatively close to the wavenumber origin. Thus, a shift in the location of k_{jet} by only $2\pi/L$, the wavenumber resolution of the system, results in a large change in angle.

Thus, in both cases it can be seen that the jets tend to align perpendicular to the barotropic PV gradient, which we will refer to from now on as ‘barotropic control’. In the one-layer case, this is the only PV gradient there is, and the system appears to better conform to the angle, shown by the tight fit in figure 3.7a and the change in jet spacing seen in figure 3.3. The fit is not as strong in the two-layer case, (see figure 3.7), and the system shows an increase in the jet spacing as h_x increases, (see figure 3.4) which is discussed in section 3.3.2.

The hypothesis that the jets align perpendicular to the barotropic PV gradient, \mathbf{G}_{BT} , can be further confirmed by looking at the total barotropic PV fields for the two-layer simulations. Figure 3.8 shows snapshots of total barotropic PV for each of three simulations with $h_x = 0.0, 0.2$ and 0.3 respectively, alongside mean histograms of the total barotropic PV. In the two simulations with $h_x = 0.2$ and 0.3 , as both simulations have

1 jet crossing the y -axis, i.e. $m = 1$, there is only one unique jet in each simulation which wraps around the domain multiple times due to the double periodicity, as discussed previously. We can take advantage of this fact to improve the resolution of the histograms by remapping all the values of the total barotropic PV into a range of the unique PV values for these two simulations. This results in a histogram of a single jet, which for comparison has been replotted n times. It can be seen, in comparison with figure 3.4, that there are clear eddy transport barriers associated with the jets in all three cases, characterised by minima in the PV histograms. Thus, the barotropic PV gradient is providing the dominant direction for the system, and the barotropic PV structure is composed of coherent jets which show clear signs of anisotropy.

3.3.2 Jet Spacing

Panetta (1993) and Thompson (2010) showed that in two-layer models such as these, the jet spacing is given by a Rhines scale dependent on the eddy velocity, V , and the magnitude of the planetary vorticity gradient, β . In this case, we consider the relevant gradient to be the barotropic PV gradient, \mathbf{G}_{BT} , the background barotropic PV gradient, equal to \mathbf{G} in the one-layer case, as defined in (3.3), and as defined in (2.17) in the two-layer case, and equal to β in both Panetta (1993) and Thompson (2010):

$$l_\beta = 2\pi \sqrt{\frac{V}{|\mathbf{G}_{\text{BT}}|}}, \quad (3.10)$$

where l_β is the Rhines scale. In the two-layer case, we use the eddy velocity, $V = \sqrt{<|\nabla\psi'_1|^2 + |\nabla\psi'_2|^2>}$, and this seems to fit the data well, as can be seen in the right hand plot in figure 3.7b. The fit is not as close at larger jet separations, although we believe this is related to the jet quantisation effect discussed in section 3.3.1, cf figure 3.6. This supports the identification of the barotropic PV gradient, \mathbf{G}_{BT} , as dominating in determining the geometric properties of the jets in the simulations. For the one-layer case, the eddy velocity, $V = <|\nabla\psi'|^2>^{1/2}$, gives a Rhines scale that underestimates the jet scale significantly. As discussed extensively in chapter 2, the Rhines scale is based on an estimate of the wavenumber at which the inverse cascade of energy halts, k_β . We expect that $k_\beta > k_{\text{jet}}$, the jet wavenumber, and thus that $l_\beta < l_{\text{jet}}$. However, we expect both to be of the same order of magnitude, not seen here. In this case, both Rhines and Kolmogorov scale estimates of the halting wavenumber overestimate k_β (not shown), which we interpret as due to the forcing scale k_0 skewing the eddy scales as it is not

necessarily well separated in wavenumber space from the majority of the system energy.

The over-bar indicates, here and throughout, an *along-jet* mean, and primes indicate that the along-jet mean has been removed, i.e. $\psi' = \psi - \bar{\psi}$. The angular brackets indicate an integration over turbulent fluctuations and the doubly periodic domain. We choose along-jet velocity scales as this allows for the clearest comparison between simulations, whereas comparing zonal velocity scales would lead to obfuscation due to the differing directions of the strongest flow in different simulations.

The results of section 3.3.1 show that an increase in h_x leads to an increase in angle and an increase in the jet spacing for the two-layer case. Taking into account that increasing h_x acts to strengthen $|\mathbf{G}_{\text{BT}}|$, and that the two-layer system has been seen to obey the Rhines scaling as defined in (3.10), it can be deduced that when h_x increases there must be a larger increase in the velocity scale, associated with the eddy velocity. This is investigated in the next section, which looks at how the eddy energy production of the system varies with our parameters.

3.3.3 Eddy Energy Production

One-Layer Case

Through manipulation of (3.1), we can find the following expression for the balance of energy in the system:

$$\frac{1}{2} \left\langle \frac{\partial}{\partial t} |\nabla \Psi|^2 \right\rangle + \langle \Psi \cos(k_0 x) \rangle = -\kappa \langle |\nabla \Psi|^2 \rangle + d, \quad (3.11)$$

where all quantities are non-dimensionalised as previously described. In statistically equilibrated states, the eddy energy production, $\varepsilon = \langle \Psi \cos(k_0 x) \rangle$, is balanced by energy loss to bottom friction (since d is small); both terms are equivalent and provide a measure of the eddy energy production of the system.

The variation of ε at statistical equilibrium with β^* and h_x can be seen in figures 3.9a and b, measured by calculating $\kappa \langle |\nabla \Psi|^2 \rangle$. We also calculate the angle between \mathbf{G} and the zonal direction, see figure 3.2, defined in this case as

$$\theta = \tan^{-1}(\beta^*/h_x), \quad (3.12)$$

and so $\theta = \pi/2 - \phi_{\text{BT}}$. For each numerical simulation, once statistical equilibrium is reached, the system is allowed to progress for at least twice the time taken to reach

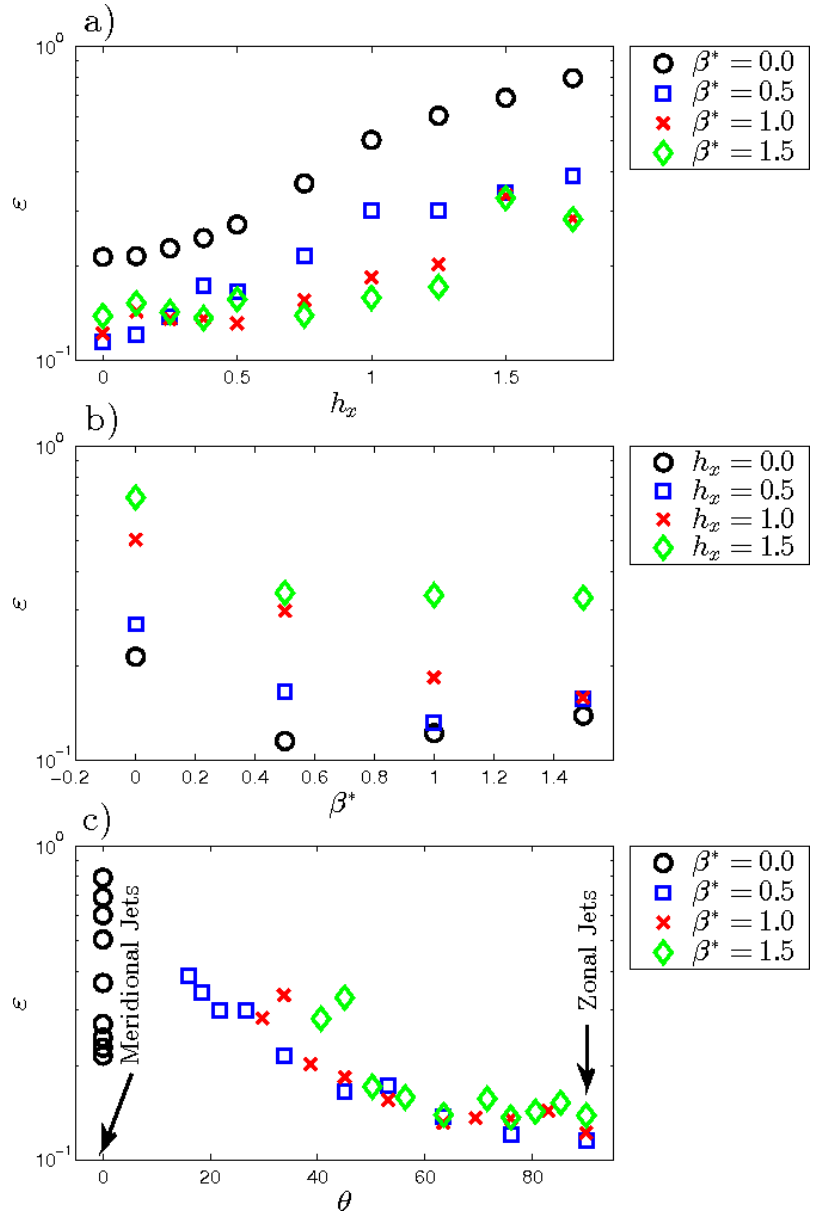


Figure 3.9: Time-mean eddy energy production after statistical equilibrium is reached for all one-layer runs, displayed in a) against h_x , in b) against β^* and in c) against θ , the angle between \mathbf{G} , as defined in equation (3.12), and the zonal direction. No errorbars are shown as the deviation in the measurements was smaller than the size of the markers shown.

statistical equilibrium, then the time mean and standard deviation in eddy energy production is taken. Figure 3.9a shows ε against h_x , and it is clear that the introduction of the zonal bottom slope, h_x , produces an increase in energy production for all values of β^* . Figure 3.9b shows ε against β^* , showing no clear relationship. However, figure 3.9c shows a clear increase in ε with decreasing θ , although the increase is moderate. This implies a relationship with the direction of the Barotropic PV gradient, with relatively little variation with β^* . Thus we conclude that θ , the direction of \mathbf{G} , not only determines the tilt of the jets, but also determines the energetics of the system.

Note that for a finite value of β^* , $\theta = 0$ is only possible if $h_x \gg \beta^*$, which we do not investigate here for two reasons. Firstly, as higher h_x results in higher eddy energy production, the time-step required for a numerically stable simulation at fixed spatial resolution becomes smaller - the length of time required to run these simulations to statistical equilibrium increase. Secondly, as seen in chapter 2, with increased ε , the jet and cascade barrier wavenumbers, k_{jet} and k_β respectively, decrease, i.e. the jets get larger and larger. Thus, for sufficiently larger ε , the energy of the system reaches the domain scale and cannot cascade any further, and so a larger domain would be required to allow the system to reach statistical equilibrium, again increasing the simulation length. So, with finite computing resources available it was not practical to run large ε/h_x simulations.

Two-Layer Case

By manipulation of (2.26), we can find an equivalent expression for the energy balance in the two-layer case:

$$\left\langle \frac{\partial}{\partial t} \left[|\nabla \psi_1|^2 + |\nabla \psi_2|^2 + \frac{1}{2}(\psi_1 - \psi_2)^2 \right] \right\rangle + \langle \psi_2 \psi_{1x} \rangle = -\kappa \langle |\nabla \psi_2|^2 \rangle + d. \quad (3.13)$$

The first (time-varying) term represents the total energy of the system, split into kinetic energy terms (the first two terms) and a potential energy term. Neglecting d , then, as before, at statistical equilibrium the eddy energy production, $\varepsilon = \langle \psi_1 \psi_{2x} \rangle$, is balanced by the loss to bottom friction. The variation of ε with h_x , h_y and β can be investigated as previously, taking the time mean and standard deviation of ε once statistical equilibrium has been reached, by measuring $\kappa < |\nabla \psi_2|^2 >$. Note that none of these three parameters enter into the energy balance directly (see Thompson and Young (2007)), and the non-dimensionalisation by \mathcal{U} removes any dependence on forcing. It should be noted that while Smith (2007) calculates the *kinetic* energy, and Arbic and Flierl (2004b) calculate the *total* energy of the system, these are both intrinsically related to our ε after statistical

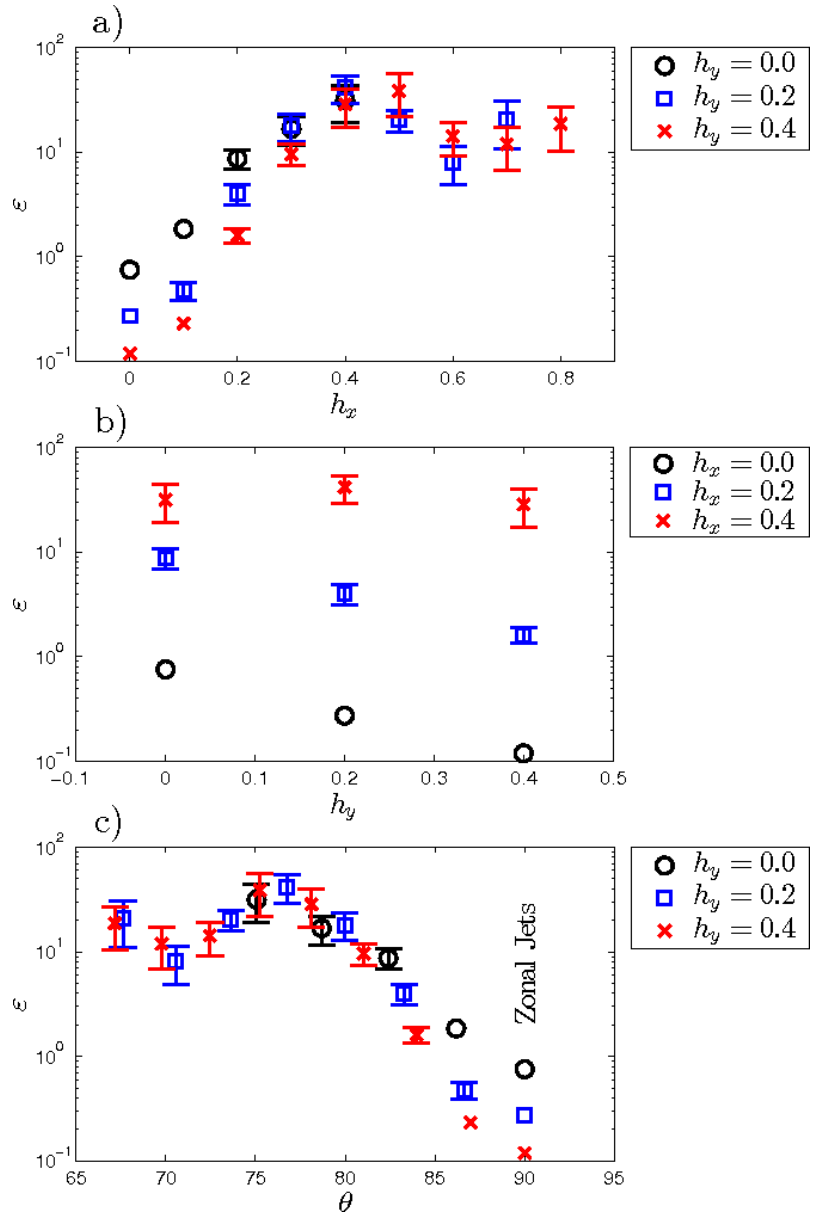


Figure 3.10: Time-mean eddy energy production after statistical equilibrium is reached for all two-layer runs with β fixed at 0.75, displayed in a) against h_x , in b) against h_y and in c) against θ_{BT} , the angle between \mathbf{G}_{BT} and \mathbf{S} , as defined in equation (3.14). The error bars show the standard deviation over the time that the mean was taken, shown only for points where this is bigger than the marker shown.

equilibrium has been reached, as seen from (3.13), and the qualitative behaviour of the results found do not change if we use kinetic energy or total energy instead. To compare with the work of Arbic and Flierl (2004b), as discussed in section 3.1, we calculate the angle between \mathbf{G}_{BT} and \mathbf{S} , defined as

$$\theta_{\text{BT}} = \tan^{-1} \left(\frac{\beta + h_y/2}{h_x/2} \right). \quad (3.14)$$

Thus, $\theta_{\text{BT}} = 90^\circ$ corresponds to \mathbf{G}_{BT} being perpendicular to the fixed zonal shear, \mathbf{S} , resulting in zonal jets, and $\theta = 0^\circ$ would correspond to the two vectors being parallel, impossible while $\beta \neq 0$ (N.B. $\theta_{\text{BT}} = 90^\circ - \phi_{\text{BT}}$). For each numerical simulation, once statistical equilibrium is reached, the system is allowed to progress for at least twice the time taken to reach statistical equilibrium, then the time mean and standard deviation of ε is taken. Figures 3.10a and b shows an increase in eddy energy production with increasing h_x for all values of h_y , with a particular jump in the $h_y = 0.4$ series between $h_x = 0.2$ and 0.3, and again no clear pattern with increasing h_y . Once again, a clear relationship of increasing energy as θ_{BT} decreases is seen in figure 3.10c, although it does not hold at the lower values plotted.

Thus, these results confirm the previous finding, in section 3.3.2, that the system shows a large increase in eddy velocity with increasing h_x , which results in an increase in the Rhines scale and so the jet spacing, even whilst the total magnitude of the barotropic PV gradient, \mathbf{G}_{BT} , is increasing. The two-layer system shows a change in energies over several orders of magnitude, whilst the one-layer system does not, which we postulate is due to the two-layer case producing across-PV contour jets, and the subsequent increase in relative vorticity in order to conserve PV. We do not expect similar orders of magnitude as the one-layer model does not contain baroclinic instability by definition, and so is describing very different dynamics than the two-layer model. This is discussed further in section 3.3.5.

The effect of increasing h_x is to move the direction of the barotropic PV gradient (\mathbf{G}_{BT}) closer to the direction of the background shear (see figure 3.1). Thus the increase of eddy energy production with h_x , and the overall trend in the relationship with θ_{BT} is consistent with Arbic and Flierl (2004b), who found a maximum in energy when $\theta_{\text{BT}} = 180^\circ$ (assuming that the pattern seen in figure 3.10c would be symmetric about $\theta_{\text{BT}} = 90^\circ$, as has been found in a few test cases). It appears that at high values of θ_{BT} there is a large decrease in the magnitude of ε as h_y is increased, even though θ_{BT} changes very little. This is due to the well-known stabilising effect of h_y , similar to that of β (Pedlosky,

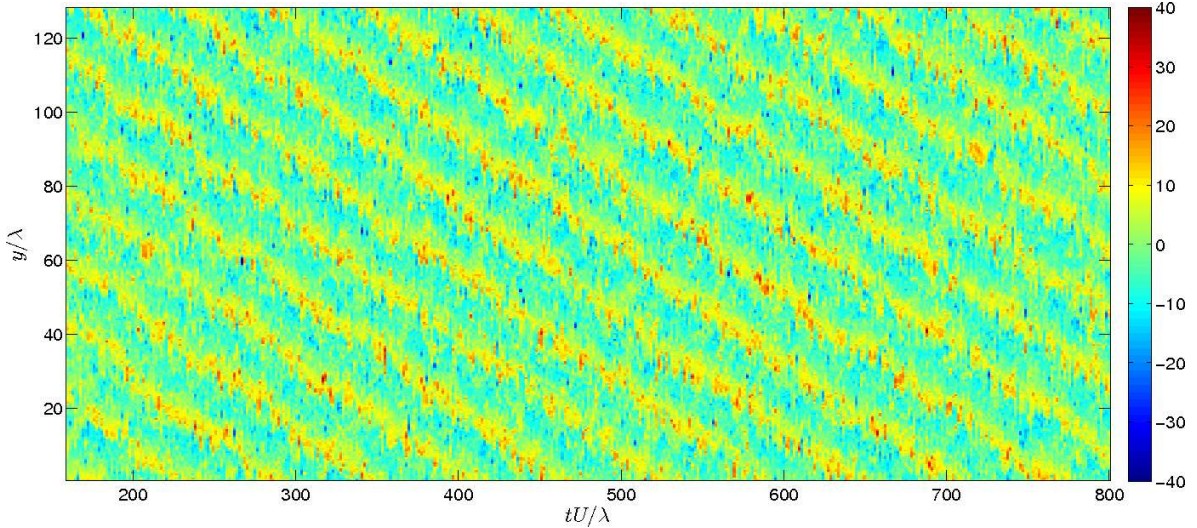


Figure 3.11: Hovmöller diagram showing the non-dimensional upper layer perturbation PV field, $q_1\lambda/U$, at $x/\lambda = 0$ versus time (tU/λ) for a two-layer simulation with $\beta = 0.75$, $h_y = 0$ and $h_x = 0.1$. The jets, characterised by the maxima in the PV gradient, can be seen to be moving with a constant speed in the negative y -direction.

1987).

We do not include simulations with as low values of θ as in the barotropic case because the numerical limitations of high ε/h_x simulations discussed previously are reached sooner in the baroclinic simulations because ε increases more strongly with h_x in these simulations and the extra layer introduces an extra computational drain. Several simulations at higher resolution (square grids with sides 512 or 1024 points) were carried out in order to assess any resolution dependence, however the results found were indistinguishable from the equivalent lower resolution simulations.

3.3.4 Jet Drift

During analysis of the results, it was noted that one- and two-layer simulations with tilted jets exhibited ‘jet drift’, that is, the jets present changed their position within the domain over time. An example Hovmöller (space-time) diagram for a two-layer simulation with $\beta = 0.75$, $h_y = 0$ and $h_x = 0.1$ can be seen in figure 3.11.

It is observed that the more tilted the jets, the more they tilt, as can be seen in figure 3.12, upper panel, which shows the measured jet drift v_{jet} against jet angle. The jet drift was measured by taking Radon transforms¹ of Hovmöller diagrams such as the

¹Integral transforms often used in image processing to find straight lines, see e.g. Deans (1983)

one seen in figure 3.11. At high jet angles ($\phi_{\text{jet}} > 15^\circ$) the statistically steady states show higher variability (as has been mentioned before), and so the drift rates cannot be well quantified. We postulate that this drift is the result of two factors. First, that the drift is partly a manifestation of ‘westward’ Rossby wave drift (the fact that the phase speed of the supported Rossby waves is westward relative to the orientation of the PV gradient, northwards for a β plane). To test this, we take the position of the most energetic wavenumber, found at $(K, \theta) = (K_{\text{jet}}, \phi_{\text{jet}})$, where $K_{\text{jet}} = 2\pi/l_{\text{jet}}$ ¹ and $\theta = \tan^{-1}(k/l)$ is a polar coordinate, and calculate the theoretical linear Rossby phase speeds at this point (see chapter 2 for more details of the linear behaviour of the system). The apparent drift of such waves in the y -direction at a fixed x point will then be:

$$c_y' = c_y + c_x \tan \phi_{\text{jet}}, \quad (3.15)$$

where $c_{x,y}$ are the theoretical Rossby wave speeds derived as described above. Figure 3.12, lower panel, shows this quantity plotted against the measured jet drift as before. Although the magnitudes do not match, there is an apparent relationship which suggests that Rossby wave drift could be a part of the reason for the observed drift.

The second factor we believe is at play is the barotropic control, resulting in jets that are not perpendicular to the PV gradients in individual layers. Therefore, there is systematic advection of layer-wise PV across the local gradient and, potentially, the systematic growth of PV anomalies aligned with the jets. The system could be compensating through continuous displacement of the jets, which in particular means that the long-time average velocity at any location in the direction parallel to the PV gradient in a layer is zero. In the upper layer the PV gradients are in the y -direction, therefore the angle ϕ_{jet} between the jet direction and the x -axis is one measure of the PV advection by the jets. There is, of course, also PV advection by the jets in the lower layer, but in the lower layer (a) the PV gradient is weaker, (b) q_2 is not materially conserved because of bottom friction and (c) there is no imposed mean flow as in the upper layer. Thus upper layer dynamics may have stronger control over the drift.

The results presented in section 3.5, which shows drifting jets over stepped topography when the jets are not aligned with the large scale upper layer PV contours, and stationary jets when they are, supports the role of this second factor. See section 3.5 for more details, however we have highlighted in this section that jet drift is a manifestation of PV conservation. The nature of the periodic domain in this study means that generation of

¹The jet spacing is calculated as the perpendicular distance between jets, see section 3.3.2.

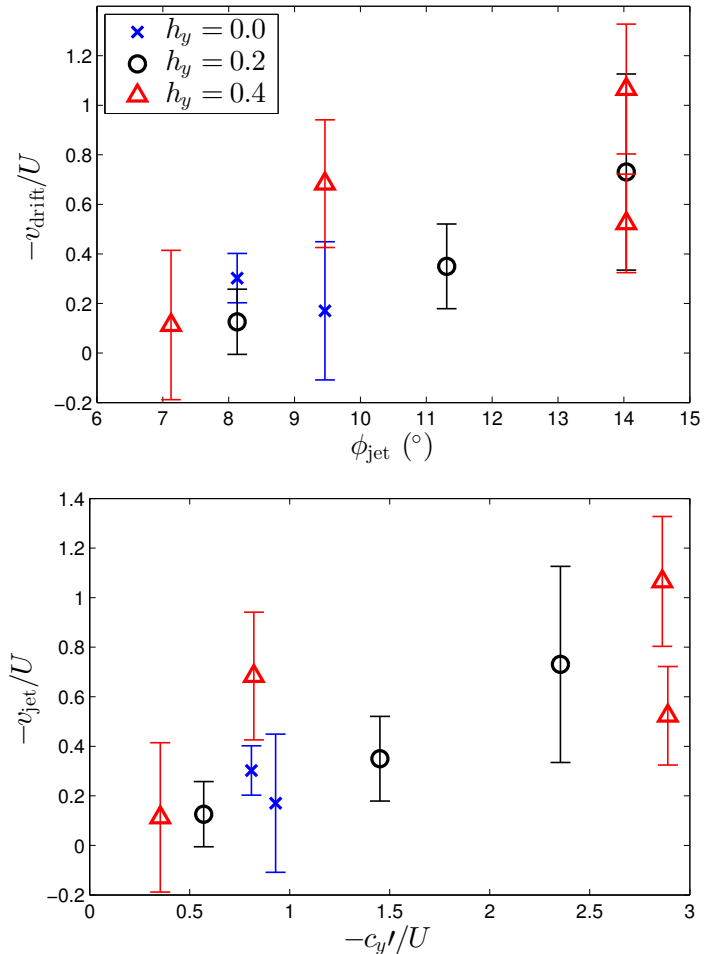


Figure 3.12: Non-dimensionalised jet drift in the y -direction, v_{jet} , in the upper panel plotted against the jet angle ϕ_{jet} , and in the lower panel against the theoretical apparent phase speed, c_y' , see (3.15). All quantities are averages over time after statistical equilibrium, and the error-bars represent the standard deviation over time.

relative vorticity may be insufficient to counter advection across layer-wise PV contours over long periods of time. We note, however, that in realistic flows, jet displacement and the subsequent modification to the planetary vorticity is a potential mechanism for conserving PV in strongly steered flows (see [Thompson and Richards \(2011\)](#)).

3.3.5 Transport

Whilst the PV histograms give an idea of the transport properties of the two-layer simulations, to analyse them more quantitatively we employ the effective diffusivity diagnostic, κ_{eff} , as developed by [Shuckburgh and Haynes \(2003\)](#), based on work by [Nakamura \(1996\)](#), and discussed further in section 4.1. κ_{eff} provides a measure of the relative mixing by considering the complexity of a tracer contour. Transport barriers are associated with regions of low mixing, therefore simple tracer contours and low values of κ_{eff} . Conversely, high values of κ_{eff} are associated with regions of strong mixing.

Theoretical Background

The effective diffusivity is calculated for a passive, conservative tracer, following an evolution equation as follows:

$$\frac{\partial C}{\partial t} + \mathbf{u} \cdot \nabla C = \nabla \cdot (k \nabla C), \quad (3.16)$$

where C is the tracer concentration, \mathbf{u} is the advecting velocity and k_d is the diffusivity. This can be recast in terms of the area bound by a tracer contour, A , as follows:

$$\frac{\partial C}{\partial t} = \frac{\partial}{\partial A} \left[K_{\text{eff}}(A) \frac{\partial C}{\partial A} \right]. \quad (3.17)$$

Alternatively, we can choose to write quantities in terms of an equivalent latitude, defined such that A is the area enclosed by the latitude circle, or the area below the latitude (y -coordinate) line in the domain in this study. $K_{\text{eff}}(y_e)$ depends on the true tracer diffusivity and the equivalent length L_{eq}^2 of the tracer contour:

$$K_{\text{eff}} = k_d L_{\text{eq}}^2 = k \frac{\frac{\partial}{\partial A} \int_A |\nabla C|^2 dA}{\left(\frac{\partial C}{\partial A} \right)^2}, \quad (3.18)$$

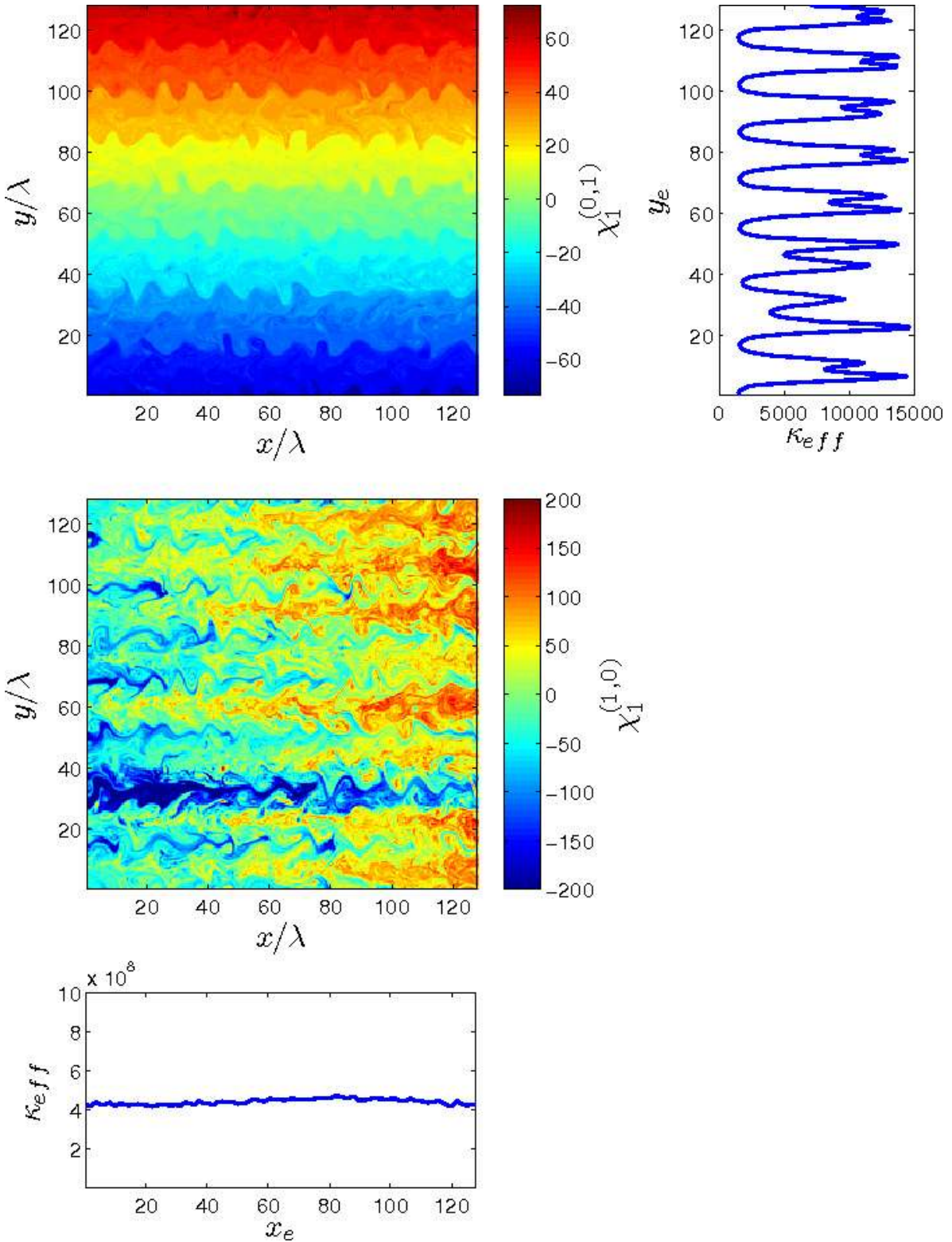


Figure 3.13: Snapshots of the tracer fields $\chi_1^{(0,1)}$ and $\chi_1^{(1,0)}$, upper and middle left panels respectively, for a simulation with $h_x = h_y = 0$ and $\beta = 0.75$, some time after statistical equilibrium. The effective diffusivities, κ_{eff} , averaged over statistical fluctuations, for $\chi_1^{(0,1)}$ and $\chi_1^{(1,0)}$ are shown against the equivalent latitude, y_e , and the equivalent longitude, x_e , in the upper right panel and lower left panel, respectively.

where $L_{\text{eq}}^2 \geq L^2$, the true length of the tracer contour. K_{eff} does not have units of diffusivity - the true effective diffusivity is defined as

$$\kappa_{\text{eff}} = k_d \frac{L_{\text{eq}}^2}{L_{\min}^2}, \quad (3.19)$$

where L_{\min} is the minimum possible length of a given tracer contour, equal to the length of the domain for a zonally orientated periodic flow.

Effective Diffusivity Calculation

To use this diagnostic, we include a conserved passive tracer with an imposed large-scale gradient, \mathbf{g} , so that the tracer concentration, $\chi^{\mathbf{g}}$, in the i th layer may be written in the form $\chi_i^{\mathbf{g}} = \chi_i^{\mathbf{g}'} + \mathbf{g}_i \cdot \mathbf{x}$, where $\chi_i^{\mathbf{g}'}$ is doubly periodic:

$$\frac{\partial \chi_i^{\mathbf{g}}}{\partial t} + J(\Psi_i, \chi_i^{\mathbf{g}}) = d, \quad i = 1, 2 \quad (3.20)$$

$$\frac{\partial \chi_i^{\mathbf{g}'} }{\partial t} + J(\Psi_i, \chi_i^{\mathbf{g}'}) = d + \mathbf{g}_i \cdot \mathbf{u}, \quad (3.21)$$

where $\mathbf{g}_i = (a_i, b_i)$, $\mathbf{x} = (x, y)$, $\mathbf{u} = (-\Psi_y, \Psi_x)$, and d is small scale dissipation, applied as in (3.1). (This is analogous to the equations for PV constrained by β , and could be achieved in practice by considering a very large rectangular domain, the major part of which was filled with many copies of the flow represented by the doubly periodic simulation. The tracer concentration would be imposed at the boundaries of the domain to be consistent with the large scale gradient \mathbf{g} .) By choosing either $a_i = 0$ or $b_i = 0$, it is possible to get a measure of the extent of meridional or zonal transport respectively.

We calculate the non-dimensional ratio:

$$\kappa_{\text{eff}}(y_e, t) = \frac{L_{\text{eq}}^2(y_e, t)}{L_{\min}^2}, \quad (3.22)$$

where L_{eq} is the equivalent length of a stirred contour, L_{\min} is the minimum contour length, equal to the domain width for purely zonal jets, and y_e is the equivalent latitude, defined as the latitude a given contour would have were it to be remapped to be zonally symmetric whilst retaining its internal area. Note that κ_{eff} is not a true diffusivity as it is dimensionless: the true effective diffusivity also depends on the numerical diffusion experienced by the tracer, see above. However, [Shuckburgh and Haynes \(2003\)](#) show that the true effective diffusivity is largely independent of the tracer numerical diffusivity.

The evolution equation for the tracers χ_i , (3.21), is linear in χ_i , and so once initial conditions have been forgotten (i.e. the tracer distribution has become independent of the initial distribution), χ_i are linear functions of the background gradient \mathbf{g} , so that

$$\chi_i^{p\mathbf{g}+q\mathbf{h}} = p\chi_i^{\mathbf{g}} + q\chi_i^{\mathbf{h}}. \quad (3.23)$$

Therefore, if $\chi_i^{(1,0)}$ and $\chi_i^{(0,1)}$ are evaluated by taking $\mathbf{g} = (1, 0)$ and $\mathbf{h} = (0, 1)$ respectively, then $\chi_i^{\mathbf{g}}$ can be deduced for a general $\mathbf{g} = (a, b)$ as

$$\chi_i^{\mathbf{g}} = a\chi_i^{(1,0)} + b\chi_i^{(0,1)}. \quad (3.24)$$

The tracer fields $\chi_i^{(1,0)}$ experience a zonal background gradient, and the tracer fields $\chi_i^{(0,1)}$ experience a meridional background gradient, and so we gain information about zonal transport from $\chi_i^{(1,0)}$ and information about meridional transport from $\chi_i^{(0,1)}$. If we look at fields with $\mathbf{g} = (a, b) = (\sin \alpha, \cos \alpha)$, where $0 \leq \alpha \leq 90$, then the fields $\sin \alpha \chi_i^{(1,0)} + \cos \alpha \chi_i^{(0,1)}$ are equivalent to the fields simulated with a tracer gradient in the direction α . Thus, we can gain information about transport properties in a range of directions without having to run separate simulations for each value of α we are interested in.

We begin by testing this concept for a case with purely zonal jets, i.e. $h_x = 0$, which are known from various studies to be good transport barriers in the meridional direction and bad transport barriers in the zonal direction. Snapshots of the full tracer fields in the upper layer, $\chi_1^{(0,1)}$ and $\chi_1^{(1,0)}$, can be seen in figure 3.13 alongside the calculated κ_{eff} plotted against y_e and on the relevant tracer contours. It is immediately apparent that the zonal jets are excellent barriers to meridional transport, and excellent mixers in the zonal direction. The mixing of a tracer with a zonal gradient, $\chi_1^{(1,0)}$, by zonal jets can be directly compared to the shear dispersion of PV noted by [Smith \(2007\)](#). Note that y_e , the equivalent latitude, is an area co-ordinate, and so does not necessarily increase in the y -direction, as may be implied. In the case of $\chi_1^{(0,1)}$, the area contained by contours of successively larger tracer values does indeed increase in the positive y -direction. However, in the case of $\chi_1^{(1,0)}$, it makes more sense to think of an equivalent *longitude*, x_e , and so we have plotted the κ_{eff} against x_e in this case in figure 3.13 to avoid confusion, although it is the same quantity in both cases.

Using the approach described above, we can also calculate κ_{eff} in both upper and lower layers for the full range of values of α , see figure 3.14 for a plot of the harmonic mean of κ_{eff} over effective latitude y_e and time for two simulations with $h_x = 0$ or $h_x = 0.4$.

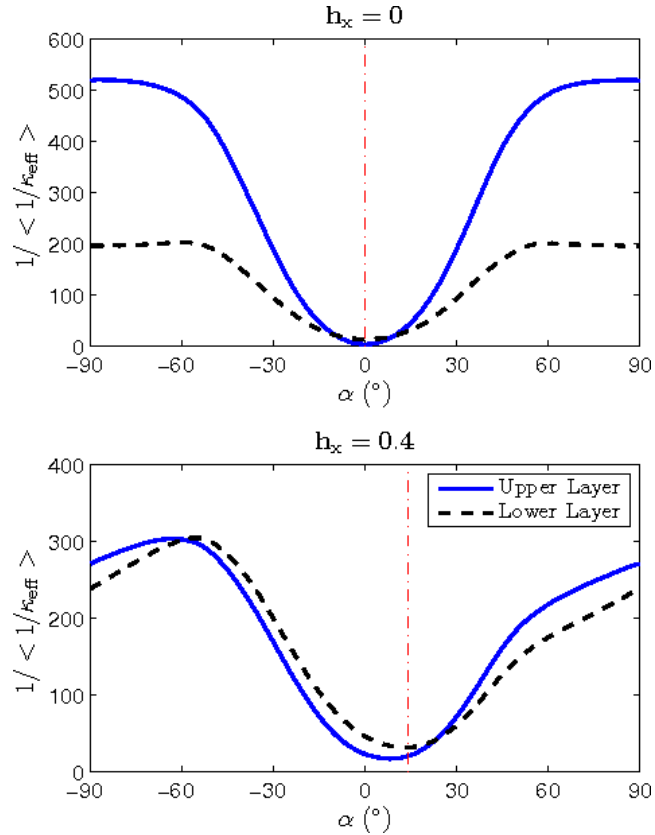


Figure 3.14: Harmonic mean over equivalent latitude, y_e , and time (after statistical equilibrium) of the effective diffusivity, κ_{eff} , of the tracer fields χ_i^α , against the ‘mixing angle’ α , for simulations with $h_y = 0$, $\beta = 0.75$, $\kappa = 0.1$, and $h_x = 0$ (upper panel) or 0.4 (lower panel). The red dash-dotted lines indicate ϕ_{jet} for each simulation.

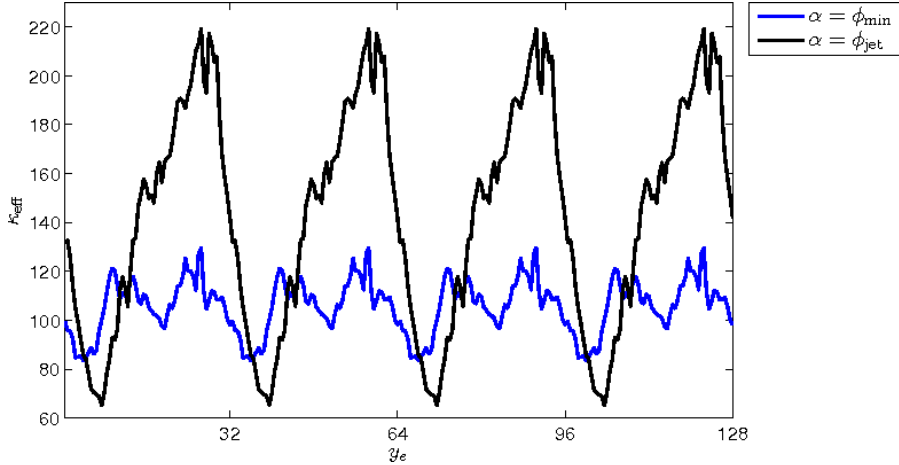


Figure 3.15: Effective diffusivity vs equivalent latitude for the upper layer of a simulation with $h_y = 0$, $\beta = 0.75$, $\kappa = 0.1$, and $h_x = 0.4$. The blue line corresponds to the angle of the minimum harmonic mean $\alpha = \phi_{\min}$, and the black line to $\alpha = \phi_{\text{jet}}$.

As expected, for $h_x = 0$ the minimum in transport is seen for $\alpha = \phi_{\text{jet}}$, shown by the red dash-dotted line, corresponding to a meridional gradient in tracer concentration, and a maximum in transport for $\alpha = \pm 90$, corresponding to a zonal gradient in tracer concentration, in both upper and lower layers. For $h_x = 0.4$, the minimum of the harmonic mean is close to the jet angle for the lower layer, but below this in the upper layer. The shape of the harmonic mean is no longer symmetric around the minimum angle, and so the maximum transport is not at 90 degrees to the minimum angle. We expect symmetry in the $h_x = 0$ case as the jets are aligned with the shear and perpendicular to the PV gradients. However, when $h_x \neq 0$, the jet direction is no longer aligned with the shear or perpendicular to the upper layer PV gradient, and so we do not expect behaviour to be symmetric. Figure 3.15 shows the calculated κ_{eff} against y_e in the upper layer for this simulation for the angle corresponding to the minimum harmonic mean $\alpha = \phi_{\min}$ and for $\alpha = \phi_{\text{jet}}$. Whilst the jets are more visible for $\alpha = \phi_{\text{jet}}$ than for ϕ_{\min} , with sharp low κ_{eff} , there is also higher mixing in between the jets. This higher mixing in between the jets leads to a higher tracer contrast across the jets, and so a higher tracer flux across the jets as measured by the harmonic mean.

If we repeat the above analysis for other simulations with a range of jet deflection angles, we can compare the location of the minimum in the harmonic mean of effective diffusivity, $1/\langle 1/\kappa_{\text{eff}} \rangle$, with the calculated angle of deflection, ϕ_{jet} . Figure 3.16 shows the time mean minimum flux angles for each layer, ϕ_{\min}^i , against h_x for simulations with

values from 0 to 0.4. Also shown (red squares) are the measured jet angles for comparison. Both minimum flux angles are consistently below ϕ_{jet} for $h_x \neq 0$, although the lower layer angle is always closer to it, and for $h_x = 0.3$ is within the standard deviation of the minimum flux direction. We postulate that this mismatch between the minimum transport direction and the across-jet direction is related to the jet drift discussed in section 3.3.4, or the effects of the zonal background velocity, which is absent in the lower layer, perhaps explaining the closer match.

Figure 3.14 also shows that the maximum in transport for the two layers goes from around ± 90 degrees for the upper layer, and around ± 60 degrees for the lower layer (although this is not a sharp maximum, with similar values between 60 and 90 degrees) in the $h_x = 0$ simulation to around -50 degrees in both layers in the $h_x = 0.4$ simulation. Looking at other simulations, in the lower layer the maximum transport direction decreases with increasing h_x , with similar magnitude shifts as for the minimum transport angle, whereas in the upper layer, the maximum transport direction drops substantially with increasing h_x (not shown), happening to be close to the lower layer value for $h_x = 0.4$. As for the minimum transport value, we expect the drift and/or the background velocity to be affecting the tracer fluxes and so the maximum transport direction in both layers. However, this does not explain why the maximum transport direction in the lower layer starts close to 60 degrees for $h_x = 0$, rather than 90, and why the maximum transport direction in the upper layer seems much more dependent on h_x than the minimum transport direction does. Analysis is ongoing on these points.

We might expect the tilted jets to be less good barriers to across jet transport, as compared to their zonal counterparts. Figure 3.17 shows the values of across-jet transport (measured using $\alpha = \phi_{jet}$) for various simulations with different magnitudes of barotropic PV gradient ($|\mathbf{G}_{BT}|$) and different measured deflection angles (ϕ_{jet}) in both the upper and lower layers. With ϕ_{jet} held fixed, an increase in $|\mathbf{G}_{BT}|$ results in a decrease in across-jet transport, due to the strengthening of the jets (this is more pronounced in the lower layer transport where the jets are relatively weaker). However, there is a clear increase in across-jet transport with increasing ϕ_{jet} , despite increasing $|\mathbf{G}_{BT}|$. We postulate that this is because the more tilted the jets, the more they cross the layer-wise PV contours and so the more they mix. The pattern is clearer in the upper layer, as the layer-wise PV gradient is stronger here. Overall, it is clear that tilted jets are weaker barriers to transport than their zonal counterparts, and that this tilt has a stronger effect than the change in the magnitude of the driving PV gradient, $|\mathbf{G}_{BT}|$.

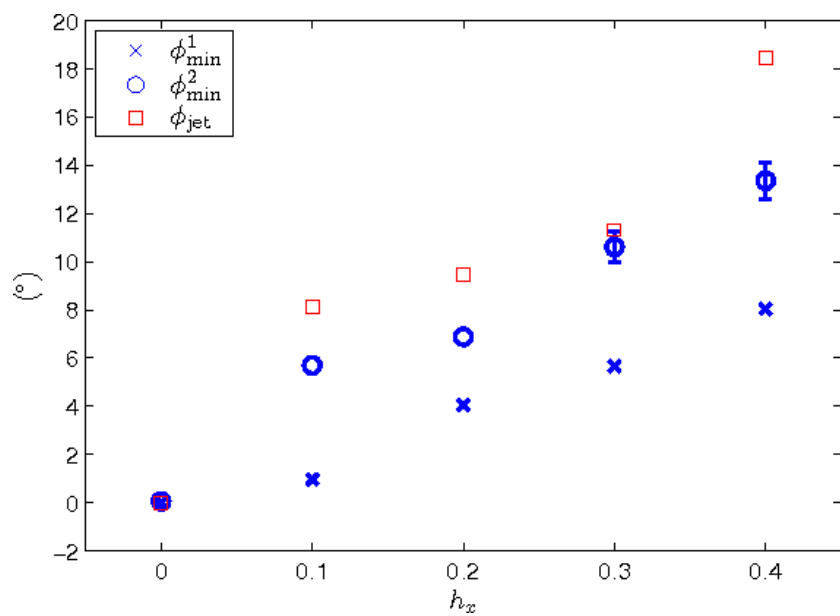


Figure 3.16: Mean minimum flux angles for each layer against the zonal slope in bottom topography h_x . Errorbars indicate the standard deviation, and are not shown where they are smaller than the marker plotted. The red squares show the measured jet angle for the same time period.

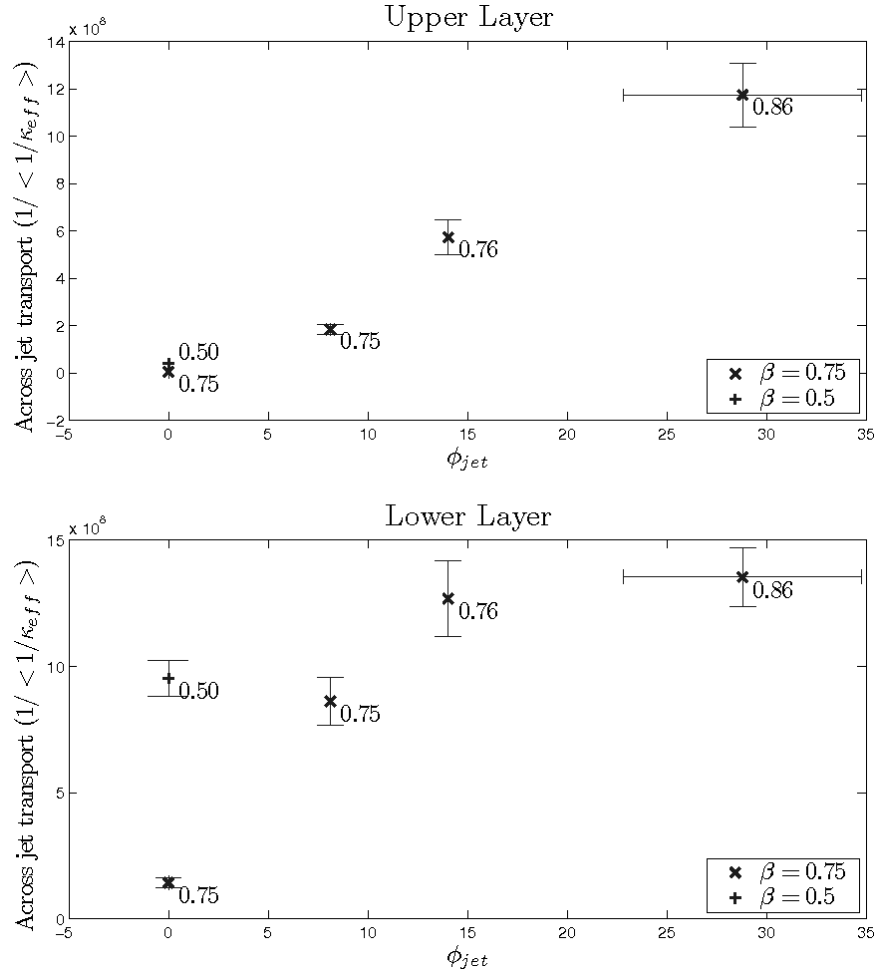


Figure 3.17: Comparison of across-jet transport properties for simulations with various barotropic PV gradients ($|\mathbf{G}_{BT}|$, the label on each point) and jet angles (ϕ_{jet}). The across-jet transport is the harmonic mean of the effective diffusivity, $1/\langle 1/\kappa_{eff} \rangle$, calculated from the fields $\chi_i^{g=(\sin \phi_{jet}, \cos \phi_{jet})}$, see (3.24). The error bars are the standard deviation over the time after statistical equilibrium. It is clear that the more tilted the jet, the greater the across-jet transport, despite increasing barotropic PV gradient magnitude.

3.4 Unequal Layer Depths

Until now we have been considering the case of equal layer depths, that is each layer is of depth $H/2$, where H is the total depth of the system. We now consider altering the relative depths, so that the total depth is now defined as:

$$H = H_1 + H_2 = \delta_2 H + \delta_1 H, \quad (3.25)$$

where H_1 and H_2 are the upper and lower layer depths respectively, and

$$\delta = \frac{H_1}{H_2}, \quad \delta_1 = \frac{1}{1 + \delta}, \quad \delta_2 = \frac{\delta}{1 + \delta}. \quad (3.26)$$

This leads to the alterations of the definitions of the non-dimensional system equations by the factors δ_i , such that (2.29) and (2.17) are redefined as follows:

$$\mathbf{G}_i = \left(0, \beta + \mathbf{2\delta}_i (-1)^{i-1} \frac{U}{\lambda'^2} \right) + \mathbf{2\delta}_i \delta_{i2} (h'_x, h'_y), \quad i = 1, 2, \quad (3.27)$$

$$\begin{aligned} \mathbf{G}_{\text{BT}} &= (\mathbf{2\delta}_1 \mathbf{2\delta}_2 h'_x, \beta + \mathbf{2\delta}_1 \mathbf{2\delta}_2 h'_y) \\ &= (h_x/2, \beta + h_y/2), \end{aligned} \quad (3.28)$$

where the modifications have been marked in bold font, $\lambda'^2 = 4\delta_1\delta_2\lambda^2$ and $h' = h/4\delta_1\delta_2$. Note that if $\delta_1 = \delta_2 = 1/2$, then the original equations are recovered, and that the barotropic PV remains unchanged regardless of the layer depths. One might expect that the barotropic PV would become dominated by the PV of one layer as that layer became relatively large, and so the barotropic PV would show some layer depth dependence. However, due to the inverse dependence of layer-wise PV on layer depth, as a layer becomes smaller, it contributes relatively less to the barotropic PV, but the PV of the layer becomes larger. The PV of an infinitesimally small layer is infinite, thus the barotropic PV still depends on the layer's PV if the layer remains defined. This is obviously unrealistic, but one would first break the quasi-geostrophic assumption of small depth perturbations relative to the layer depth before reaching this limit.

The form of $2\delta_1\delta_2$ can be seen in figure 3.18, where it is plotted against δ_1 , the fractional depth of the lower layer. As can be seen, the factor peaks at $\delta = 1$, the case of equal layer depths. For $\delta > 1$ or < 1 , the factor drops off as either the depth of the lower layer depth increases, decreasing the effect of the topography, or the upper layer depth increases, reducing the importance of the lower layer.

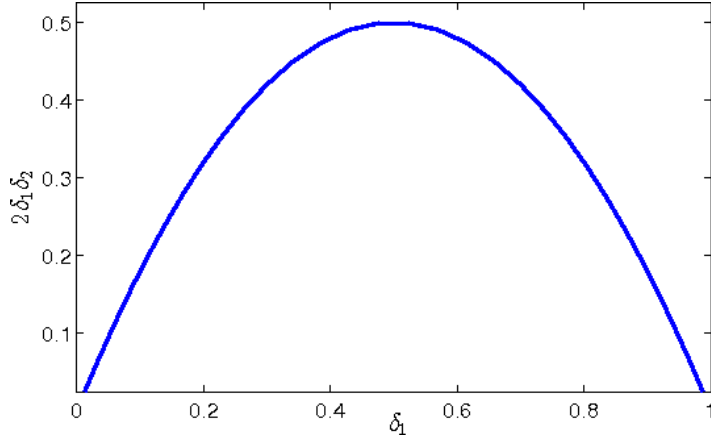


Figure 3.18: Variation of $2\delta_1\delta_2$, which appears in (3.28), with δ_1 , the fractional depth of the lower layer. These quantities are defined in (3.26).

To determine whether the barotropic behaviour noted in the equal layer system persists when the layers are not equal, we carried out a series of simulations with the same parameters as previous simulations, but with different values of δ and $h'_x = 0.1$ or $h'_x = 0.2$. The measured jet angle, ϕ_{jet} , the energy production, ε , and the Rhines scale, l_β , for these simulations are plotted in figure 3.19 with the $\delta = 1$ results for comparison. All quantities were measured as previously. As can be seen in figure 3.19a, the jet angles in simulations with $\delta > 1$ ($\delta = 1.25, 1.5, 1.75, 2.1, 2.2, 2.3, 10$) or $\delta < 1$ ($\delta = 0.25, 0.5, 0.75$) lie close to the values measured for $\delta = 1$, and fit closely to the angle perpendicular to the barotropic PV gradient, ϕ_{BT} . Similarly, figures 3.19b and c show eddy energy production levels and Rhines scales for $\delta > 1$ and $\delta < 1$ close to those for $\delta = 1$. This strongly suggests that the barotropic behaviour reported for the equal-layer simulations holds for unequal layer depths, and all the previous interpretations hold for unequal layer depths.

These results make it clear that differing layer depths (albeit staying within the quasi-geostrophic assumptions) do not affect the results presented in the previous sections. In the real ocean, the relevant layer depths can be related to the depth at which the PV gradient reverses, as discussed in [Tulloch et al. \(2011\)](#). This varies throughout the ocean, but in the Southern Ocean, a zonal average of locally calculated PV gradients shows that this level is at roughly 1-2km, see their figure 2, which, assuming a depth of ~ 3 km, is equivalent to $\delta \approx 0.5-2$. It should be noted, however, that the zonally averaged picture hides significant regional variation, see, for example, [Thompson \(2010\)](#), where calculating PV on a deep isopycnal in an ocean model reveals the presence of negative gradients in certain regions and not in others.

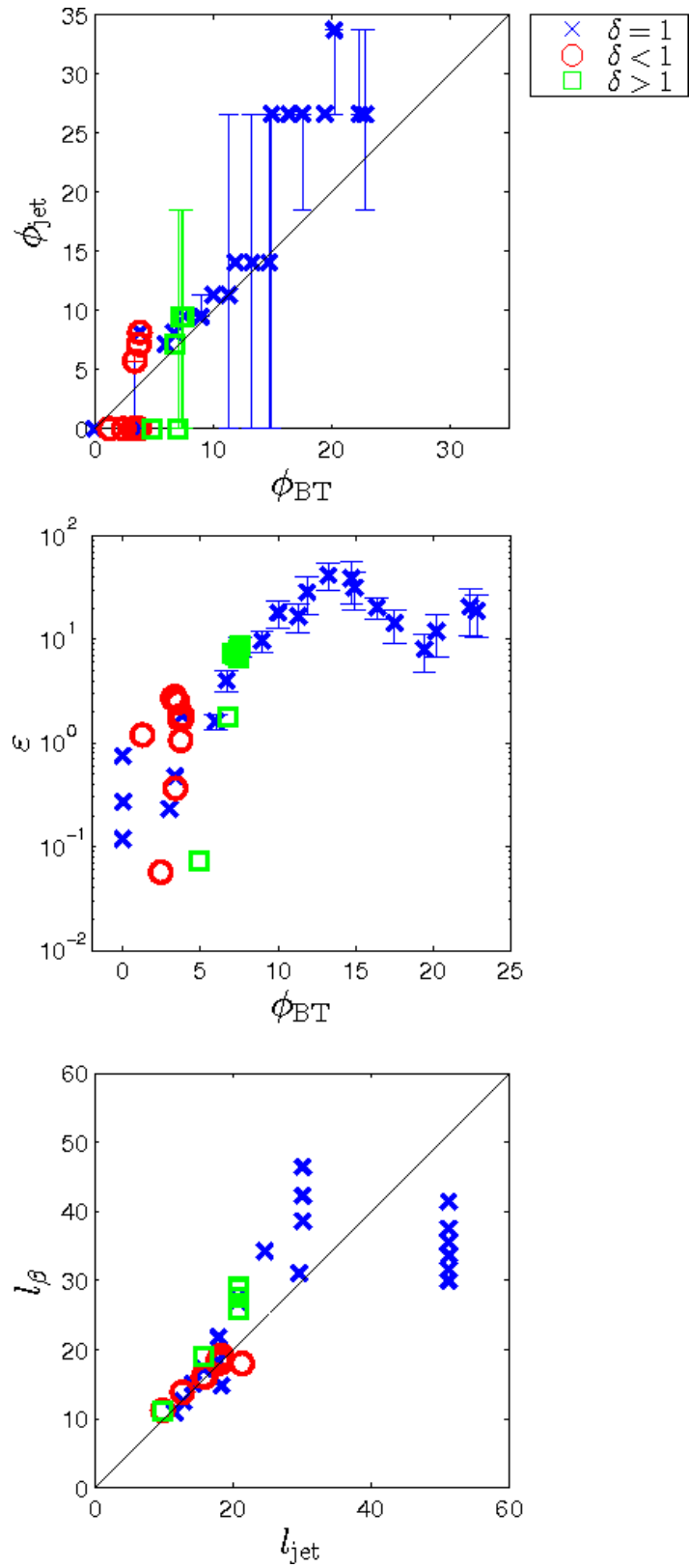


Figure 3.19: Comparison of simulations with different layer depths, where δ is defined in (3.26). a) Measured jet angle, ϕ_{jet} , versus the angle perpendicular to \mathbf{G}_{BT} , ϕ_{BT} ; b) Eddy energy production, ε , versus ϕ_{BT} ; c) Rhines scale, l_β , versus jet scale, l_{jet} .

3.5 Ridged topography

A constant slope in bottom topography was modelled in sections 3.2 and 3.3 under the assumption of a doubly periodic domain, meaning that the dynamics were assumed to be representative of a localised region of a flow on a large scale, weak slope, with the region, or indeed many copies of it, being smaller than the scale of spatial inhomogeneities in slope. A key question is whether simulations with more general topographies resemble the doubly periodic models in localised regions over large scale, weak zonal slopes. Alternatively, taking a simulation with more general topography, if one averaged flow quantities over a patch of the domain, would forcing a doubly periodic model with the same quantities produce a similar statistically equilibrated flow? Note that these questions depend on whether there exists scale separation, in that a scale exists larger than the eddy scale, such that averages of quantities on this scale are statistically steady, but smaller than the scale of topographic inhomogeneities.

In this section, we attempt to answer these questions through the investigation of a variety of bottom topographies which have changing zonal slopes in rectangular domains. Unlike previously, the absolute topographic height, as well as the topographic gradients, are consistent across the periodic boundaries, and so the periodic domain represents one part of a series of meridional ridges. An example of possible topography - stepped topography with constant slopes $h_x \lambda^2/U = \pm 0.4$ in certain regions - can be seen in figure 3.20, where it should be noted that the y -axis has been chosen to emphasise the form of the topography, but the height of the topography is small compared to the thickness of the fluid layers. From now on, we will refer to one copy of the simulated grid - one ridge - as the ‘domain’, and a ‘cell’ will refer to one grid of a doubly periodic simulation, which, when tiled, is assumed to represent a patch of the ridged domain, see figure 3.21, a schematic of a domain (thick black line) containing two possible cells (dashed lines, labelled A/B). It is these cells that should exist in the intermediate scale between eddy lengths and the topographic inhomogeneities described above to successfully reproduce the domain simulated behaviour.

The system equations remain as before, except that the term h_x is now a periodic function of x rather than a constant, and $h_y = 0$. The non-dimensional layer PVs are now defined as

$$Q_i = q_i + \int_0^x \mathbf{G}_i(\mathbf{x}) \cdot d\mathbf{x} = q_i + (\beta + (-1)^{i-1})y + \delta_{i2}h, \quad i = 1, 2 \quad (3.29)$$

where $h = \lambda f h'/U$, $h' = T/H$, $T(x)$ is the topography, all other symbols are as previously

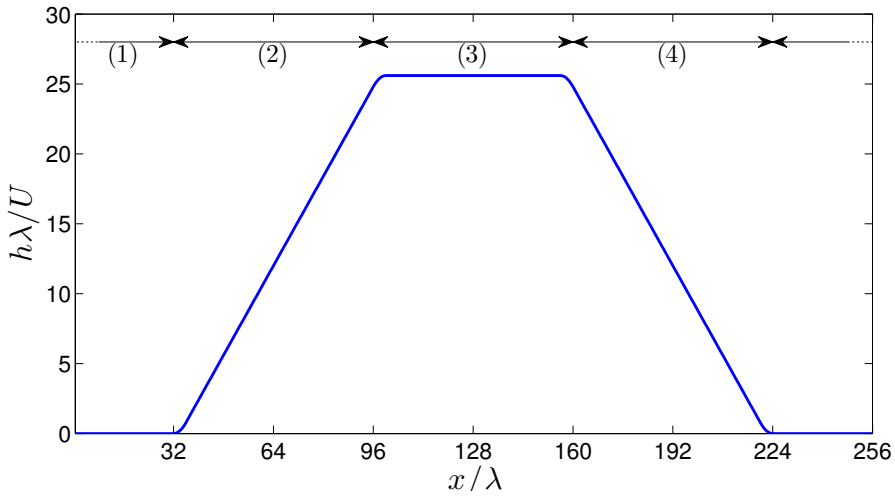


Figure 3.20: Representative side view of the topographic height for a stepped simulation. In this case, the slopes have gradients $h_x \lambda^2 / U = \pm 0.4$. The various regions - flat and sloped - have been labelled for future reference.

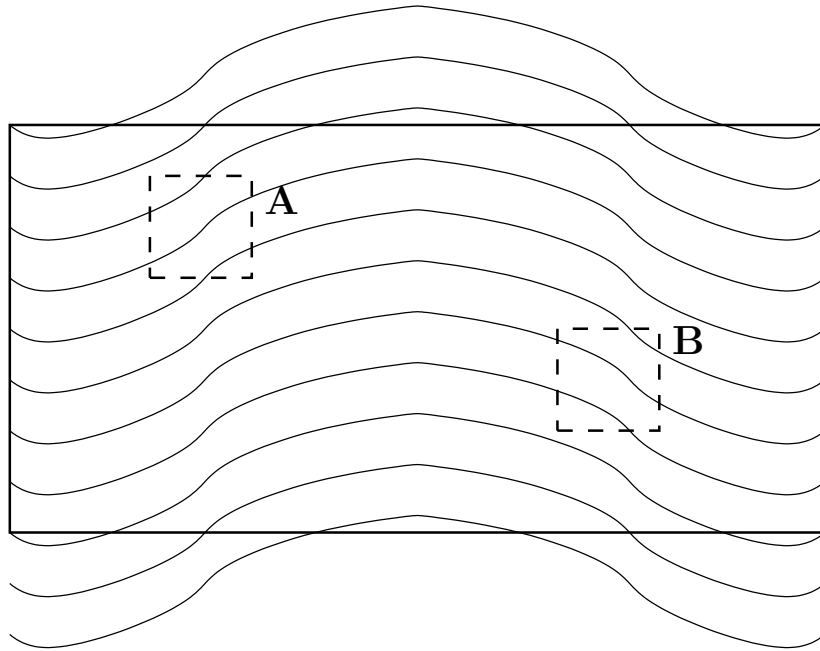


Figure 3.21: Schematic of a possible streamfunction or PV field in a simulated domain (thick black line) and possible cell choices (dashed lines, labelled A and B). We wish to know if a doubly periodic simulation of A or B resembles the same cell in the larger simulation domain.

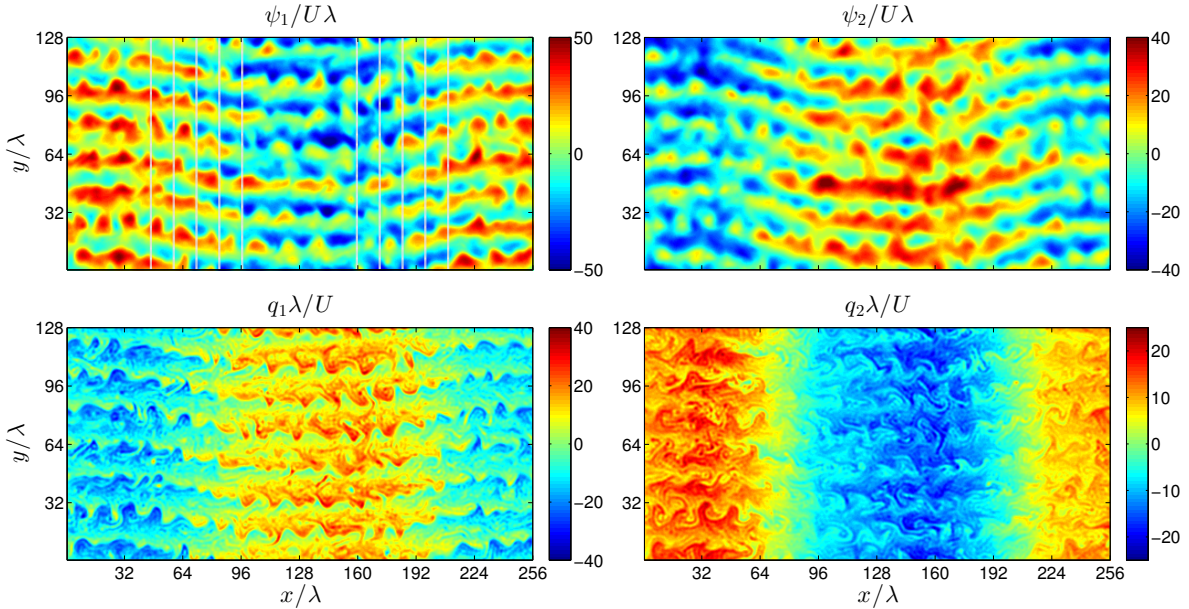


Figure 3.22: Upper and lower layer streamfunction and PV perturbation snapshots from a ridged topography simulation with $h_x\lambda^2/U = \pm 0.4$ slopes. The white dashed lines are contours of topography.

defined, and (3.29) simplifies to (2.27) in the case of constant h_x .

Upper and lower layer streamfunction and PV perturbation snapshots for a simulation with the topography depicted in figure 3.20 can be seen in figure 3.22. Jets can be clearly seen in both layers, tilting southwards over the rising slope and northwards over the falling slope, consistent with previous results for the doubly periodic case. This is discussed further in section 3.5.1. On the domain scale, the PV perturbation field can be seen to be relatively high in the upper layer over the raised region, and relatively low over the raised region in the lower layer, with the associated changes in the streamfunction fields also visible.

This is an important difference from the previously studied doubly periodic case. There, large-scale quantities are assumed to be homogeneous - in particular, quantities averaged over a single cell of the doubly periodic flow are assumed to be the same as for all other cells. In the simulations reported in this section, there are large scale variations within the domain - see for example the time-averaged meridional velocity profiles in figure 3.23. Whilst the domain average of $\langle v \rangle = 0$ is maintained, locally there are large variations. These large scale background velocities have important implications for the question of whether the sloped regions could be represented by a doubly periodic

simulation, which are discussed in section 3.5.3.

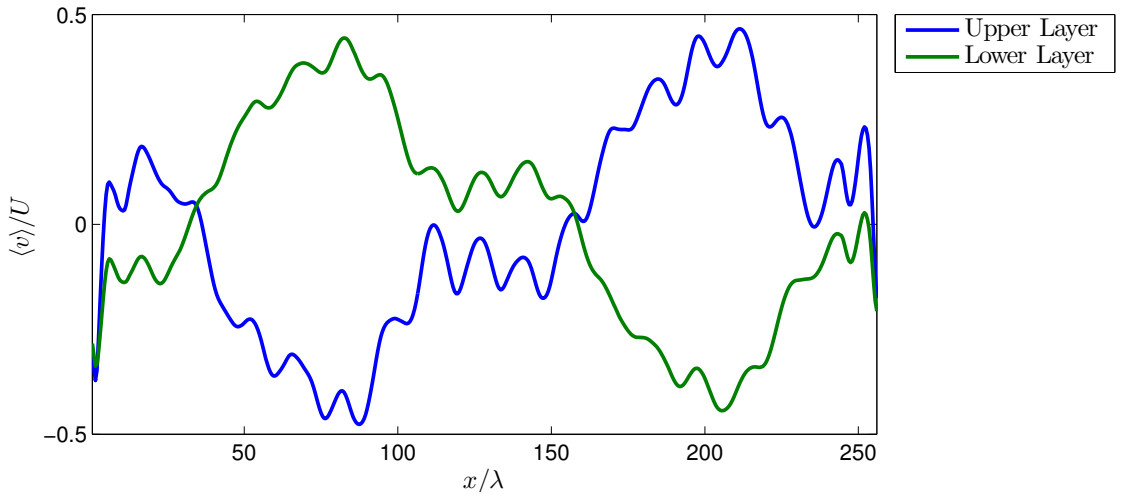


Figure 3.23: Time mean meridional velocity profiles from the same simulation as figure 3.22. Calculated by taking a time mean, followed by a meridional mean, followed by smoothing in x .

In this section, we first investigate if the barotropic control of the previous sections persists in the presence of more complicated topography, where we define barotropic control as meaning that the barotropic PV gradient sets the direction of the jets that form. We look at this in detail for stepped topography of the type shown in figure 3.20, determining how the barotropic control varies with slope magnitude and the fraction of the domain that is sloped. We then look briefly at the large scale baroclinic PV gradients and the jet drift observed in a number of simulations. Although we have not investigated these phenomena fully, we set out the basic behaviour and some preliminary analysis, as well as the implications for the questions outlined above.

3.5.1 Barotropic Control: Varying Slope Magnitude

Figure 3.24 shows the time mean fields for two ridged simulations with slopes of $h_x \lambda^2 / U = \pm 0.4$ and ± 0.8 . This figure demonstrates that, similarly to the previous sections, the jets are steered along contours of barotropic PV, i.e. perpendicular to barotropic PV gradients, and that as the magnitude of the slope is increased the jets tilt more. The sharp jets (associated with the well defined gradients in the PV field) seen confirm that the jets are aligned with the barotropic PV contours (white contours), and produce transport barriers at their core, consistent with the doubly periodic slope results of the previous sections.

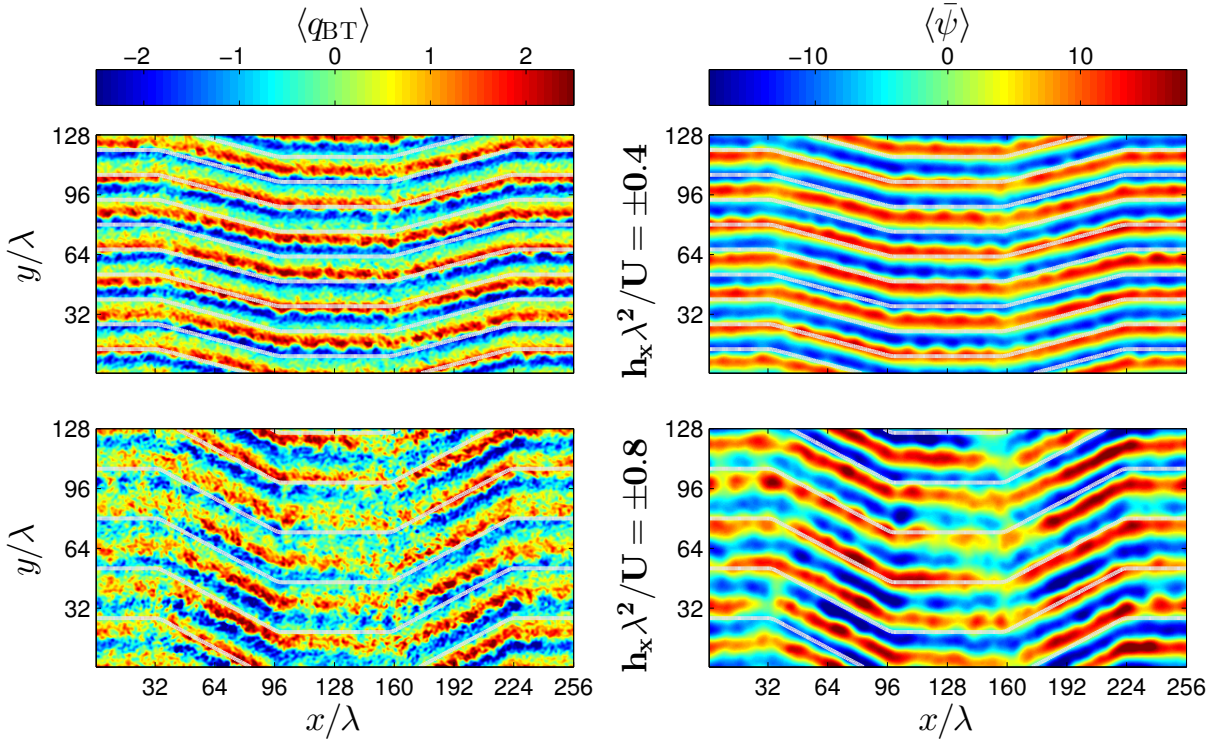


Figure 3.24: Time mean barotropic PV perturbations, q_{BT} , and barotropic streamfunctions, $\bar{\psi}$, for two ridged simulations with h_x values as shown. The time mean clearly shows the jets, aligned with the background barotropic PV (white contours).

The jets aren't as sharp in the simulation with the steeper slopes, with less well-defined PV gradients, especially just upstream of the sloped regions, which we interpret as due to the more extreme adjustment in jet direction required moving from the flat region to the slopes in this case.

As the topographic slope increases and the jets tilt more, the difference between the coherence of the jets over the sloped and flat regions becomes more pronounced. This may be due to the competition between the number of jets that the system dynamics would prefer being increasingly different between the sloped and flat regions. There is an increase in jet separation (decrease in jet number) as the slopes tilt more, as was also observed in the doubly periodic simulations. However, the increase is not as great as in that seen in section 3.3.1, although the jets in these simulations can be tilted at any angle (and take any separation), not constrained by the geometric effects of the doubly periodic simulations. Whilst a change in the jet separation over the slopes with increased jet tilt could have been expected from previous results, the fact that the jets over the

flat regions are also changing their separation so as to maintain a consistent number of jets in the domain might not have been expected. Doubly periodic simulations with the same parameters (flat bottom) have 8 jets, and so this is one indication that the different regions of these stepped simulations are not dynamically independent of one another, and are not locally similar to doubly periodic simulations with the same parameters.

For a variety of stepped topographies such as that seen in figure 3.20, to more quantitatively measure how close the barotropic PV gradient is controlling the direction of the jets in each region of the domain, we measure the angle of the jets as follows. The perturbation streamfunctions, ψ_i , are split into the four regions labelled in figure 3.20, then the angle is measured as in section 3.3, by finding the maxima in the power spectra of the stream function. Figure 3.25 shows how the mode angle (measured over time after statistical equilibrium) of the jets in each region varies with region for ridged simulations with $h_x\lambda^2/U$ values of ± 0.4 and ± 0.8 . We use the mode here rather than the mean because, as discussed in section 3.3.1, ϕ_{jet} can only take a discrete set of values for a given number of jets, and so using the mode ensures that ϕ_{jet} is an angle that is actually seen in the simulation, rather than an intermediate value determined by the exact time-dependence of the angle variability. For both simulations, the mode, or most common, jet angle is close to the direction perpendicular to the barotropic PV gradient, ϕ_{BT} , for each region. However, the $h_x\lambda^2/U = \pm 0.8$ simulation shows increased variability, with a larger spread of jet angles over time.

Increased variability with increased topographic slope is a persistent feature of the simulations, as can be seen in figure 3.26. Figure 3.26 shows, for simulations with slope magnitudes $|h_x|\lambda^2/U = 0.1\text{--}1.0$, the maximum absolute difference between ϕ_{jet} and ϕ_{BT} over all four regions, for each layer, denoted $|\Delta\phi|$. Additionally, as the jets at larger slope magnitudes are less coherent, see figure 3.24, so the jet angle becomes harder to define. Both effects are reflected in the error bars, which show the max/min $|\Delta\phi|$ over the same time period. For $|h_x|\lambda^2/U = 0.1\text{--}0.7$, $|\Delta\phi|$ is relatively low and constant. For $|h_x|\lambda^2/U > 0.7$, $|\Delta\phi|$ increases rapidly. We interpret this as the increased adjustment in ϕ_{jet} required over the slopes causing increasingly less coherent jets, both in terms of consistency over time and confinement in space, where jets from one region extend downstream into the next region slightly. The increased jet angle variability with increased slope magnitude is consistent with the doubly periodic simulations of the previous sections, see figure 3.7. The increased variability also reflects that defining a single jet angle ϕ_{jet} may become increasingly meaningless with no coherent jets present, as the angle is a measure of the location of the maximum of system energy, see section 3.3.1. So whilst the simulations

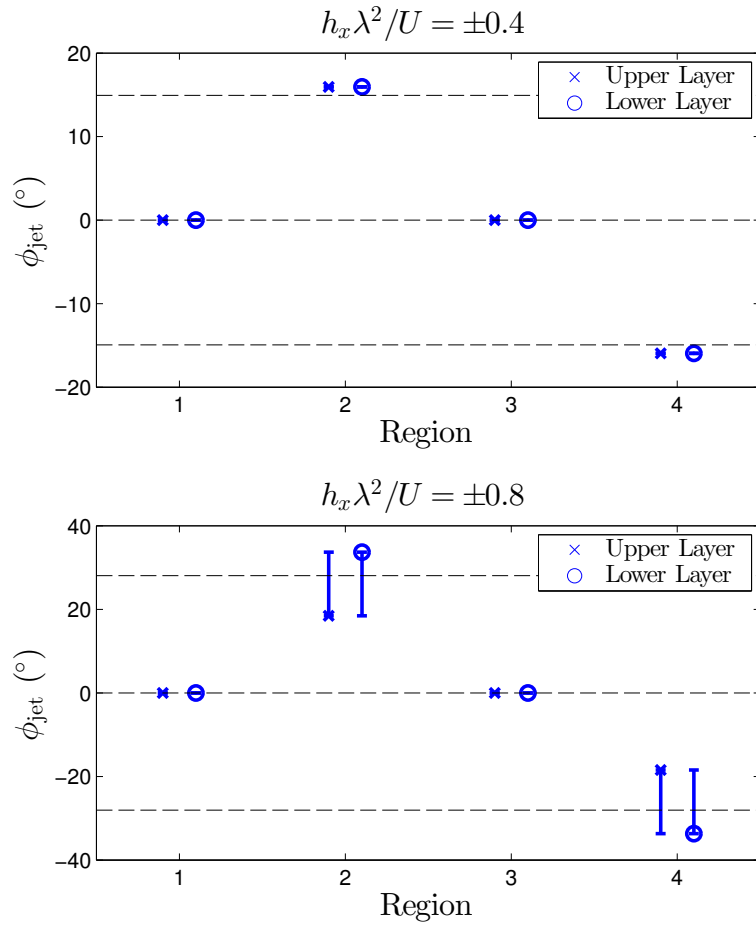


Figure 3.25: Measured jet angle in the upper (crosses) and lower (circle) layers in each region of the topography for simulations with h_x as shown. The markers show the mode, or most common, angle over time after statistical equilibrium has been reached, and the error bars show the max/min values over the same time period. The data points for each layer are slightly separated in the x -direction for clarity. The black dashed lines indicate the direction perpendicular to the barotropic PV gradient, ϕ_{BT} , in each regions.

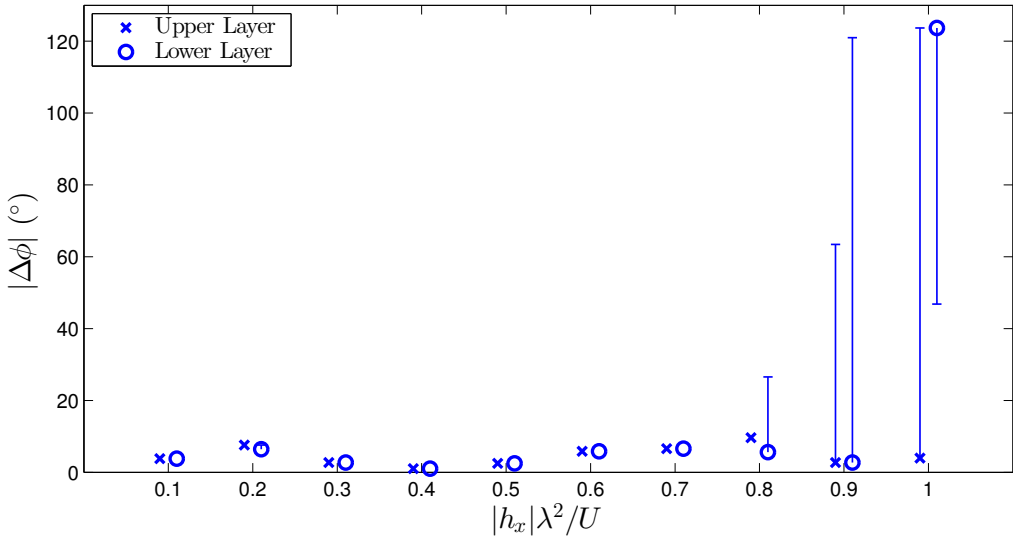


Figure 3.26: Maximum absolute difference between ϕ_{jet} and ϕ_{BT} over the four labelled regions in figure 3.20, $|\Delta\phi|$, for each layer, for a range of ridged simulations with slope magnitudes $|h_x|$ as shown.

with $|h_x|\lambda^2/U = 0.9$ or 1.0 may not provide information about jet behaviour, they do inform us about the limits of these simulations.

3.5.2 Barotropic Control: Varying Ridge Width

As well as varying the steepness of the topographic slopes of the stepped simulations, it is also possible to vary the fraction of the total domain that is sloped. The simulations discussed in the previous section had a total fraction of 0.5 of the domain sloped, regions 2 and 4, as seen in figure 3.20.

Similarly to section 3.5.1, we can measure the jet angle in each region of the domain and compare it to ϕ_{BT} in that section. Figure 3.27 shows, for simulations with $h_x\lambda^2/U = \pm 0.4$ and slope fractions 0.1–0.9, the maximum absolute difference between ϕ_{jet} and ϕ_{BT} over the slopes (regions 2 and 4) for each layer, denoted $|\Delta\phi|$. Initially, a sharp decrease in $|\Delta\phi|$ as the domain fraction increases is seen, as could be expected as the sloped region becomes long enough for the jets to adjust to the barotropic PV gradient change. There is a slight increase in $|\Delta\phi|$ at higher fractions, which is likely due to the influence of the oppositely sloped region, which will get closer with increased fraction due to the shrinking of the flat region.

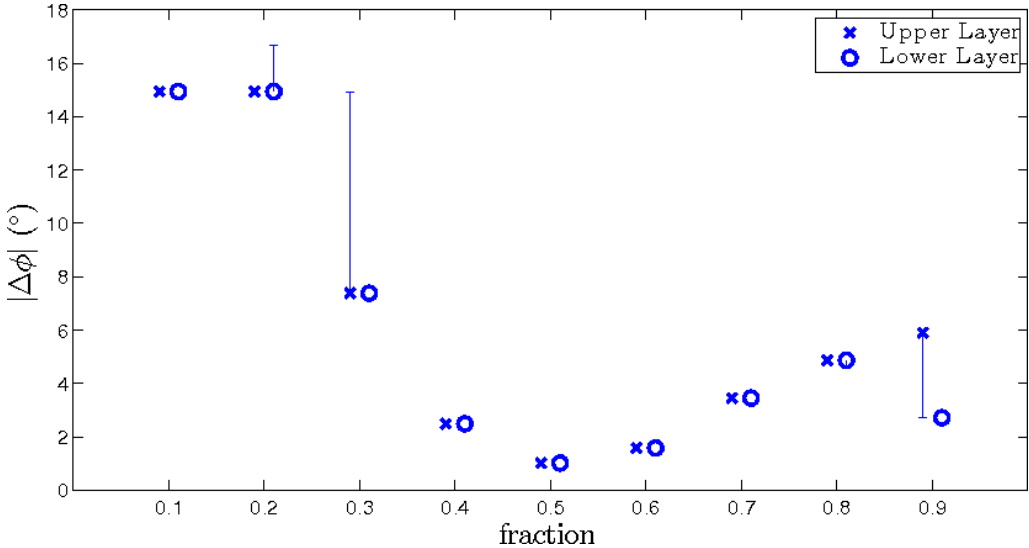


Figure 3.27: Maximum absolute difference between ϕ_{jet} and ϕ_{BT} , $|\Delta\phi|$, for each layer, against slope fractions, for simulations with $h_x \lambda^2 / U = \pm 0.4$.

3.5.3 Large Scale Baroclinic Compensation

In many of the simulations mentioned, we observed large scale alignment of the baroclinic field with the topography, as can be seen in figure 3.28, which shows the time mean perturbation barotropic and baroclinic streamfunction fields for a simulation with the stepped topography seen in figure 3.20. The barotropic and baroclinic streamfunctions make up the layer-wise streamfunctions ($\psi_1 = \bar{\psi} + \tau$, $\psi_2 = \bar{\psi} - \tau$). The barotropic streamfunction shows clear jets, closely aligned perpendicular to the background barotropic PV gradient (white contours show the background barotropic PV). The baroclinic PV, however, shows close large scale alignment with the topography (white contours), i.e. there are large scale gradients in the baroclinic PV field aligned with the topographic slopes, but with an oppositely signed slope. Significantly, the baroclinic perturbation field does not average to zero over a cell you might choose, as depicted in figure 3.21, as it did in the doubly periodic simulations, but contributes a large scale gradient. This results in an upper layer PV field ($Q_1 = \nabla^2 \psi_1 - \tau/\lambda^2 + \int \mathbf{G}_1 \cdot d\mathbf{x}$) with a large scale background gradient similar to the barotropic PV gradient, as can be seen in figure 3.29 which shows the full upper and lower layer PV fields, including the background gradients, as well as the barotropic PV (white contours). Note that the degree of alignment with the barotropic PV is not symmetric in the domain - indeed Q_1 shows slightly sloping contours over the middle, flat region. This demonstrates that non-local effects must be at play, given that

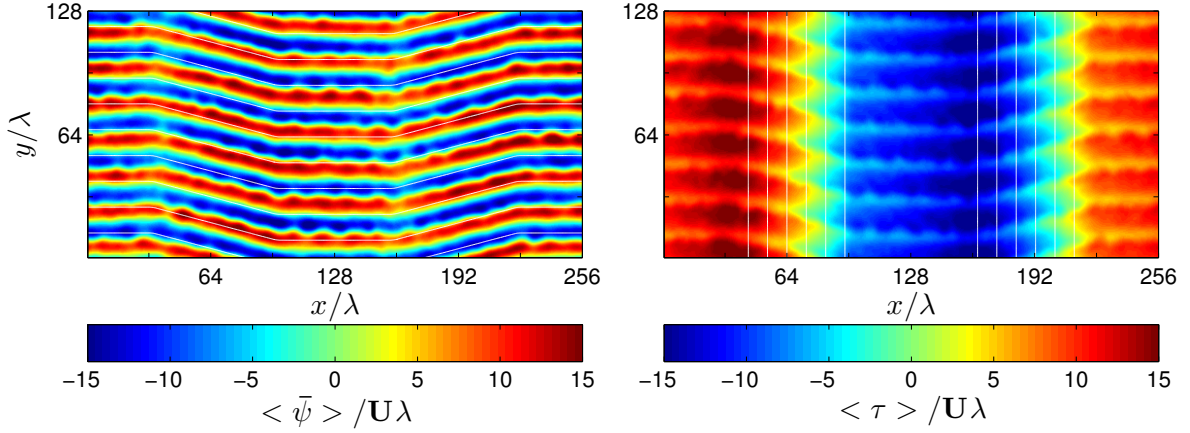


Figure 3.28: Time mean barotropic and baroclinic streamfunctions from a stepped topography simulation with $h_x \lambda^2 / U = \pm 0.4$ slopes, $\beta \lambda^2 / U = 0.75$ and $\kappa \lambda / U = 0.1$. The barotropic field shows jets aligning with the barotropic PV (white contours), and the baroclinic field shows large scale gradient alignment with the topography (white contours).

we would expect exact alignment in a simulation containing no topographic slope. From now on we will refer to ‘partial baroclinic compensation’ as the phenomenon where the baroclinic field has a large scale gradient aligned with the topographic gradient such that the upper layer total PV gradient is close to being aligned with the barotropic PV gradient. Crucially, as the direction of the jets in both layers is determined by the barotropic PV gradient, good baroclinic compensation results in the jets in the upper layer being closely aligned with the upper layer PV gradient.

In order to find a possible explanation for this compensation by the baroclinic streamfunction, we look to the full dimensional system equations in terms of the baroclinic and barotropic perturbation streamfunctions, τ and $\bar{\psi}$ respectively:

$$\begin{aligned} \nabla^2 \bar{\psi}_t + \nabla \bar{\psi} \times \mathbf{G}_{\text{BT}} + \nabla \tau \times \mathbf{G}_{\text{BC}} + U \nabla^2 (\bar{\psi} + \tau)_x - \frac{U}{\lambda^2} \tau_x + \\ J(\bar{\psi}, \nabla^2 \bar{\psi}) + J(\tau, (\nabla^2 - \frac{1}{\lambda^2}) \tau) = -\frac{\kappa}{2} \nabla^2 (\bar{\psi} - \tau), \end{aligned} \quad (3.30)$$

$$\begin{aligned} (\nabla^2 - \frac{1}{\lambda^2}) \tau_t + \nabla \bar{\psi} \times \mathbf{G}_{\text{BC}} + \nabla \tau \times \mathbf{G}_{\text{BT}} + U \nabla^2 (\bar{\psi} + \tau)_x - \frac{U}{\lambda^2} \tau_x + \\ J(\bar{\psi}, (\nabla^2 - \frac{1}{\lambda^2}) \tau) + J(\tau, \nabla^2 \bar{\psi}) = -\frac{\kappa}{2} \nabla^2 (\tau - \bar{\psi}), \end{aligned} \quad (3.31)$$

where $\mathbf{G}_{\text{BT}} = (h_x/2, \beta + h_y/2)$, $\mathbf{G}_{\text{BC}} = (-h_x/2, U/\lambda^2 - h_y/2)$. If we linearise these

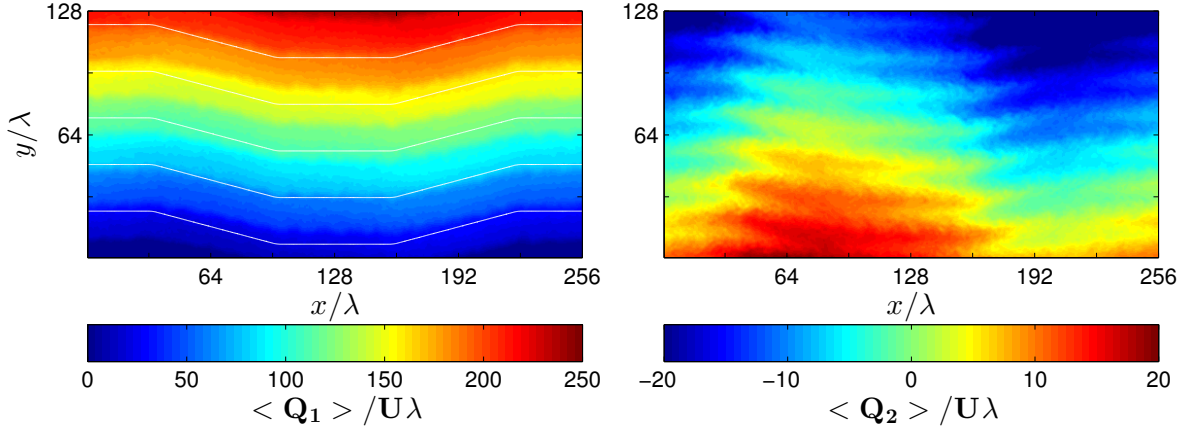


Figure 3.29: Time mean upper and lower layer total PV fields from the stepped topography simulation shown in figure 3.28. The upper layer PV is close to being aligned with the barotropic PV (white contours) due to the contribution from the baroclinic perturbation field.

expressions, we get:

$$\nabla^2 \bar{\psi}_t + \nabla \bar{\psi} \times \mathbf{G}_{\text{BT}} + \nabla \tau \times \mathbf{G}_{\text{BC}} + U \nabla^2 (\bar{\psi} + \tau)_x - \frac{U}{\lambda^2} \tau_x = -\frac{\kappa}{2} \nabla^2 (\bar{\psi} - \tau), \quad (3.32)$$

$$(\nabla^2 - \frac{1}{\lambda^2}) \tau_t + \nabla \bar{\psi} \times \mathbf{G}_{\text{BC}} + \nabla \tau \times \mathbf{G}_{\text{BT}} + U \nabla^2 (\bar{\psi} + \tau)_x - \frac{U}{\lambda^2} \tau_x = -\frac{\kappa}{2} \nabla^2 (\tau - \bar{\psi}). \quad (3.33)$$

Looking for large scale balances, we throw away any ∇^2 terms and keep the $1/\lambda^2$ ones (although strictly this is only valid where these terms appear together), expanding the definition of \mathbf{G}_{BC} we get

$$\nabla \bar{\psi} \times \mathbf{G}_{\text{BT}} - 1/2 \nabla \tau \times \nabla h \approx 0, \quad (3.34)$$

$$-\frac{1}{\lambda^2} \tau_t + \nabla \bar{\psi} \times \mathbf{G}_{\text{BC}} + \nabla \tau \times \mathbf{G}_{\text{BT}} - \frac{U}{\lambda^2} \tau_x \approx 0. \quad (3.35)$$

Note that the form of these expressions depends on the choice of background velocities, i.e. $\mathbf{U}_1 = (2U, 0)$, $\mathbf{U}_2 = (0, 0)$. A similar system with $\mathbf{U}_1 = (U, 0)$, $\mathbf{U}_2 = (-U, 0)$ [not a solution to the system equations] would result in the same shear between the two layers, and the same barotropic PV gradient, but would crucially alter the terms in the system equations relating to the advection of PV gradients by the background velocity, $\mathbf{U}_i \cdot \nabla q_i$ in the layer-wise form.

Interpreting these expressions, (3.34) implies that, if there is no large scale gradient in the barotropic perturbation streamfunction ($\nabla \bar{\psi} \approx 0$), which is what is observed in

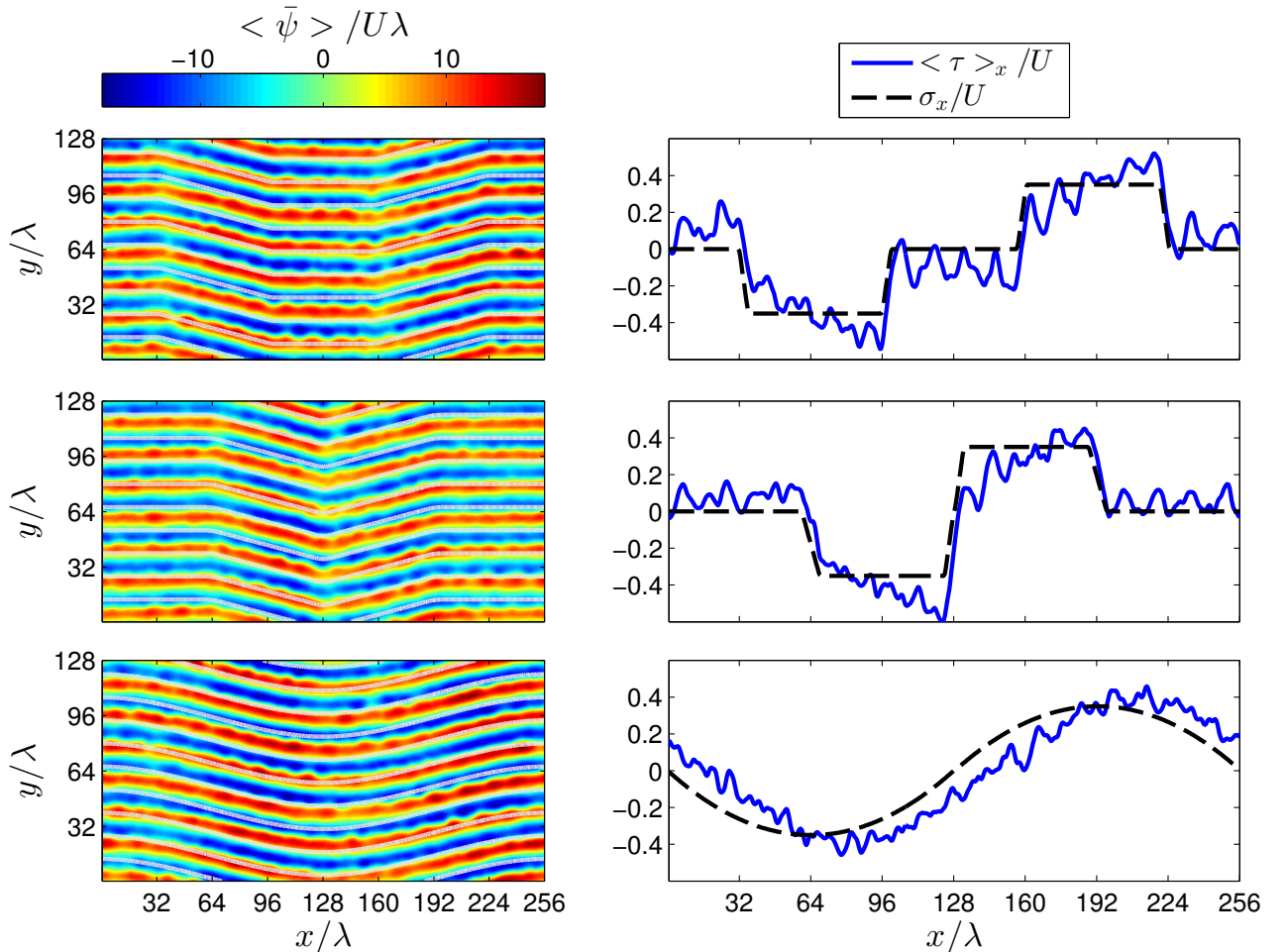


Figure 3.30: Time-mean barotropic streamfunctions (left panels) and time-mean baroclinic streamfunction gradients (right panels) for stepped simulations of size $256\lambda \times 128\lambda$ with various topography. The white contours in the left panels show the barotropic PV, and the black dashed lines in the right panels show the exactly compensating barotropic PV σ_x , defined in (3.39). There is relatively good agreement between τ_x and σ_x for these simulations.

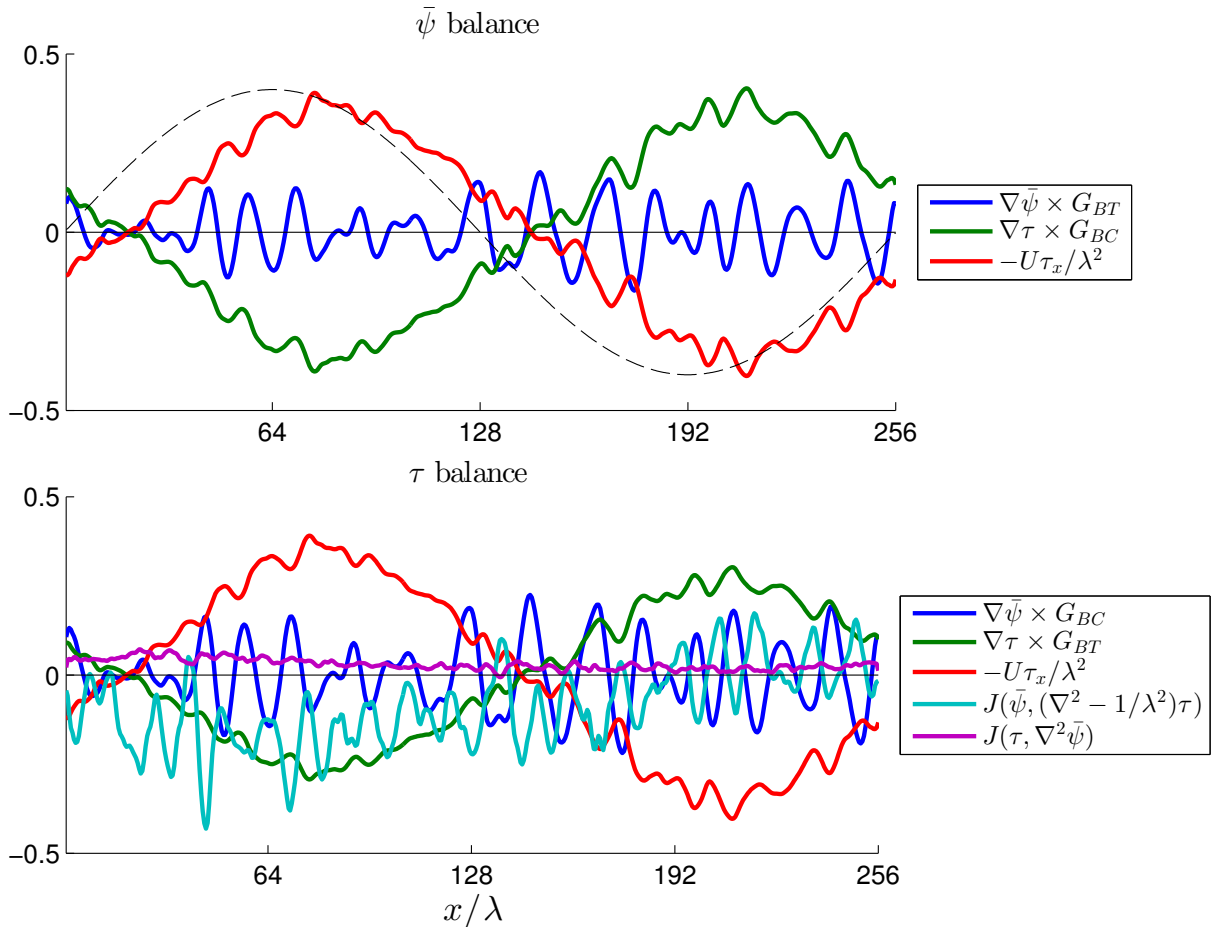


Figure 3.31: Dominant terms in (3.30) (upper panel) and (3.31) (lower panel) from a sinusoidal simulation with $\max|h_x\lambda^2/U| = \pm 0.4$. The black dashed line shows h_x .

the simulations (e.g. figure 3.28), then $\nabla\tau \times \nabla h \approx 0$, i.e. any large scale gradient in the baroclinic perturbation streamfunction ($\nabla\tau$) must either be 0 or aligned with the topography - as is observed in some simulations. If we say $\tau_t = \nabla\bar{\psi} = 0$ at these scales, as observed, then (3.35) becomes:

$$\nabla\tau \times \mathbf{G}_{\text{BT}} - \frac{U}{\lambda^2}\tau_x = (\beta - \frac{U}{\lambda^2})\tau_x + \frac{1}{2}\nabla\tau \times \nabla h \approx 0, \quad (3.36)$$

which is automatically satisfied if $\nabla\tau = 0$, but not necessarily otherwise.

We can test these predictions by directly plotting all the terms in (3.30) and (3.31) - figure 3.31 shows the largest terms after taking time then meridional means of all terms for a sinusoidal topography simulation with $\max|h_x|\lambda^2/U = 0.4$ (black dashed line). In the upper panel, we do find that $\nabla\tau \times \mathbf{G}_{\text{BC}} - U\tau_x/\lambda^2 = -(\nabla\tau \times \nabla h)/2 \approx 0$, and the only other term of comparable magnitude is $\nabla\bar{\psi} \times \mathbf{G}_{\text{BT}}$, as predicted, but it does not have any large wavelength structure. For this simulation, $\beta\lambda^2/U = 0.75$, and so (3.36) predicts that $\nabla\tau \times \mathbf{G}_{\text{BT}}$ and $U\tau_x/\lambda^2$ should almost balance, as is observed in figure 3.31, lower panel. However, there are also non-trivial contributions from the two Jacobian terms and $\nabla\bar{\psi} \times \mathbf{G}_{\text{BC}}$, reflecting the inexact balance. A similar picture is found for other simulations, and those on larger domains, although the large scale terms become more and more out of phase with the topography at higher topographic slopes and in longer domains.

This confirms that the baroclinic compensation is consistent with the large scale linear balance of the system, although the Jacobian terms also play a non-trivial role. Locally, the meridionally integrated balance of terms is maintained, which implies that the drift is a more local effect. However, this does not shed any more light on what determines the length scale of the compensation or the magnitude of jet drift.

For the compensation to be exact, ‘perfect’ baroclinic compensation, the baroclinic field would have to alter the upper layer PV so that the altered upper layer PV was aligned with the barotropic PV, i.e.:

$$\theta'_1|_{\tau_x=\sigma_x} = \theta_{\text{BT}}, \quad (3.37)$$

where θ'_1 is the upper layer PV gradient angle taking into account large scale contributions from the baroclinic streamfunction, τ . (3.37) defines σ as the baroclinic field such that

compensation is exact. Equivalently:

$$\tan^{-1} \left(\frac{-\sigma_x/\lambda^2}{\beta + U/\lambda^2} \right) = \tan^{-1} \left(\frac{h_x}{2\beta} \right), \quad (3.38)$$

$$\Rightarrow \sigma_x/U = -h_x \lambda^2/U \left(\frac{\beta + U/\lambda^2}{2\beta} \right), \quad (3.39)$$

where we have set $h_y = 0$ (as is the case for all topographies in this section). Note that upper layer PV aligned with barotropic PV implies that the lower layer PV is co-aligned.

Partial compensation by the baroclinic field persists across a range of topographic shapes (stepped, triangular and sinusoidal) with the same maximum zonal slope ($\max|h_x| = 0.4$) and same domain size ($256\lambda \times 128\lambda$), see figure 3.30. This figure shows time-mean barotropic perturbation streamfunction fields $\langle \bar{\psi} \rangle$ alongside the gradient in the time-mean baroclinic perturbation streamfunction $\langle \tau \rangle_x$ compared with the perfectly compensating σ_x for three different topographies in a $256\lambda \times 128\lambda$ domain. Also shown in white contours is the background barotropic PV. The barotropic streamfunction shows good alignment with the background barotropic PV, and the baroclinic streamfunction shows large scale compensation, matching the topographic slope. Note again that the compensation is not symmetric, with non-zero σ_x over the flat regions, indicating again that non-local effects are playing a role.

Varying the magnitude of the topographic slope, the domain size, and β changes this behaviour. Figure 3.32 shows the same topographic shapes as figure 3.30, but in a domain sized $512\lambda \times 128\lambda$, twice as long. The same fields are plotted, but note that a snapshot of $\bar{\psi}$ is shown, rather than a time-mean, because these simulations display jet drift, as discussed further in section 3.5.4. This makes the jets harder to see, and indeed there are regions in which there is not a well defined number of jets. However, plotting PV histograms and Hovmöller diagrams (not shown) confirms the presence of jets. It appears that in the $512\lambda \times 128\lambda$ cases, there is not compensation, but large scale variation in τ_x where the topographic slope changes, and this does not always bring τ_x close to σ_x . For the upper two simulations, the regions in which τ_x shows large scale variation have a horizontal length scale of order $\sim 64\lambda$, but this may be a function of the topographic slope magnitude. The case with sinusoidal topography (bottom panels) shows variation in τ_x throughout the domain, whereas the two topographies with constant slope regions show zonally limited regions of large-scale τ_x .

Figure 3.33 shows how the large scale τ_x varies for a variety of sinusoidal simulations with various values of $\beta\lambda^2/U$ and $\max|h_x|\lambda^2/U$, in both $256\lambda \times 128\lambda$ and $512\lambda \times 128\lambda$

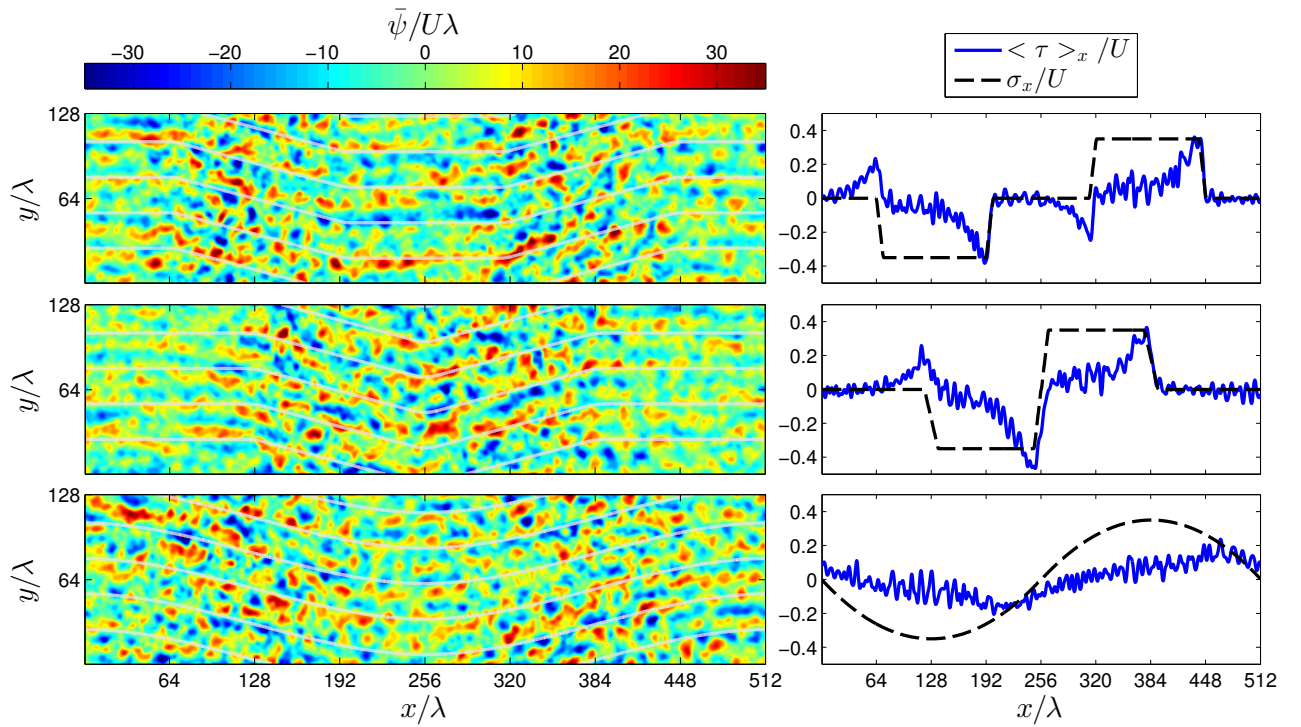


Figure 3.32: Barotropic streamfunction snapshots (left panels) and time-mean baroclinic streamfunction gradients (right panels) for stepped simulations $512\lambda \times 128\lambda$ with various topography. The white contours in the left panels show the barotropic PV, and the black dashed lines in the right panels show the exactly compensating barotropic PV σ_x . There is limited agreement between τ_x and σ_x at for these simulations, which seems to be positioned where there is a change in σ_x for the upper two simulations.

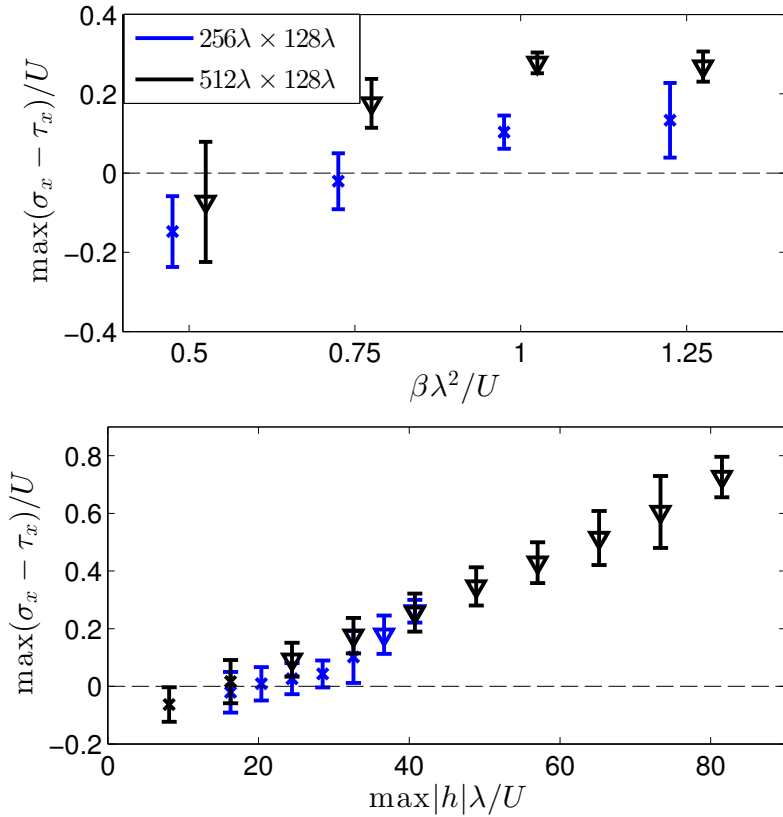


Figure 3.33: The exact compensation value of the baroclinic streamfunction gradient σ_x , minus the measured large scale baroclinic streamfunction gradient τ_x , against $\beta\lambda^2/U$, upper panel [where the two domain sizes have been artificially separated in the x -direction for clarity], and the maximum topographic height, lower panel, for sinusoidal topography. Values are time-mean maxima, with errorbars showing the standard deviation over time. Blue symbols: $256\lambda \times 128\lambda$ domain; black symbols: $512\lambda \times 128\lambda$. Crosses indicate simulations which do not drift, and triangles those that do, see section 3.5.4.

domains. All simulations have $h_y\lambda^2/U = 0$ and $\kappa\lambda/U = 0.1$. We have plotted the difference between the exact compensation value for $\max|h_x|\lambda^2/U$ and the maximum value of the large-scale barotropic PV gradient, $\sigma_x/\lambda^2 - \tau_x/\lambda^2$, against $\beta\lambda^2/U$ and the maximum topographic height. As can be seen, there is a positive relationship between both β and h_x and the goodness of the compensation. Both domain sizes lie on the same curve with respect to $\max|h|\lambda/U$, which suggests this, rather than the magnitude of the slope, is the primary control on the degree of compensation. There also appears to be some over-compensation ($\sigma_x/\lambda^2 - \tau_x/\lambda^2 < 0$) for $\beta\lambda^2/U = 0.5$ in the $256\lambda \times 128\lambda$ domain.

Whilst the upper layer total PV aligns well with the barotropic PV in the shorter domain, shallower sloped simulations, the lower layer PV, however, shows a very different background PV gradient, see figure 3.29. The lower layer PV gradient is also affected by any large scale gradients in the baroclinic field:

$$\tan \theta_2 = \frac{h_x + \tau_x/\lambda^2}{\beta - U/\lambda^2}, \quad (3.40)$$

where θ_2 is the lower layer PV gradient angle. One might expect that, if the upper layer shows partial baroclinic compensation, that the lower layer might too, given that perfect compensation would result in them being co-aligned. To see why this is not the case in the simulations shown, we define any baroclinic field as a combination of the perfect compensation value and the deviation from this value: $\tau = \sigma + \tilde{\tau}$, and insert this into the definitions of θ_1 and θ_2 , using (3.39) to find:

$$\tan \theta_1 = \tan \theta_{\text{BT}} + \frac{\tilde{\tau}_x/U}{\beta\lambda^2/U + 1}, \quad (3.41)$$

$$\tan \theta_2 = \tan \theta_{\text{BT}} + \frac{\tilde{\tau}_x/U}{\beta\lambda^2/U - 1}. \quad (3.42)$$

In all the simulations shown, $\beta\lambda^2/U = 3/4$, and so $|\beta\lambda^2/U + 1| > 1$ and the contribution to θ_1 by the deviations $\tilde{\tau}_x$ is relatively reduced. However, $|\beta\lambda^2/U - 1| < 1$ and so the contribution to θ_2 by the deviations $\tilde{\tau}_x$ is amplified and in fact, for all the simulations shown, dominates over the first term, the barotropic PV gradient. Thus, even in the simulations with relatively good partial compensation, the jets in the lower layer are still crossing their local PV contours, although the lack of PV conservation in this layer due to the presence of bottom friction perhaps explains why this does not result in jet drift in these cases.

The baroclinic compensation also manifests itself as a large scale meridional flow

in both layers, see figure 3.23. In the simulation shown, these large scale meridional background velocities bring the overall background flow in the upper layer [including the prescribed upper layer flow of $\mathbf{U}_1 = (2U, 0)$] into alignment with the barotropic PV contours where the velocity v is maximum. Thus, baroclinic compensation not only results in an upper layer PV gradient almost aligned with the barotropic PV gradient, but also a large scale flow fairly well aligned with the barotropic PV contours. Given that we have seen that the upper layer jets are also closely aligned with the barotropic PV contours, the upper layer dynamics over the sloped regions become simplified - the large scale flow, large scale PV gradient and jets are all co-aligned, to the extent that the baroclinic compensation is exact. This means that, over the sloped regions, the upper layer resembles a rotated form of the upper layer of a zonal, β plane flow, and, given that the local flux balances are maintained, could presumably be represented by a cell of a similarly forced doubly periodic simulation.

However, the lower layer has no prescribed background flow [$\mathbf{U}_2 = (0, 0)$], and so the lower layer large scale flow is determined by the meridional velocity profile in figure 3.23. In this layer, the PV gradient (which is not aligned with the barotropic PV gradient, see figure 3.29), jets (aligned with the barotropic PV contours) and background flow are all un-aligned. Even if the baroclinic compensation was perfect (i.e. $\tau_x = \sigma_x$ everywhere), the jets and local PV contours would become aligned, but the background flow would still be un-aligned. Thus, the lower layer over the sloped regions does not resemble any dynamically consistent doubly periodic flow - the only background flows which are solutions to the system equations are those aligned with the background PV contours or no flow, see discussion in section 3.2.1. Thus no dynamically consistent *two layer* representation can be made of the sloped regions in simulations where the baroclinic compensation occurs. This is likely an indication that these regions are subject to non-local effects, and thus cannot be treated locally as being far from inhomogeneities in the bottom topography, i.e. the flow is altered downstream of the topography.

3.5.4 Jet Drift

As mentioned previously, some of the simulations with more complicated topography exhibit jet drift, similarly to the constant slope simulations presented in section 3.3. The simulations where there is good large-scale compensation by the baroclinic streamfunction, such as that seen in figures 3.28 and 3.29, do not show drift. This can be seen in figure 3.33, where the triangle markers indicate simulations that drift, and the crosses

those that do not. In both sizes of domain shown, there appears to be a correlation between simulations with good baroclinic compensation (i.e. small $\sigma_x - \tau_x$) and those that do not drift. This is postulated to be because the large scale gradient introduced by τ results in an upper layer PV gradient aligned with the barotropic PV gradient (c.f. figure 3.29 left panel and figure 3.24 upper panel), and so the upper layer jets are aligned with the upper layer PV contours. However, systems such as those shown in figure 3.32 do not have good compensation by τ , and so, due to the requirement of upper layer PV conservation, the jets translate across the domain.

Unlike previously, because the topographic slope changes sign and magnitude throughout the domain, so the drift also changes sign and magnitude throughout the domain. To calculate the drift, as previously we take Radon transforms of high time-resolution Hovmöller diagrams at a given x -coordinate. We then take the drift as the mean of the angle of the 10 largest magnitude responses in the Radon transform, and its error as the standard deviation of the same. Figure 3.34 shows calculated drifts for three $512\lambda \times 128\lambda$ simulations with stepped, triangular and sinusoidal topography, top to bottom. The topographic slopes h_x are also shown, and we do not plot any drifts where the non-dimensional error > 0.1 . The drift appears out of phase with the topography, such that the drift the would be expected to compensate for a given slope is found upstream of that slope. A positive value of h_x would be compensated for by negative v_{drift} , as seen in section 3.3 - and negative v_{drift} is seen upstream of positive h_x in all three simulations. In fact, the form of the drift seems to resemble the form of the topography, rather than the topographic slope.

For the simulations in figure 3.34, the non-dimensional drift v_{drift}/U is of similar magnitude as the non-dimensional topographic slope $h_x\lambda^2/U$, however this is not observed for other simulations. Figure 3.35 shows the maximum absolute drift for various sinusoidal simulations with varying values of $\beta\lambda^2/U$ and $\max|h_x|\lambda^2/U$. The maximum drift was calculated by taking the mean of the 10 most frequent drift values from those calculated at every x grid point as in figure 3.34, again excluding those with a non-dimensional error > 0.1 . The error on these points is estimated from the error of the drift at the x grid point used. Another indication of the error is the value calculated applying the same technique to a simulation which doesn't drift - as is plotted in figure 3.35 for a $256\lambda \times 128\lambda$ simulation with $\max|h_x|\lambda^2/U = 0.8$. The upper panel shows the dependence of the drift on $\beta\lambda^2/U$ - there is no clear relationship, but perhaps a decrease in drift with increasing $\beta\lambda^2/U$. The lower panel shows that the maximum drift is fairly constant for the $512\lambda \times 128\lambda$ simulations that drift. Only two $256\lambda \times 128\lambda$ simulations that drift are shown, so no

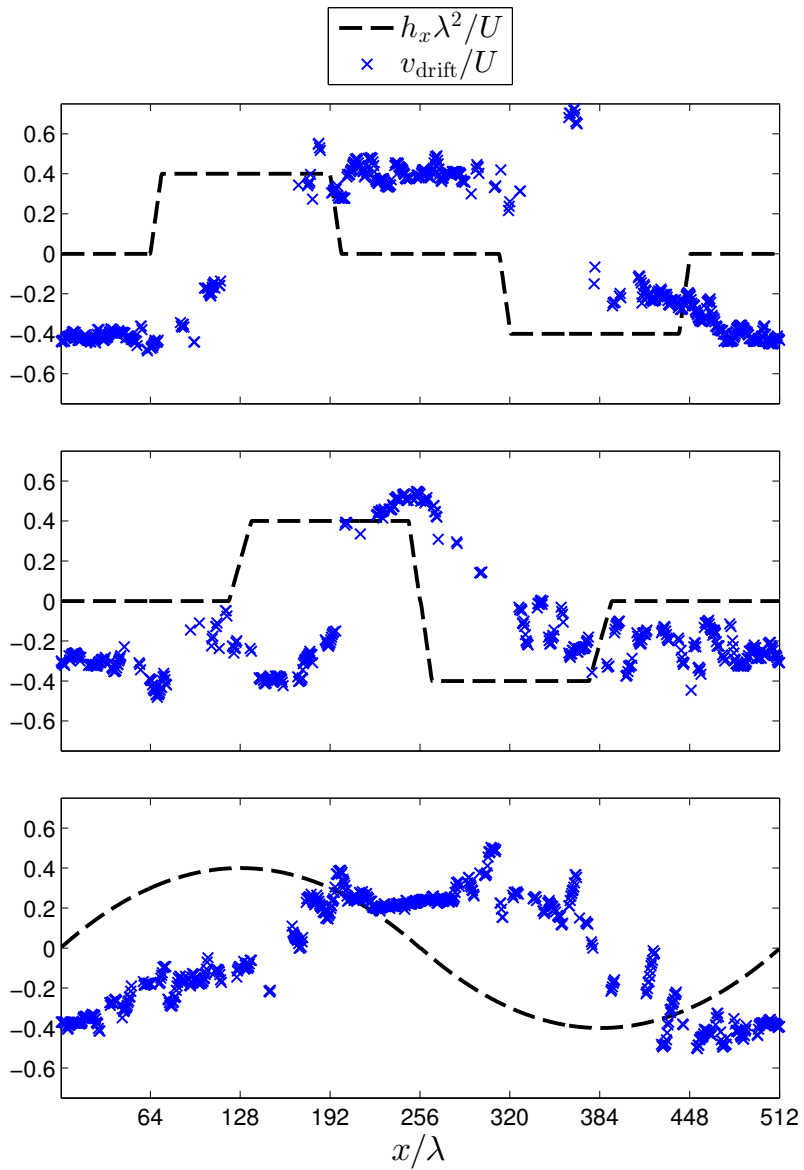


Figure 3.34: Observed jet drift (blue crosses) in various $512\lambda \times 128\lambda$ simulations with topographic slopes h_x (dashed black lines). At each x grid point, the drift is calculated from the Radon transform of a Hovmöller diagram (such as figure 3.11). Drift points with an estimated (non-dimensional) error > 0.1 are omitted.

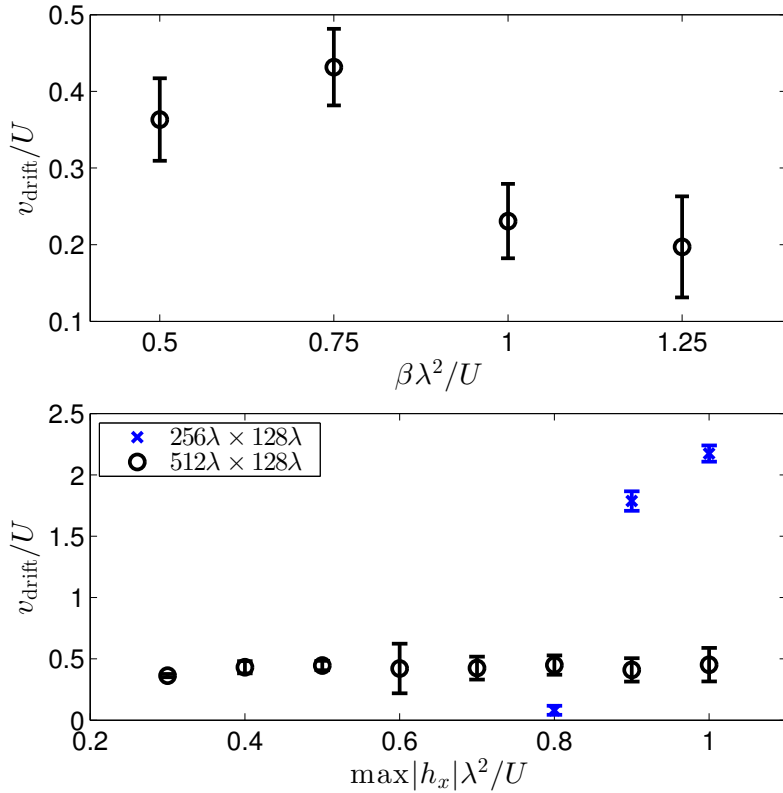


Figure 3.35: Maximum absolute jet drift for various sinusoidal topographies in $512\lambda \times 128\lambda$ (black circles) and $256\lambda \times 128\lambda$ (blue crosses) domains. See text for details of calculation from Radon transforms. There appears to be little dependence on $\max h_x \lambda^2 / U$, and less drift with increasing $\beta \lambda^2 / U$. The $256\lambda \times 128\lambda$ simulation with $\max h_x \lambda^2 / U = 0.8$ does not drift, but the calculation has been included for comparison. Note the different scales on the y -axis.

relationship can be inferred, but the drift is an order of magnitude higher than the longer domain simulations.

If the drift is caused by a mismatch between the jet direction (determined by the orientation of the background barotropic PV gradient) and the orientation of the background upper layer PV gradient (fixed in the meridional direction), then we might expect the drift velocity to depend on the angle of the barotropic PV gradient, which determines the extent of the mismatch, the strength of the upper layer PV gradient, which determines the PV gained/lost by fluid particles advected across it, and the velocity scale of the jets, ditto. However, figure 3.35 shows no clear dependence on $h_x \lambda^2 / U$, which determines the orientation of the background barotropic PV gradient. We leave further investigation of this phenomenon to future work.

3.5.5 Summary

It has been shown that the tilting of jets across local layer-wise PV contours due to slopes in non-zonal topography is persistent in the presence of zonally variable bottom slopes (e.g. sinusoidal or stepped topography). These jets are again shown to align perpendicular to the local barotropic PV gradient, ϕ_{BT} , as previously. However, the closeness of ϕ_{jet} to ϕ_{BT} is affected by the magnitudes of the zonal slopes in topography and the fraction of the domain containing these slopes. This implies that ability of the jets to adjust to the local barotropic PV gradient is impaired by large changes in h_x and by the zonal extents of these slopes.

We have briefly described the presence of large scale baroclinic compensation in many simulations. This manifests as a large scale gradient in the baroclinic streamfunction which, for a number of simulations, results in an upper layer PV field and background flow closely aligned with the barotropic background PV field. The closeness of the compensation is seen to be proportional both to $\beta \lambda^2 / U$ and $\max |h| \lambda / U$. We also observe that the maximum length of any compensation is of order $\sim 64\lambda$ for constant slopes of $h_x \lambda^2 / U = \pm 0.4$ in $512\lambda \times 128\lambda$ domains. We briefly investigated the linear properties of the barotropic and baroclinic streamfunctions, and found that the compensation is consistent with the large scale linear balance of the system. Nonetheless, nonlinear terms also play a non-trivial role in the balance locally, showing that eddy-eddy interactions are important to local properties. We have not investigated the compensation fully and leave further investigation to a future study.

The simulations that exhibit baroclinic compensation, therefore, are *not* locally like

the doubly periodic slope simulations investigated previously, in which there was no large scale gradient in the baroclinic field. Crucially the upper layer jets are perpendicular to the upper layer PV gradient, rather than crossing PV contours as previously. Additionally, there is a large scale background meridional velocity over the slopes, aligning the upper layer background flow with the upper layer PV contours - making it a rotated version of a single layer β plane simulation with no zonal topographic slope. However, the lower layer has no consistent representation as there is also a non-zero meridional flow in this layer. As such, there is no dynamically consistent two-layer representation of the sloped region, as the only dynamically consistent background flow solution would be no flow in the lower layer, given that the lower layer PV gradient is not aligned with the upper layer PV gradient.

We have briefly presented the drift exhibited by a number of simulations. There appears to be a correlation between good baroclinic compensation and non-drifting jets, which supports our previous conjecture (see section 3.3) that the drift is a manifestation of PV conservation: if the upper layer jets are not aligned with the upper layer PV contours, then the drift counteracts the gain of PV that fluid parcels would otherwise experience. Again, we have not fully explored what sets the magnitude of the drift, or what determines the spatial pattern of drift across the domain.

Such simulations without good baroclinic compensation are closer to the doubly periodic slope simulations investigated previously - the jets in both layers are not aligned with their local PV contours and drift. In particular the larger domain simulations show only localised large-scale variations in the baroclinic streamfunction, and so the regions where the large-scale variation is not present do indeed resemble the doubly periodic slope simulations, and could presumably be represented by a dynamically consistent doubly periodic cell.

The implications of the baroclinic compensation and drift observed are that zonally variable topography is capable of producing jets with a wide variety of properties - stationary coherent jets or quickly drifting structures - dependent on the amplitude of the topographic slopes, the amplitude of the topography, its zonal extent, the planetary vorticity gradient, and the background flow.

In summary, what might appear to be a simple extension to the previous study, the inclusion of zonally varying zonal topographic slopes, has introduced a wide range of interesting dynamical effects. We have not been able to fully investigate these, but have outlined the behaviour observed, and leave a thorough investigation to a future study. Additionally, the assumption that the doubly periodic slope simulations of the

previous sections in this chapter are representative of the sloped regions in more general topographies has been shown to hold in some regions of the larger domain simulations, and the smaller domain simulations show interesting dynamical behaviour that could not be represented in a doubly periodic slope simulation.

3.6 Conclusions

In chapter 2 we focused on theoretical explanations for jet formation in the baroclinic system investigated in this study. In particular, we explored the extent to which linear Rossby wave theory could apply, and found this could explain the barotropic control exhibited here. The anisotropy of the Rossby wave dispersion relations determines the preferred direction of the jets.

In this chapter, we investigated the jets that result from the introduction of arbitrarily orientated linear slopes in bottom topography to simple barotropic and baroclinic quasigeostrophic models. The resulting structures have been analysed for their transport properties and the production of energy. The most significant finding is that the formation of coherent jets, familiar from many studies without topography and also with topographic slope in the meridional direction, persists under the addition of a topographic slope in the zonal direction. The corresponding jets tilt relative to the zonal direction and cross layer-wise PV gradients, with significant implications for transport of layer-wise PV. Investigation of length and velocity scales show that the tilted jets followed Rhines scaling in both the one- and two-layer cases, although different velocity scales were used in each case, see section 3.3.2.

In the two-layer case, jets follow the barotropic PV gradient, the mean of the two layer PV gradients. Analysis of the total barotropic PV through histograms confirmed that the jets formed were barriers to barotropic PV, although mixing layer-wise PV. This motivates the interpretation of the two-layer case as a single barotropic field driven by the baroclinic instability generated by the shear between the two layers.

This has interesting implications for mixing in that it implies that in regions with large-scale bottom topography, it is possible that the jet direction and layer-wise PV gradients decouple. That is, the alignment and so mixing properties of jets near the surface are determined by the direction of the barotropic PV gradient. Of course, the model presented is a highly idealised system, however it is its very simplicity that provides further scope for testing these ideas.

Analysis of the eddy energy production, ε , in the two-layer case shows an increase in ε with decreasing angle between the background PV gradient, \mathbf{G}_{BT} , and the zonal direction. This implies a maximum of eddy energy production when the barotropic PV gradient, \mathbf{G}_{BT} is aligned with the shear, \mathbf{S} , and a minimum when \mathbf{G}_{BT} is at right angles with \mathbf{S} , see figure 3.1. These findings are consistent with those of Smith (2007), who finds large values of ε with \mathbf{G}_{BT} and \mathbf{S} aligned, and Arbic and Flierl (2004b), who find

a maximum in ε with \mathbf{G}_{BT} and \mathbf{S} anti-aligned and a minimum with \mathbf{G}_{BT} and \mathbf{S} at right angles. This implies that the shearing of the PV gradients by the un-aligned background velocity is responsible for producing the extremely energetic eddies, as described in [Smith \(2007\)](#). The fact that the same order of magnitude increase is not seen in the barotropic simulations is due to the absence of shear.

The increase in energy with θ_{BT} , whilst moderate in the one-layer case, was over several orders of magnitude in the two-layer case. So whilst we may interpret the two-layer case in terms of forced single-layer dynamics, it is clear that representing the baroclinic processes (which provide the small-scale forcing in the single-layer interpretation) is essential to capture the full behaviour of the system.

Observations that the tilted jet simulations exhibited ‘jet drift’ led to the hypothesis that between-jet particles in well-mixed regions are constantly transported up/down the layer-wise PV gradients in both the one- and two-layer simulations, and thus gain/lose PV. This necessitates the jet drift that counteracts this gain/loss in order for the system to reach statistical equilibrium. This finding highlights the importance of PV conservation, and in more realistic flow regimes, generation of relative vorticity as well as jet displacement may act to generate jet variability.

A comparison of the transport properties of zonal and non-zonal jets in the two-layer model was undertaken using an effective diffusivity diagnostic. A comparison of across-jet transport showed that jets that cross layer-wise PV gradients are weaker barriers to transport than zonal jets, which do not. This can also be thought of similarly to the simulations of [Smith \(2007\)](#), which show that meridional jets (extreme versions of our tilted jets) are subject to dispersion of the non-zonal shear (equivalent to our tilted barotropic PV gradient) by the beta effect, increasing cross-flow mixing. However, note that here we have set up a mechanism for shear dispersion that is internally consistent as our driving background shear is a solution to the quasi-geostrophic equations.

Varying the relative layer depths in the system showed that the barotropic control persists, with the barotropic PV gradient not depending on layer depth. This is expected, as the results of chapter 2 are not altered by the addition of the layer-depth scale factors, as the relevant modes are also altered by changing layer-depths. Thus, as the definition of the barotropic PV gradient remains unchanged, its central role in determining the anisotropy of the kinetic energy spectra and so the direction of the jets is not altered. Studies such as [Tulloch et al. \(2011\)](#) which calculate local PV gradients in the Southern Ocean show that the equivalent layer depths may be in the region $\delta \approx 0.5\text{--}2$, and so the effects noted here could be realised in the Southern Ocean.

Topographies made up of zonally varying slopes (e.g. stepped and sinusoidal topographies), were briefly investigated. Jet formation persisted, and the jets conformed to the local barotropic PV gradient in each part of the domain, tilting over the sloped regions. However, there was variation in the degree of conformation, affected by the magnitude of the slope and the relative portion of the domain that was sloped. Simulations in smaller domains and with lower magnitude PV gradients exhibited large scale structure in the baroclinic streamfunction, which ‘compensates’ the upper layer PV such that the large scale gradient aligns with the background barotropic PV, and so with the jets. In these cases no drift was observed. In other simulations, where the baroclinic compensation was not as good, the jets drifted, dependent on the magnitude of $\beta\lambda^2/U$ and the domain size but not on $\max|h_x|\lambda^2/U$. The drift varied in sign and magnitude across the domain, appearing out of phase in the upstream direction with the topography. This confirmed the hypothesis stated above, that conservation of upper layer PV requires the translation of the jets if the background upper layer PV is not aligned with the background barotropic PV contours. There remains further work to be done in this area to determine what controls the magnitude of the baroclinic compensation and jet drift.

The simulations with good baroclinic compensation resulted in systems not locally similar to cells of doubly periodic simulations - whilst the upper layer background flow, jets and large scale PV contours are aligned, the lower layer shows un-aligned jets, PV contours and, crucially, background flow, meaning a dynamically doubly periodic simulation with the same local properties is not possible. Conversely, the systems with poor baroclinic compensation, which exhibited jet drift, are locally similar to the doubly periodic cells - non-zonal drifting jets crossing layer-wise PV gradients and zonal background flow. Poor compensation is associated with large amplitude topography, and larger domains only exhibit local compensation, and so this suggests that the assumption that the sloped regions are locally similar to cells of doubly periodic simulations is valid when the topography is relatively long or high.

The model presented adds to the work of those such as [Thompson \(2010\)](#), [Wolff et al. \(1991\)](#) and [Witter and Chelton \(1998\)](#) in furthering the understanding of topography feedback within simplified models. These models have proved to be useful guides to understanding dynamics in more complex and realistic circulation models, for instance in the Southern Ocean. Our study points to the role topography may play in allowing a mean flow to develop that is not orthogonal to (layer-wise) mean, or background, PV gradients, which may be of importance in the ocean. However, as this study considers a broad and uniform slope, we would not seek to apply these conclusions directly to any

specific part of the ocean. In particular, the quasi-geostrophic assumption requires that variations in the topography are small compared to the layer depths, which limits the magnitude of slopes that can be realistically represented by this model. Alignment of the jets along the barotropic PV contours may be sensitive to the strength of the topographic slope and the layer thicknesses. As it is well known that QG often provides reasonable results well outside of formal QG scalings, we have briefly explored simulations with values of h_x and h_y one and two orders of magnitude larger than the simulations discussed here. Overall the simulations produce similar results, in particular the jet alignment continues to be controlled by the barotropic PV gradient, $h_x/(2\beta + h_y)$. We note here that in this case the topographic slope dominates over the PV gradient contributions from both β and the mean vertical shear, such that the lower layer PV gradient is much greater in the upper layer and so the lower layer jets are much stronger than those in the upper layer, and the barotropic PV gradient is very close to the lower layer PV gradient. It would be useful to explore this steep topography regime further in a primitive equation framework.

There are also many possible ways to develop the current models to make them more relevant to localised topographical regions in the Southern Ocean. We would be interested to discover if the barotropic behaviour held in multiple-layer systems with more realistic stratifications and topographies. We also plan to motivate any further development of the model through a combination of modelling and data analysis of topographically complex regions of the Southern Ocean.

Chapter 4

Effective Diffusivity in the Southern Ocean

4.1 Introduction

The work presented in chapters 3 and 2 demonstrates the wide range of interesting dynamic behaviour present in a simple model containing jets and eddies. The advantage of such models is the ability to carry out multiple, varied calculations on the system at minimal computational cost. Whilst they will never fully reproduce the behaviour of the real ocean, they can provide insights into processes that can lead to a greater understanding of the observed dynamics. However, as discussed in chapter 1, there is still a lack of quantitative understanding of some of the basic dynamical properties of the Southern Ocean. In particular, quantifying the eddy diffusivity (representing mixing and stirring by meso-scale eddies), and how it varies spatially and temporally is a major open question.

The principle set out in Prandtl (1925), that eddy diffusivity in turbulent flows may be parametrised as $\kappa_e \propto VL_{\text{mix}}$, where V is an eddy velocity, has lead many studies to seek to define a mixing length L_{mix} from measured properties. The work of Holloway (1986), Keffer and Holloway (1988), and Stammer (1998) developed a parameterisation for L_{mix} based on r.m.s. variations in SSH, see section 4.4, which found peak κ_e along the ACC in the Southern Ocean. On the other hand, the strong zonal mean flow in the Southern Ocean is thought to suppress mixing, as eddies propagate much slower than the mean flow, and so their effective mixing length is shortened. The mixing length parameterisation was updated by Ferrari and Nikurashin (2010), and then developed further in Klocker et al. (2012), to take account of these mean flow effects. However,

there still remain unknown parameters that have to be deduced by comparison against other estimates, and thus the results are ‘tuned’ to a certain extent.

Other studies have parametrised eddy diffusivity in terms of eddy kinetic energy [EKE] (Eden and Greatbatch, 2008), and the results of Sallée et al. (2008), based on float and drifter data, also find dependence on EKE for high EKE regions. Several other studies have also used Lagrangian in-situ measurements to infer eddy diffusivities, see a recent review in LaCasce (2008). The advantage of the latter measurements is that Lagrangian properties are more directly relevant to the mixing experienced by fluid particles, and the observations are in-situ rather than remote, however it is unclear how to compare these measurements to Eulerian model diffusivities, and the method is limited by the spatial and temporal coverage of the data.

In this chapter we present the results of an effective diffusivity calculation, utilising surface velocity fields derived from satellite altimetry. We used a data set of weekly sea level anomaly from January 1993 to December 2010, in combination with the current mean sea surface height, the details of which are discussed in more detail in section 4.2. For all calculations, we advected the tracer using the MIT global circulation model (Adcroft et al., 2004) in offline mode, having first interpolated the velocity fields onto finer grids and rendered them non-divergent.

The effective diffusivity estimate was based on the advection of a tracer field covering the entire Southern Ocean. This work sought to update the results of Shuckburgh et al. (2009a) using new generation satellite data that has a longer spatial duration and has been reprocessed since that study. We first quantify the differences between the old and new generation satellite data, and discuss alternative mean-anomaly decompositions of the sea surface height field in section 4.2.

The effective diffusivity used, κ_{eff} , was the same as that used in chapter 2, which was that based on the diffusivity first developed by Nakamura (1996), and first used in the ocean by Marshall et al. (2006). Since then, Shuckburgh et al. (2009a) have looked at the temporal variability of the eddy diffusivity in the Southern Ocean, also using altimetry, finding enhanced diffusivity equator-ward of the ACC core. Abernathay et al. (2010) use data from the SOSE model to calculate κ_{eff} on neutral density surfaces, which reveal a sub-surface maxima in mixing. The advantage of the effective diffusivity is that it does not require the tuning of any parameters, and uses the flow itself to diagnose the diffusivity. The disadvantage is that the calculation produces a streamwise averaged quantity by definition, and so zonal variations in mixing will be smeared out, investigated in Shuckburgh et al. (2009b) where the calculation on longitudinal

sections is compared to the full Southern Ocean calculation to diagnose local effects. After describing the calculation of the effective diffusivity in detail, we analyse the spatial and temporal variability of our results in section 4.3, and compare it with the previous estimates mentioned.

The eddy diffusivity parametrisations in Ferrari and Nikurashin (2010) and Klocker et al. (2012) relied on effective diffusivity calculations based on the old generation altimetry to define tuning parameters. Both studies had success in matching the form of their diffusivities, which crucially contain mean flow suppression effects, to the effective diffusivity, albeit under assumptions of stationary mean flows. Thus, in section 4.4, we test if the parameters found in Ferrari and Nikurashin (2010) hold for our effective diffusivity under less stringent assumptions, and attempt to fit a similar expression.

4.2 Altimetric Data

Satellite altimetry works by measuring round trip times for radar pulses. If the satellite knows its own location accurately, this determines the height of the sea surface relative to an arbitrary reference ellipsoid, known as the sea level anomaly (SLA). A mean sea surface height relative to the ellipsoid can be determined from long term measurements, known as the mean dynamic topography (MDT), which combines with the SLA to give the total sea surface height (SSH) or absolute dynamic topography (ADT). Via geostrophic balance, this gives an approximation of ocean surface currents. However, there was not sufficient spatial and temporal resolution to adequately observe the meso-scale eddy field until the Topex/Poseidon satellite launched in 1992, alongside the previously launched ERS-1 (European Remote Sensing satellite). Since then, the use of multiple satellites has allowed for the production of a dataset suitable for offline mesoscale calculations. Throughout this chapter, we used delayed time altimeter products produced by Ssalto/Duacs, which have been post-processed and passed through quality control measures¹. In particular, we used a data set of weekly SLA merged from two satellites for continuity², on a $1/4^\circ$ by $1/4^\circ$ Cartesian grid, from January 1993 to December 2010, in combination with the current MDT based on 1993-1996 SLA.

4.2.1 Comparison with previous generation altimetry

The investigations of Shuckburgh et al. (2009a) and Shuckburgh et al. (2009b) used merged satellite altimetry from the Topex/Poseidon and ERS-1 satellites, produced at 10 day intervals from January 1996 to December 2000 on $1/4^\circ$ by $1/4^\circ$ grid, as described in detail in the appendix of Marshall et al. (2006). The MDT field was produced from the same data averaged from January 1996 to January 2000. In 2010, the Ssalto/Duacs project released a reprocessed set of delayed time merged satellite data intended for time series analysis. This reprocessing included “new mean profiles computed in coherency with the new standards and algorithms” and “complete re-computation of the empirical cross-calibration and homogenisation processes”, and in particular increased the temporal resolution to every 7 days, see the Aviso website for further details. It also brought the time series up-to-date with the use of the Jason and Envisat satellites from 1997 onwards, such that the delayed time series used in this work extends to the end of 2010 due to

¹Distributed by Aviso, with support from Cnes, [see here for more details](#).

²Topex/Poseidon only contributes from 23 December 1993 to 10 April 1994, otherwise see Aviso for details of the two satellites used.

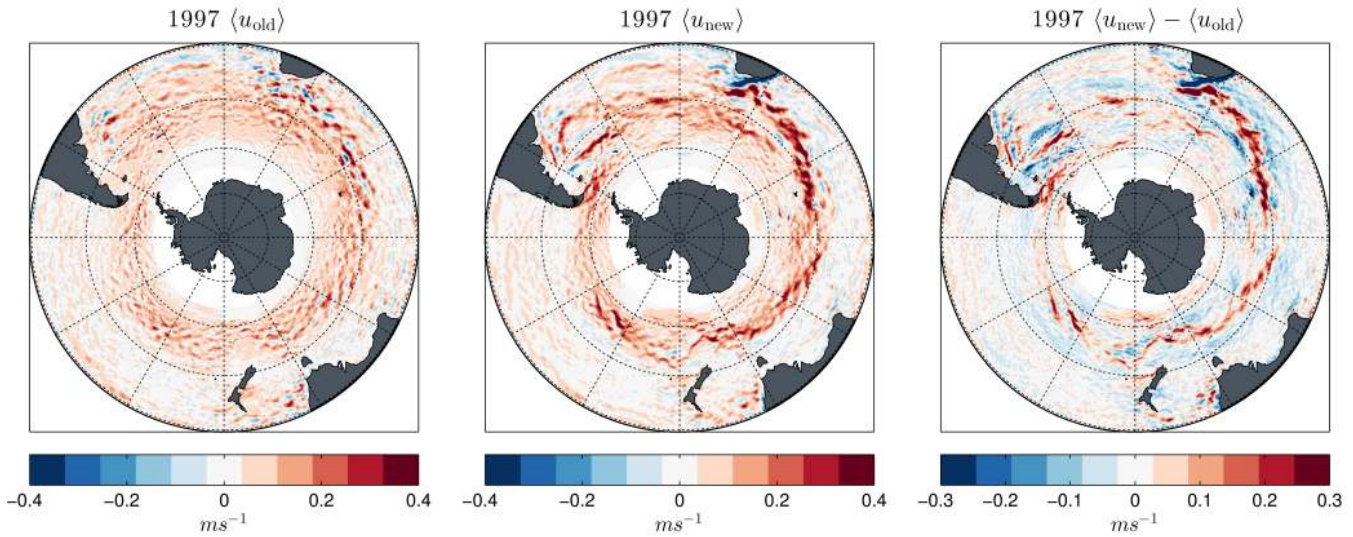


Figure 4.1: Comparison of altimetric data sets - 1997 mean of zonal velocities in old and new data sets, as well as the difference between the two. The new data set shows higher eastward velocities in the highly energetic parts of the ocean - western boundary currents and the ACC.

subsequent data released.

Figures 4.1 and 4.2 show Southern Ocean comparisons between the ‘old’ dataset, used in Shuckburgh et al. (2009a) and Shuckburgh et al. (2009b), and the ‘new’ dataset, used in this work. As the datasets are at different temporal resolutions, we compare the time mean fields for 1997 - over 37 snapshots spaced every 10 days for the old dataset, and over 53 snapshots spaced every 7 days for the new dataset. Figure 4.1 shows the 1997 mean zonal velocity $\langle u \rangle$ for the old dataset, the new dataset, and the difference between the two, and figure 4.2 shows the same for the meridional velocity.

There are large differences in both fields in the Agulhas current region off the east coast of Africa and the Brazil current region off the east coast of South America - these are due to large, coherent velocity structures present in the new dataset not seen in the old. In figure 4.1 we see a large eastward velocity increase throughout the core of the ACC, and a slight decrease either side, relative to the old dataset. This is confirmed if we compare probability density functions (PDFs) of $\langle u \rangle$ for the old and new datasets, see figure 4.3, upper panel. Large eastward magnitudes are more frequent in the new dataset, but the values peak at low values, slightly westward of the old data - a most common value of 0.8 cm s^{-1} instead of 3.1 cm s^{-1} . I.e. at low values the new dataset is slightly more westward, but at high values more eastward, leading to no overall change

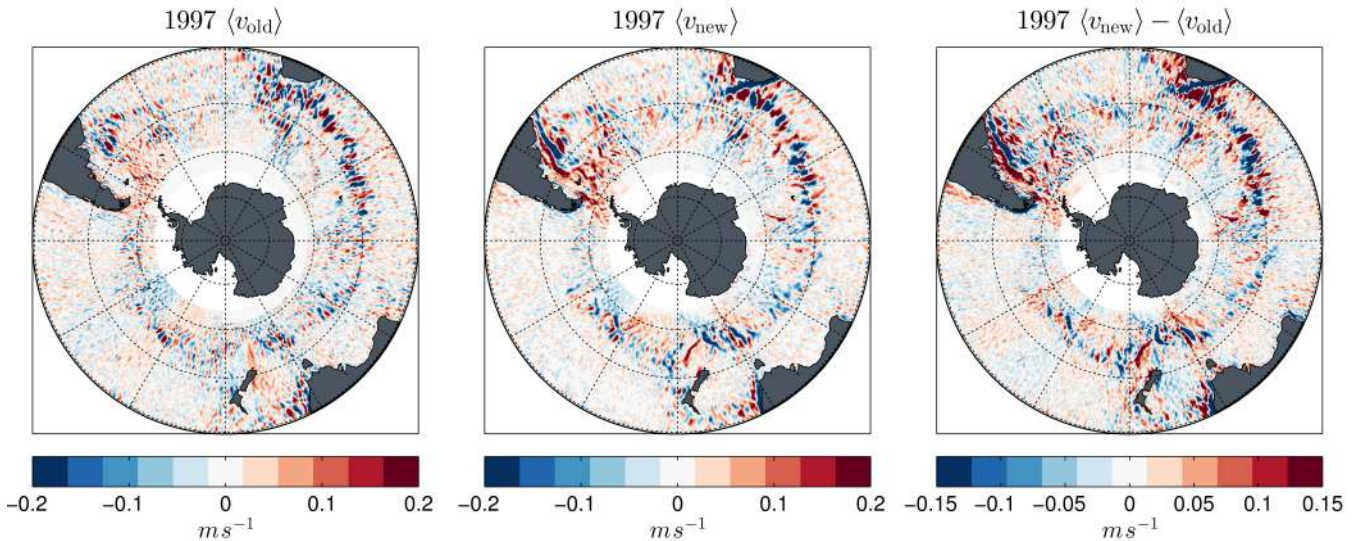


Figure 4.2: Comparison of altimetric data sets - 1997 mean of meridional velocities in old and new data sets, as well as the difference between the two. The new data set shows higher velocity magnitudes in the highly energetic parts of the ocean - western boundary currents and the ACC.

in the mean zonal velocity of 4.6 cm s^{-1} . In figure 4.2 we see the meridional velocity differences are largest in the western boundary currents and throughout the ACC, where the meridional velocities in both datasets are largest. The new dataset appears to have lower magnitudes outside of the ACC. The PDFs of these fields (see figure 4.3, lower panel) show that both data sets have a similar frequency of large velocities, but that the new dataset shows a sharper peak at low velocities - showing significantly more frequent small values and less intermediate values.

The largest differences in the PDFs are at small velocities - suggesting that the new dataset is better resolving smaller SSH gradients. The spatial pattern of the differences shows the largest magnitude differences are in regions of high eddy activity, which suggests the new dataset is representing eddy structures more accurately.

4.2.2 Mean-anomaly decompositions

We have compared two methods of decomposing the full SSH into mean and anomaly contributions, one using the AVISO MDT and SLA fields to define \bar{h} and h' , and the other using a time-filtering method to decompose the same field. The form of decomposition is an important choice - it defines what is identified as an eddy and what is not, and

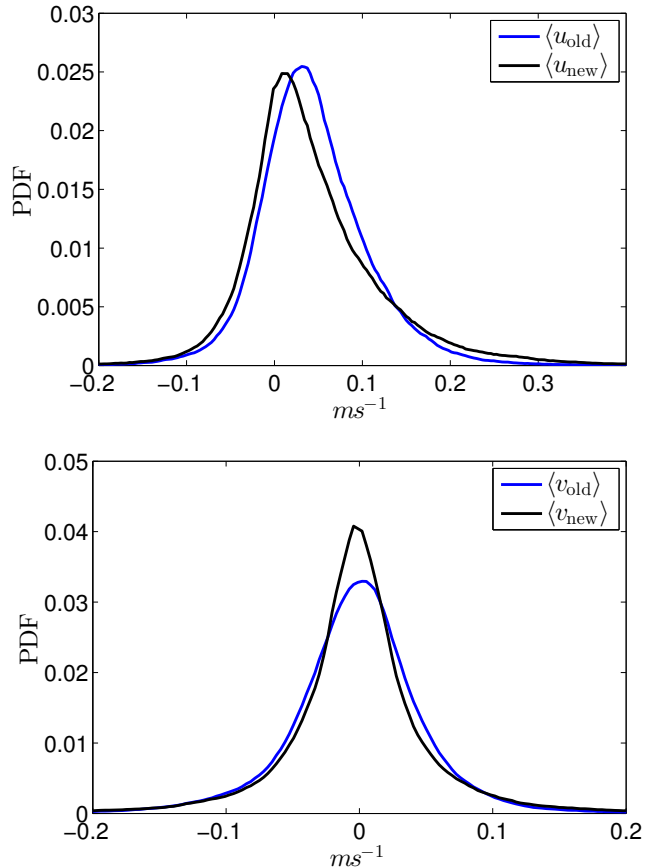


Figure 4.3: Comparison of PDF's of 1997 mean velocities derived from old and new altimetry. The upper panel shows zonal velocities - the new curve is relatively westward of the old, but has more frequent high eastward velocities. The lower panel shows meridional velocities - the new data has a more peaked PDF with more frequent small velocity values.

meso-scale eddies are believed to be a crucial source of mixing in the Southern Ocean. It also informs our interpretation of mean flow-eddy interactions, thought to be important in producing a minimum in lateral surface mixing in the ACC core, see section 4.4.

When producing the time-filtered decomposition, in order to ensure that only short-lived eddies were included in h' , and not slowly varying features associated with a persistent flow, we created a running mean field $\bar{h}(t)$ by passing the SSH field $h(t) = \bar{h} + h'(t)$ through a low-pass Butterworth filter with a cut-off of 3 months (the results were not found to be sensitive to the exact cut-off). Time series of the domain averages of the quantities from both decompositions can be seen in figure 4.4, where it can be seen that using the running mean of the SSH to define the anomaly field removed the effects of sea-level rise and the seasonal cycle, leaving only truly short-lived eddies. This also allowed for long term meanders in the ACC to be included in the mean field, which would be smeared out in a standard time mean field. Figure 4.5 shows a snapshot of the various fields in the section south of Africa. It can be seen that the filtered $\bar{h}(t)$ contains more structure, such as a standing eddy off the SW coast of Africa, than the MDT \bar{h} . Consequently, the filtered eddy field h' shows less activity, although it does pick up eddies in the same region as the SLA field.

We can see the effect this has on derived quantities in figures 4.6 and 4.7, which show the forms of U_0 (the time mean of \bar{u}), the eddy phase speed c and $\overline{\text{EKE}}$ from both decompositions, along with c/U_0 . The phase speed fields were calculated from h' for 1993-2010 (using a code courtesy of C. Hughes, NOC), by tracking absolute maxima. Thus, the fields shown here represent the phase speeds of the most energetic energies, although the real Southern Ocean will contain eddies with a spectrum of phase speeds.

Both c fields (figs 4.6a and 4.7a) show the highest phase speeds are seen to the east of South America, around New Zealand and over the Kerguelen Plateau in the central south Indian ocean. The time-filtered decomposition also shows large negative values in the Pacific and Argentine basins. Both EKEs (figs 4.6b and 4.7b) have their largest values south in the western boundary current regions and throughout the core of the ACC, similarly to Shuckburgh et al. (2009a), although the time-filtered decomposition has lower values overall (note the different colour scales), and a strong peak south of Africa. The difference in magnitudes could be expected as the EKE is directly derived from the gradients of the anomaly SSH field h' , which is of lower magnitude in the mean-anomaly decomposition (see figs 4.4 and 4.5), leading to weaker gradients. U_0 (figs 4.6c and 4.7c) and c/U_0 (figs 4.6d and 4.7d) are very similar in both decompositions, with the latter being generally positive and < 1 throughout the ACC core, but much larger to the

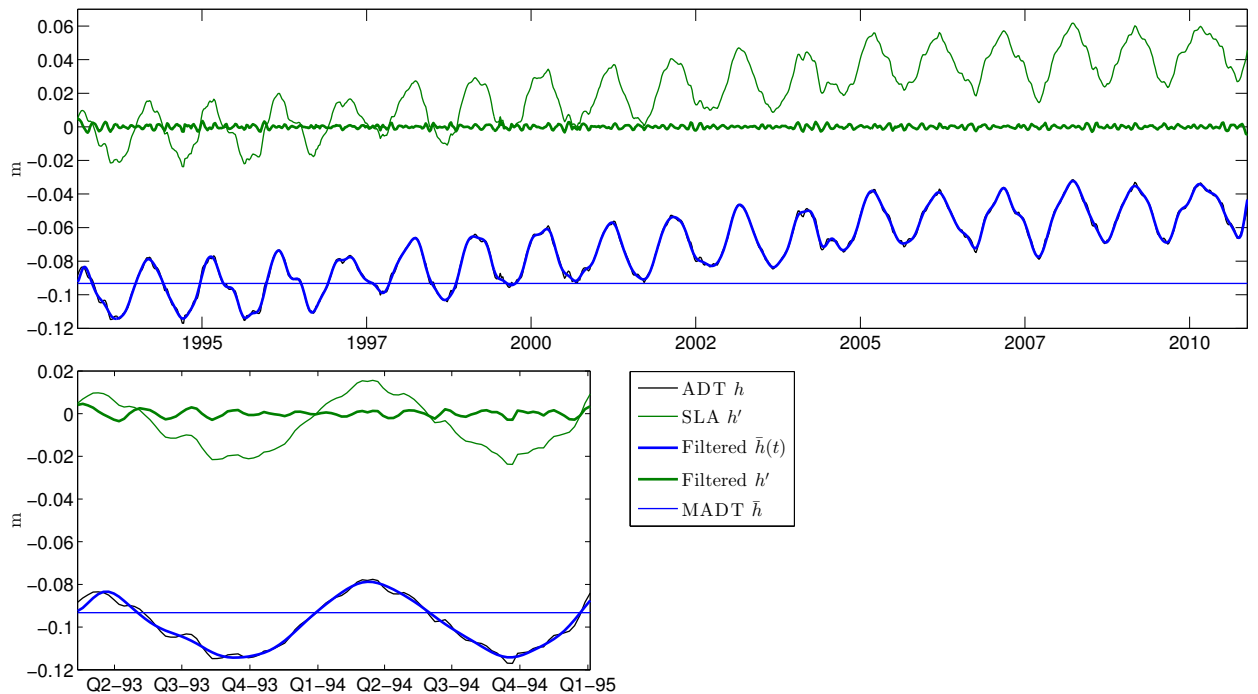


Figure 4.4: Domain mean ADT (black line), decomposed into mean (blue lines) and anomaly (green line) components, either using the AVISO MADT to define the mean (thin lines) or a 3 month high-pass Butterworth filter (thick lines). The lower panel is a magnification of the beginning of the series.

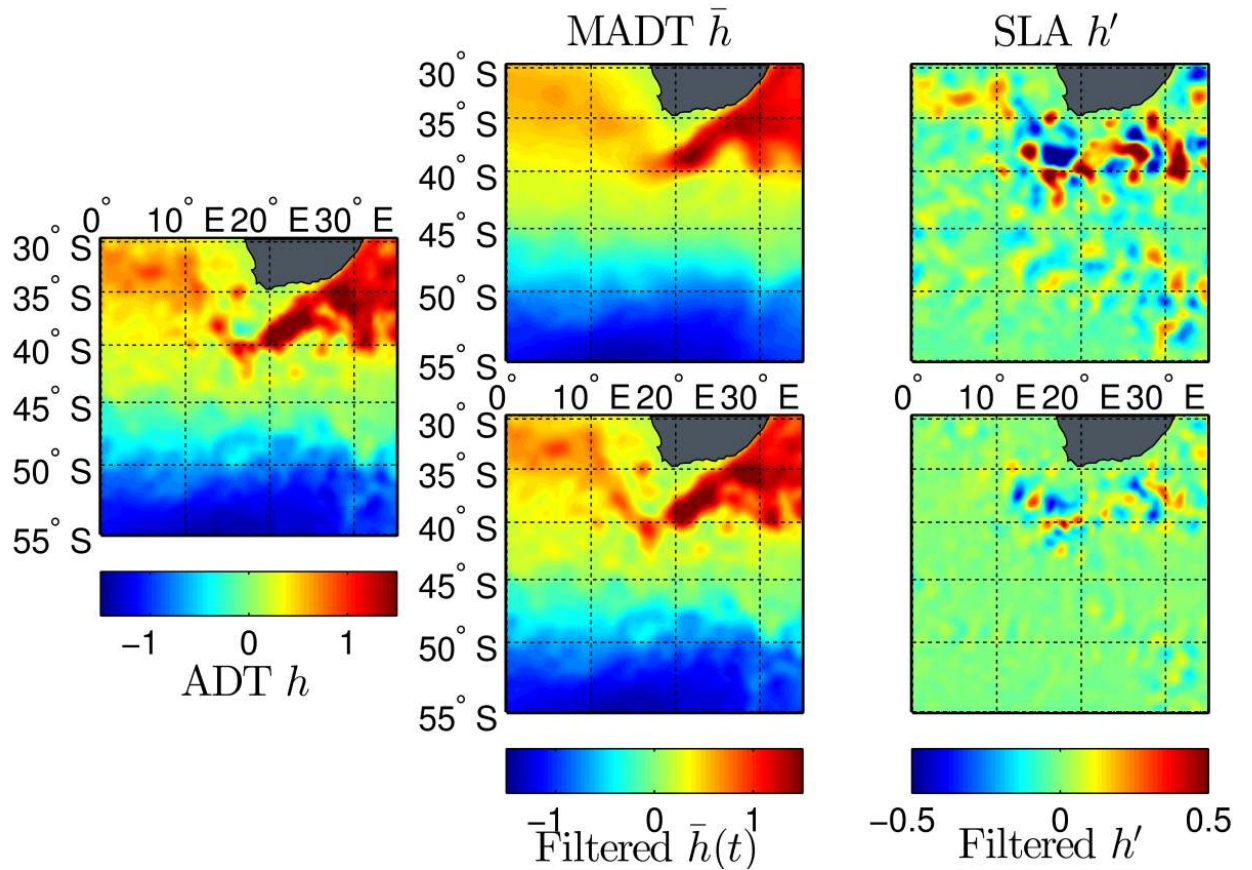


Figure 4.5: Example decomposition of the ADT from 29th Dec 1993, left hand panel, into mean (central panels) and anomaly components (right hand panels). Upper row: MADT and SLA fields from AVISO. Lower row: high-pass filtered ADT and the residual anomaly.

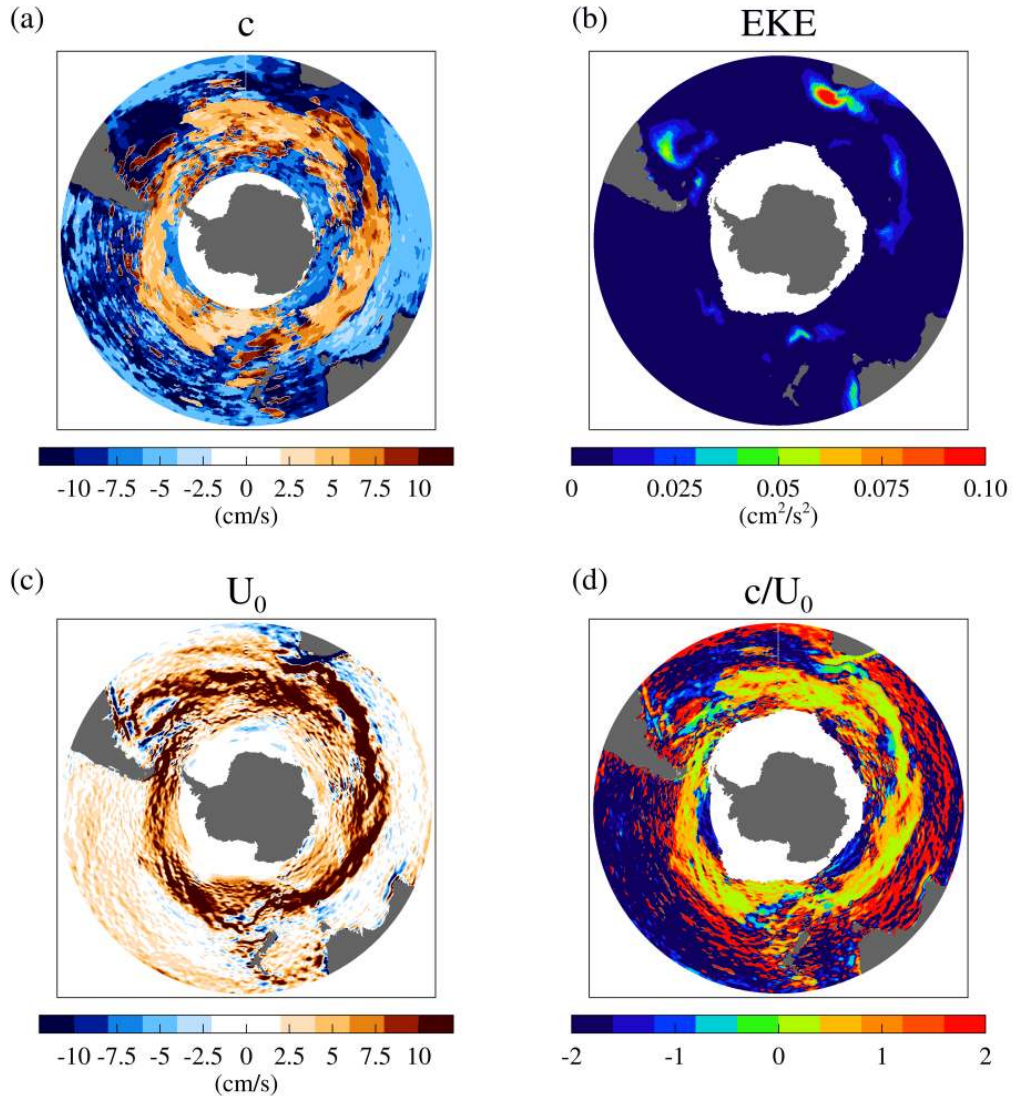


Figure 4.6: Using the time-filtered mean-anomaly decomposition: a) observed phase speed c of eddies, derived from altimetry b) Eddy kinetic energy \overline{EKE} and c) time mean zonal velocity U_0 and d) c/U_0 . b)-d) averaged over the time period 1993-2010, over which a) is calculated.

north and varying in sign.

We compare the AVISO decomposition fields with the same fields derived from the previous generation altimetry in [Shuckburgh et al. \(2009a\)](#) in figure 4.8. The stream-wise averages are compared, and because these depend on the streamlines used to perform the average (the respective AVISO mean streamlines in each case), we compare this effect by averaging all quantities with both streamlines. The stream-wise average of the c fields reveals that they are very similar in the ACC core (when comparing the averages along the same streamlines, they are close together), but that the new streamline averaging reduces the values in the core. However, both averaging methods show a distinct increase in negative values in the north of domain in the new data compared with the old (comparing the full 2D fields this seems to be mainly caused by a corresponding decrease in Pacific basin values).

The choice of streamwise averaging has little effect on the form of the mean zonal velocity (figure 4.8 upper right panel), and the new data has distinctly stronger zonal velocities in the ACC core and weaker zonal velocities in the north. Because the EKE values are very patchy, the streamwise averaging has a large effect on the form, see figure 4.8 lower left panel, but both averages show a decrease in EKE in the new data compared with the old.

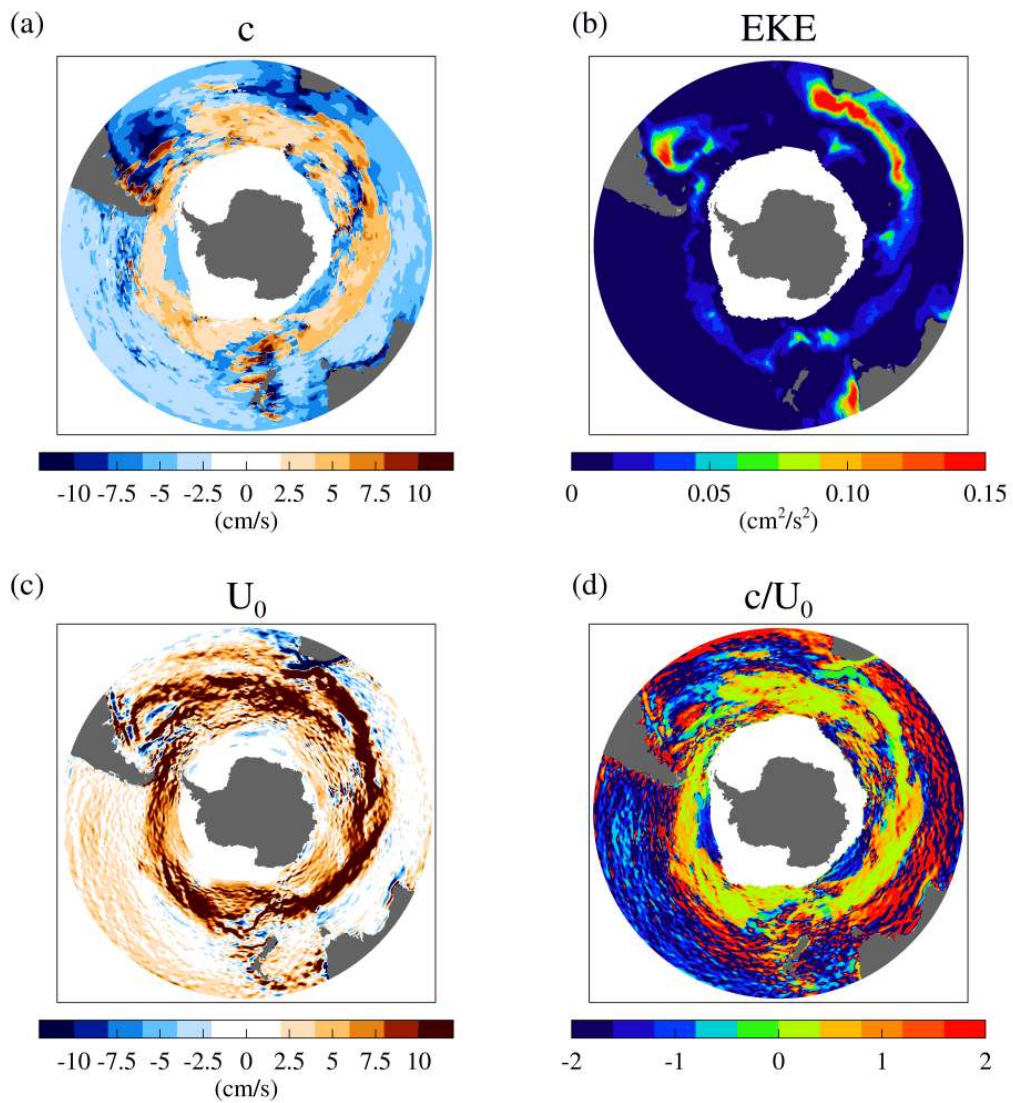


Figure 4.7: As in figure 4.6, but for the AVISO decomposition.

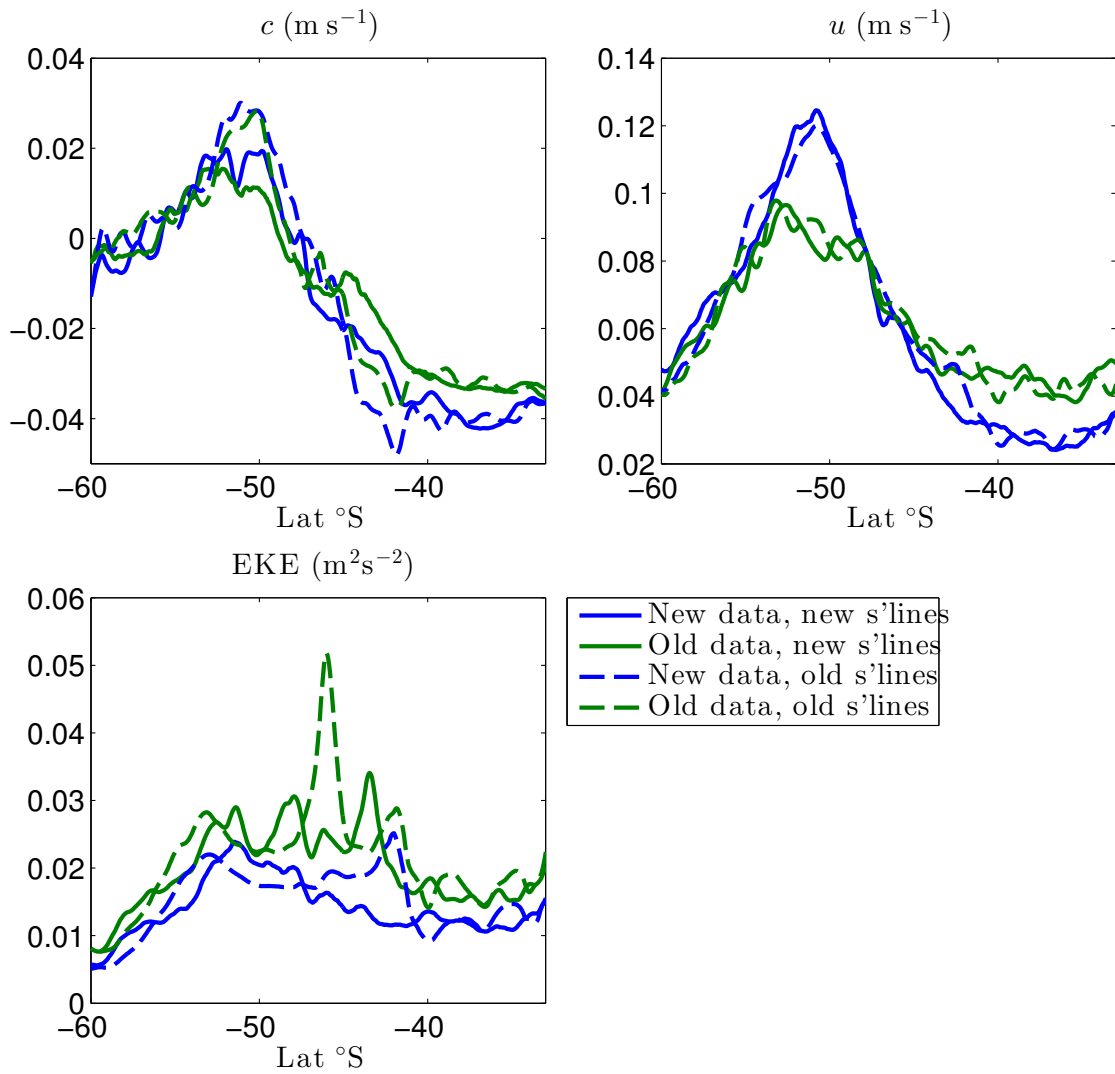


Figure 4.8: Comparison of the stream-wise averages of quantities derived from the new (blue) and old (green) altimetry, averaged along the new mean streamlines (solid lines) or the old (dashed lines).

4.3 Effective Diffusivity Calculation

We use the Nakamura effective diffusivity, κ_{eff} , as defined in section 3.3.5. For this particular calculation, we define the equivalent latitude such that $A = 2\pi r^2(1 - \cos y_e)$ is the area enclosed by the latitude circle y_e .

4.3.1 Numerical Simulation Description

For this study, we time stepped (3.16) in the offline mode of MITgcm, where \mathbf{u} were geostrophic velocities derived from the altimetric data discussed in section 4.2. The velocities were first interpolated on to a $1/20^\circ$ grid, running circumpolarly in longitude and from 29.75S to 65.95S, and then rendered non-divergent using the method described in Marshall et al. (2006). We carry this out separately for the MDT and SLA fields before adding them together, as the non-divergent operator is not linear, as discussed in Abernathey and Marshall (2013). We used a time step of 6 minutes in a 2nd order forward-difference scheme. Due to numerical effects, the true diffusivity experienced by the tracer is larger than that set by the parameters of the model. To calculate the true numerical diffusivity, one solves the following expression (found by multiplying (3.16) by C),

$$\frac{1}{2} \frac{\partial \langle C^2 \rangle}{\partial t} = -k_{\text{num}} \langle |\nabla C|^2 \rangle, \quad (4.1)$$

where $\langle . \rangle$ indicates integration over the domain of calculation. Marshall et al. (2006) and subsequent studies have shown that κ_{eff} is largely independent of k_{num} if it is calculated accurately, indicating the robustness of the calculation. See figure 4.9 for an example κ_{eff} vs y_e for several values of k_{num} . As the diffusivity is reduced, the regime where κ_{eff} is largely independent of k_d is reached, at around $k_d \sim 50 \text{ m}^2 \text{s}^{-1}$. The prescribed values of diffusivity, denoted k_d , used in the simulations are shown in the legend, but calculated values of k_{num} (close to k_d in each case) were used for κ_{eff} .

Given that the calculation of the equivalent length depends on gradients of the tracer field, it is most accurate when gradients are strong and contours can be well defined. However, the calculation will only reflect the properties of the flow well if the tracer is allowed to evolve long enough to become independent of its initial conditions. To this end, we re-initialised the tracer field (aligned with the mean flow derived from the MDT) at periodic intervals, overlapping with previous calculations. Figure 4.10 shows an example of κ_{eff} averaged over equivalent latitude bands (denoted by the dashed lines in figure 4.9) from two overlapping 100 week simulations, initialised identically 40 weeks

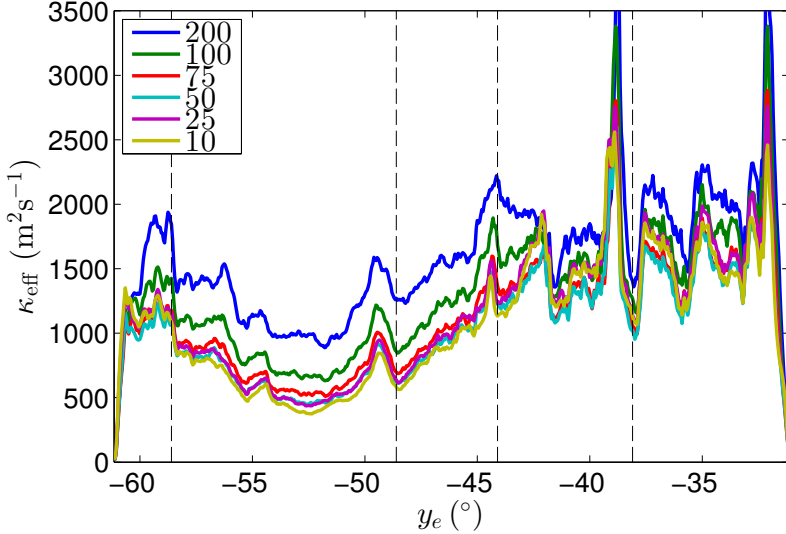


Figure 4.9: Example effective diffusivity vs. equivalent latitude for various values of prescribed diffusivities k , as labelled, in m^2s^{-1} . The vertical dashed lines indicate the equivalent latitude bands referred to throughout the rest of the chapter.

apart. Theoretically, once the initial conditions are forgotten and the tracer is aligned with the instantaneous flow, as long as there are still well-defined gradients in the tracer field, the effective diffusivity calculation should produce the same result regardless of the simulation time. However, as can be seen in figure 4.10, this is not true for the two most northerly equivalent latitude bands, 31.15S to 38.10S and 38.15S to 45.10S, and for the most southerly band, 58.65S to 61.15S. The average κ_{eff} for the two northerly regions shows an initial spike, and then a consistent decay throughout the simulation. The most southerly region initially behaves well, but also exhibits the same decay throughout the simulation, with the second simulation rising above the first at around 50 weeks. However, the 2 bands from 44.15S to 58.60S behave as expected, with $\langle \kappa_{\text{eff}} \rangle$ from both simulations matching well across most of the overlapping time period.

To further investigate this mismatch, we remapped the effective diffusivity (a one-dimensional quantity) back onto the two-dimensional tracer contours in order to visualise its spatial distribution. Figure 4.11 shows snapshots of the tracer fields (left panels), and κ_{eff} (right panels) from 60E to 120E at week 100 for the two simulations shown in figure 4.10. Sub-script A refers to the first simulation, initialised at 0 weeks, and B the second, initialised at 40 weeks. The bottom panels show the absolute difference between the upper two panels. The two tracer fields, $C^{A,B}$, have very similar structure, although

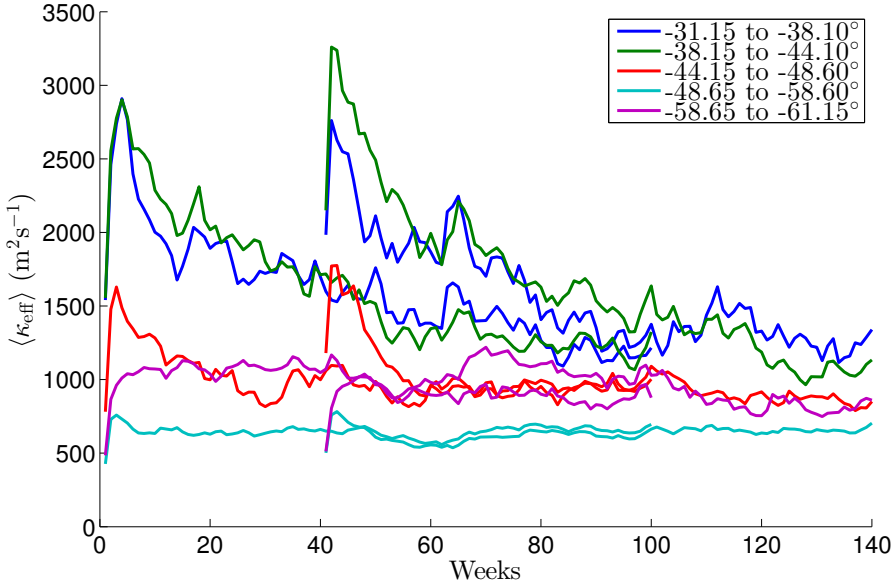


Figure 4.10: Examples of overlapping simulations, initialised identically 40 weeks apart and time-stepped for 100 weeks. The coloured lines are κ_{eff} averaged over equivalent latitude bands, as indicated in the legend, which are denoted by the grey lines in figure 4.9. Both simulations have prescribed $k = 50 \text{ m}^2 \text{s}^{-1}$.

the absolute values are different due to the longer simulation (C^A) having a smaller across-stream contrast in tracer. The largest differences in tracer are found to the east of the domain shown, between 45S and 50S. The effective diffusivity fields, however, are very similar throughout the southern half of the domain, and show the largest difference in the northeast of the domain, where the tracer difference is lowest. This behaviour is also found throughout the rest of the domain - the largest differences in effective diffusivity are largely found to the north of the domain, where tracer differences are generally small.

Thus, the calculation behaves as expected in the south of the domain - overlapping simulations have different absolute values of tracer, but the contour structure is largely the same, resulting in largely similar κ_{eff} . However, in the north of the domain, where absolute tracer difference is small, the contour structure is different and therefore, so is κ_{eff} . Analysing the regions where this is found, we concluded that this mismatch in contour structure is due to a combination of two effects: firstly, a significant portion of the flow crossing the northern boundary of the domain, resulting in discontinuous tracer contours, known to adversely affect the calculation of κ_{eff} . Secondly, high eddy activity resulting in well-mixed tracer, with little gradient contrast and so ill-defined contours. The mismatch seen in the most southerly equivalent latitude band, 58.65S to 61.15S, is

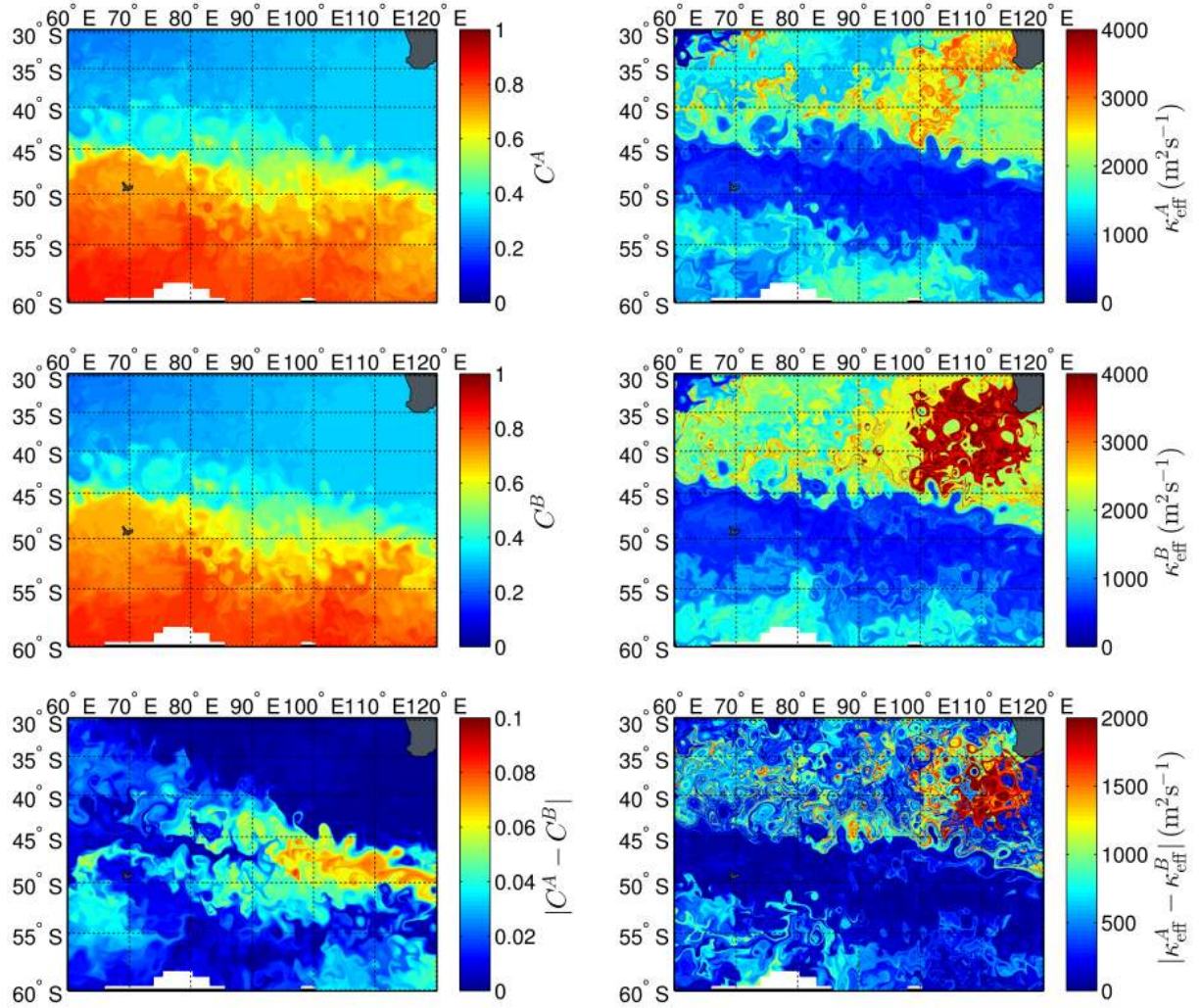


Figure 4.11: Week 100 snapshots of the two simulations shown in figure 4.10 - tracer fields on the left and re-mapped κ_{eff} on the right - in the region southwest of Australia. The bottom panels are the absolute difference between the upper two, where A refers to the simulation initialised at 0 weeks, and B at 40 weeks. The white region indicates sea ice. Note that the largest differences in tracer value do not correspond to the largest difference in κ_{eff} .

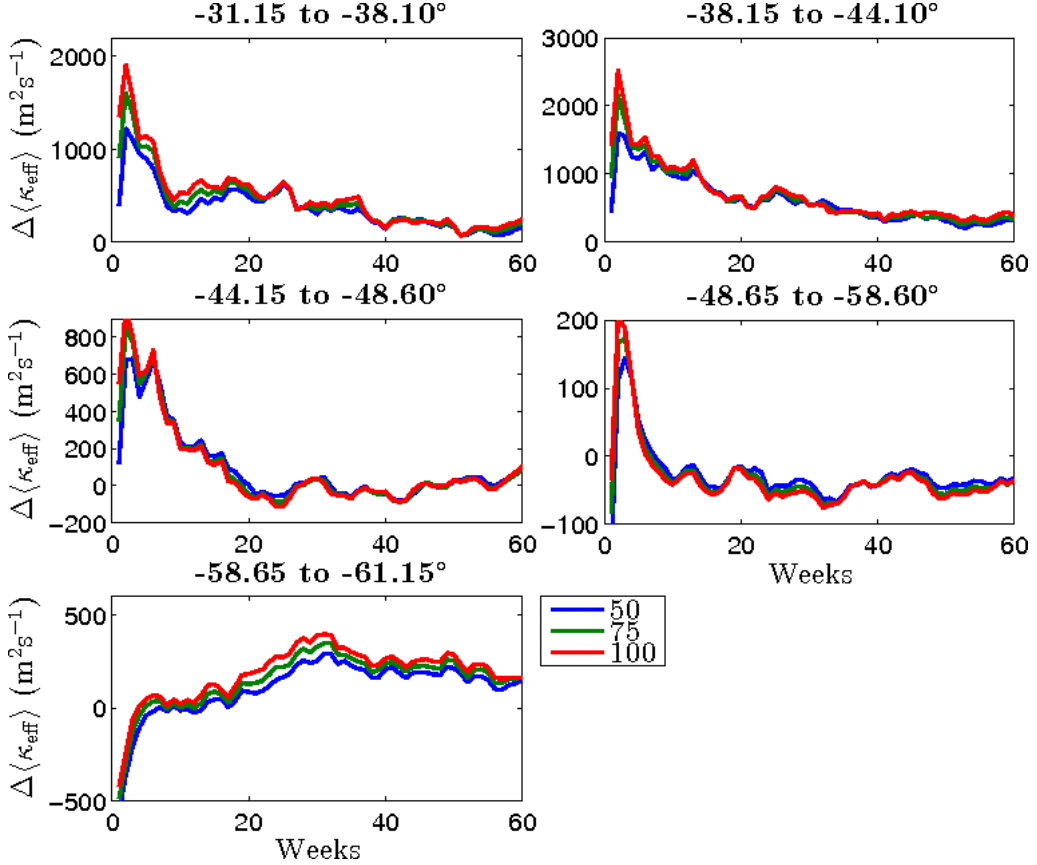


Figure 4.12: The difference in $\langle \kappa_{\text{eff}} \rangle$ for different latitude bands between overlapping runs started 40 weeks apart, as in figure 4.10, for various applied diffusivities (in m^2s^{-1}) as indicated. All differences settle after 20-30 weeks.

due to localised instances of contours that intersect the southern boundary (not shown). We were thus not able to create a consistent time series of κ_{eff} for these regions, and so have excluded them from future time series plots, although we have included them in some spatial plots for completeness.

In order to assess the optimal over-lap time and numerical diffusivity for the simulations, we calculated the difference between the two overlapping simulations ($\Delta \langle \kappa_{\text{eff}} \rangle$) in figure 4.11 as a function of time, as seen in figure 4.12. Each panel is the difference in the y_e band $\langle \kappa_{\text{eff}} \rangle$, and the colours indicate different applied diffusivities $k_d = 50, 75$, and $100 \text{ m}^2\text{s}^{-1}$. Whilst the differences between the two most northern and the most southerly sections do not settle close to 0, all sections show a settling of the difference after 20-30 weeks, with $k_d = 50 \text{ m}^2\text{s}^{-1}$ showing the smallest differences. Thus we chose to simulate the full time period of data (Jan 1993 to Dec 2010) in 100 week runs, overlapping for

30 weeks, with $k_d = 50 \text{ m}^2\text{s}^{-1}$. If we were to extend the ‘spin-up’ period to allow the differences in the other sections to settle further, we would end up with a tracer field that had been mixed too much, without well-defined gradients with which to define the effective diffusivity.

4.3.2 Results: Spatial Distribution

Figure 4.13 shows the time mean effective diffusivities κ_{eff} from this study and Shuckburgh et al. (2009a), where we have only plotted the effective diffusivity for this study in the robust region (-58.6 to -44.15°S, see discussion in section 4.3.1). [The results of Abernathey et al. (2010) are extremely similar to Shuckburgh et al. (2009a) at the surface, which is not surprising as the SOSE model velocity fields used in Abernathey et al. (2010) assimilate the same (old) altimetry used in Shuckburgh et al. (2009a), although for 2005–2006.] There are broad similarities between both studies: there is a minimum in κ_{eff} at the latitudes of the ACC core, -55° to -50°, and rising values to the north and south. The magnitudes are largely similar on the ACC flanks, but this study has minimum values around 60% lower in the ACC core: $\sim 500 \text{ m}^2 \text{s}^{-1}$ compared with $\sim 800 \text{ m}^2 \text{s}^{-1}$. This is consistent with the theory that the mean flow in the ACC suppresses mixing, given that the new generation altimetry shows stronger zonal flow throughout the ACC core (see figure 4.8 and discussion in section 4.2). This effect is investigated further in section 4.4.

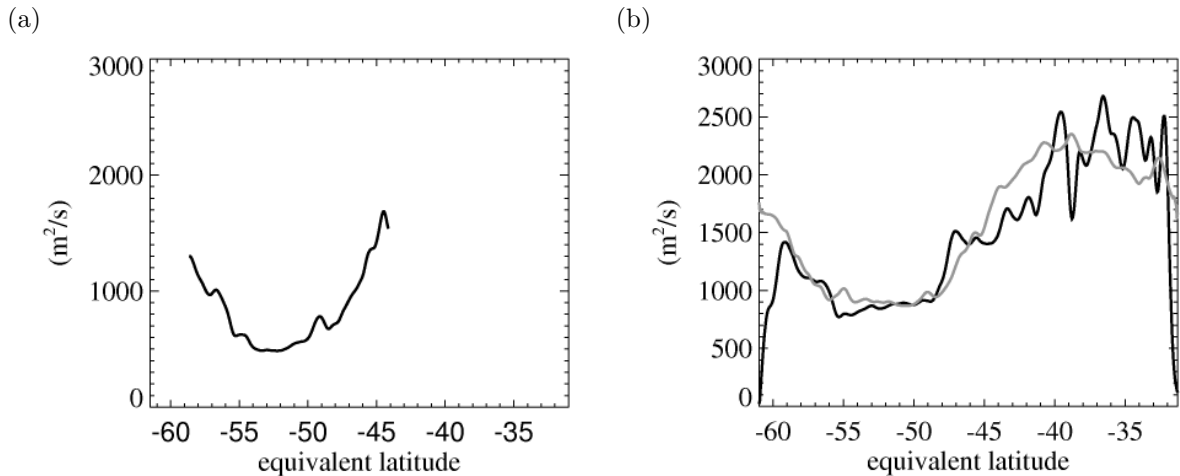


Figure 4.13: Effective diffusivity from a) this study, average 1993–2010, robust region only; b) from Shuckburgh et al. (2009a), average 1996–2001. The light grey line in b) is the time mean $\text{EKE}/(u - c)^2$ from that study, see section 4.4.

The spatial pattern of the calculated effective diffusivity in two dimensions depends on the shape of the tracer contours, which determine the equivalent latitude bands. We can see this in figure 4.14, where the right-hand panels show effective diffusivity replotted on tracer contours to show the spatial distribution. Note, however, that the effective diffusivity is a one-dimensional quantity and that one value is plotted along each tracer

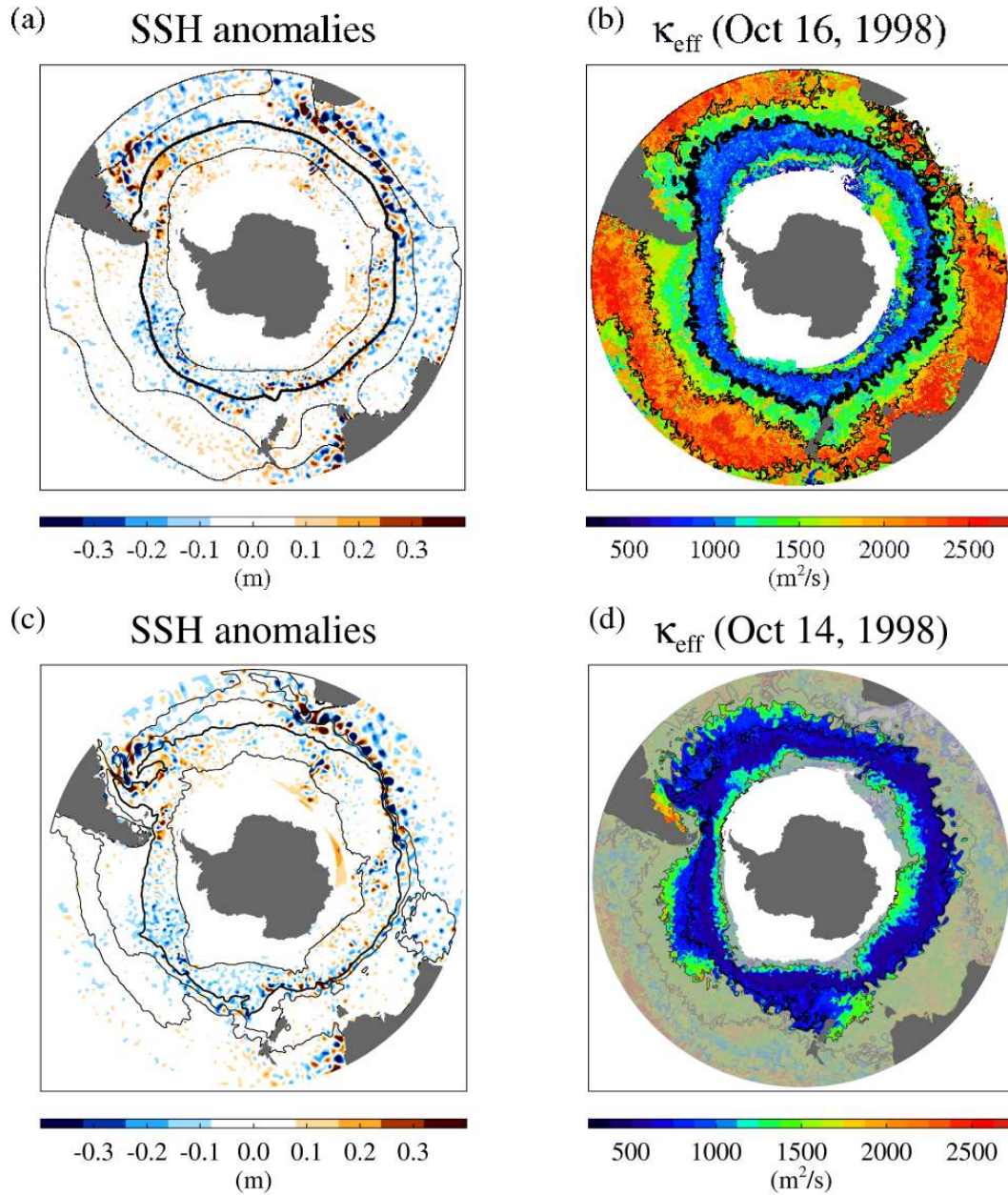


Figure 4.14: a,c) SSH anomalies and b,d) effective diffusivity for Oct 16 1998 from Shuckburgh et al. (2009a) (upper panels) and Oct 14 1998 from our updated calculations (lower panels). Streamlines are overlaid: $-9, -5, 0$, and $6 \times 10^4 \text{ m}^2\text{s}^{-1}$ upper panels, and $-6, -4, -1$, and $8 \times 10^4 \text{ m}^2\text{s}^{-1}$ lower panels [AVISO mean in a,c), instantaneous in b,d)]. Grey shading indicates the non-robust region in d).

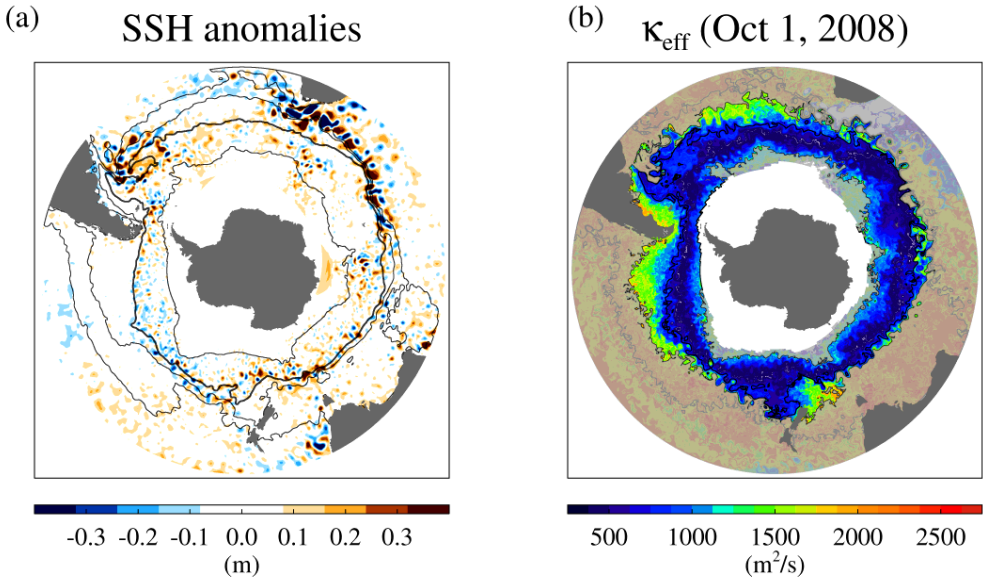


Figure 4.15: a) SSH anomalies and b) effective diffusivity for Oct 1, 2008 from this study. Streamlines are overlaid $-6, -4, -1$, and $8 \times 10^4 \text{ m}^2 \text{s}^{-1}$ [mean in a) instantaneous in b)]. Grey shading indicates the non-robust region in b)

contour. The equivalent mean streamlines and instantaneous SSH anomalies can be seen in the left-hand panels. The upper panels show results from [Shuckburgh et al. \(2009a\)](#), and the lower panels from this study. The results are shown from two days close together, 16th October 1998 (upper panels) and 14th October 1998 (lower panels).

Comparing a) and c), the SSH anomalies are very similar in magnitude and distribution in both studies. The mean streamlines are a lot smoother in a), showing a more complex structure in c), which shows some closed contours near the continents, representative of standing eddies. The κ_{eff} snapshots, b) and d), show similar properties to the time means seen in figure 4.13, with the minimum in κ_{eff} in the core of the ACC in both studies, and are qualitatively similar in the robust region (unshaded in figure 4.14d). There is, however, notable difference in the form of the instantaneous streamlines - as was discussed previously, the streamline structure is more non-zonal, with more streamlines crossing the northern boundary of the domain, in this study compared with [Shuckburgh et al. \(2009a\)](#). This results in tracer contours that do the same, which, as discussed previously, is detrimental to the effective diffusivity calculation (we have shaded the non-robust results in figure 4.14d).

4.3.3 Results: Temporal Variability

To assess how the spatial distribution changes with time, we can compare the results of the calculation 10 years later (1st October 2008) in figure 4.15. Comparing with figure 4.14, we see elevated SSH values in 2008, with slightly higher κ_{eff} on the north ACC flank. The values in the ACC core are slightly lower in 2008 compared with 1998 (minimum 380 vs $470 \text{ m}^2 \text{s}^{-1}$). The temporal variability of κ_{eff} can be seen more clearly in figure 4.16. This shows κ_{eff} over the full time period of integration, from 1993 to 2010, with two curves representing averages over two equivalent latitude bands. The upper band (mean $\sim 1100 \text{ m}^2 \text{s}^{-1}$) is averaged over $y_e = 44.15$ to 48.60°S , or the -4 to $-1 \times 10^4 \text{ m}^2 \text{s}^{-1}$ streamlines, and the lower band (mean $\sim 700 \text{ m}^2 \text{s}^{-1}$) is averaged $y_e = 48.65$ to 58.60°S , or the -1 to $8 \times 10^4 \text{ m}^2 \text{s}^{-1}$ streamlines. The mean location of these streamlines can be seen in figure 4.15a. As discussed in section 4.3.1, we exclude the time series for κ_{eff} north of 43.15°S and south of 58.60°S as the calculation is affected by the presence of high eddy activity and non-circumpolar tracer contours.

The grey lines show the results from the individual 100 week simulations, not including a 20 week spin-up period, which are thinner in the overlap regions between two consecutive simulations. The overlap between consecutive simulations is relatively good when compared to the poor overlap seen in the more northerly sections in section 4.3.1, and when compared with that observed in [Shuckburgh et al. \(2009a\)](#) (cf. their figure 9, noting the different axis limits).

Overlaid in black is the full time series, smoothed using a 5th order Butterworth low-pass filter ([Butterworth, 1930](#)) with a cut-off frequency of 12 weeks. There is no obvious trend in either section. The northern section shows higher variability than the south, ACC core, section, but they are similar when scaled by the mean values. The two vertical black lines indicate the dates of the snapshots seen in figures 4.14 and 4.15, which show that the northern section has a higher value of κ_{eff} in 2008, and the ACC section has a slightly lower value.

The seasonal variability of κ_{eff} can be seen in figure 4.17, where the monthly mean (black lines) and ± 1 standard deviations (dashed lines) are plotted against month for the two same equivalent latitude sections. There is the hint of a peak in values in October for both sections, although the variability is of the same order of magnitude as the maximum difference in the means. Comparing with the same calculation in [Shuckburgh et al. \(2009a\)](#) (see their fig. 10), we see that there is a similar seasonal trend seen in the two most southerly equivalent latitude bands, with peaks around September.

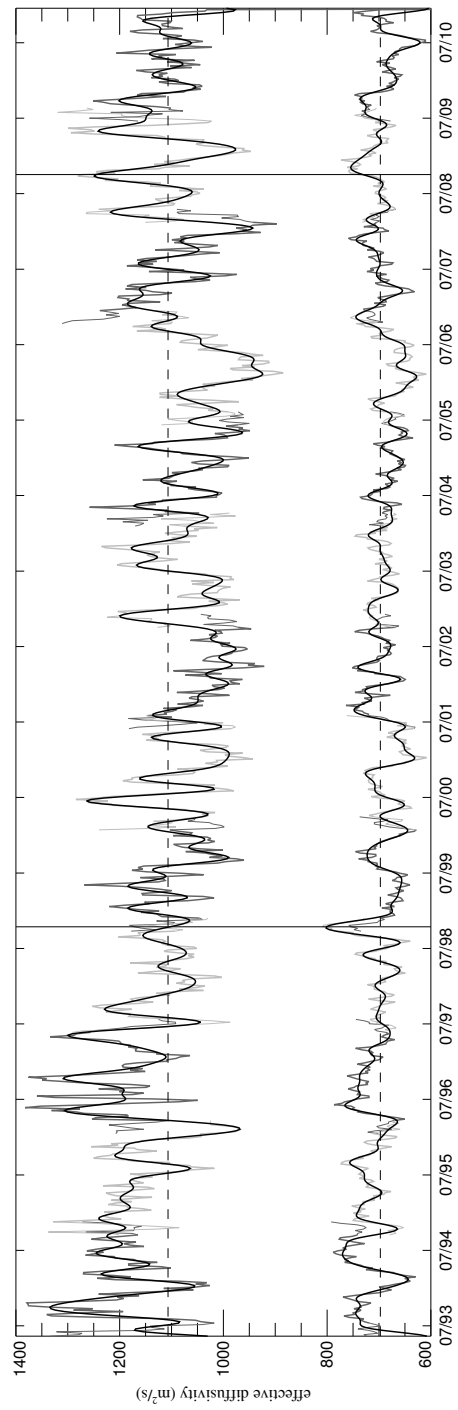


Figure 4.16: Effective diffusivity from 1993 to 2010, averaged over the two most poleward equivalent latitude bands indicated in the lower panels of figure 4.14, the lowest values being the most poleward, $48.65\text{--}58.60^\circ\text{S}$, and the higher values at mid-latitudes $44.15\text{--}48.60^\circ\text{S}$

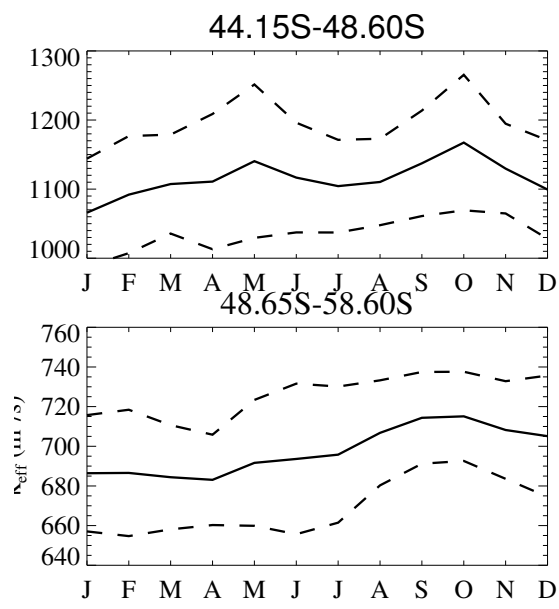


Figure 4.17: Seasonal cycle of effective diffusivity from 1993-2010 over equivalent latitude bands as labelled. Solid line: mean; dashed lines: ± 1 std dev. A slight peak in October is seen in both bands.

4.4 Other mixing parameterisations

As well as comparing the results of the new calculation with the old, we also compared it to alternative mixing parameterisations. As mentioned in section 4.1, the literature contains several parameterisations based on mixing length theory. In particular, one can derive an expression for the form of surface Eady waves in a stochastic surface quasigeostrophic model, as outlined in full in the appendix of [Ferrari and Nikurashin \(2010\)](#), or the form of baroclinic Rossby waves in a barotropic quasigeostrophic model, see [Klocker et al. \(2012\)](#). Both result in the following expression for a meridional diffusivity:

$$\kappa_y = \frac{k^2}{K^2} \frac{\gamma}{\gamma^2 + k^2(U_0 - c)^2} \text{EKE}, \quad (4.2)$$

where k^2 is the zonal eddy wavenumber, $K^2 = k^2 + l^2$ is the total wavenumber, γ is the eddy decorrelation time scale, EKE is the eddy kinetic energy, U_0 is the zonal jet velocity, assumed not to vary horizontally, and c is the eddy phase speed. The dependence on EKE can be interpreted as saying that mixing will be strongest where eddies are most active, and containing $(U_0 - c)^2$ that this will be most enhanced when the eddies are stationary with respect to the mean flow, with an upper limit determined by γ .

In order to determine κ_y from available altimetric observations, [Ferrari and Nikurashin \(2010\)](#) make several assumptions. First, they assume that the eddies are isotropic, i.e. $K^2 = 2k^2$. They use a scaling argument to assume the decorrelation time $\gamma = d_0 \sqrt{K^2 \text{EKE}}$, where d_0 is a dimensionless constant; this is supported by the results of [Klocker et al. \(2012\)](#). Finally, they assume the phase speed of eddies is proportional to the jet speed, i.e. $c = (1 - \alpha)U_0$, and that $c \ll U_0$. The above theories assume a scale separation between the jet speed U_0 and the eddy field, and so [Ferrari and Nikurashin \(2010\)](#) use the MDT field \bar{h} for U_0 , and the SLA field h' for EKE, such that $\text{EKE} = 0.5g^2f^{-2}K^2\bar{h}^2$, and $U_0^2/\text{EKE} = 2|\nabla \bar{h}|^2/|\nabla h'|^2$, where the apostrophe and over-bar represent anomaly and time mean contributions respectively. These assumptions result in (4.2) becoming

$$\kappa_{FN} = d_1 \frac{g}{|f|} \frac{(\bar{h}^2)^{1/2}}{1 + 2d_2 |\nabla \bar{h}|^2/|\nabla h'|^2}, \quad (4.3)$$

where $d_2 = 0.5\alpha^2 d_0^2$ and the dimensionless constants d_i are found by the authors by tuning to an effective diffusivity calculation for the Pacific sector of the ACC (chosen for the approximately zonal flow in this region, far from continental boundaries), giving $d_1 = 0.32$ and $d_2 = 4$. Using these parameters for the full ACC, they then find good

agreement between κ_{FN} and κ_{eff} . Relating c to U_0 is the most questionable assumption, and is only justified a posteriori by the agreement of the result with the effective diffusivity calculation. Given that this agreement is only due to the direct tuning of two constants, it could be argued that this is not a robust result.

[Klocker et al. \(2012\)](#) also estimate κ_y at the surface from altimetry data. They write κ_y in the following form:

$$\kappa_{\text{KFL}} = \frac{\kappa^0}{1 + k^2(U_0 - c)^2/\gamma^2}, \quad (4.4)$$

where κ^0 is the diffusivity of a stationary eddy (when $c = U_0$). This is identified as the eddy only diffusivity $K|_{U=0}$ in [Ferrari and Nikurashin \(2010\)](#) (under the assumption $c \ll U_0$) and K_{1y}^0 in [Klocker et al. \(2012\)](#). They carry out a number of effective diffusivity calculations using the anomaly velocity field combined with a range of constant mean velocities U_0 , again using the same Pacific sector as [Ferrari and Nikurashin \(2010\)](#). At each latitude they look at the κ_{eff} vs U_0 curve, identify c as the value of U_0 at the maximum diffusivity κ^0 , and identify k^2/γ^2 from the curvature. The forms of the fully reconstructed κ_{KFL} and κ^0 match well with the respective effective diffusivity calculations for the Pacific sector. The results give c values of around 1 cm s^{-1} within the ACC core, which is smaller than those identified from observations, see figures 4.7a and 4.6a. The authors explain this as being a result of the most energetic eddies dominating the phase speed calculation, which tracks maxima in the h' field, whereas the eddies that mix most will in fact be slower and larger - giving a larger mixing length. Whilst the success of this method in reproducing the form of κ_{eff} lends it support, tuning k^2/γ^2 separately at each latitude allows for a complete lack of coherence, i.e. adjacent latitudes could be dominated by eddies with different wavenumbers, despite the implied eddy size being larger than the resolution of the calculation.

Both [Ferrari and Nikurashin \(2010\)](#) and [Klocker et al. \(2012\)](#) use the older version of the altimetry fields to estimate κ_y , and both calculate expressions based on time mean values. They also assume a mean flow field that doesn't vary meridionally, so both make the calculation in the Pacific sector of the ACC, where the mean flow is largely zonal. However, [Ferrari and Nikurashin \(2010\)](#) go on to use the same parameters found in the Pacific sector for the entire ACC, and show a good match with the full κ_{eff} . We wanted to test their assertion that the parameterisation is applicable Southern Ocean-wide, and to test whether a similar expression based on time varying quantities could be compared to our time varying κ_{eff} calculation. We expect that the stationary AVISO mean flow will result in the best fit, as it most closely fits the assumptions in deriving κ_y . Given

that the new altimetry fields have different properties to the old, see section 4.2, we also wished to test whether one of the forms of κ_y could be applied to our new results. We chose to try to base the form of k^2/γ^2 on the properties of the flow, as in Ferrari and Nikurashin (2010), rather than trying to find them at each latitude as in Klocker et al. (2012), which would involve the assumption that each is independent. We wished to remove the assumption that c is proportional to U_0 . The results of Klocker et al. (2012) imply that the estimates of c from altimetry, as presented previously, are not relevant. However, neither Ferrari and Nikurashin (2010) or Klocker et al. (2012) directly tested this, and so we investigated if this was true.

Removing the assumption that c is proportional to U_0 , and using time varying quantities rather than time means, results in the following expression for the instantaneous meridional diffusivity:

$$\kappa^\alpha(x, y) = d_1 \frac{g}{|f|} \frac{|h'|}{1 + 0.5d_0^2(\bar{u} - c)^2/EKE} = \frac{\kappa^0}{1 + 0.5d_0^2/E}, \quad (4.5)$$

where $\kappa^0 = d_1 g |h'|/|f|$, related to the eddy diffusivity derived in Holloway (1986), and the constants d_i have the same meanings as in Ferrari and Nikurashin (2010). $E = EKE/(\bar{u} - c)^2$ includes the effects of mean flow mixing suppression. Thus the time means $\bar{\kappa}^0 = d_1 g \overline{|h'|}/|f|$, $\bar{E} = \overline{EKE}/(\bar{u} - c)^2$ and we define the related quantities in terms of time means $\hat{\kappa}^0 = d_1 g |\bar{h}'|^2/|f|$, $\hat{E} = \overline{EKE}/(\bar{u} - c)^2$. Henceforth, any symbol with an overbar ($\bar{\cdot}$) is the time-mean of that quantity, calculated in terms of time-varying variables, and any symbol with a hat ($\hat{\cdot}$) is the quantity calculated in terms of time-mean variables.

4.4.1 Comparison with κ_{FN}

We directly tested the robustness of κ_{FN} by comparing it with our effective diffusivity calculation. Figure 4.18 shows comparisons between κ_{eff} (solid blue lines) and $\kappa_{eff}|_{\bar{u}=0}$ (dashed blue lines, calculated identically to κ_{eff} but using the anomaly velocity field only to advect the tracer). Figure 4.18a shows the time-filtered mean-anomaly decomposition and fig 4.18b shows the AVISO decomposition. Both figures contain the same κ_{eff} curve but the y -axis scales are different, and we only show the robust effective diffusivities, but show the other quantities for the full region for reference. For the time-filtered anomaly-only calculation (fig 4.18a), $\kappa_{eff}|_{\bar{u}=0}$ is lower than κ_{eff} apart from in the ACC core. This shows that the time-filtered mean field enhances mixing except for right in the ACC core where it suppresses it. In contrast, the AVISO anomaly-only calculation

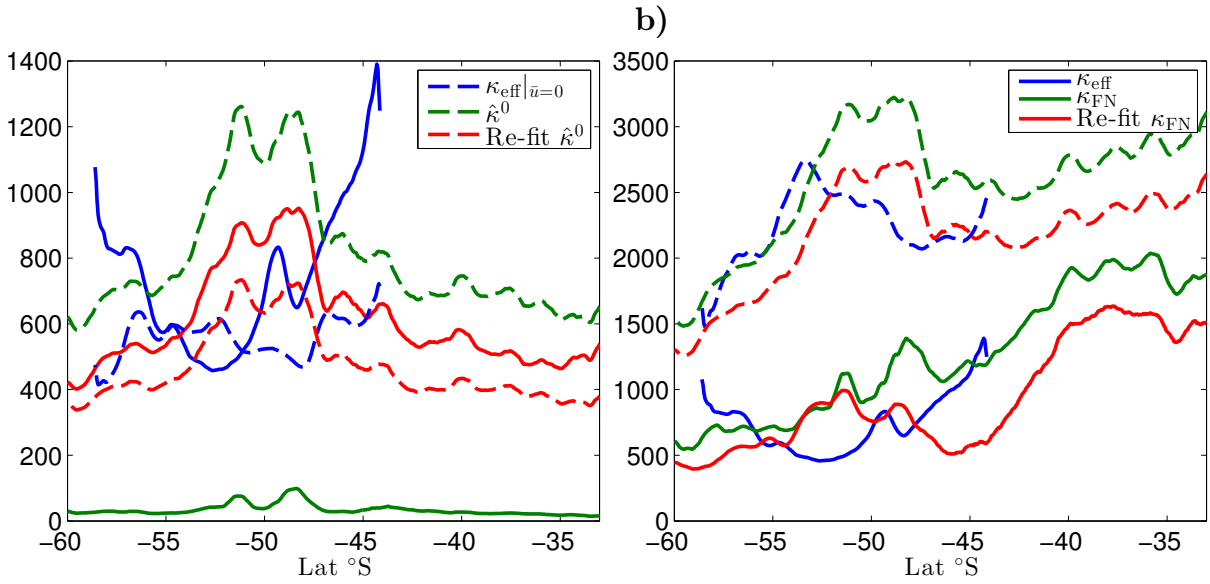


Figure 4.18: Comparison between κ_{eff} (blue lines) and κ_{FN} using [Ferrari and Nikurashin \(2010\)](#) constants (green lines) and re-fit to κ_{eff} (red lines) for a) time-filtered and b) AVISO mean-anomaly decompositions. Dashed lines indicate the calculation without the respective mean flow, solid with the full velocity field. Note the different y -axis scales.

(fig 4.18b) is higher than κ_{eff} throughout the robust region, showing that the AVISO mean field suppresses the flow throughout the region, with maximum suppression in the ACC core. This is as expected, as the AVISO anomaly field from this decomposition is larger in amplitude than in the filtered decompositions (see figures 4.4 and 4.5), and so more actively mixing. The AVISO decomposition results are in agreement with both [Ferrari and Nikurashin \(2010\)](#) and [Klocker et al. \(2012\)](#), who similarly find mean-flow suppression throughout the ACC, with similar values for $\kappa_{\text{eff}}|_{\bar{u}=0}$.

The green lines in fig 4.18 show κ_{FN} calculated with the fitting parameters derived by [Ferrari and Nikurashin \(2010\)](#). Given they were calculated using the AVISO mean-anomaly decomposition, we would not necessarily expect them to match the time-filtered decomposition calculation, and indeed they do not (fig 4.18a), for either the full calculation (solid lines) or the eddy-only calculation (dashed lines). However, the magnitudes match better for the AVISO decomposition (fig 4.18b), although the variations with latitude are not well matched.

We attempted to re-fit the parameters d_i to our results as follows: first, we made a least-squares fit between $\kappa_{\text{eff}}|_{\bar{u}=0}$ and $\kappa_{\text{FN}}|_{\bar{u}=0} = \hat{\kappa}^0$ to find d_1 ; second, we made a least-squares fit between κ_{eff} and κ_{FN} using this d_1 to find d_2 . The results of these fits are

the red curves in figure 4.18, where again the solid line is the full form and the dashed line is the anomaly-only form. For d_1 we find 0.21 for the time-filtered and 0.31 for the AVISO decompositions, the latter being very close to the 0.32 from Ferrari and Nikurashin (2010). For d_2 we find -0.01 for the time-filtered and 0.5 for the AVISO decompositions, compared with 4 from Ferrari and Nikurashin (2010) (some of this difference is due to the fact that κ_{FN} was calculated in 2D before streamwise averaging, whereas the re-fit was carried out on the streamwise average of the constituent quantities, which is why both curves are relatively similar). However, it can be seen that, whilst it is possible to tune the magnitudes of the expressions to be nearly correct, the qualitative forms of the κ_{FN} curves do not match those of the κ_{eff} curves. The full velocity κ_{eff} calculation shows a distinct minimum in the ACC core, whereas both fits to κ_{FN} show peaks around the same location. Both $\kappa_{eff}|_{\bar{u}=0}$ curves do have a peak in the ACC core, but both fits to κ^0 show the peak too far north, and neither capture the increased mixing the northern flanks.

The failure to fit κ^0 to $\kappa_{eff}|_{\bar{u}=0}$ suggests that we cannot make the assumption that $c \ll U_0$, and that the κ^0 is related to the stationary eddy mixing, when $c = U_0$, and not the eddy-only mixing (in the absence of the mean flow), as assumed in κ_{FN} . The failure to find a fit to κ_{FN} that accurately captures the results of the mean-flow mixing suppression in either decomposition additionally implies that the assumption of $c \propto U_0$ is not valid.

4.4.2 Spatial distributions

Finding that κ_{FN} was not consistent with our results, we further analysed the spatial distributions of the relevant quantities that form κ_y and attempted to fit κ^α to our effective diffusivity calculation.

The distribution of eddy-mixing and mixing suppression

The form of U_0 (the time mean of $\bar{u}(t)$), c , EKE, and c/U_0 can be seen in figures 4.6 and 4.7, for both mean-anomaly decompositions discussed in section 4.2. Whilst c/U_0 is largely positive and small within most of the ACC, there are localised regions with very different values for both decompositions and it is definitely not a positive constant outwith the ACC. This suggests that κ_{FN} should fit better within the ACC than outwith, where the Ferrari and Nikurashin (2010) assumption of $c \propto U_0$ holds better. Indeed, figure 4.18 shows the largest differences between the re-fits of κ_{FN} are outside the ACC

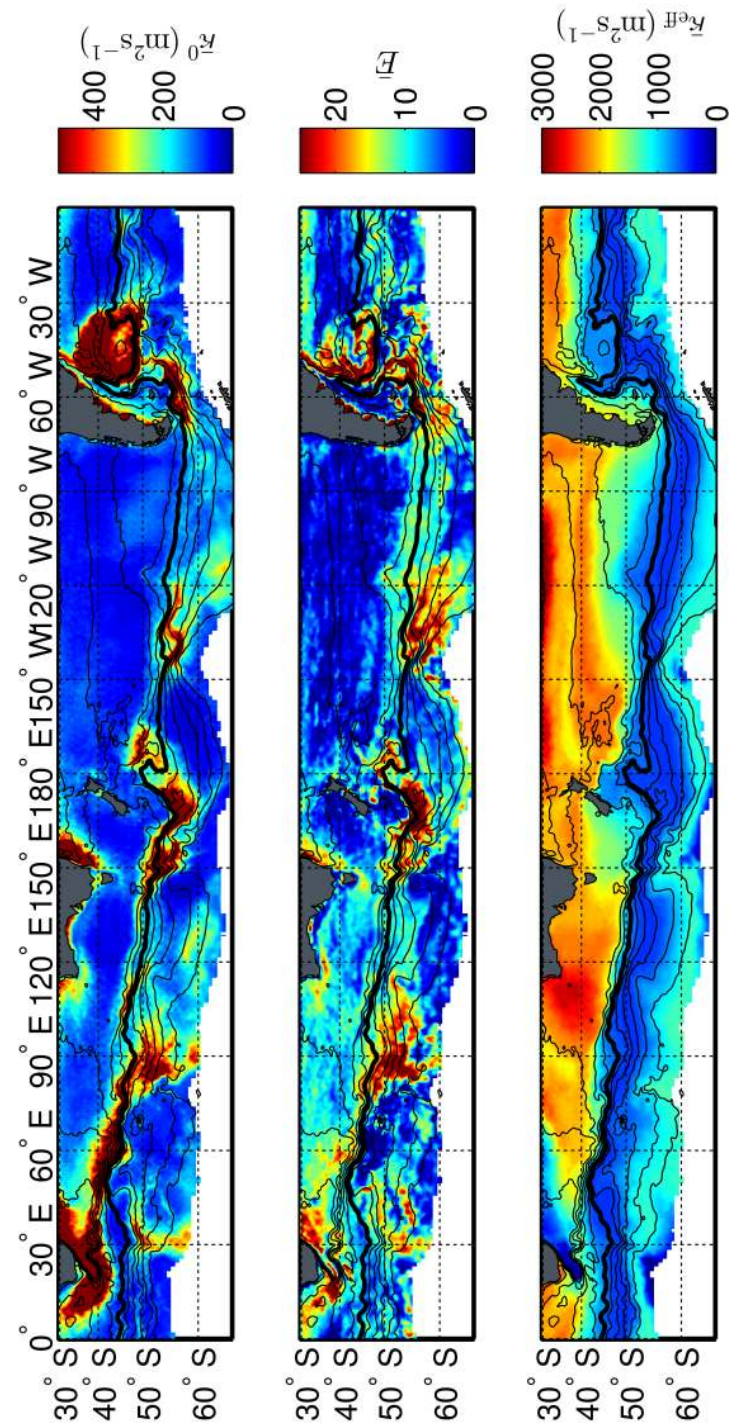


Figure 4.19: Top panel: $\bar{\kappa}^0$; middle panel: $\bar{E} = \text{EKE}/(\bar{u} - c)^2$; bottom panel: κ_{eff} , mean from 1993-2010. $\bar{\kappa}^0$, EKE, \bar{u} and c are calculated from altimetry, see text for details. Note that κ_{eff} is a 1D quantity and the spatial distribution is found by plotting it along tracer contours. Mean SSH contours in black.

core, although the qualitative match is still generally poor.

The form of $\bar{\kappa}^0$ (the stationary eddy mixing) and $\bar{E} = \overline{\text{EKE}/(\bar{u} - c)}$ (the contribution from suppressed mixing) can be seen in figure 4.19, along with the full time mean replotted κ_{eff} , where we have used d_1 as found in the previous section for defining κ^0 . $\bar{\kappa}^0$ shows raised values along the ACC near topographic features (Drake Passage, Kerguelen Plateau, Macquarie Ridge, and the Pacific Antarctic Ridge), as well as in the western boundary currents. \bar{E} is more noisy, but generally shows similar structure to $\bar{\kappa}^0$, with additional activity in patches in the ACC core. Calculating the same quantities in the time mean, i.e. $\hat{\kappa}^0$ and \hat{E} , has little effect on the form of either, but affects the magnitude of both.

This can be seen in figure 4.20 which shows the streamwise-means of the quantities in figure 4.19 [$\bar{\kappa}^0$ and \bar{E}] (solid lines) as well as $\hat{\kappa}^0$ and \hat{E} (dashed lines). Note that $\hat{\kappa}^0$ (green dashed lines) is the same quantity plotted in figure 4.18, and we have rescaled E to fit it on the same axes. In both mean-anomaly decompositions, κ^0 has a pronounced peak in the ACC core. The time-filtered decomposition shows fairly uniform structure elsewhere, whereas the AVISO decomposition shows raised values to the North. E is similar in both decompositions, with lower values to the north of $\sim 45^\circ\text{S}$. This is the opposite of what is found in Shuckburgh et al. (2009a), as can be seen in figure 4.13b which shows the streamwise-mean of \bar{E} in light grey, with higher values to the north of the ACC. This is largely due to the very low values of E that we find in the Pacific, see figure 4.19, due to the larger phase speeds and lower u found here in comparison to Shuckburgh et al. (2009a) (see figure 4.8). Thus, whilst we found quantitatively similar values of E within the ACC as in Shuckburgh et al. (2009a), in the streamwise average we find lower values to the north, and not higher as in that study.

Effective diffusivity with and without a mean flow

Both Ferrari and Nikurashin (2010) and Klocker et al. (2012) use effective diffusivity calculations with $U_0 = 0$ to provide further information for determining their free parameters by using it to define the magnitude of the mixing suppression. We find:

$$\kappa^\alpha|_{\bar{u}=0} = \frac{\kappa^0}{1 + 0.5d_0^2c^2/\text{EKE}}, \quad (4.6)$$

and so

$$\frac{\kappa^\alpha}{\kappa^\alpha|_{\bar{u}=0}} = \frac{E/0.5d_0^2 + c^2/(\bar{u} - c)^2}{E/0.5d_0^2 + 1}. \quad (4.7)$$

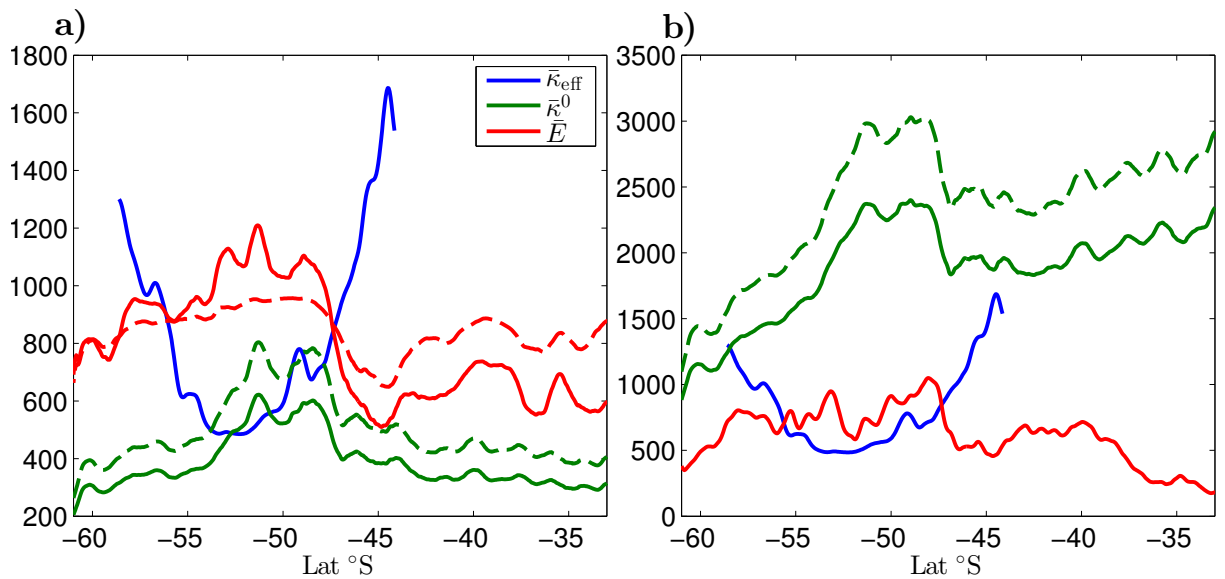


Figure 4.20: Streamwise averages of κ_{eff} , κ^0 (eddy-only mixing), and $E = \text{EKE}/(\bar{u} - c)^2$ (mean-flow suppressed mixing), where E has been scaled arbitrarily fit on the same axes. The solid lines indicate time-means of quantities calculated at each time step, and the dashed lines $\hat{\kappa}^0$ and \hat{E} , see text for details. Mean-anomaly decompositions from a) time filtering and b) AVISO.

We can attempt to fit this to the form of $\kappa_{\text{eff}}/\kappa_{\text{eff}}|_{\bar{u}=0}$ to find d_0 : the form of this and $c'^2 = c^2/(\bar{u} - c)^2$ can be seen in figure 4.21, where again both the means $\overline{c'^2}$, $\overline{\kappa_{\text{eff}}/\kappa_{\text{eff}}|_{\bar{u}=0}}$ (solid lines) and quantities in terms of means $\hat{c}'^2 = \hat{c}^2/(\bar{u} - c)^2$, $\bar{\kappa}_{\text{eff}}/\bar{\kappa}_{\text{eff}}|_{\bar{u}=0}$ (dashed lines, noting \hat{c}'^2 is equal to $\overline{c'^2}$ for the AVISO mean-anomaly decomposition) are shown for the time filtering mean-anomaly decomposition. The ratio is different for the two decompositions as the effective diffusivity calculation for $\bar{u} = 0$ is based on the respective mean fields, see figure 4.18 for the full forms of $\bar{\kappa}_{\text{eff}}|_{\bar{u}=0}$. In the robust region $\kappa_{\text{eff}}/\kappa_{\text{eff}}|_{\bar{u}=0}$ has a minimum in the ACC core for both decompositions, and is < 1 , indicating mixing suppression.

We see extremely close results for $\overline{\kappa_{\text{eff}}/\kappa_{\text{eff}}|_{\bar{u}=0}}$ and $\bar{\kappa}_{\text{eff}}/\bar{\kappa}_{\text{eff}}|_{\bar{u}=0}$, indicating that the ratio is fairly time invariant. However, in figure 4.21a, c'^2 is affected by the method of calculating, with \hat{c}'^2 showing higher values and no clear minimum in the ACC core, whereas \hat{c}'^2 has a similarly located minimum. In figure 4.21b there is only one form of c'^2 as both c and \bar{u} are time invariant. This shows a qualitatively similar minimum to the effective diffusivity close to the ACC core.

The ratio $\kappa^\alpha/\kappa^\alpha|_{\bar{u}=0}$ is bounded by c'^2 [$d_0^2 \rightarrow 0$] and 1 [$d_0^2 \rightarrow \infty$]. This means that, in order to find a real value of d_0 , $\kappa_{\text{eff}}/\kappa_{\text{eff}}|_{\bar{u}=0}$ must lie between 1 and c'^2 . This is not consistently satisfied for either mean-anomaly decomposition, for either $\overline{\kappa_{\text{eff}}/\kappa_{\text{eff}}|_{\bar{u}=0}}$ or $\bar{\kappa}_{\text{eff}}/\bar{\kappa}_{\text{eff}}|_{\bar{u}=0}$, which means we cannot fit (4.7). This implies that the values of c derived from altimetry are not the relevant phase speeds (as implied by the [Klocker et al. \(2012\)](#) results), or that \bar{u} is not sufficiently spatially uniform or zonal to fulfil the theoretical assumptions in the derivation of κ_y .

For reference we also show least-squares fits of $\kappa_{\text{FN}}/\kappa^0 = 1/(1 + 2d_2|\nabla\bar{h}|^2/|\nabla h'|^2)$ to $\kappa_{\text{eff}}/\kappa_{\text{eff}}|_{\bar{u}=0}$ in figure 4.21 (black lines). For the time-filtered decomposition, we find negative values of d_2 for both ratios: -0.01 for fitting $\bar{\kappa}_{\text{eff}}/\bar{\kappa}_{\text{eff}}|_{\bar{u}=0}$ to $\hat{\kappa}_{\text{FN}}/\hat{\kappa}^0$ (solid lines), and -0.3 for fitting $\overline{\kappa_{\text{eff}}/\kappa_{\text{eff}}|_{\bar{u}=0}}$ to $\overline{\kappa_{\text{FN}}/\kappa^0}$ (dashed lines), and the fit doesn't show qualitative agreement, being flat throughout the domain. d_2 is negative as $\kappa_{\text{eff}}/\kappa_{\text{eff}}|_{\bar{u}=0} > 1$ for most of the region, and the form of $\kappa_{\text{FN}}/\kappa^0$ only allows for mixing enhancement via $d_2 < 0$ if $|\nabla\bar{h}|^2 > |\nabla h'|^2$, as indeed it is for both decompositions. For the AVISO decomposition we see similarly flat structure, but find positive $d_2 = 0.4$ for $\bar{\kappa}_{\text{eff}}/\bar{\kappa}_{\text{eff}}|_{\bar{u}=0}$ and 2 for $\overline{\kappa_{\text{eff}}/\kappa_{\text{eff}}|_{\bar{u}=0}}$. The $\bar{\kappa}_{\text{eff}}/\bar{\kappa}_{\text{eff}}|_{\bar{u}=0}$ d_2 values are close to those we found previously by tuning the full form of κ_{FN} , but as previously, we find no qualitative agreement with our effective diffusivity calculation.

Thus, while the magnitudes of κ_{FN} and κ^0 matched our results for the same constants found in [Ferrari and Nikurashin \(2010\)](#), we did not find good agreement with the

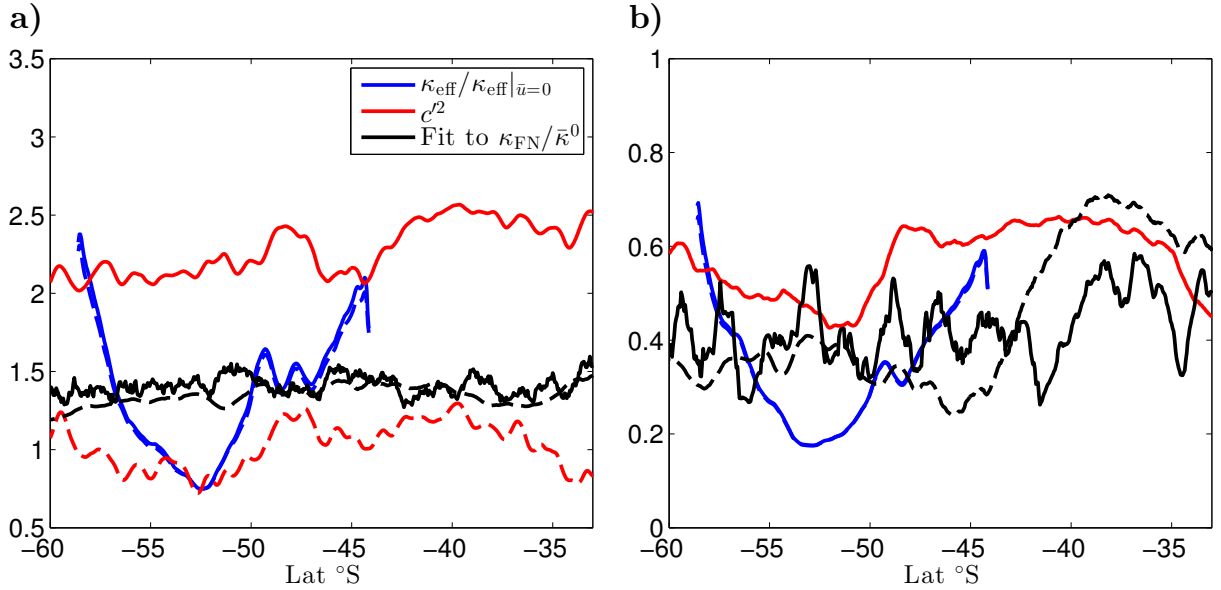


Figure 4.21: Ratio of effective diffusivities from tracer fields advected with and without the mean flow field (blue lines); c'^2 (red lines); and least squares fit to $\kappa_{\text{FN}}/\bar{\kappa}^0$ (black lines). Solid lines: time means (\cdot); dashed lines: in terms of time means (\cdot). Mean-anomaly decomposition from a) time filtering and b) AVISO.

streamwise average of either κ_{FN} or κ^α to κ_{eff} . The failure to fit κ_{FN} rules out $c \propto U_0$ or $c \ll U_0$. The failure to fit κ^α could indicate that a) the c derived from altimetry is indeed unrelated to the mixing eddies or b) the theory does not apply, because the mean-flow mixing suppression is a non-linear effect, the spatial scale separation assumption between the mean and anomaly fields is not satisfied, or the mean field is not sufficiently uniform and zonal. The latter argument is weakened by the fact that the very spatially smooth AVISO mean field does not result in a fit any better than that resulting from the more structured time-filtered mean field.

The success of [Ferrari and Nikurashin \(2010\)](#) at fitting κ_{FN} using the previous generation altimetry must be related to the properties of the old altimetry data. We have seen that the EKE is somewhat lower in the new dataset, and the zonal velocities are generally larger in the ACC core, leading to the larger mixing suppression effect seen here (we see a minimum of $\bar{\kappa}_{\text{eff}}/\bar{\kappa}_{\text{eff}}|_{\bar{u}=0} = 0.2$ for the AVISO decomposition in the ACC core, compared to ~ 0.4 in [Ferrari and Nikurashin \(2010\)](#) for the full ACC calculation). We have also seen that the mean flow field is much less spatially uniform and smooth in the new dataset (see figure 4.14) Thus we postulate that the combination of a more active

eddy field, and a weaker more uniform and zonal mean flow in the previous altimetry lent it to decompose more readily and better fit the assumptions of κ_{FN} .

4.4.3 Temporal Variability

Although we cannot match the form of κ^α or κ_{FN} to the spatial distribution of κ_{eff} , we can compare the temporal variability of κ^0 and E with κ_{eff} to see if they have any correlation. Figure 4.22 shows time series of all three over the same two latitude bands as in figure 4.16, where we have rescaled κ^0 and E to have the same mean and standard deviation as κ_{eff} , and both are calculated using the time-filtered mean-anomaly decomposition. κ^0 is not closely linked to κ_{eff} in the northern latitude band, but E is weakly correlated ($R^2 = 0.24$) with statistical significance ($p < 0.05$). In the ACC band, both are correlated with κ_{eff} , however E is slightly more strongly correlated ($R^2 = 0.50$) than κ^0 ($R^2 = 0.46$). This is complemented by the fact that κ_{eff} is not significantly correlated with \bar{u} or EKE in the northern band, but in the southern band shows significant and similarly moderate anti-correlation with \bar{u} ($R^2 = -0.31$) and correlation with EKE ($R^2 = 0.50$). If we calculate the same correlations with the AVISO mean-anomaly decomposition, we find no significant correlation between E and κ_{eff} , and find κ^0 is weakly *anti*-correlated with κ_{eff} in both latitude bands ($R^2 \sim -0.3$). We find no significant correlation between the AVISO mean-anomaly EKE and κ_{eff} in either latitude bands.

The fact that the time-filtered decomposition produces higher and more significant correlations with κ_{eff} suggests that it is capturing the temporal properties of the relevant mixing mechanisms better than the AVISO decomposition. The higher correlation coefficient for E in the ACC core is consistent with the finding that the mean-flow suppression is maximum in this region.

Also shown in figure 4.22 is the Southern Annular Mode (SAM) index time-lagged by two years (dashed grey line), which is the leading mode of atmospheric variability in the Southern Hemisphere. The index was obtained from the National Centers for Environmental Protection website¹, and is calculated by projecting the daily 700mb height anomalies poleward of 20°S onto the loading pattern of the Antarctic Oscillation, itself obtained from year-round monthly mean anomaly data. Morrow et al. (2010) use the AVISO SLA to calculate EKE from 1993-2008, and find correlations between EKE and a two-three year lagged SAM index, with maximum $R^2 \sim 0.5$ found in the South Pacific. We found weak positive correlation between both EKE series (derived from either

¹<http://www.ncep.noaa.gov>

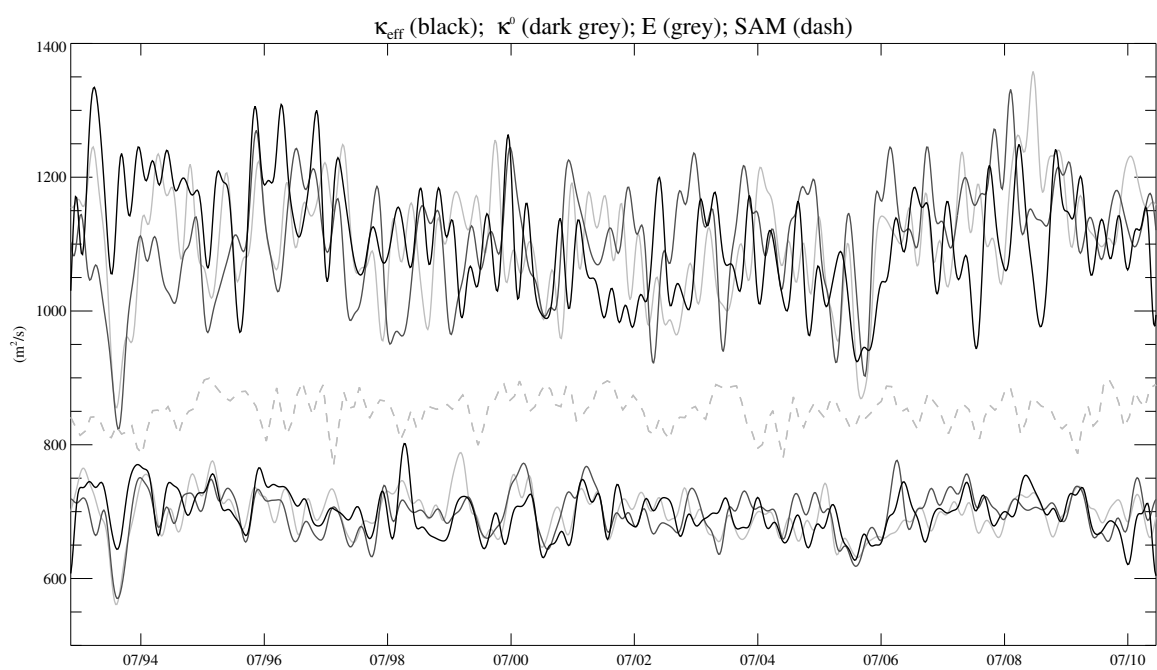


Figure 4.22: Time series of κ_{eff} (black), κ^0 (dark grey), and E (grey), averaged over the equivalent latitude bands $44.15\text{--}48.60^\circ\text{S}$ (upper curves) and $48.65\text{--}58.60^\circ\text{S}$ (lower curves). Dashed line: SAM index.

mean-anomaly decomposition) and the SAM index at ~ 2 years lag, but this was not significantly different from weak correlations at other lags. Similarly, we found no significant correlation between the SAM index at lags of up to 4 years and κ_{eff} . This may be due to the localised nature of the correlations found in [Morrow et al. \(2010\)](#), which are smeared out in the stream-wise averaging of κ_{eff} and EKE. This indicates that their result, and a similar result found in [Meredith and Hogg \(2006\)](#), while possibly relevant locally, is not significant dynamically in the stream-wise average on an intra-decadal scale.

4.5 Conclusions

This chapter has investigated the effect a new generation of altimetry has on an effective diffusivity calculation in the Southern Ocean, and the implications this has for mixing mechanisms and alternative mixing parametrisations.

Direct comparison between the old and new altimetry sets showed that the new set showed a westward change at small zonal velocities, but stronger zonal velocities throughout the ACC core. Meridional velocities decreased generally, with the largest changes in eddy-active regions. The mean EKE was lower throughout the Southern Ocean, and the phase speeds of the most energetic eddies were similar within the ACC but more strongly westward to the north, especially in the Pacific.

We also compared two alternative mean-anomaly decompositions of the full sea surface height (absolute dynamic topography). The first was the decomposition provided by AVISO, who produced the altimetry data set, which used the mean dynamic topography 1996-1999 to define anomalies. For the second we produced a time-varying mean field by passing the full SSH through a low-pass Butterworth filter with a cut-off of 3 months. This produced a mean field that was less spatially uniform, but that removed the effects of sea-level rise and seasonal cycles from the anomaly field.

Using the new altimetry, we calculated an effective diffusivity for 18 years from 1996 to 2010. This was carried out in overlapping 100 week runs, by advecting a tracer field initialised with the mean SSH field. Discounting a 30 week spin-up period, we found overlapping robust values from effective latitudes 58.60°S to 43.15°S . However, the better resolution of eddy structures in the velocity fields is thought to have caused the calculation of effective diffusivity to be non-robust in the northern parts of the domain. The effective diffusivity is calculated in area-based coordinates, and is dependent on the length of tracer contours, deformed by the velocity field. Comparing effective diffusivities at a single time from simulations of different lengths (initialised at different times) showed that the regions of high eddy activity contained many tracer contours that passed out of the domain, closed loop contours, as well as relatively high homogeneity of tracer values. All of these are detrimental to the effective diffusivity calculation, and so the calculations in this region showed dependence on time since initialisation beyond the expected adjustment time. This led to the calculation at equivalent latitudes north of 43.15°S being non-robust, and so these were left out of temporal analysis.

The stronger zonal flow in the ACC core (thought to suppress mixing) in the new altimetry resulted in a reduced time mean 1996-2010 eddy diffusivity of $\sim 500\,\text{m}^2\text{s}^{-1}$

in the ACC core ($55 - 50^{\circ}\text{S}$), rising to $\sim 1500 \text{ m}^2\text{s}^{-1}$ to the north, compared with $\sim 900 \text{ m}^2\text{s}^{-1}$ and $\sim 1500 \text{ m}^2\text{s}^{-1}$, respectively, in Shuckburgh et al. (2009a) for 1996-2001 and Abernathey et al. (2010) for 2005-2006, from the old altimetry. These results are almost identical to those of Abernathey and Marshall (2013), who use the same (new) altimetry for an effective diffusivity calculation in an east Pacific sector (180° to 130°W). Liu et al. (2012) estimate eddy diffusivities from the GECCO¹ synthesised observations and STORM² model output separately, defining the mixing length as the minimum of the first baroclinic deformation radius and the Rhines scale, and similarly find very low values in the ACC core, with peaks of $1000\text{-}2000 \text{ m}^2\text{s}^{-1}$ on the northern flanks. Sallée et al. (2008) use real and numerical float tracks to estimate surface Lagrangian diffusivities, and find much larger values, with a background of $1800 \pm 1000 \text{ m}^2\text{s}^{-1}$ and peaks of $10^4 \text{ m}^2\text{s}^{-1}$ in western boundary currents and over topographic features in the ACC. However, as discussed in detail by the authors, this measure is not directly comparable to effective diffusivities as it measures mixing on a much coarser scale, and is not streamwise-averaged.

The lower values of diffusivity found in the ACC core found here have interesting possible implications for the surface buoyancy fluxes and water-mass formation processes in this region. Badin and Williams (2010) examine in detail these processes using an isopycnal framework applied to three observation-based datasets, and find that an increase in eddy diffusivity of $500 \text{ m}^2\text{s}^{-1}$ leads to a 3 W m^{-2} decrease in the surface heat flux and slight decreases in the dense water formation rates. Thus we might expect that the decrease in eddy diffusivity found here might imply an increase in the surface flux and formation rates. Marshall et al. (2006) similarly investigate the implications of their effective diffusivity for surface buoyancy fluxes in a stream-wise averaged momentum balance, and we would like to investigate this further in future work - especially given that buoyancy fluxes observations in this region are poorly constrained.

Looking at the temporal variability of the effective diffusivities averaged over two latitude bands, one covering the ACC core ($58.60 - 48.65^{\circ}\text{S}$) and the other to the north ($48.60 - 44.15^{\circ}\text{S}$) we found no discernible trend in values over the full 18 years. The northern band exhibited higher variability than the poleward, but had an equivalently higher mean value. There was a weak seasonal cycle in both bands, showing a slight peak in October.

Previous studies have attempted to use the results of effective diffusivity calculations to tune alternative eddy diffusivities based on the altimetric fields. Both Ferrari and

¹German Estimating the Circulation and Climate of the Ocean, see Köhl et al. (2007)

²See <https://verc.enes.org/community/projects-and-partnerships/projects/storm>

Nikurashin (2010) and Klocker et al. (2012) tune similar eddy diffusivity expressions to effective diffusivities based on the previous generation of altimetry. The eddy diffusivities are based on linear analysis of quasi-geostrophic flows, and crucially assume spatial scale separation between the zonal mean flow and the eddy (anomaly) field. The expressions take the form of a stationary eddy mixing term, similar to that of Holloway (1986), which is modified by a mean-flow term, dependent on eddy scales, the mean flow, and the phase speed of the eddies, resulting in maximum mixing when the eddies are stationary relative to the mean flow.

As in Ferrari and Nikurashin (2010) and Klocker et al. (2012), we find mixing suppression by the mean flow throughout the ACC when we compare effective diffusivity calculations with and without the AVISO mean flow. Comparing magnitudes, the maximum suppression is higher in this study, consistent with the stronger mean zonal flow compared to the older altimetry. The time-filtered mean flow, however, was only found to suppress mixing in the ACC core, and enhanced mixing elsewhere.

Whilst Klocker et al. (2012) tuned their expression independently at each latitude in a Pacific sector of the ACC, Ferrari and Nikurashin (2010) assumed that the phase speed of the mixing eddies was proportional to, and much less than, the zonal mean flow, and found an expression, κ_{FN} , that matched their effective diffusivity for the full ACC and only depended on two tuned parameters. However, we did not find that this expression matched our effective diffusivity qualitatively, even though the magnitudes were similar.

Given that the forms of κ_{FN} or κ^0 did not fit our effective diffusivity calculations, with or without mean flow respectively, we attempted to fit a similar expression, κ^α , which relaxed the assumption that the eddy phase speed c is proportional to the zonal mean flow. Klocker et al. (2012) asserted that c calculated from altimetry was not related to the eddies responsible for mixing, and we tested this by using it in the calculation of the mixing suppression. Whilst we found that the qualitative form of the mixing suppression from κ^α more closely resembled the mixing suppression from the effective diffusivity than κ_{FN} , it was not possible to find parameters to match our data.

The failure to fit κ_{FN} to our data suggests that the new altimetry does not fit the assumptions of Ferrari and Nikurashin (2010), whereas the old did. The additional failure to fit κ^α suggests that either the assumptions of the linear quasi-geostrophic theory, for example the spatial separation between the mean flow and the eddies, are not satisfied, or that the relevant eddy phase speed is not that identified from altimetry. The former could be because even the relatively smooth AVISO mean field has more structure in the new altimetry than the old. The latter is consistent with the success of Ferrari and Nikurashin

(2010) if indeed $c \propto U_0$ in the old altimetry, but not in the new, due to the differences in U_0 . Both imply that the altimetry alone cannot produce a simple eddy diffusivity that matches the effective diffusivity, unless one makes the assumptions of each latitude being independent as in Klocker et al. (2012).

Finally, we compared the temporal variability of the various quantities thought to determine the eddy diffusivity with the variability of the effective diffusivity averaged over the same two latitude bands as before. Using the time-filtered mean-anomaly decomposition, we found significant but relatively moderate correlation between the contribution to mixing by mean flow interactions, $EKE/(\bar{u} - c)^2$, and the effective diffusivity in both latitude bands, with a stronger correlation in the ACC band. In the ACC band, we additionally found similar correlations with κ^0 and EKE, and anti-correlation with \bar{u} . This is consistent with the results of Sallée et al. (2008), who find that their surface Lagrangian mixing coefficient is proportional to the EKE within the ACC, but not without¹. Using the AVISO mean-anomaly decomposition, the only significant relationship was a moderate anti-correlation between κ^0 and κ_{eff} in both latitude bands. These results indicate that the time-filtered mean-anomaly decomposition better captures the temporal variability of the mixing occurring, which suggests it better represents the relevant eddy field.

Comparisons between the EKE of both decompositions and the Southern Annular Mode index (the leading mode of atmospheric variability in the Southern Hemisphere) found no significantly enhanced correlation at lags of 2-3 years, as found locally in the Southern Ocean by Meredith and Hogg (2006) and Morrow et al. (2010). This suggests that these results are not relevant at the streamwise averaged scale, on intra-decadal time scales.

¹Note that Klocker et al. (2012) attribute this result of Sallée et al. (2008) to their method not capturing mean flow suppression.

Chapter 5

DIMES: A tracer experiment in the Southern Ocean

5.1 Introduction

Chapter 4 presented the results of an effective diffusivity calculation, which described both the mixing and advection of the mesoscale eddy field at the surface, utilising surface velocity fields derived from satellite altimetry. This chapter presents work that utilised the same surface velocity fields, but rather than a large scale effective diffusivity instead sought to estimate a small-scale Fickian isopycnal diffusivity on a fixed neutral density surface. This was found by comparing data from a tracer release experiment with various simulations reproducing the same release, using an advection scheme with a varied diffusion coefficient. The offline MITgcm model was run at eddy-resolving scales ($1/20^\circ$ or $1/50^\circ$), and so the physical interpretation of this diffusivity is that it represents the sub-mesoscale eddy mixing and stirring active between the molecularly dominated scale and the resolved scales. This is thought to take the form of along-streak strain and across-streak diffusion, see descriptions in Garrett (1983); Ledwell et al. (1998), and neglects vertical mixing, which is many orders of magnitude lower. Note however, that the vertical mixing is important for along-isopycnal mixing, see, for example, Smith and Ferrari (2009).

The literature contains widely varying estimates of the Southern Ocean interior isopycnal diffusivities, and direct measurements are rare, see discussion in Zika et al. (2009). Most in-situ estimates are over relatively large scales, such as Garabato et al. (2007), who estimate an along-isopycnal effective diffusivity of $360 \pm 330 \text{ m}^2\text{s}^{-1}$ in the frontal regions of the ACC and an area average of $1860 \pm 440 \text{ m}^2\text{s}^{-1}$ on the $\gamma_n = 27.98 \text{ kg m}^{-2}$ neutral

density surface using observations over an area of size ~ 1000 km cross-stream by 5000 km along-stream. This is found from the width of cross-stream spreading of a tracer, using floats to estimate time scales. By utilising an eddy-resolving advection scheme, this study gives the opportunity to assess the eddy diffusivity on a smaller scale than would be possible using the observations alone, and which will be relevant to the latest generation of eddy-resolving ocean models.

The Diapycnal and Isopycnal Mixing Experiment in the Southern Ocean (DIMES) is a joint UK and USA program designed to measure interior mixing in the Southern Ocean, through collaborative effort involving observationalists, theoreticians and modellers. The project is motivated by the importance that mixing in the Southern Ocean is believed to play in setting the MOC, as discussed in chapter 1. The experimental side of DIMES was designed to encompass the relatively smooth bathymetry of the east Pacific sector of the Southern Ocean and the relatively rough bathymetry of Drake Passage and the Scotia Sea, see figure 1.2.

Figure 5.1 shows a schematic of the experimental side of the project. This began in early 2009 with the release of a fluorocarbon tracer in the east Pacific sector of the ACC (yellow star), chosen for its low background concentrations and the ability to measure very small concentrations accurately, at the depth of the $\gamma_n = 27.9 \text{ kg m}^{-3}$ neutral density surface. There have been four return research cruises to date to measure the displacement of the tracer, with two more planned. This has coincided with fine- and micro-structure measurements of the turbulence in the region, and a mooring array of instruments deployed in late 2009 (blue star). Over 200 RAFOS (deep Lagrangian drifter) floats were also released (dark blue dots), tracked by sound sources deployed throughout the region (cyan dots).

5.1.1 Results so far

Ledwell et al. (2011) presents the results of the US2 cruise, one year after initial deployment. These show that there is relatively weak mixing in the east Pacific sector upstream of Drake Passage, with tracer measurements giving average diapycnal diffusivities of $(1.3 \pm 0.2) \times 10^{-5} \text{ m}^2 \text{s}^{-1}$. Microstructure measurements from the same cruise give $(0.75 \pm 0.2) \times 10^{-5} \text{ m}^2 \text{s}^{-1}$, around half the value derived from the tracer. Time series from float data show a peak in vertical shear variance in June 2009, which could explain the discrepancy as the tracer diffusivity is inferred from the tracer evolution over a year, whereas the microstructure measurements were taken over one month in Feb/Mar 2010.

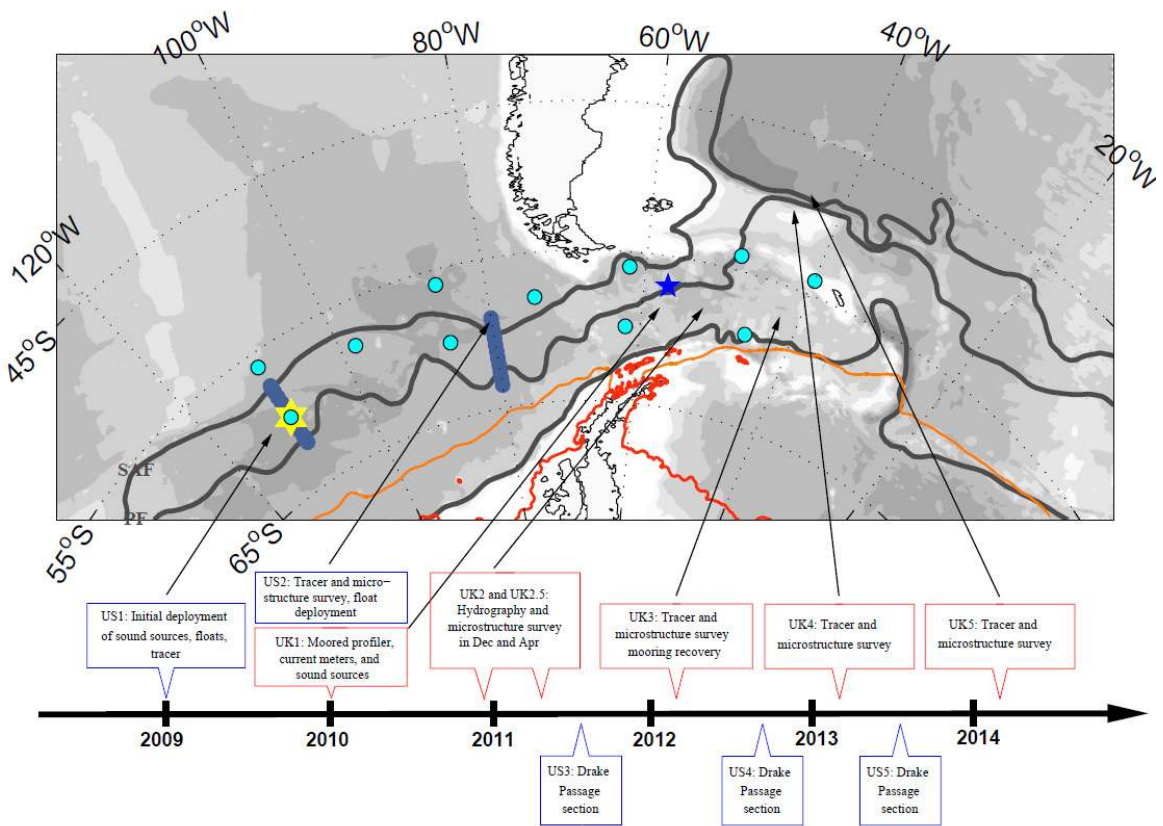


Figure 5.1: Schematic of the DIMEs observational studies. Yellow star: location of tracer release in early 2009; blue star: mooring array deployed late 2009; blue spots: float deployment; cyan spots: sound sources for float tracking. Also shown is the approximate location of the Sub-Antarctic and Polar fronts, the bathymetry, and the mean summer and winter-time sea ice extents. Image from Gille et al. (2012).

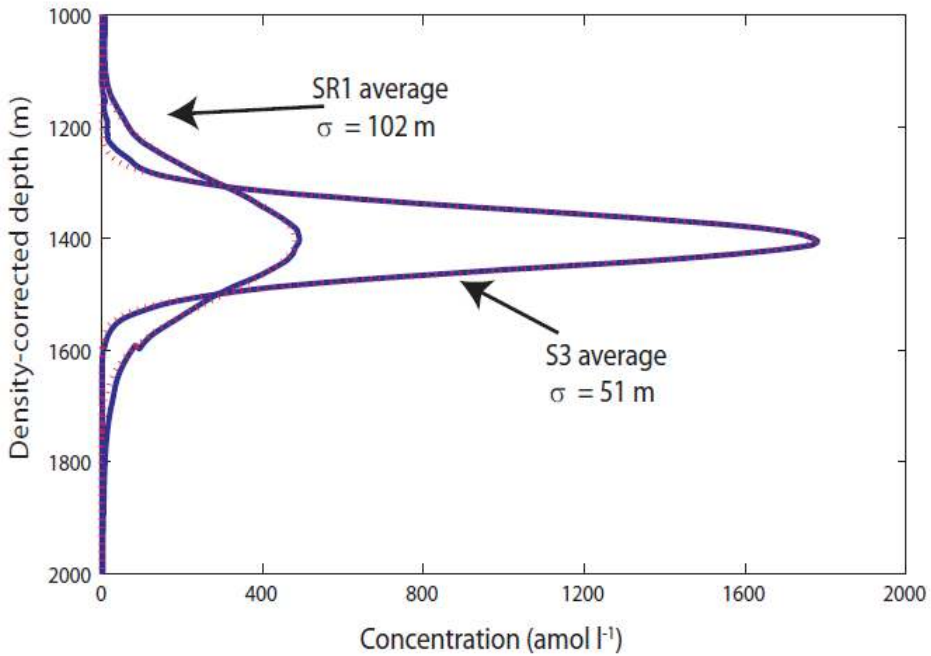


Figure 5.2: Average vertical tracer profiles from DIMES cruise UK2.5, which imply an average diffusivity of $\sim 6 \times 10^{-4} \text{ m}^2 \text{s}^{-1}$ across Drake Passage. Red dotted lines show Gaussian fits to the data. Image from [Gille et al. \(2012\)](#).

Both are similar to background levels measured in other parts of the ocean, which [Ledwell et al. \(2011\)](#) interpret to mean that, despite the high winds found in the region, no extra interior mixing is generated by internal waves.

In contrast, the results presented in [St Laurent et al. \(2012\)](#), which also includes measurements from the UK2 and UK2.5 cruises, show a mean diapycnal diffusivity of $\sim 6 \times 10^{-4} \text{ m}^2 \text{s}^{-1}$ between two meridional transects: the S3 transect, west of Drake Passage and the SR1 transect, east of Drake Passage (see figure 5.4). The tracer measurements used to make this estimate can be seen in figure 5.2, which shows mean vertical profiles along each transect (blue solid lines), along with Gaussian fits to the curves (red dotted line). This confirms that the diapycnal mixing over the rough topography of Drake Passage is much higher than that found upstream - according to [Gille et al. \(2012\)](#), taking into account stratification differences, it is about 30 times larger. The microstructure measurements of shear from this time are consistent with the tracer measurements, showing diffusivities at the tracer release level ($\gamma_n = 27.9 \text{ kg m}^{-3}$ neutral density surface) over rough topography at around 65°W an order of magnitude higher than that found up-

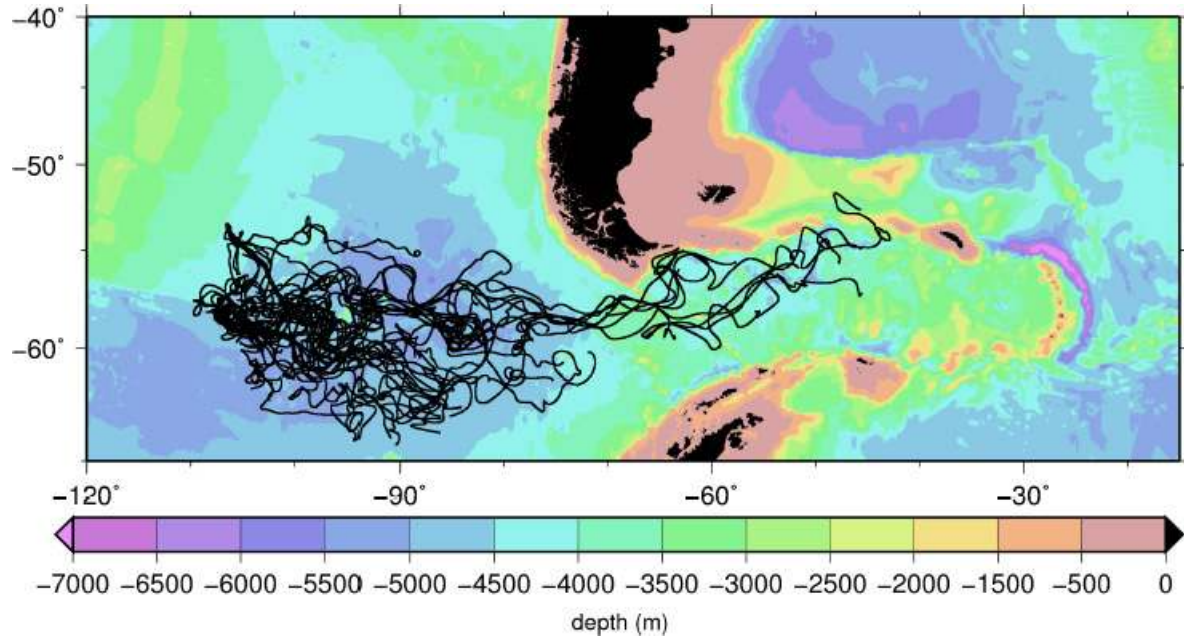


Figure 5.3: RAFOS float trajectories for 44 floats over two years. Colour shows the bathymetry. Most floats remained in the east Pacific basin, but a few were quickly advected downstream towards the Scotia sea. Image from [Gille et al. \(2012\)](#).

stream on the previous cruise, and over smoother topography 3 times higher than the previous cruise. Additionally, there is evidence from vertical microstructure profiles that there is enhanced mixing close to the bottom - over rough topography typical diffusivity values of $10^{-3} \text{ m}^2\text{s}^{-1}$ were measured within 1 km of the bottom.

5.2 2-D simulations

In an attempt to estimate the isopycnal diffusion experienced by the vertically averaged DIMES tracer, we carried out a series of tracer advection numerical simulations using the MITgcm in offline mode, as described in chapter 4, and compared them with observations. Although the real tracer field exists in three dimensions, we advected the tracer in only two dimensions along an isopycnal surface, for the reason that it allowed us to use the measured surface velocity field (from satellite altimetry) to estimate the 2D velocity field on the tracer level. Many observations, e.g. Phillips and Rintoul (2000), and model studies, e.g. Killworth and Hughes (2002), have shown the ACC flow to be equivalent barotropic, and thus we postulated that the flow on the tracer neutral density surface is a constant fraction of that at the surface. 2D simulations are also less computationally intensive than 3D, allowing us to go to greater spatial resolution and carry out multiple realisations of the experiment. Additionally, as can be seen in figure 5.2, the majority of the tracer remains close to the release neutral density surface, as horizontal mixing and diffusion is much greater than that in the vertical on the scales we are investigating - thus although the result is a vertically averaged diffusivity, we assume it is dominated by the diffusivity at the release neutral density.

The disadvantage of this method is that it neglects vertical transport, which, whilst smaller than the horizontal transport, will affect the form of the measured vertically integrated tracer field - as tracer mixed vertically will subsequently be advected at a different speed to that on the original neutral density surface. Additionally, even if the ACC is equivalent barotropic, the relationship between the velocity at the tracer level and the surface velocity may not be constant in space and/or time, and thus reducing the surface velocity by a single constant fraction may be a gross simplification. Keeping these disadvantages in mind, we sought to find a region-wide average approximate isopycnal diffusivity consistent with observations.

5.2.1 Experiment description

We simulated the tracer release by creating an initial tracer field with the same concentration at the same location and time of the real tracer release. We then allowed the simulation to run for 2.5 years, in order to cover the timing of the US2, UK2 and UK2.5 cruises, see figure 5.1.

We initially tested a simple second-order central difference advection scheme, but found that a significant percentage of the tracer field became negative within a few weeks

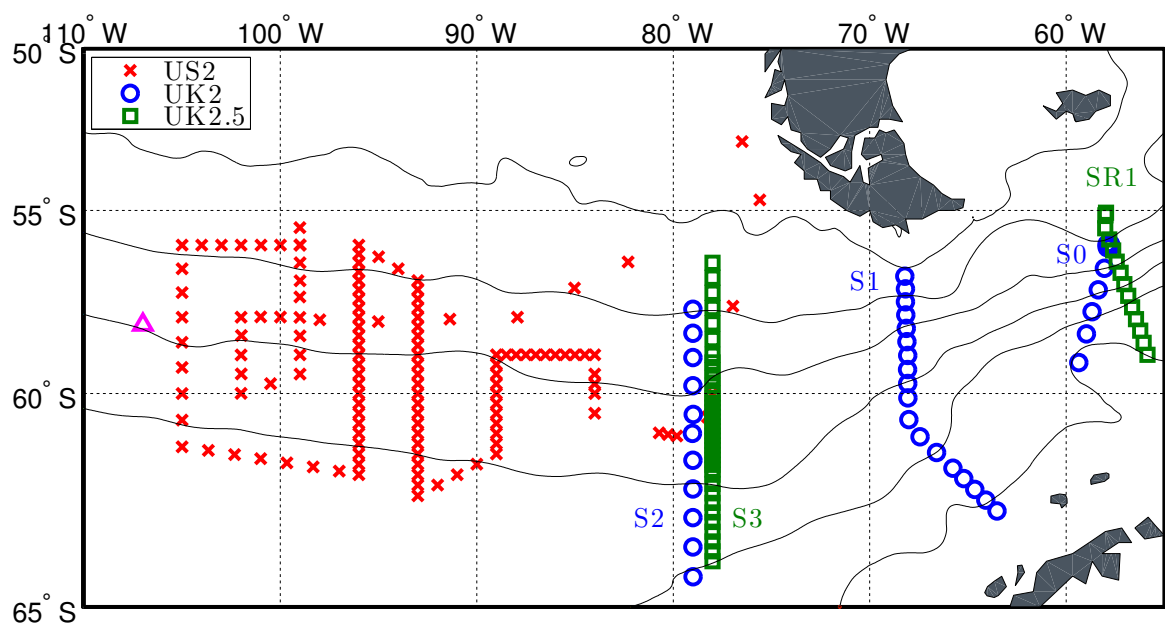


Figure 5.4: Location of tracer measurements in the US2, UK2 and UK2.5 cruises, as indicated. The pink triangle shows the location of the tracer release on the US1 cruise. The lines from the UK2 and UK2.5 cruises are labelled. The contours are mean streamlines, separation $2 \times 10^4 \text{ m}^2 \text{s}^{-1}$.

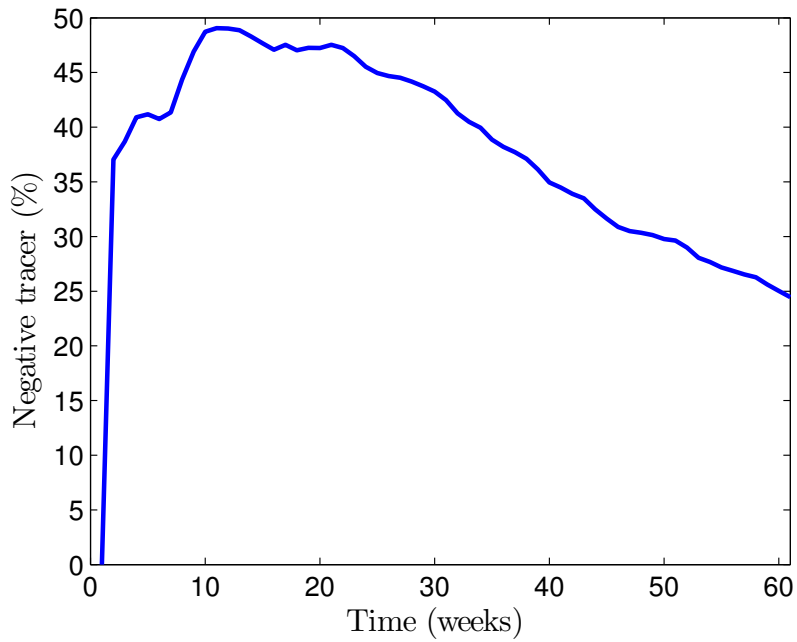


Figure 5.5: Percentage of the non-zero valued tracer field grid cells which are negative, against time in weeks, for a second order central difference $1/20^\circ$ simulation with $k_d = 20 \text{ m}^2\text{s}^{-1}$.

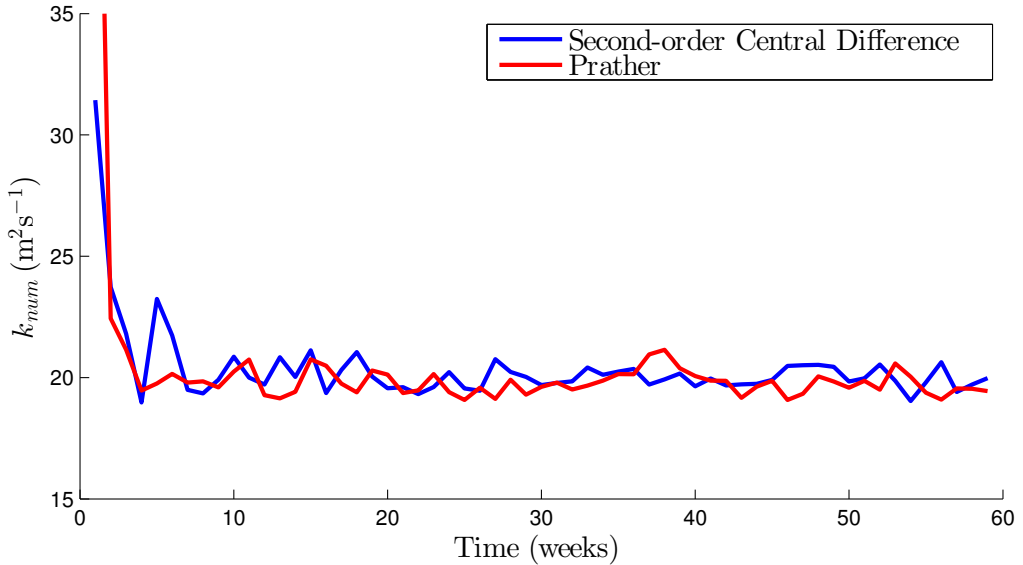


Figure 5.6: Numerical diffusivity calculated from the tracer field versus time for a $1/20^\circ$ simulation with $k_d = 20 \text{ m}^2\text{s}^{-1}$, under a second-order central difference (blue) or Prather (red) advection scheme. Both show quick convergence to a relatively steady value.

of simulation, see figure 5.5. Instead, we chose a second-order moment advection scheme (Prather, 1986) with a limiter ensuring no negative tracer values. The Prather scheme has been shown to be more accurate with better numerical behaviour (see, for example Müller (1992)). In order to reduce the amount of numerical diffusion, one ideally chooses a short time step, but computational limitations result in extremely small time steps being impractical. We settled on a time step of 6 minutes, which results in a small but acceptable amount of numerical diffusion. This can be seen in figure 5.6, which shows the actual numerical diffusivity k_{num} , calculated as in section 4.3.1, for a $1/20^\circ$ simulation with an applied diffusivity of $20 \text{ m}^2 \text{s}^{-1}$, for both Prather and second-order central difference advection schemes. Both advection schemes show quick convergence (after ~ 4 weeks) to a relatively stable value. Figure 5.7 shows an example of the simulated tracer field on the 10th of February 2010 (during the UK2 cruise), with a horizontal diffusivity of $k_d = 2 \text{ m}^2 \text{s}^{-1}$, velocity fraction of 38% and resolution of $1/50^\circ$.

5.2.2 Velocity field analysis

In order to assess the appropriate scale factor to reduce the surface velocities to tracer level velocities (which we will call the ‘velocity fraction’), we looked at two methods. Firstly, we directly calculated the implied velocities given by the RAFOS float locations, as shown in figure 5.3. Each of 42 deep floats (designed to remain on the tracer neutral density surface) had its location recorded daily for up to two years from early 2009, and the locations were turned into approximate velocities using a finite difference approximation. These were then compared with the weekly surface velocities derived from satellite altimetry mentioned previously, linearly interpolated to the same locations and times.

The results of this calculation can be seen in figure 5.8, which shows histograms of the ratio between these two derived velocities, where each point is representative of one velocity measurement on one day. These have been divided up into four longitudinal sections, with roughly the same number of points in each of the first three most westerly sections, but fewer in the fourth as only a small number of floats travelled east of 70°W in the two years of data used. Also shown (red numbers) are the mode (i.e. most common) fractions from the histogram, chosen because the distributions are skewed. These histograms show a longitudinal dependence, with a pronounced increase moving eastward (although the most eastern section has few points), and point to a velocity fraction of 25-43%. This is comparable with the values found within the ACC in the OCCAM model at depths of $\sim 1\text{-}2$ km, see Killworth and Hughes (2002) [their figure 7].

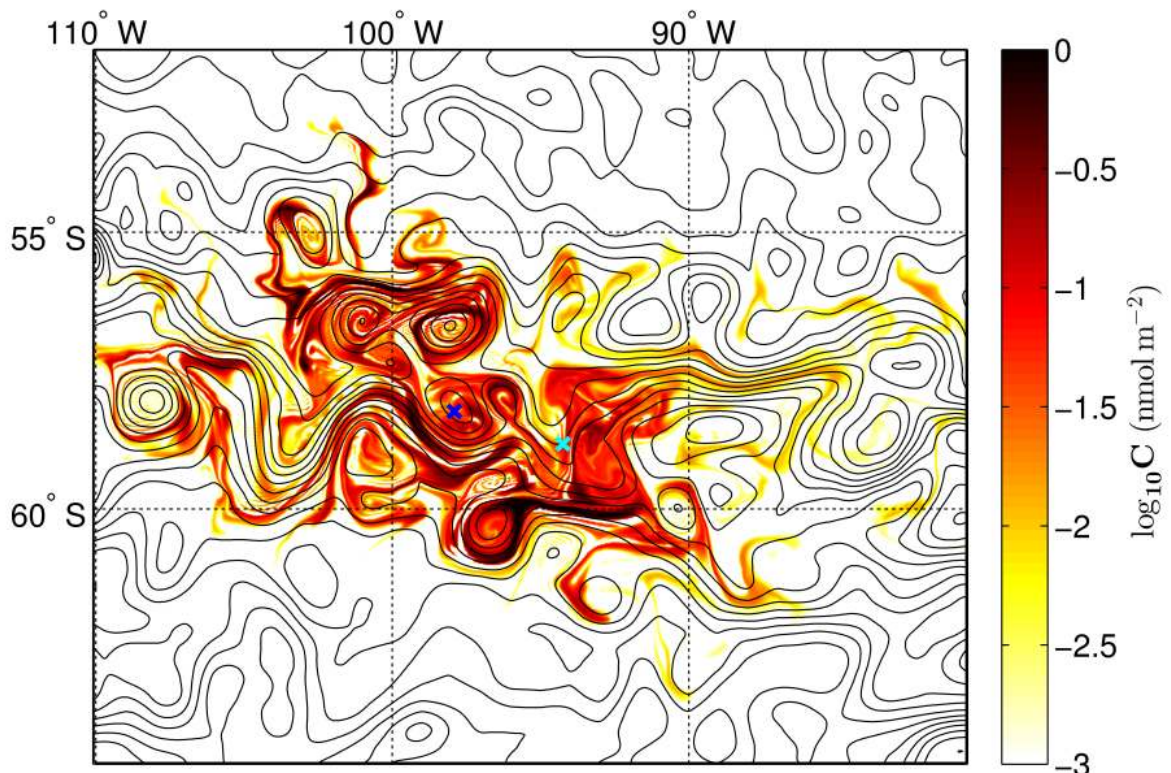


Figure 5.7: Snapshot of tracer concentration (colour, log-scale) on 10th Feb 2010 from MITgcm simulation with $k_d = 2 \text{ m}^2 \text{s}^{-1}$, a velocity fraction of 38%, $1/50^\circ$ resolution. The contours show instantaneous streamlines, the crosses show the tracer centre-of-mass from both simulation (dark blue cross) and the US2 cruise measurements (cyan cross).

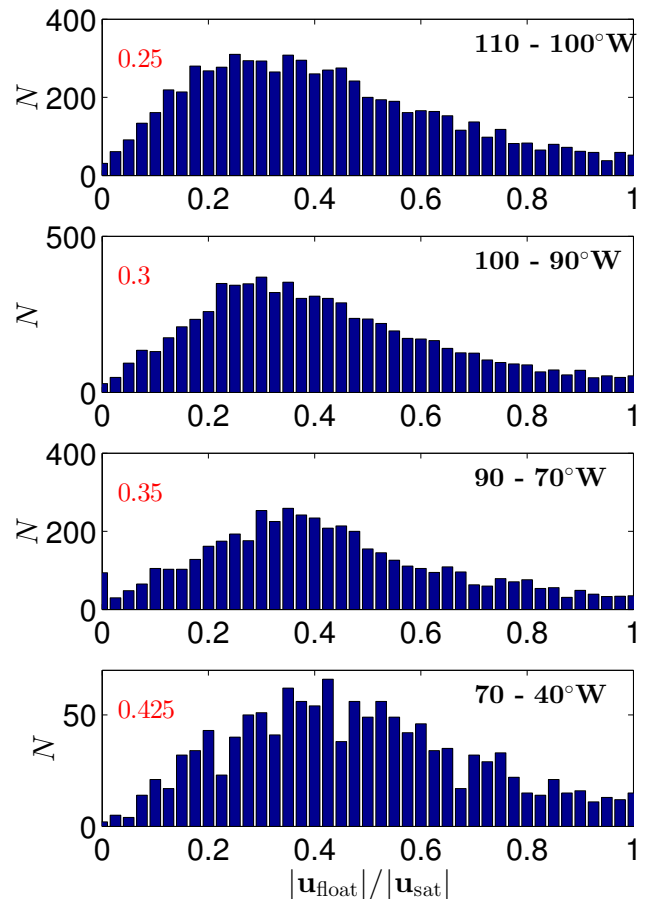


Figure 5.8: Histograms of the ratio between the satellite derived surface velocities and the RAFOS float derived tracer level velocities, divided into 4 longitudinal sections. Also shown are the peak velocity fraction from each histogram.

5.2.3 Varying the velocity fraction

The second method we used to assess the most suitable velocity fraction was to carry out a variety of simulations at fixed horizontal diffusivity and variable velocity fraction, and compared the centre-of-mass of the simulations with the observations. We sub-sampled the simulated tracer field at the same location that tracer measurements were made on the cruises, which can be seen in figure 5.4. At each station, tracer measurements were made at several depths (see fig 5.2), and so we compared the vertically integrated measurement or column integral at each station. Figure 5.9 shows the observed tracer column integrals (black crosses) on the first three return cruises against the along-track distance for each cruise. The first few stations of the US2 cruise are omitted as these are relatively spaced out and have low values of tracer measured. The UK2 and UK2.5 cruises are split into the transects as labelled in figure 5.4, and arranged such that the transects are progressively up-stream, or further to the west, from left to right. Also shown are the tracer fields along the cruise path (coloured lines) and the sub-sampled values at the measurement station locations (coloured circles) from three MITgcm simulations with velocity fractions from 28-48%, and fixed $k_d = 20\text{m}^2\text{s}^{-1}$, $1/20^\circ$ resolution. The lowest velocity fraction, 28%, shows higher up-stream concentrations, similar to the observations, but with a more pronounced asymmetry. As expected, the highest velocity fraction, 48%, has the opposite effect, with higher concentrations downstream. The 33% simulation perhaps appears closest to the magnitudes of the observations.

This can be seen more clearly by directly comparing the centre-of-mass of the observations and the simulations. This can be seen in figure 5.10, where the centre-of-mass of all observations on each cruise is marked by a black circle. The centre of mass of the simulations, sub-sampled identically to the observations, are marked with coloured crosses, with velocity fraction as labelled. The centre-of-mass of the UK2.5 observations is actually further upstream than the UK2 observations, despite being measured at a later date. This is due to the higher number of measurements on the upstream S3 line on this cruise - see figure 5.9. As expected, the spread between the different simulations increases with time, top to bottom, but the observations remain consistently between the 33% and 37% simulations, but closer to 33%, suggesting that the velocity fraction that would reproduce the observations most closely lies at a value of $\sim 34\%$.

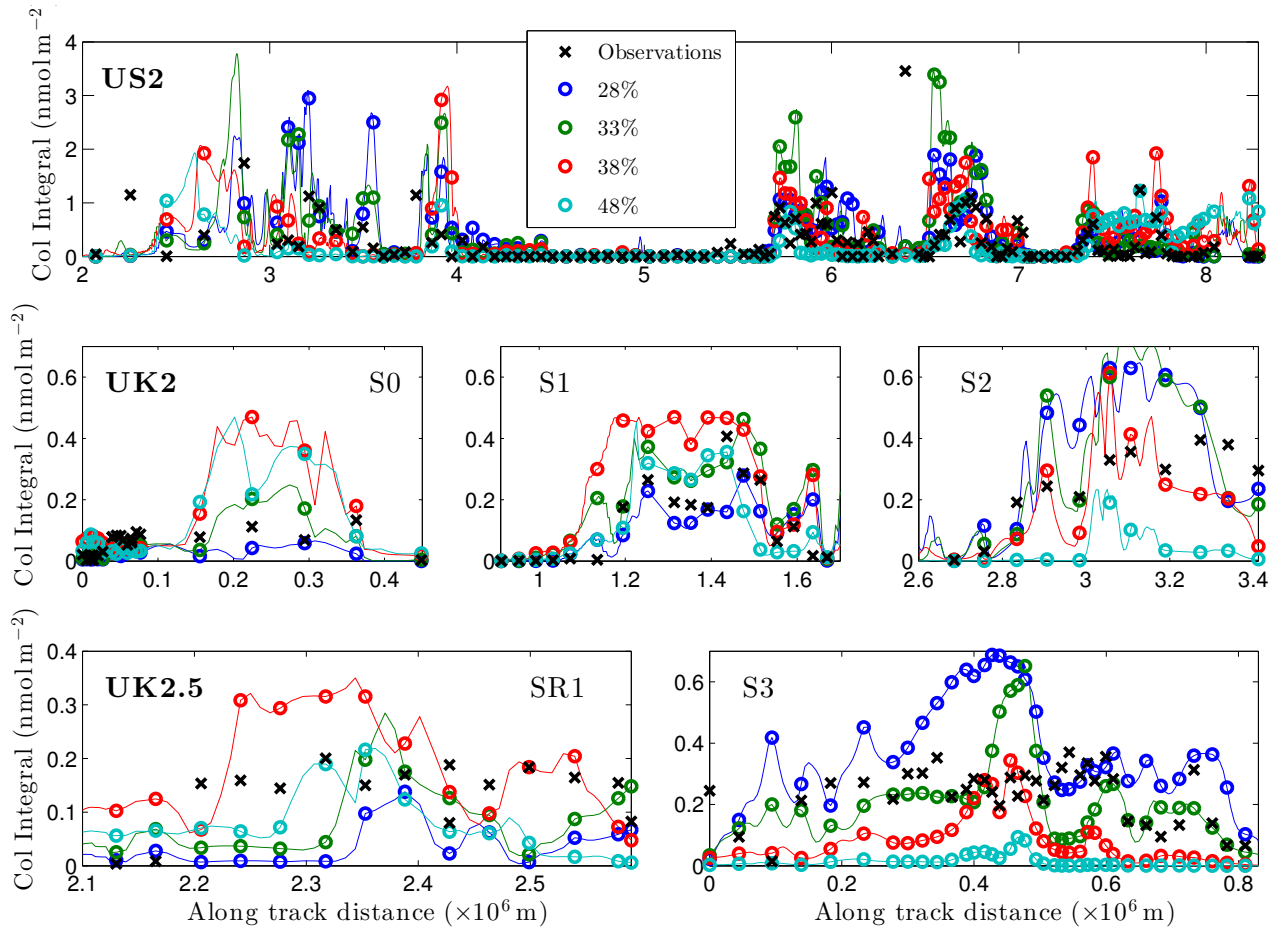


Figure 5.9: Tracer measurements (black crosses) from the first three cruises, as shown in figure 5.4, against the cruise along track distance. Also shown are sub-sampled $1/20^\circ$ simulations (coloured circles) with a fixed horizontal diffusivity of $k_d = 20\text{m}^2\text{s}^{-1}$ as labelled and various velocity fractions, as labelled, with the thin coloured lines showing the simulated tracer between sample points.

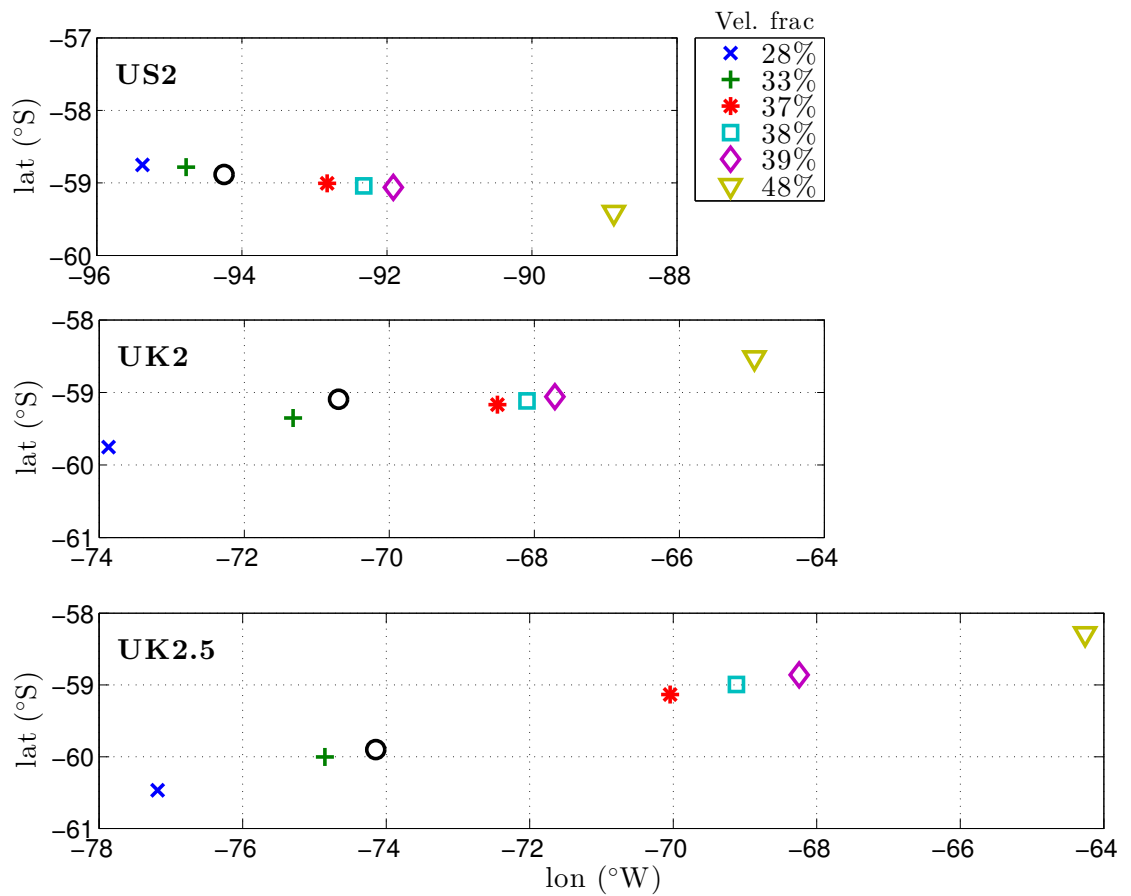


Figure 5.10: Centre-of-mass comparison between observations on the various cruises (black circle) and simulations with $k_d = 20\text{m}^2\text{s}^{-1}$, $1/20^\circ$ resolution and velocity fractions as indicated.

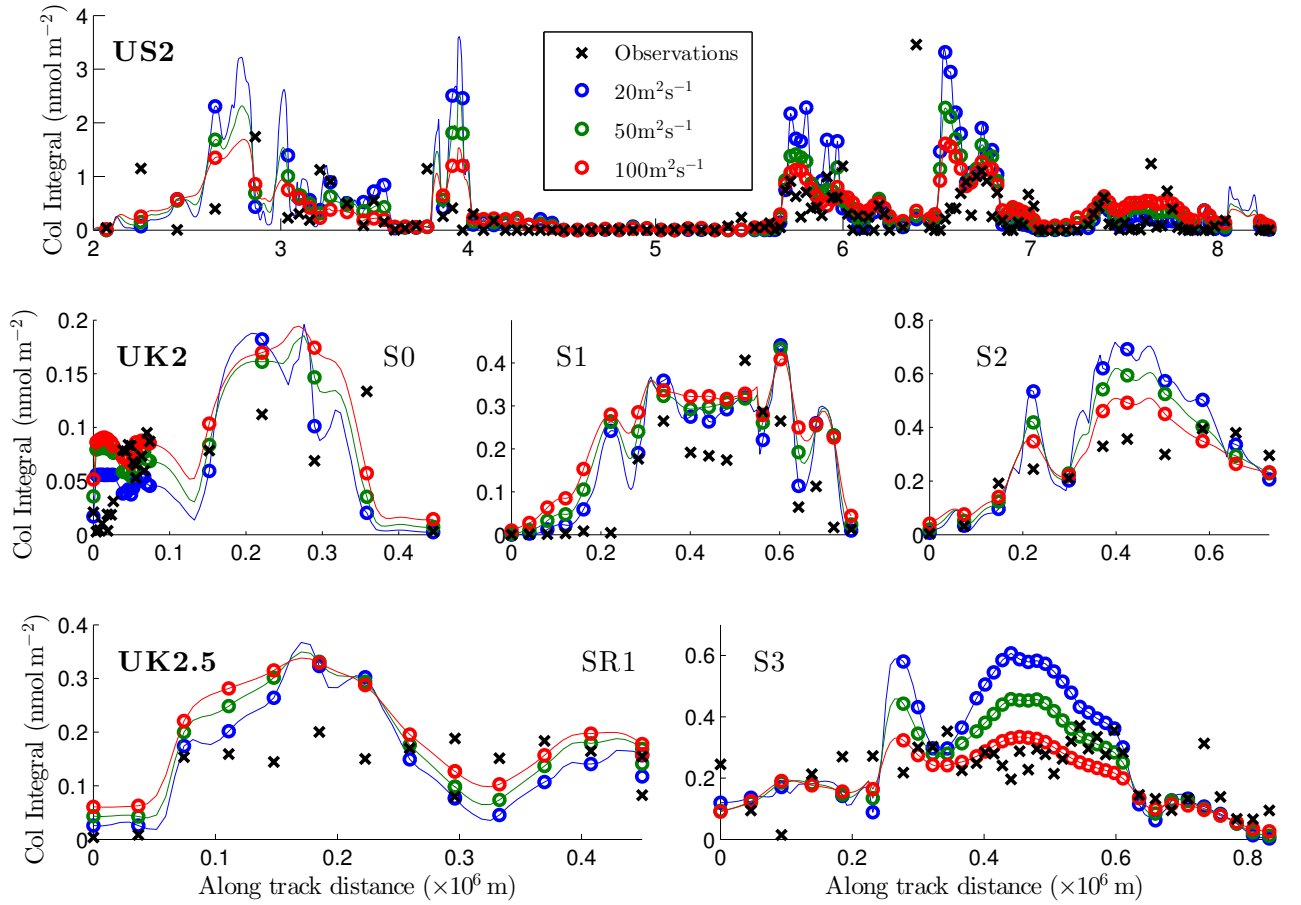


Figure 5.11: As in figure 5.9, but with fixed velocity fraction 33%, $1/20^\circ$ resolution, and different horizontal diffusivities as labelled.

5.2.4 Varying the horizontal diffusivity

Given that a velocity fraction of 33% seems close to the appropriate value needed to ensure the tracer centre-of-mass matches observations, we now turn to assessing the appropriate horizontal diffusivity. Figure 5.11 shows the results from three MITgcm simulations with various horizontal diffusivities $k_d=20, 50, 100\text{m}^2\text{s}^{-1}$ as labelled. All three simulations had a velocity fraction of 33% and a resolution of $1/20^\circ$. Across all of the cruises, the effect of increasing horizontal diffusion can be seen in the smoothing of the tracer field, resulting in less extreme spikes.

The measurements taken on the US2 cruise, one year after release, show remarkable similarity to the simulations, especially in the second half of the cruise track. The simulations and cruise results are less well matched for UK2 and the UK2.5 cruises, but

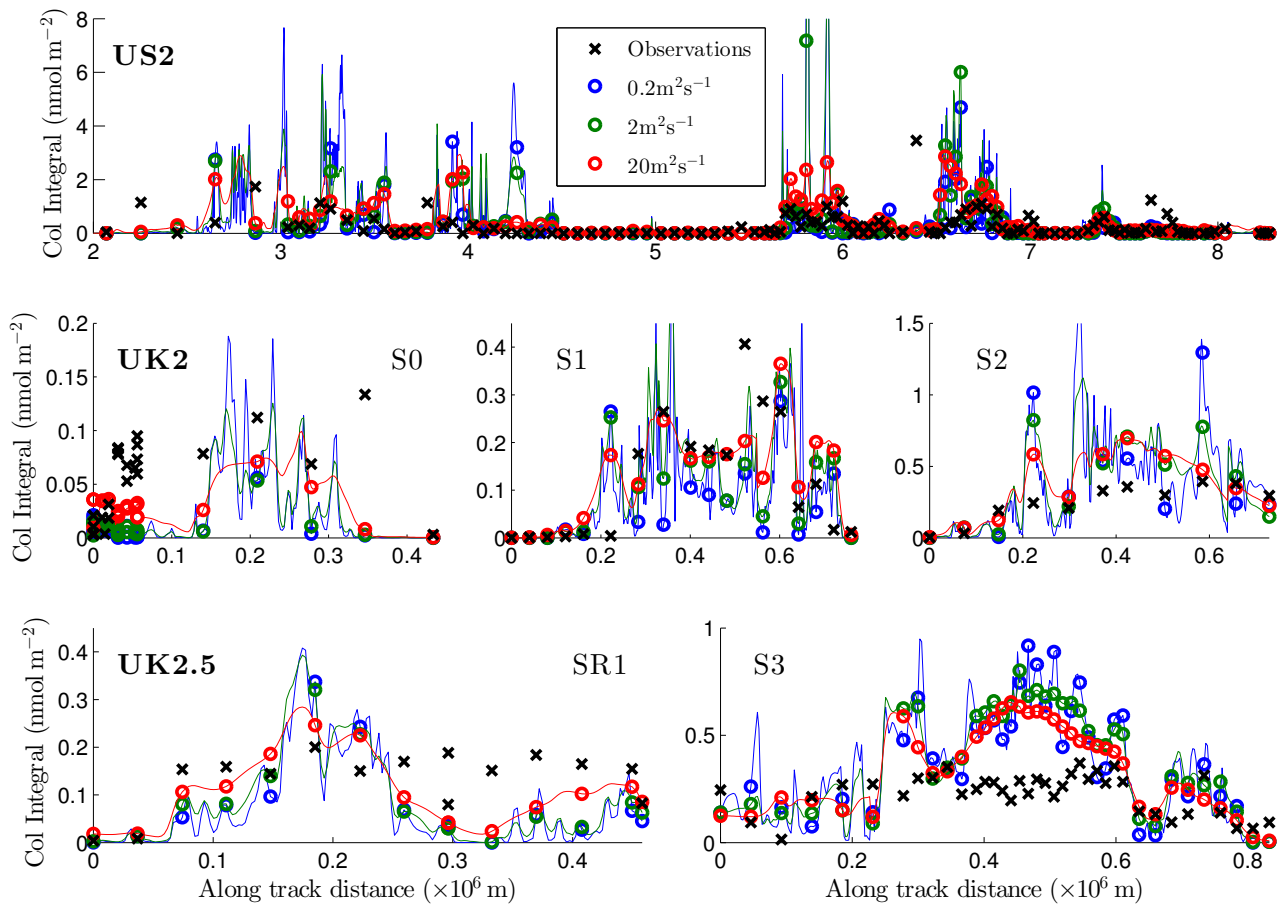


Figure 5.12: As in figure 5.11, but with $1/50^\circ$ simulations and different horizontal diffusivities as labelled. Note that the vertical scales are different from figure 5.11

we expect the difference between the simulation and the observations to increase with time, because we have seen that the velocity fraction is a spatially varying quantity (figure 5.8), so the velocity fraction that matches the centre-of-mass most accurately is likely to be a domain averaged value. Additionally, figure 5.10 shows that the centre-of-mass of the 33% simulation becomes further from the observations with time. The differences between the simulations and measurements is also expected to increase with time due to the limitations of the simulations - imperfect knowledge of initial conditions and the velocity field, static boundary conditions, etc. - compounding over time.

Figure 5.12 shows the same observations as figure 5.11, but with simulations with diffusivities $k_d=0.2, 2, 20\text{m}^2\text{s}^{-1}$ as labelled and a horizontal resolution of $1/50^\circ$. Note that the vertical axes have changed scale, but the horizontal axes are as before. Whilst the qualitative form of the simulated measurements has not changed drastically, the lower diffusivities result in peaks far above those seen in the observations.

Tracer Variance

In homogeneous, isotropic, stationary turbulence, it was first shown in Taylor (1921) that the dispersion of a tracer field can be related to a constant turbulent diffusivity, κ_T :

$$\frac{1}{2} \frac{\partial \overline{X^2}}{\partial t} = \kappa_T, \quad (5.1)$$

where $\overline{X^2}$ is the mean squared displacement of the tracer field. This implies $\overline{X^2} \propto \kappa_T t$, i.e. if we wait longer or the turbulence is stronger, the tracer field will spread further. In our case, where we have discrete samples of the tracer in two dimensions, we define the displacement as:

$$\overline{X^2} = \frac{\sum_i^N R_i^2 C_i}{\sum_i^N C_i}, \quad (5.2)$$

where C_i is the tracer column integral (from observations) or concentration (from simulations), and R_i is the distance of the observation from the centre-of-mass. Note that this is effectively the second-order moment of the tracer spread, where the centre-of-mass is the equivalent first-order moment.

To use (5.1) to examine our simulations and tracer observations, we assume that the centre-of-mass is advected by the mean flow, but that any spreading of the tracer is due to eddy effects, parametrised by a single diffusivity κ_T . Of course, our numerical simulations resolve stirring by meso-scale eddies, but all spreading of the tracer, including stirring,

is included in κ_T . Thus we expect κ_T to depend on our sub-mesoscale diffusivity k_d , but not be equal to it, i.e. $\kappa_T = f(k_d)$ and so $\overline{X^2} \propto f(k_d)t$.

Figure 5.15 shows $\overline{X^2}$ as calculated from the full simulated tracer field at the time of each cruise against the simulation diffusivity, k_d . As expected, we see a general increase in $\overline{X^2}$ with k_d at fixed resolution for each cruise. Comparing simulations with equal k_d across cruises, we see a general increase in $\overline{X^2}$ between each successive cruise, consistent with the expected time dependence of $\overline{X^2}$. We see the largest difference in variances between the US2 and UK2 cruises, which have the largest time difference.

The apparent separation between the $1/50^\circ$ and $1/20^\circ$ curves, resulting in the difference in variance between the $k_d = 20 \text{ m}^2\text{s}^{-1}$ simulations, is due to slight differences in the initial conditions of simulations at the two resolutions. The initial condition was chosen to mimic the estimate made on the release cruise of the location and amount of tracer released. The initial condition for the $1/50^\circ$ simulations is interpolated from the $1/20^\circ$ initial condition, and the centre-of-mass of each turn out to be slightly different, by hundredths of a degree. This slight difference in initial conditions leads to differing paths of the centres-of-mass, leading to the $1/50^\circ$ simulations having centres-of-mass roughly 5° further west and 1° further south than the $1/20^\circ$ simulations after 2.5 years of simulation.

This difference can be seen more clearly by comparing the along-track tracer from both $k_d = 20 \text{ m}^2\text{s}^{-1}$ simulations, see figure 5.14. Because the calculation of the variance depends on the centre-of-mass, this leads to the slight difference between the two resolutions, on the order of 10-20% at $k_d = 20 \text{ m}^2\text{s}^{-1}$. While the difference in the centre-of-mass between the two resolutions is not ideal, it gives an indication of the sensitivity of the variance to initial conditions. Given that we cannot know the exact centre-of-mass of the real tracer, this tells us with what accuracy we can use the variance to compare simulations with the measured tracer.

In fact, the total variance varies very little with k_d (note the vertical axis limits), with the magnitude of $\overline{X^2}$ being of order 10^{11} m , implying an overall eddy diffusivity $\kappa_T \sim \overline{X^2}/\text{time}$ on the order of $10^3 \text{ m}^2\text{s}^{-1}$ (consistent with Garabato et al. (2007), see discussion in section 5.1). Given $\kappa_T \gg k_d$, it is clearly dominated by stirring and advection effects.

We can compare the variance calculated not from the full tracer field, but from the sub-sampled tracer at the cruise locations, and compare with the variance of the measured tracer, see figure 5.15, which shows $\overline{X^2}$ as calculated from the sub-sampled simulations for each cruise against the simulation diffusivity, k_d . We can see the same broad features as in figure 5.13, with the same general dependence of the variance on k_d and time at

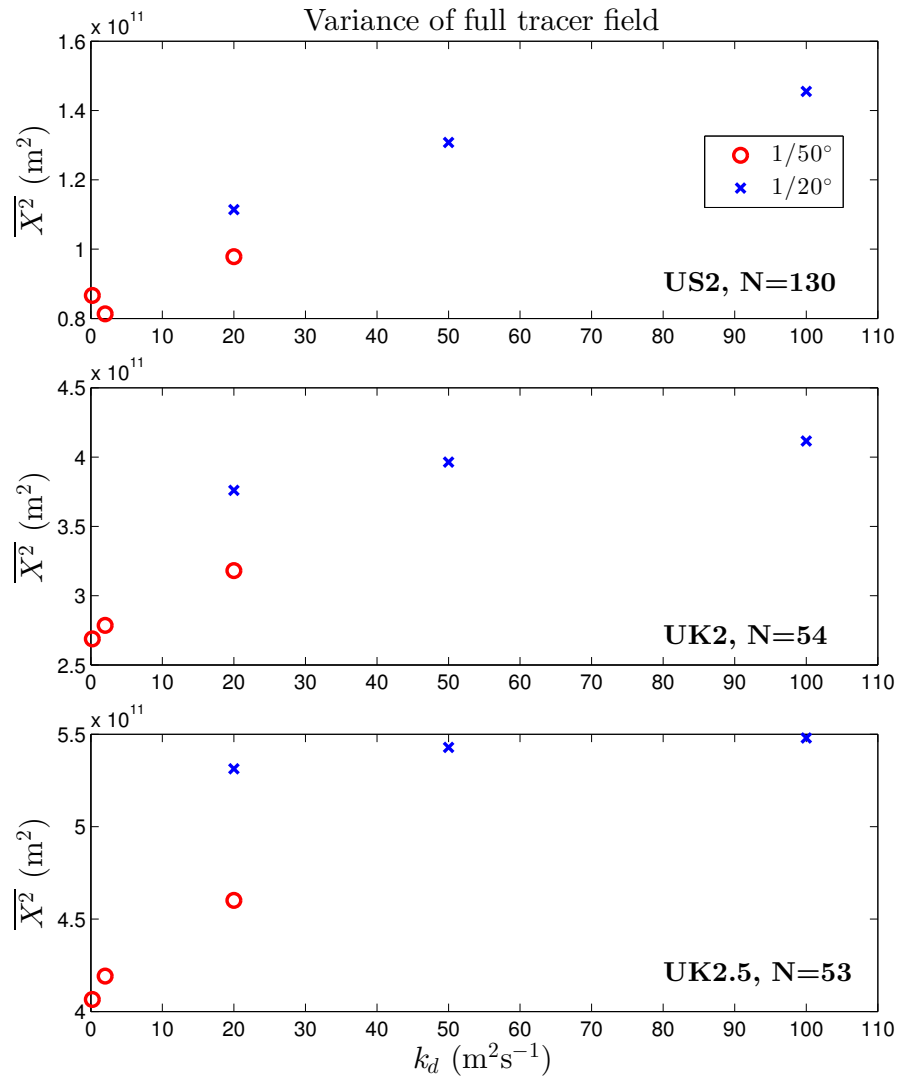


Figure 5.13: Mean squared displacement of the full tracer field, $\overline{X^2}$, against the horizontal simulation diffusivity, k_d , for $1/20^\circ$ (blue crosses) and $1/50^\circ$ (red circles) resolution simulations at the times of the three cruises, as indicated. The black dashed lines indicate $\overline{X^2}$ for the relevant cruise observations.

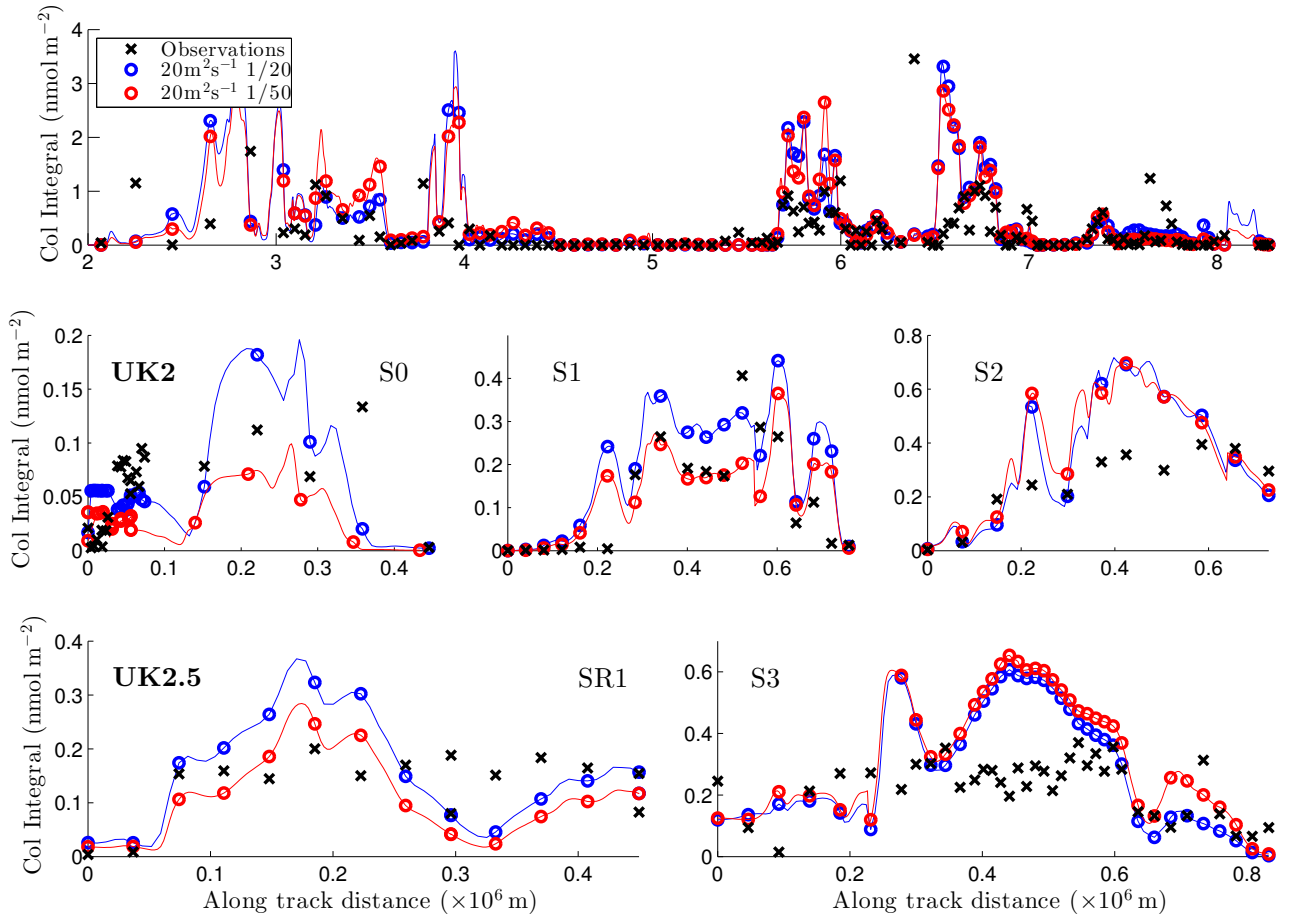


Figure 5.14: Tracer measurements (black crosses) from the first three cruises, against the cruise along track distance, and sub-sampled $1/20^\circ/1/50^\circ$ simulations (coloured circles) with a fixed horizontal diffusivity of $k_d = 20\text{m}^2\text{s}^{-1}$ as labelled and various velocity fractions, as labelled, with the thin coloured lines showing the simulated tracer between sample points.

a given resolution. We again see very little sensitivity to k_d overall, and two apparently different curves for the simulations at different resolutions.

We have assumed that the time between measurements on the cruises (taken over a number of weeks) is much smaller than the time between cruises (roughly one year between US2 and UK2 and four months between UK2 and UK2.5), and so treated the measurements as representative of a fixed tracer field in order to calculate $\overline{X^2}$. Also shown (black dashed lines) is $\overline{X^2}$ calculated from the observations made on each cruise, under the same assumption.

The sensitivity to k_d is so weak, one cannot realistically compare values with the observations to determine the most representative k_d , although we do at least get the same order of magnitude for the real tracer as for the simulations. The fact we don't know the true centre-of-mass of the real tracer field means that we can't determine which curve is best to compare to.

Even were the tracer centre-of-mass accurately represented in the simulations, use of the variance relies on the applicability of (5.1) to the eddying turbulence of the Southern Ocean and our simulations. This crucially depends on the assumption that the advection of the centre-of-mass is due to a separable mean-flow component, independent of the eddy field, which is wholly responsible for the tracer spread, assumed to be homogeneous. The use of a constant sub-mesoscale diffusivity k_d in our simulations similarly assumes isotropic, homogeneous turbulence on these scales, but crucially we resolve the advection and stirring caused by eddies above this scale, whereas the use of (5.1) requires the assumption that the whole eddy field is isotropic and homogeneous.

Looking at figure 5.14 we want to find a way to get at the properties of the tracer field directly affected by k_d , and find a measurement sufficiently sensitive to it that we can discriminate between simulations. The ideal method would identify the fact that the ‘spikiness’ or ‘streakiness’ of both $k_d = 20 \text{ m}^2\text{s}^{-1}$ simulations is extremely similar, rather than seeing the slight difference in the centres-of-mass. Thus we seek to find a further method to compare the simulations with observations in order to ascertain the most suitable value of k_d .

5.2.5 Aside: Roughness calculation

Whilst we do not expect an exact quantitative match to a simulation at every observation point, we might hope that the properties of the tracer that relate to the horizontal diffusivity - the ‘streakiness’ or ‘spikiness’ - could be matched, such that the two curves

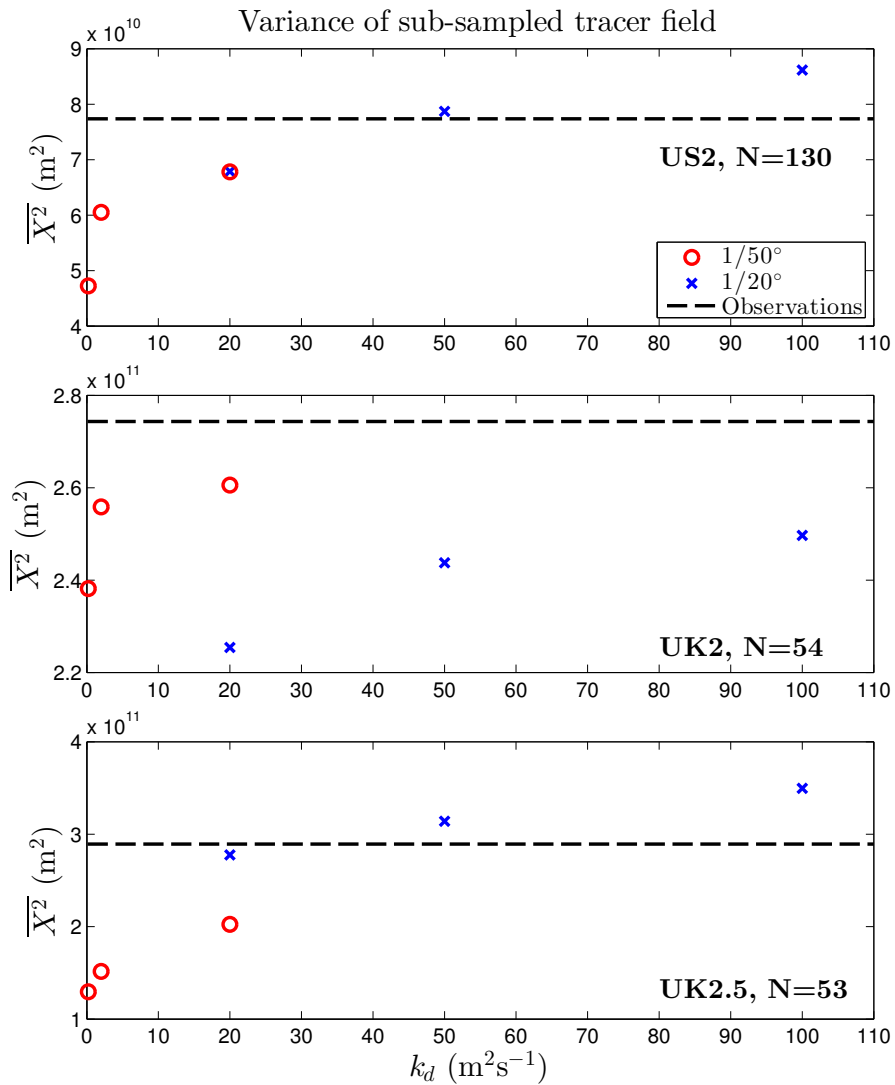


Figure 5.15: Mean squared displacement of the sub-sampled tracer field, $\overline{X^2}$, against the horizontal simulation diffusivity, k_d , for $1/20^\circ$ (blue crosses) and $1/50^\circ$ (red circles) resolution simulations, as indicated. The black dashed lines indicate $\overline{X^2}$ for the relevant cruise observations.

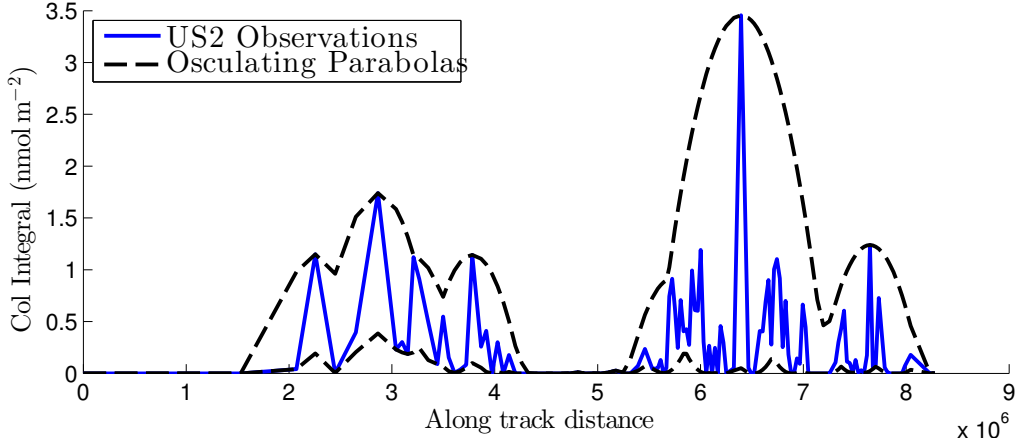


Figure 5.16: US2 observations (blue line) and osculating curves y_p^+ and y_p^- (black dashed lines) with curvatures $p = 0.1$. The roughness $\Phi(p)$ is a function of the area between these two curves, see text for details of the calculation.

in figure 5.14 would be identified as having similar ‘streakiness’. To more objectively compare the ‘streakiness’ of the simulations with the observations and assess which most closely matches, we used a roughness parametrisation as previously used in Legras et al. (2003) to match simulations of various diffusivities with observations. This assesses the roughness of a series of measurements as a function of the area between two osculating curves fit around the data. The two curves are constructed from a series of parabolas with curvature p , of the form

$$2p(y - y_c) = (x - x_c)^2. \quad (5.3)$$

At each measurement point (x_i, y_i) , the value of the osculating curve $y_p^+(x_i)$ is the smallest value of y_c such that the parabola with $x_c = x_i$ and curvature $-p$ lies above all measurement points. Similarly, $y_p^-(x_i)$ is the largest value of y_c such that the parabola with curvature p lies below all points. Examples of two such osculating curves can be seen in figure 5.16, which shows the tracer measurements from the US2 cruise against along-track distance (blue line) and the two osculating curves y_p^+ and y_p^- (black dashed lines) for $p = 0.1$. The roughness $\Phi(p)$ for N measurements is then defined as

$$\Phi(p) = \frac{1}{N} \sum_{i=1}^N (y_p^+(x_i) - y_p^-(x_i))^2. \quad (5.4)$$

Comparing the roughness $\Phi(p)$ of the observations with the roughness of the simulated tracer should thus provide an objective way of assessing which diffusivity best matches the streakiness of the observations.

Examples of the roughness curves from simulations can be seen in figure 5.18, which shows the results from all three cruises, but with only the S1 transect from UK2 and the S3 from UK2.5. The thick solid blue and green lines show the roughness of the cruise-imitating samples (sub-sampled at the identical times and locations of the cruise observations, as plotted in figures 5.11 and 5.12) for simulations with $k_d = 0.2\text{m}^2\text{s}^{-1}$ and $100\text{m}^2\text{s}^{-1}$ respectively.

Uncertainty in the roughness calculation

In order to assess the uncertainty in such a calculation, we used two different techniques. Technique A involved perturbing the sampling of the simulations in space and time, maintaining the spacing between sample points in space and time equal to the observations. Examples of two such tracks for UK2 S1 can be seen in figure 5.17, LH panel. Note that perturbation is also carried out in time, which is not shown. After perturbing a maximum of $\pm 3/20^\circ$ in both latitude and longitude, and ± 17 hours in time, we repeated the roughness calculation on each of the 54 new tracks produced, and took the maximum and minimum roughness found as the uncertainty limits. Examples of these limits can be seen in figure 5.18, which shows the roughness calculation for the 3 cruises and the $0.2\text{ m}^2\text{s}^{-1}$ and $100\text{ m}^2\text{s}^{-1}$ simulations (solid lines), and uncertainty A (dashed lines).

Technique B was a boot-strapping analysis as follows: we randomly re-sampled the full resolution simulated track with the same number of points as observations, allowing for re-sampling, 1000 times, and found the confidence intervals from the distribution of the roughness of these tracks. One example of such a track can be seen in the RH panel of figure 5.17, for UK2 S1. The confidence interval widths are similar to the uncertainty bands from technique A, although they place the cruise-imitating sampling at the rough end of the uncertainty bands - close to the 75% interval. The 75% and 95% intervals can be seen in figure 5.18 as the dark and light shading respectively.

In general, we found that the uncertainty from both techniques was inversely dependent on the number of points N and the diffusion of the simulation - with lower uncertainties at high N or higher diffusivities. This is confirmed by artificially increasing the number of samples, which reduces the uncertainty. The different horizontal diffusivity simulations for transects with low N were indistinguishable from one another, and so we have not shown those transects (S0 and S2 from UK2 and SR1 from UK2.5). We have in-

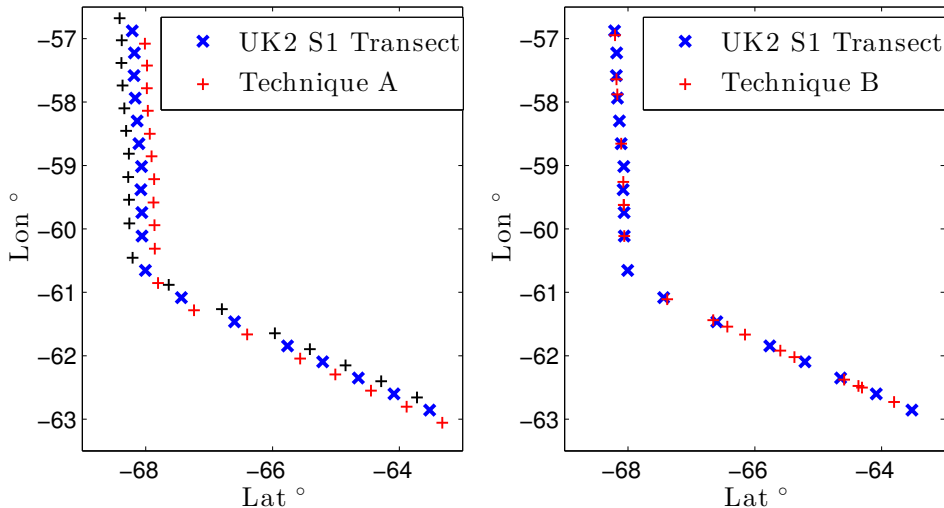


Figure 5.17: Examples of tracks used in estimating the uncertainty of the roughness for the UK2 S1 Transect. The original cruise transect (large blue crosses) as well as two from technique A (small crosses, LH panel) and one from technique B (small crosses, RH panel).

cluded the calculation for S1 from UK2 for reference, but as can be seen, the uncertainty is too high to use the roughness parametrisation to distinguish between the simulations in this case.

5.2.6 Roughness calculation results

Figure 5.19 shows the results of the roughness calculation for all three cruises (black lines) and all six simulations presented so far: $k_d = 0.2, 2$ and $20 \text{ m}^2\text{s}^{-1}$ at $1/50^\circ$ resolution and $k_d = 20, 50$ and $100 \text{ m}^2\text{s}^{-1}$ at $1/20^\circ$ resolution, all with a velocity fraction of 33%. The errorbars show uncertainty A, as described in section 5.2.5. We choose to use uncertainty A when analysing the results as it relates directly to the uncertainty in comparing two roughnesses sub-sampled identically, by giving a measure of the uniqueness of the roughness with respect to uncertainties in the exact sampling location. As the observations are taken over time and space, we could choose to set our x -axis as either along-track distance (as plotted in figure 5.16) or time before carrying out the roughness calculation. This affects the apparent roughness of the tracer, and so we carried out the roughness calculation for both axes, with the results for along-track distance on the left-hand of figure 5.19 and the results for time on the right-hand.

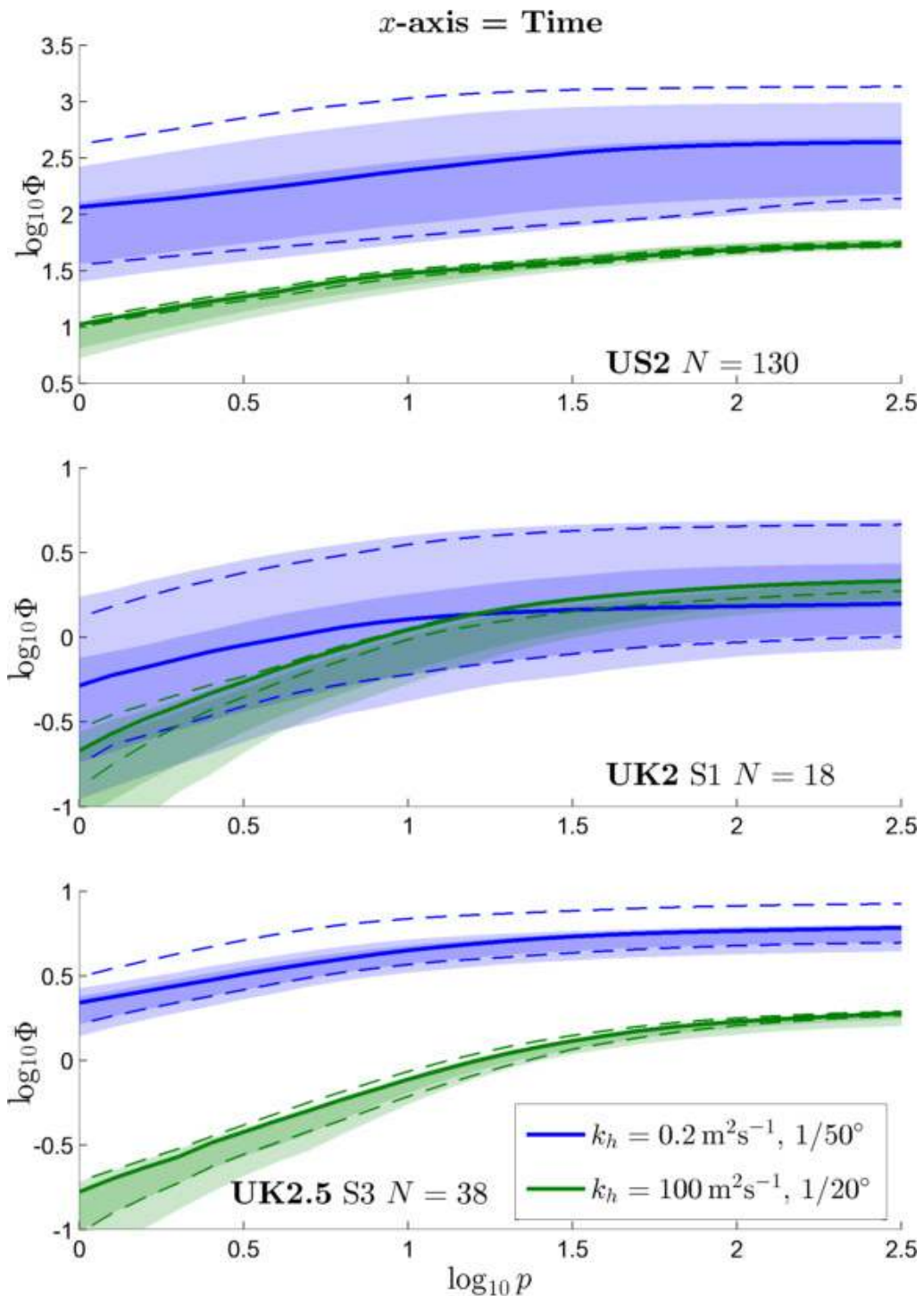


Figure 5.18: Roughness as a function of curvature p for the three DIMES cruises, transects as labelled, from two simulations with different diffusivities: $0.2 \text{ m}^2 \text{s}^{-1}$ (blue) and $100 \text{ m}^2 \text{s}^{-1}$ (green). Also shown are uncertainty limits A (dashed lines) and uncertainty limits B (shaded regions, 75% and 95% confidence intervals), see text for details.

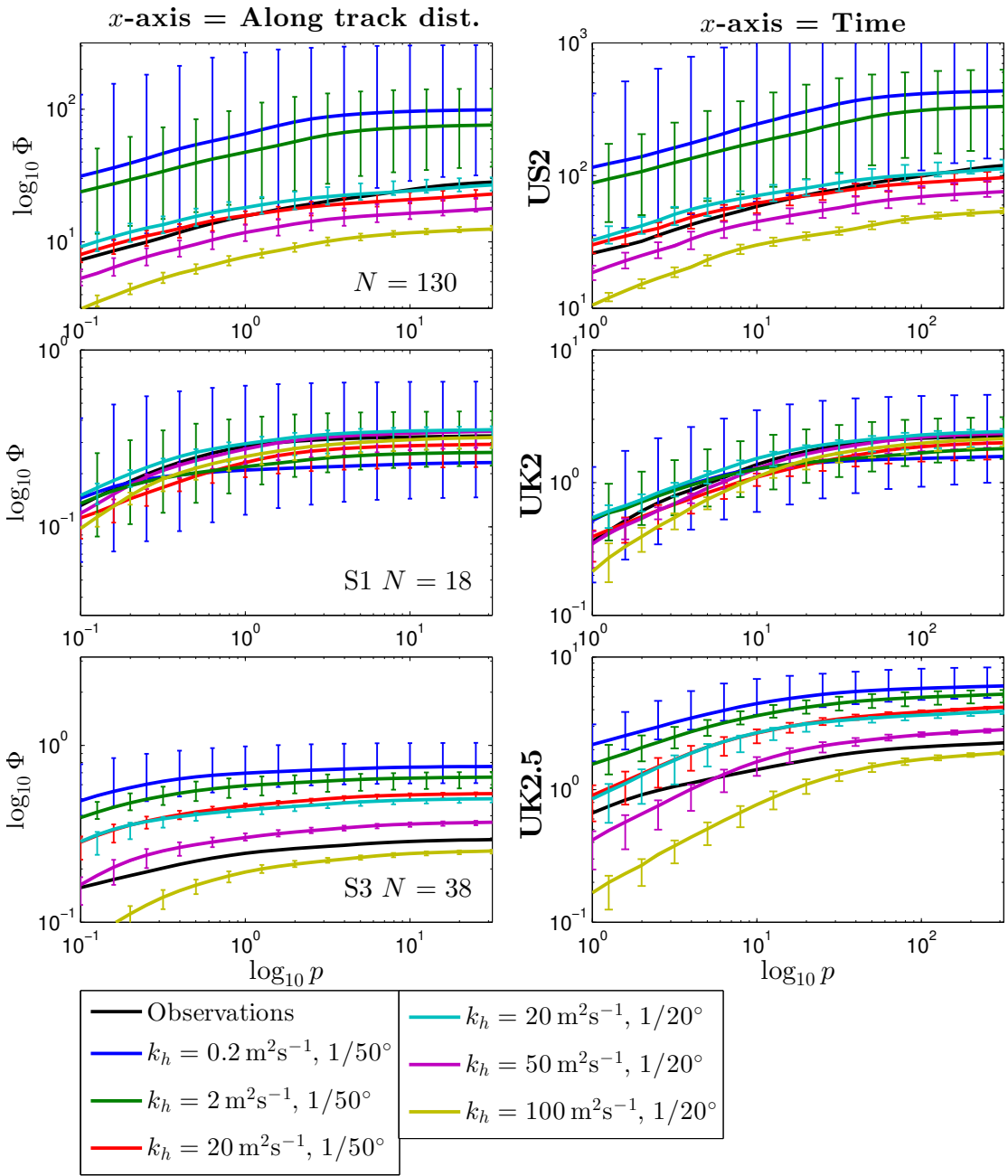


Figure 5.19: Roughness Φ versus parabola curvature p for all three cruises (top to bottom, as labelled), based on observations (black line) and $1/20^\circ$ (dot-dashed lines) and $1/50^\circ$ (dashed lines) simulations for the US2 cruise, the UK2 cruise S1 transect, and the UK2.5 cruise S3 transect. The x -axis for the calculation is either along track distance (L) or time (R). See text for details of calculation. Errorbars indicated uncertainty A.

For the US2 cruise, either using along-track distance or time as the x -axis for the roughness calculation resulted in a good match between the $k_d = 20 \text{ m}^2\text{s}^{-1}$ simulations and the observations at both resolutions. The $k_d = 0.2$ and $2 \text{ m}^2\text{s}^{-1}$ simulations for this cruise had a large estimated uncertainty. The UK2.5 results again show overlap between the $k_d = 20 \text{ m}^2\text{s}^{-1}$ simulations at both resolutions, and there is better separation between the different simulations. However, the shape of the curves do not match the observations, and as such the simulation with best agreement depends on the roughness - ranging from between $k_d = 20 - 50 \text{ m}^2\text{s}^{-1}$ to between $k_d = 50 - 100 \text{ m}^2\text{s}^{-1}$. The poor agreement for the UK2.5 results may also be due to the effect of the velocity fraction. As seen in section 5.2.2, the velocity fraction increases downstream, and figure 5.10 shows that the UK2.5 cruise results are better matched by a velocity fraction greater than 33%. A higher diffusivity may match better here because this will transport more tracer downstream, compensating for the low velocity fraction.

To more accurately assess the effect the velocity fraction has on the roughness of the sub-sampled tracer, we repeated the roughness calculation as previously for those simulations with variable velocity fraction, but with fixed diffusivity $k_d = 20 \text{ m}^2\text{s}^{-1}$. Figure 5.20 shows the results from the calculation, in the same form as in figure 5.19. Once again, using either the along track distance or time as the x -axis resulted in qualitatively similar results. The error-bars again represent the estimated uncertainty A , calculated as previously, and for each cruise we only show the transect with the largest number of points (US2, UK2 S1, and UK2.5 S3). There is no clear relationship between velocity fraction and roughness apparent. For the US2 cruise, the observations lie between the 33% and the 38% curves, with the uncertainty interval for the 28% simulation also overlapping, which does not contradict the choice of 33% as the closest fit. For UK2 S1, the 33% simulation again appears to be the closest. For UK2.5 S3, the observations lie closest to the 38% simulation, but are also close to the 33% confidence interval for low roughness when the x -axis is time. Taken in conjunction with figure 5.19, this implies that the closest match to UK2.5 would be achieved with a velocity fraction 33-38% (slightly lowering the roughness of the simulations) and so $k_d = 20 - 50 \text{ m}^2\text{s}^{-1}$.

In summary, these results show that a simulation with 33% and $k_d = 20 \text{ m}^2\text{s}^{-1}$ provides the closest match to the ‘roughness’ of the US2 observations. The results also suggest that the tracer measured in the UK2.5 cruise experienced a higher diffusivity ($20 - 50 \text{ m}^2\text{s}^{-1}$), and a higher velocity fraction (33-38%), although the roughness calculation does not give good agreement with a single simulation.

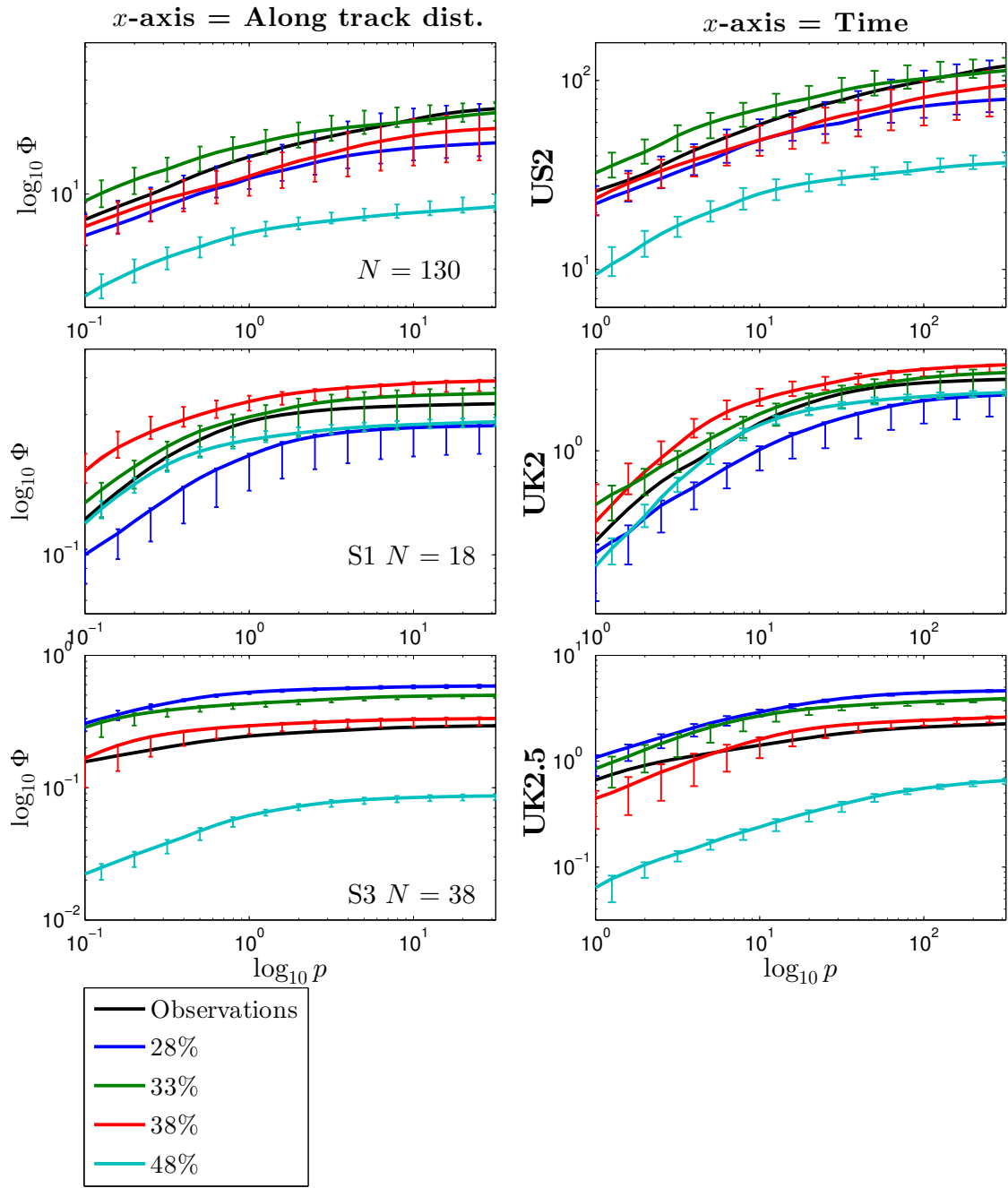


Figure 5.20: As in figure 5.19, but with fixed $k_d = 20\text{m}^2\text{s}^{-1}$, $1/20^\circ$ resolution, and different velocity fractions as labelled.

Using the roughness calculation to optimise sampling choices

When comparing two roughness curves, one from observations and one from simulation, we would argue uncertainty A is most relevant when the sampling technique is kept identical between the two. Thus, if attempting to design cruise track to allow accurate determination of the diffusion experienced by the tracer field through comparison of roughness with a simulation, one wishes to reduce this uncertainty.

One might expect there to be a balance between sampling at high enough resolution to capture the ‘streakiness’ of the tracer, whilst sampling across a wide enough region to ensure that the measurement is representative of the full field. Whilst testing this systematically for all possible tracks across the full three dimensional parameter space (longitude, latitude, and time) was beyond the scope of this study, we made a simple test of these ideas as follows. Taking a 30° full resolution longitudinal transect of the simulation tracer field from the $1/50^\circ$ simulation, see figure 5.21a, we limited our maximum sampling resolution to $1/50^\circ$ and our maximum number of samples N to 100, and sought to find the optimal sampling technique for a given N .

For each given N and resolution, we took the roughness of all possible tracks covering the transect seen in figure 5.21a, allowing for tracks to be re-entrant, and then took the standard deviation of the roughness of these tracks, averaged over the curvature p , which gave an estimate of uncertainty A. Because the roughness is compared on a log scale, we scaled the standard deviation by the mean of the roughness at each p before taking the mean over p . An example of this estimate of uncertainty A for $N=20$ can be seen in figure 5.21b (blue line). We also calculated the mean difference between roughness of the sub-sampled tracks and the ‘true roughness’ - the roughness of the full $N=1500$ $1/50^\circ$ transect - which we called the ‘accuracy’. The mean accuracy $\Delta\Phi(p)$, averaged over possible tracks and then p , for $N=20$ can be seen in figure 5.21b (red line). It can be seen that indeed both measures show that both too high and too low a resolution can lead to high uncertainty or inaccuracy.

For each N , the optimal resolution was defined as that which minimises uncertainty A, i.e. the blue circle in figure 5.21b. For reference, we also calculated the resolution with most accuracy, i.e. the red cross in figure 5.21b. Both can be seen plotted against N in figure 5.21c. As can be seen, the optimal resolution increases with increasing N for both measures, with that for uncertainty A being generally lower than the most accurate resolution at low N , but being higher for large N . For $N=20$, the optimal resolution w.r.t. uncertainty A is 1.30° , and example sampling at this resolution is seen in figure 5.21a with the blue circles. The most accurate, however, is 0.92° . Not surprisingly, we saw a

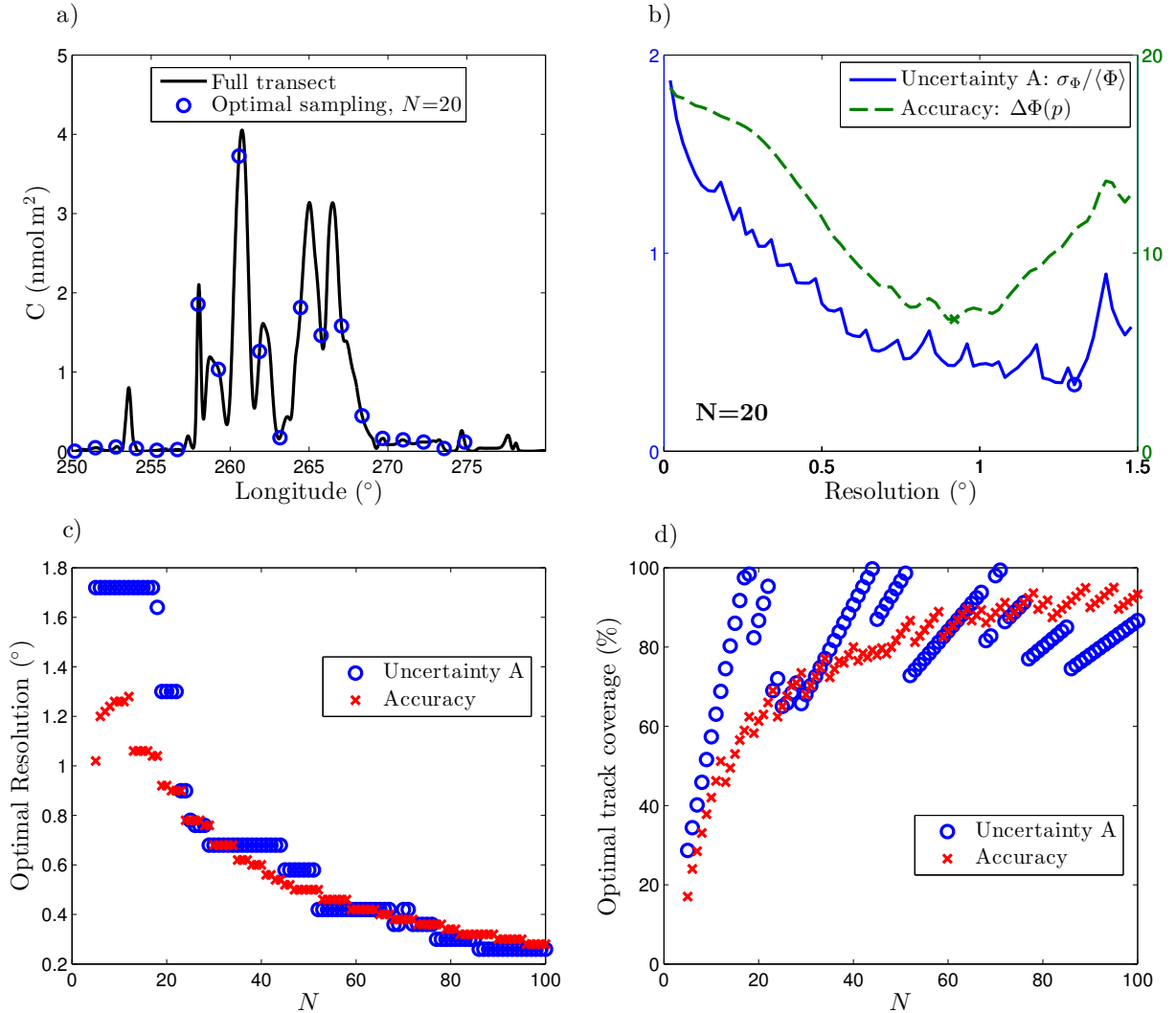


Figure 5.21: a) Transect from 1/50° simulation: tracer concentration vs longitude (black), example of an optimally spaced sampling for $N=20$ (blue circles). b) Uncertainty A (blue), and accuracy (red), for tracks with $N=20$, with minima marked. c) Optimal sample resolutions vs N and d) optimal sample track coverages vs N - most robust w.r.t. uncertainty A (blue circles) and most accurate (red crosses).

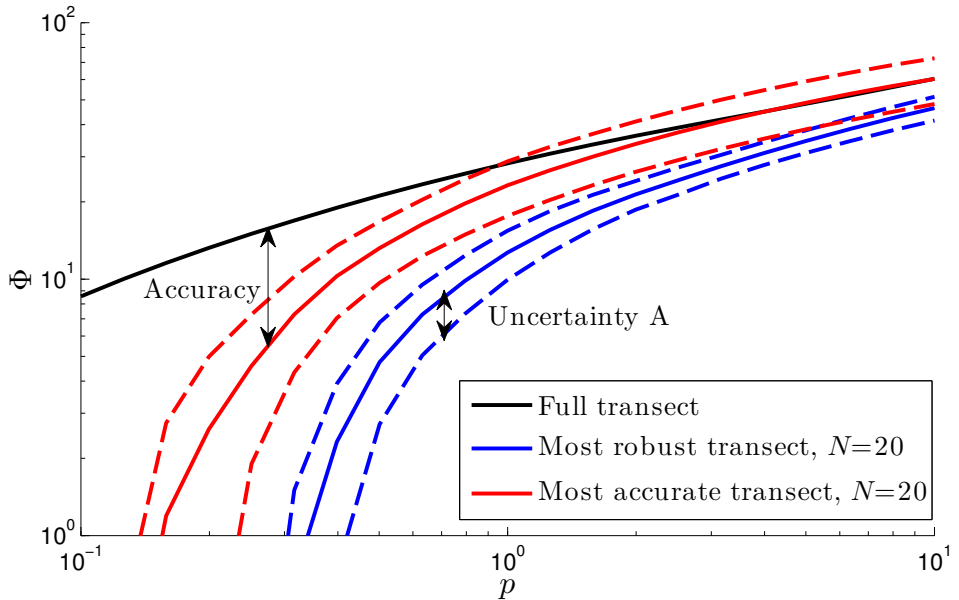


Figure 5.22: Roughness of: the full transect in figure 5.21a (black line), the most robust resolution track for $N=20$ (blue line) and the most accurate track (red line). The dashed lines indicate one standard deviation over possible tracks, uncertainty A.

general increase in robustness and accuracy with increasing N (not shown), and the most robust and accurate transects were found with the maximum $N=100$.

The length of the sub-sampled transect is $N \times$ resolution, and figure 5.21d shows the optimal transect length as a percentage of the full width (30°) against N . This rises from $\sim 20\%$ for $N=5$ and slowly approaches 100% for large N for the most accurate resolution (red crosses). Conversely, the most robust resolution w.r.t. uncertainty A (blue circles), varies much more widely, and ranges between full coverage (100%) and similar values to the most accurate coverage. Figure 5.22 shows the roughness curve for the full transect in figure 5.21a (black line), along with both the most accurate and most robust roughness for $N=20$, with uncertainty A and the accuracy labelled. It can clearly be seen here that the most accurate roughness curve (red line) has a larger uncertainty (indicated by the dashed lines) than the optimal roughness curve (blue line).

Figures 5.21c and d show that choosing the most robust sampling scheme is not as simple as choosing the most accurate - indeed, for low N it appears that it is preferable to choose a lower resolution in order to cover a larger distance. A more thorough investigation would be required to discover if these conclusions are robust and applicable

Cruise	Transect	N	Mean Transect Res.	Optimal Res.
US2		130	0.56°	0.56°
UK2	S0	9	0.42°	0.24°
	S1	18	0.38°	0.26°
	S2	11	0.60°	0.34°
UK2.5	SR1	15	0.28°	0.16°
	S3	38	0.20°	0.14°

Table 5.1: Optimal sampling resolutions for past cruises, assessed by reducing uncertainty A on the $1/50^\circ 20 \text{ m}^2\text{s}^{-1}$ simulation.

in general, but this could provide a scheme for designing cruise transects by utilising simulations validated against previous cruises to simulated future cruises.

We can also use this concept to assess the suitability of the previous cruise sampling schemes for measuring the roughness of the tracer. For each transect, we repeated the process as described above for the full $1/50^\circ 20 \text{ m}^2\text{s}^{-1}$ simulated transect, but keeping N the same as the actual number of observations, and calculated the optimal resolution w.r.t. uncertainty A. This meant that we could not assess resolutions lower than the mean resolution of the observations, as this would have required us to define a wider transect, and we chose to limit the problem to assessing the roughness of the given transect with a fixed N . Thus we can only assess whether a higher resolution would have been the most robust, and not a lower one. Table 5.1 shows the mean resolution of the observed transects, as well as the optimal resolution, assessed as described previously. Thus we can see that for the US2 cruise, the optimal resolution was equal or lower than that of the observations, i.e. $\geq 0.56^\circ$. However, for the UK2 cruise and UK2.5, the roughness of all transects would have been more robust at higher resolutions.

For our test case, figure 5.21, the optimal resolution increased with increasing N . However, for the actual cruises, there is a general increase in the optimal resolution as the cruises progress - resulting in a much higher optimal resolution for the UK2.5 transects than for the US2. This suggests that, as the tracer peak values become lower as time passes and the field becomes more diffuse, the roughness is harder to distinguish at low resolutions. This suggests that future cruises should concentrate on measuring the tracer at higher and higher resolution in order to make a meaningful comparison with simulations.

However, as mentioned previously, further work would be required to assess the robustness of this result, especially as we did not take into account the effect of small temporal or cross-transect shifts on uncertainty A for the cruise transects. Additionally,

for future cruises, one would need to assess whether other uncertainties expected in the simulation of the tracer itself, introduced by the assumptions of isopycnal only advection, the invariant sea-ice field, etc., which compound with time, would become large enough that such comparisons would not be meaningful.

5.3 Conclusions

In this chapter we have presented a method attempting to estimate interior isopycnal diffusivities in the Southern Ocean using altimetry derived surface velocity fields to advecting a conserved 2-D tracer field in the offline mode of MITgcm using non-divergent versions of those velocity fields. The diffusivity estimate was obtained through comparison with a tracer release experiment (the Diapycnal and Isopycnal Mixing Experiment in the Southern Ocean, or DIMES).

In order to obtain the velocity field at the depth of the tracer (neutral density surface $\gamma_n = 27.9 \text{ kg m}^{-3}$), we adjusted the surface velocity fields from altimetry by a constant ‘velocity fraction’, under the assumption of an equivalent barotropic flow. In order to assess the most suitable value, we utilised 44 RAFOS floats released at the tracer depth in the experiment region during the experimental cruises. The velocities derived from the float paths were compared with the altimetry derived surface velocities. These results suggested a longitudinally dependent velocity fraction, varying from 25% in the south Pacific to 43% in Drake Passage, which are comparable to the values found in models ([Killworth and Hughes, 2002](#)).

Additionally, comparisons of simulations with a range of domain-wide velocity fractions and a fixed isopycnal diffusivity of $20 \text{ m}^2 \text{s}^{-1}$, revealed that a velocity fraction close to 33% best matched the centre of mass of the sub-sampled simulation with observations from 3 separate cruises.

Proceeding with the velocity fraction of 33%, we carried out a range of simulations with a range of horizontal diffusivities and resolutions. In order to assess the most suitable isopycnal diffusivity to match the observations, we utilised a roughness parametrisation as previously used in [Legras et al. \(2003\)](#), which assesses the ‘streakiness’ of a series of measurements. We investigated the robustness of this roughness measure by assessing the uncertainty in the measure via two different techniques. It was found that in general, robustness increased with increasing observations. We also found that, for a given number of observations, there was an optimal resolution for the least uncertainty in the measured roughness, which was lower than the most accurate resolution. Testing the previous DIMES cruises, we found that the US2 cruise was at or above the most robust resolution, but that the UK2 and UK2.5 cruises were sampling at too low resolution. However, there is the need to carry out a more systematic study to more accurately assess the robustness.

When comparing the roughness of simulations with the cruise measurements, it was found that some of the cruise tracks did not contain enough measurements to accurately

distinguish their roughness, due to large uncertainty in the measure. However, the US2 cruise and the UK2.5 S3 transect both contained sufficient measurements to distinguish the roughness of simulations with different diffusivities.

Taken together, the roughness parametrisation and comparisons of the centre of mass of observations pointed to a best match of a velocity fraction of 33% and a small-scale isopycnal diffusivity of $20 \text{ m}^2\text{s}^{-1}$ for the US2 cruise, and a velocity fraction of 33–38% and a small-scale isopycnal diffusivity of $20 - 50 \text{ m}^2\text{s}^{-1}$ for the UK2.5 cruise. The velocity fraction results agree with the observed longitudinal dependence in the RAFOS derived measurements. The raised diffusivity in Drake Passage also agrees with previous observations and model studies which suggest that this is a region of relatively intense mixing. Whilst no directly comparable measurements have been made before, McKeeague et al. (2005) find a meridional diffusivity of $100 \pm 50 \text{ m}^2\text{s}^{-1}$ on the $\gamma_n = 28 \text{ kg m}^{-3}$ surface in the South Atlantic, Garabato et al. (2007) find a frontal isopycnal diffusivity of $360 \pm 330 \text{ m}^2\text{s}^{-1}$ on the $\gamma_n = 27.98 \text{ kg m}^{-3}$ surface and Zika et al. (2009) find $300 \pm 150 \text{ m}^2\text{s}^{-1}$ for $\gamma_n = 27.4 - 28 \text{ kg m}^{-3}$. Our results are not inconsistent with previous estimates, which we expect to be larger due to including advection effects our simulations resolved, and when considering the differing methodologies, depths, regions and times involved in each, as well as the large error bars.

The unique nature of the DIMES experiment, with multiple cruises returning to measure the tracer field, allowed for meaningful comparison with 2-D simulations of the same experiment. Despite the lack of representation of 3-D processes, the simulations had remarkable success at reproducing the location of the centre of mass of the observations, spaced over 2+ years, and the inferred roughness of the tracer field. The results suggest that the tracer has experienced increased isopycnal mixing in the Drake Passage, and has accelerated through this region. The robustness testing of the roughness parametrisation suggested it could be used to distinguish between different diffusivities, given enough samples. Despite the equivalent barotropic assumption only being strictly valid for circumpolar streamlines, applying a crude domain-wide velocity fraction to the surface velocities appears to be good enough for the region and time-period investigated here. However, it must be expected that as the tracer field moves further downstream, more sophisticated simulations with a domain-varying velocity fraction or 3-D velocity fields from a high resolution model will be required to match future cruise observations.

Chapter 6

Conclusions

This thesis has utilised a broad range of techniques, from a global circulation model of the Southern Ocean to a simple two layer model, and data sets from satellite observations to in-situ measurements of a chemical tracer. However, the overarching motivation behind each piece of work has been the same, namely to gain insight into the dynamics of the Southern Ocean. While the Southern Ocean's unique role in the climate system is known, the detailed dynamical processes occurring there are still poorly understood. There is an urgent need to address this scientific dearth, in order to understand what may happen in a changing climate.

Chapter 2 focused on theoretical explanations for jet formation in quasigeostrophic turbulence. There are a variety of jet formation theories in the literature, including linear Rossby wave theories, based on ideas originally discussed in Rhines (1975); ‘zonostrophic instability’ (Srinivasan and Young, 2012); ‘noodle mode’ theory (Berloff et al., 2009), and PV ‘staircase’ theory (Dritschel and McIntyre, 2008). Given the wide use of quasi-geostrophic models, the fact that the mechanism of jet formation and the jet separation scaling are still debated over 30 years after Rhines’ seminal work is surprising. We sought to test each of these ideas against a doubly periodic baroclinic system with a zonal slope in bottom topography, to see whether they could predict the orientation of the jets observed, which would in turn provide support for the theory. Resolving or refining these theories would allow for better predictability of the behaviour of more complicated systems and provide insight into the mechanisms at work in the real ocean.

Testing the ideas of zonostrophic instability would involve quasi-linear simulations and cumulant second order expansion theory, and was beyond the scope of this study. The scalings derived in Dritschel and McIntyre (2008) are for barotropic systems with a finite deformation radius, and so are not applicable to our system. The ideas of Rhines (1975) were developed in Vallis and Maltrud (1993), and, like ‘noodle mode’ theory, are

dependent on the linear stability properties of the system, and so both were investigated in this study.

Beginning with the Rossby wave theory of [Vallis and Maltrud \(1993\)](#), which was for a one-layer barotropic β plane, we first sought to extend the theory to a baroclinic system on a β plane in the absence of forcing or dissipation. The Rossby wave theory says that the inverse cascade of energy in the barotropic mode will be arrested by the excitation of Rossby waves, and so the properties of the Rossby wave frequencies determines the scale and direction of the jets. It was found that, as seen in [Vallis and Maltrud \(1993\)](#), the anisotropy of the Rossby wave frequencies corresponded with the anisotropy of the kinetic energy spectra, and so with the direction of the jets in simulations. However, the second layer introduced additional dependence on the deformation radius, which determined whether the frequencies were mutually aligned with the barotropic PV gradient (longwave limit) or individually aligned with the layer-wise PV gradients (shortwave limit). Additionally, the theory predicts a ‘cascade barrier’ k_β at which the inverse cascade of energy should be halted by Rossby wave excitation. The simulations showed qualitative agreement with the theory, with k_β depending on the magnitude of the PV gradients and the system energy.

Turning to a system additionally containing shear and bottom friction, we found similar long and shortwave Rossby wave frequencies. Whilst the shear affected the form of the shortwave frequencies, it did not significantly affect the longwave frequencies, which again aligned with the barotropic PV gradient. The nature of the baroclinic instability driving the system resulted in energy entering the barotropic mode at wavelengths of the order of the deformation radius, and thus the shortwave limit ($K \gg 1/\lambda$) is not relevant and only the longwave limit ($K \ll 1/\lambda$) is observed in simulations. We found that the anisotropy of the longwave Rossby frequencies again successfully predicted the form of the energy spectra of the simulations and the jet direction, and so this theory is indeed consistent with the observed agreement between the jet angle and the barotropic PV gradient.

We then tested the theoretical ‘cascade barrier’ scale k_β , which depends on the choice of turbulent frequency parametrisation, against the simulated spectra. We tested a Rhines scaling and a Kolmogorov scaling, which both correspond to turbulent energy scalings, and thus both were tested by their resemblance to the spectra of full simulations as well as the cascade barriers predicted. Looking at the spectra from simulations, we found that the Kolmogorov scalings for k_β agreed well for $k_\beta\lambda < 0.5$, but that a full inverse cascade did not develop for $k_\beta\lambda > 0.5$ and there was progressively worse agreement as the cascade

barrier approached the forcing scale.

The jet wavenumber is predicted in [Vallis and Maltrud \(1993\)](#) to be close to, but smaller than, k_β , as the cascade can continue along the jet direction until it is halted by bottom friction, and indeed we observe $k_{\text{jet}} < k_\beta$ for all simulations. [Smith et al. \(2002\)](#) suggest a scaling for k_{jet} dependent on the magnitude of the barotropic PV gradient and the equilibrated kinetic energy, ε/κ . For $k_\beta \lambda < 0.5$, we found some agreement with this scaling (although there were some simulations affected by the geometric effects discussed in chapter 3), and k_β itself was close to the Rhines scale. For $k_\beta \lambda > 0.5$, we found k_{jet} was close to the Rhines and Kolmogorov scales, suggesting that when the inverse cascade cannot form, the energy remains close to the cascade barrier, where the jets form. Thus, the Rhines scale seems a good predictor for the cascade barrier scale, and is close to the jet scale for smaller jet scales (larger $k_\beta \lambda$), whereas the [Smith et al. \(2002\)](#) scaling is a better fit for larger jet scales (smaller $k_\beta \lambda$).

We then analysed the unstable modes of the system in order to test the noodle mode theory of [Berloff et al. \(2009\)](#), who postulate that the secondary instabilities of the system (that is, the instability of the background flow plus primary instabilities) are responsible for jet formation. For the β plane case, in the absence of zonal slopes in topography, the primary instability produces meridionally orientated ‘elevator’ modes, and the secondary instability is perpendicular to this, producing zonal ‘noodle modes’ which [Berloff et al. \(2009\)](#) interpret as self-strengthening to form zonal jets. However, as with [Chen and Kamenkovich \(2013\)](#), we found that the most unstable ‘noodle’ mode wave-vector did not remain consistently perpendicular to the barotropic PV gradient (which determines the orientation of the primary instability) as a zonal slope in bottom topography was introduced. Thus, the noodle modes are not aligned with the eventual jet direction, and the [Berloff et al. \(2009\)](#) explanation for jet formation does not apply here.

The fact that both the predicted jet and cascade barrier wavenumbers are consistent with the Rossby wave theory when a developed inverse cascade is present lends support to the ideas of the Rossby wave theory, however it clearly cannot describe the behaviour in all cases. In particular, the cases without a developed inverse cascade also show jets forming, and the work of [Srinivasan and Young \(2012\)](#) and others have shown categorically that an inverse cascade is not necessary to form jets. We propose that the Rossby wave frequencies do indeed produce a barrier to the system energy, but that this does not require the system energy to cascade towards it, and so it might be better termed the Rossby wave barrier. This would explain the replication of jet formation in quasi-linear models without a mechanism for a direct small scale cascade - if the energy is instead

transferred via non-local interactions, the Rossby wave barrier still remains which sets anisotropy of the system and so the jet direction.

We do not claim that the current work constitutes proof of this picture, however it does provide a consistent explanation for the results found in this and other studies. The implications for the validity of this theory are, however, quite meaningful. It would allow us to make predictions about jet direction and scale from knowledge of the linear properties of a system, which would then allow us to make predictions about the energetics and transport properties of such jets, without the need for simulation. It would also provide tools for interpreting more complicated jet structures, and what might cause their behaviour to change. Further work that could provide more insight would be carrying out quasi-linear simulations as in [Srinivasan and Young \(2012\)](#) to see whether zonostrophic instability can produce tilted jets in the presence of zonal slopes in bottom topography.

Chapter 3 followed on from 2 to investigate the properties of the jets that form in a baroclinic system with a general slope in bottom topography, similar to those that form the Antarctic Circumpolar Current of the Southern Ocean. Observations show that the path of the ACC is affected by topography, and in particular studies such as [Thompson and Sallée \(2012\)](#) and [Gille \(1997\)](#) suggest that the regions downstream of topographic features are regions of increased eddy activity. We investigated topographic effects by the introduction of arbitrarily orientated linear slopes in bottom topography to simple one- and two-layer quasigeostrophic β plane models. The most significant finding was that the formation of coherent jets, familiar from many studies without topography and also with topographic slope in the meridional direction, persisted under the addition of a topographic slope in the zonal direction. The corresponding jets were tilted relative to the zonal direction and crossed layer-wise PV gradients, instead following the background barotropic PV gradient in both the barotropic and baroclinic models.

Analysis of the energy balance of the two-layer model showed an increase in eddy energy production of several orders of magnitude with decreasing angle between the barotropic PV gradient and the zonal background shear (concurrent with increased jet tilt). These findings are consistent with those of [Smith \(2007\)](#) and [Arbic and Flierl \(2004b\)](#), who find increased eddy energy in similar models with the shear and barotropic PV gradient aligned or anti-aligned. Qualitatively consistent with the observed increase in eddy activity were the results of an effective diffusivity calculation which showed that jets that cross layer-wise PV gradients are weaker barriers to transport than zonal jets, which do not.

This has interesting implications for the Southern Ocean in that it implies that in

regions with large-scale bottom topography, one might find that the direction of jets at the surface was determined by the topography at depth, and that these jets would be relatively worse transport barriers than their zonal counterparts.

To test the extent to which the doubly periodic simulations were representative of the behaviour observed over slopes in topographies with more complicated, larger scale inhomogeneities, we also investigated topographies made up of zonally varying zonal slopes. In these more complicated topographies, jet formation persisted, and once again the jets conformed to the local barotropic PV gradient, tilting over the sloped regions.

Simulations with stepped topographies in smaller domains and with lower magnitude PV gradients exhibited large scale structure in the baroclinic streamfunction, which partially ‘compensated’ the upper layer PV such that the large scale gradient aligned closely with the background barotropic PV, and so with the jets. These simulations were unlike the doubly periodic two-layer simulations, and instead resembled rotated zonal one-layer simulations in the upper layer. However, those simulations with larger maximum topographic heights or larger values of $\beta\lambda^2/U$ did not exhibit compensation, i.e. the tilted jets in the sloped regions crossed layer-wise PV gradients, as seen in the doubly periodic case. Thus, these simulations were locally similar to the doubly periodic simulations, pointing to the strength of the background PV gradient, the background shear and the height of the topography as factors which determine whether the sloped regions are sufficiently independent of topographic inhomogeneities to be represented in part by doubly periodic cells.

All of the tilted jets in the doubly periodic simulations and the un-compensated jets exhibited jet drift, whereas zonal and compensated jets maintained a fixed position in the simulation domain. The drift was interpreted as a result of the requirement of upper layer PV conservation, which implies that jets must translate if the background upper layer PV is not aligned with the background barotropic PV. There remains further work to be done to determine what controls the magnitude of the baroclinic compensation and jet drift.

Whilst the simulations with more complicated topographies confirm that, dependent on certain parameters, the doubly periodic simulations can be representative of the dynamics over zonal slopes in more general topographies, they also exhibit a new set of interesting dynamics. This richness of dynamical possibilities points to the usefulness of continuing to study these seemingly simple models. Whilst on the one hand we have demonstrated new and interesting behaviour in the steering of jets by zonal slopes in topography, we have also found unexpected phenomena such as jet drift and baroclinic

compensation which suggest there may be different regimes of behaviour for jets interacting with topography, dependent on the scales and relative directions of the PV gradients, background flows and topography. These effects merit further study to fully understand their implications.

In chapters 4 and 5 we moved from simple jet models to attempting to quantify their properties in the Southern Ocean, utilising satellite altimetry derived velocity fields to advect tracer fields in the offline mode of MITgcm to make estimates of surface and isopycnal mixing. Chapter 4 concentrated on an effective diffusivity calculation, made by advecting a tracer field covering the whole Southern Ocean with 18 years of observations to update calculations previously made in Shuckburgh et al. (2009a). The updated velocity fields were seen to be better at resolving finer structures and eddies, but this caused problems for the effective diffusivity calculation in regions with high eddy activity, due to the presence of many closed contours and contours crossing the northern boundary of the domain. Additionally, there was a smaller overall EKE and larger mean zonal velocity in the ACC core in the new data compared with the old.

The spatial structure of the time mean effective diffusivity for the entire 18 year period showed qualitative similarities to the results of Shuckburgh et al. (2009a), with a minimum in the ACC core and raised values to the north, but with lower magnitude in the ACC core due to the increased mean flow suppression from the stronger zonal mean flow and slightly lower eddy activity. Examining the temporal variability showed a slight seasonal cycle, with peaks in October, and relatively lower variability in the ACC core, but no discernible trend.

Repeating the same effective diffusivity calculation, but with an eddy-only velocity field, revealed the effects of mean-flow suppression. The eddy-only effective diffusivity was much higher, showing a peak in the ACC core, which was qualitatively somewhat similar to a tuned eddy diffusivity similar to that developed in Holloway (1986). However, we found that two alternative eddy diffusivities that included the mean flow suppression, based on linear quasi-geostrophic theories, both failed to qualitatively match the full effective diffusivity, despite the success of Ferrari and Nikurashin (2010) and Klocker et al. (2012) when using the old altimetry.

Investigating the temporal variability of the effective diffusivity, we found significant but moderate correlations with $EKE/(\bar{u} - c)^2$, the stationary eddy diffusivity κ^0 , EKE and anti-correlation with \bar{u} in the ACC core. However, these correlations were only found using a time-filtered mean-anomaly decomposition of the full SSH, and not with the AVISO supplied mean-anomaly decomposition. This suggests that the former decom-

position better represents the eddies responsible for mixing, and highlights the need for care in defining the eddy field. We failed to find any significant correlations between the EKE and Southern Annular Mode index at 2-3 years lag, as suggested by other studies, which calls into question the relevance of these highly localised correlations to the large scale properties of the Southern Ocean.

These results confirm that, at the surface, the ACC is a transport barrier, reducing the latitudinal movement of tracers such as heat and salt. The failure to fit eddy diffusivity parametrisations to the full effective diffusivity suggests that the interactions between the mean flow and the eddy field are not fully understood. However, the temporal correlations found indicate that the quantities involved in these parametrisations have some relevance to the mixing properties, although care must be taken when defining the eddy field. In future studies, further progress could be made by using the effective diffusivity in conjunction with other mixing estimates, such as in [Abernathey and Marshall \(2013\)](#), or investigating methods of estimating the relevant eddy phase speeds accurately. The problems found with the non-robustness of the effective diffusivity in the northern part of the domain could be tackled by experimenting with different initialisations of the tracer field to address the problem of low tracer gradients.

In the final chapter, an interior isopycnal diffusivity estimate was calculated by comparison between observations of a tracer field from the DIMES experiment and a simulated version of the same tracer field. Data from RAFOS floats at the tracer depth suggested that regional velocities at the tracer depth were between 25% and 43% of the surface values during the experiment. Calculating the centre-of-mass and roughness of simulations with different isopycnal diffusivities and velocity fractions suggested a velocity fraction of 33% and an isopycnal diffusivity of $20 \text{ m}^2\text{s}^{-1}$ for the US2 cruise (2010 South Pacific), and a velocity fraction of 33-38% and an isopycnal diffusivity of $20\text{-}50 \text{ m}^2\text{s}^{-1}$ for the UK2.5 cruise (2011 Drake Passage). The raised diffusivity in the Drake passage is consistent with previous studies, including those that diagnosed diapycnal mixing from the DIMES tracer, which have identified it as a region of increased mixing.

The roughness parametrisation used, as developed in [Legras et al. \(2003\)](#), was found to be robust for larger sample sizes, but did not distinguish between simulations when the number of samples was low. The robustness of the technique was found to vary with the resolution of the measurements, and so we tested the cruise sampling techniques, finding a general increase in the required resolution for the least roughness uncertainty with time. There is scope to test this further as it could possibly be used as a cruise-planning tool, if the uncertainties are better understood.

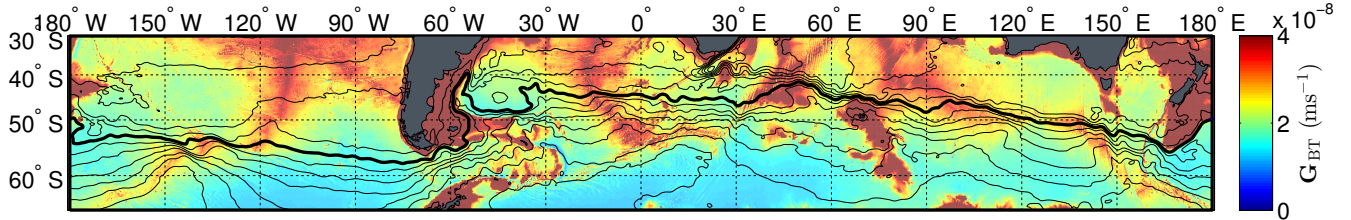


Figure 6.1: Colour: the large-scale barotropic PV gradient in the Southern Ocean, f/h . Black contours: mean AVISO streamlines, contour interval 20 cm, thicker contour indicates 0.

This calculation neglected diapycnal effects and assumed a time and spatially constant velocity fraction. Despite these limitations, the simulations performed well and allowed meaningful comparison with the data. Future work is planned to carry out full 3-D simulation of the DIMES tracer using high resolution ocean model output velocity fields, which addresses both of these limitations.

The results of chapters 2 and 3 showed the importance of the barotropic PV gradient in determining the behaviour in the two-layer baroclinic system investigated. Although the quasi-geostrophic framework places theoretical limitations on the applicability of these results, many previous studies have been shown to successfully reproduce behaviour outwith these limits. Thus we look at the full Southern Ocean background barotropic PV gradient, f/h , in figure 6.1, and plot over it the mean AVISO streamlines (black lines). This will show if there is any relationship between mean-flow direction and background PV. This is not exactly analogous to our quasi-geostrophic system, where the mean flow is prescribed, but the location of streamlines are often used to define the location of the jets of the ACC, so it is a crude approximation. There is an overall north-south slope to the PV gradient introduced by f , but it is locally dominated by topographic effects. South of Macquarie ridge and approaching the East Pacific Rise, the streamlines tilt non-zonally, in apparent alignment with the barotropic PV contours. However, the streamlines then turn, crossing PV contours over the Rise and downstream. The streamlines are strongly steered through Drake Passage, however the continental boundaries likely play a large role here. Moving east, the streamlines appear to be perturbed by latitudinally orientated topographic features, tilting to the North up-stream and then to the South down-stream, especially around Kerguelen plateau, where the streamlines become almost aligned with the local PV gradient. Overall, we can see examples of clear alignment and clear anti-alignment between the mean streamlines and the barotropic PV gradient - suggesting

that the effects studied in chapters 2 and 3 may indeed be relevant in some locations, but do not provide the whole picture of topographic interactions with jets.

The results of this thesis have drawn on a wide range of techniques to gain insight into the dynamics of the Southern Ocean. It has presented novel results on the effects of topography on jet properties, which as discussed above, may have implications for the behaviour of the ACC. The same investigation has allowed for further insight into jet formation mechanisms, adding significant results to the literature in this area. Satellite altimetry was utilised to provide both large scale estimates of surface mixing as well as to investigate the localised isopycnal mixing experienced by a tracer. Both the quasi-geostrophic models and the effective diffusivities have shown the importance of a zonal background flow in determining eddy dynamics. The DIMES diffusivity results and the quasi-geostrophic models show the importance of topography in determining mixing properties. The DIMES isopycnal diffusivity is the first such estimate we are aware of on the sub-mesoscale using observations, and the robustness of the technique as investigated here should allow for its use in future experiments of a similar nature, as well as providing a value for direct comparison for modellers working at similar resolutions. These results have both furthered the understanding of, and quantified further, the dynamical processes present in the ACC, and in this sense the stated aims of the research have been achieved.

References

- Abernathay, R., J. Marshall, M. Mazloff, and E. Shuckburgh, 2010: Enhanced isopycnal mixing at steering levels in the Southern Ocean. *J. Phys. Oceanogr.*, **40**, 170–184. [9](#), [67](#), [135](#), [154](#), [174](#)
- Abernathay, R. P. and J. Marshall, 2013: Global surface eddy diffusivities derived from satellite altimetry. *J. Geophys. Res.*, **118**, 901–916. [148](#), [174](#), [219](#)
- Adcroft, A., J. Campin, C. Hill, and J. Marshall, 2004: Implementation of an atmosphere-ocean general circulation model on the expanded spherical cube. *Mon. Wea. Rev.*, **132** (12), 2845–2863. [135](#)
- Arbic, B. K. and G. R. Flierl, 2004a: Baroclinically unstable geostrophic turbulence in the limits of strong and weak bottom Ekman friction: Application to midocean eddies. *J. Phys. Oceanogr.*, **34** (10), 2257–2273. [75](#)
- Arbic, B. K. and G. R. Flierl, 2004b: Effects of mean flow direction on energy, isotropy, and coherence of baroclinically unstable beta-plane geostrophic turbulence. *J. Phys. Oceanogr.*, **34** (1), 77–93. [68](#), [69](#), [70](#), [72](#), [76](#), [87](#), [89](#), [130](#), [216](#)
- Arnold, V. I. and L. D. Meshalkin, 1960: A.N. Kolmogorov's seminar on selected problems of analysis (1958/1959). *Uspekhi Mat. Nauk*, **15**, 247–250. [22](#), [73](#)
- Badin, G. and R. G. Williams, 2010: On the buoyancy forcing and residual circulation in the southern ocean: the feedback from ekman and eddy transfer. *J. Phys. Oceanogr.*, **40** (2), 295–310. [174](#)
- Bastin, M. and P. Read, 1998: Experiments on the structure of baroclinic waves and zonal jets in an internally heated, rotating, cylinder of fluid. *Phys. Fluids*, **10** (2), 374–389. [69](#)

- Berloff, P., I. Kamenkovich, and J. Pedlosky, 2009: A Model of Multiple Zonal Jets in the Oceans: Dynamical and Kinematical Analysis. *J. Phys. Oceanogr.*, **39** (11), 2711–2734. [18](#), [63](#), [65](#), [67](#), [213](#), [215](#)
- Beron-Vera, F. J., M. G. Brown, M. J. Olascoaga, I. I. Rypina, H. Kocak, and I. A. Udovydchenkov, 2008: Zonal jets as transport barriers in planetary atmospheres. *J. Atmos. Sci.*, **65** (10), 3316–3326. [78](#)
- Boland, E. J., A. F. Thompson, E. Shuckburgh, and P. H. Haynes, 2012: The formation of nonzonal jets over sloped topography. *J. Phys. Oceanogr.*, **42** (10), 1635–1651. [13](#)
- Böning, C. W., A. Dispert, M. Visbeck, S. R. Rintoul, and F. U. Schwarzkopf, 2008: The response of the Antarctic Circumpolar Current to recent climate change. *Nature Geoscience*, **1** (12), 864–869. [6](#)
- Butterworth, S., 1930: On the theory of filter amplifiers. *Wireless Engineer*, **7**, 536–541. [157](#)
- Chen, C. and I. Kamenkovich, 2013: Effects of topography on baroclinic instability. *J. Phys. Oceanogr.*, **43**, 790–804. [20](#), [58](#), [62](#), [65](#), [215](#)
- Danilov, S. and V. M. Gryankin, 2004: Barotropic beta-plane turbulence in a regime with strong zonal jets revisited. *J. Atmos. Sci.*, **61** (18), 2283–2295. [43](#)
- Deans, S. R., 1983: *The Radon transform and some of its applications*. Wiley (New York). [90](#)
- Dritschel, D. G. and M. E. McIntyre, 2008: Multiple Jets as PV Staircases: The Phillips Effect and the Resilience of Eddy-Transport Barriers. *J. Atmos. Sci.*, **65** (3), 855–874. [7](#), [19](#), [63](#), [213](#)
- Eden, C. and R. J. Greatbatch, 2008: Towards a mesoscale eddy closure. *Ocean Model.*, **20** (3), 223 – 239. [135](#)
- Farrell, B. F. and P. J. Ioannou, 2008: Formation of Jets by Baroclinic Turbulence. *J. Atmos. Sci.*, **65** (11), 3353–3375. [17](#)
- Ferrari, R. and M. Nikurashin, 2010: Suppression of Eddy Diffusivity across Jets in the Southern Ocean. *J. Phys. Oceanogr.*, **40** (7), 1501–1519. [134](#), [136](#), [160](#), [161](#), [162](#), [163](#), [164](#), [166](#), [168](#), [169](#), [174](#), [175](#), [218](#)

- Fyfe, J. C. and O. A. Saenko, 2006: Simulated changes in the extratropical Southern Hemisphere winds and currents. *J. Geophys. Res.*, **33** (6), L06701. [6](#)
- Garabato, A. C. N., D. P. Stevens, A. J. Watson, and W. Roether, 2007: Short-circuiting of the overturning circulation in the antarctic circumpolar current. *Nature*, **447** (7141), 194–197. [177](#), [194](#), [212](#)
- Garrett, C., 1983: On the initial streakness of a dispersing tracer in two-and three-dimensional turbulence. *Dyn. Atmos. Oceans*, **7** (4), 265–277. [177](#)
- Gill, A., 1968: A linear model of the antarctic circumpolar current. *J. Fluid Mech.*, **32**, 465–488. [11](#)
- Gille, S., et al., 2012: The Diapycnal and Isopycnal Mixing Experiment: A first assessment. *CLIVAR Exchange*, **58** (17), 46–48. [179](#), [180](#), [181](#)
- Gille, S. T., 1997: The Southern Ocean Momentum Balance: Evidence for Topographic Effects from Numerical Model Output and Altimeter Data. *J. Phys. Oceanogr.*, **27** (10), 2219–2232. [216](#)
- Gille, S. T., 2008: Decadal-scale temperature trends in the Southern Hemisphere ocean. *J. Climate*, **21** (18), 4749–4765. [68](#)
- Gordon, A. L., E. Molinelli, and T. Baker, 1978: Large-scale relative dynamic topography of the Southern Ocean. *J. Geophys. Res.*, **83** (C6), 3023–3032. [68](#)
- Greenslade, M. and P. Haynes, 2008: Vertical transition in transport and mixing in baroclinic flows. *J. Atmos. Sci.*, **65** (4), 1137–1157. [8](#)
- Haidvogel, D. B. and I. M. Held, 1980: Homogeneous Quasi-Geostrophic Turbulence Driven by a Uniform Temperature-Gradient. *J. Atmos. Sci.*, **37** (12), 2644–2660. [75](#)
- Hallberg, R., 1997: Localized coupling between surface and bottom-intensified flow over topography. *J. Phys. Oceanogr.*, **27** (6), 977–998. [19](#), [29](#), [31](#)
- Hallberg, R. and A. Gnanadesikan, 2006: The role of eddies in determining the structure and response of the wind-driven southern hemisphere overturning: Results from the Modeling Eddies in the Southern Ocean (MESO) project. *J. Phys. Oceanogr.*, **36** (12), 2232–2252. [67](#)

- Hart, J. E., 1975: Baroclinic Instability over a Slope. Part I: Linear Theory. *J. Phys. Oceanogr.*, **5** (4), 625–633. [69](#)
- Hayes, C. Z., D.E. and R. Weissel, 2009: Modeling paleobathymetry in the Southern Ocean. *Eos, Trans. Amer. Geophys. Union*, **90** (19), 165–166. [4](#)
- Held, I. M. and V. D. Larichev, 1996: A scaling theory for horizontally homogenous, baroclinically unstable flow. *J. Atmos. Sci.*, **53** (7), 946–952. [75](#)
- Hogg, A. M. C., M. P. Meredith, J. R. Blundell, and C. Wilson, 2008: Eddy Heat Flux in the Southern Ocean: Response to Variable Wind Forcing. *J. Climate*, **21** (4), 608–620. [6, 68](#)
- Holloway, G., 1986: Estimation of Oceanic Eddy Transports from Satellite Altimetry. *Nature*, **323** (6085), 243–244. [134, 162, 175, 218](#)
- Hughes, C. W., 2005: Nonlinear vorticity balance of the Antarctic Circumpolar Current. *J. Geophys. Res.*, **110** (C11). [67](#)
- Hughes, C. W. and E. R. Ash, 2001: Eddy forcing of the mean flow in the Southern Ocean. *J. Geophys. Res.*, **106** (C2), 2713–2722. [67](#)
- Ioannou, P., N. Bakas, and N. Constantinou, 2011: Organization and Sensitivity of the Antarctic Circumpolar Current. Tech. rep. [11](#)
- Ishida, A., 1994: Effects of partial meridional barriers on the Antarctic Circumpolar Current – wind-driven barotropic model. *Dyn. Atmos. Oceans*, **20** (4), 315–341. [11](#)
- Jackson, L., C. W. Hughes, and R. G. Williams, 2006: Topographic control of basin and channel flows: The role of bottom pressure torques and friction. *J. Phys. Oceanogr.*, **36** (9), 1786–1805. [10, 68](#)
- Keffer, T. and G. Holloway, 1988: Estimating Southern Ocean eddy flux of heat and salt from satellite altimetry. *Nature*, **332** (6165), 624–626. [134](#)
- Killworth, P. and C. Hughes, 2002: The Antarctic Circumpolar Current as a free equivalent-barotropic jet. *J. Mar. Res.*, **60** (1), 19–45. [182, 185, 211](#)
- Klocker, A., R. Ferrari, and J. H. LaCasce, 2012: Estimating Suppression of Eddy Mixing by Mean Flows. *J. Phys. Oceanogr.*, **42** (9), 1566–1576. [134, 136, 160, 161, 162, 163, 166, 168, 175, 176, 218](#)

- Köhl, A., D. Stammer, and B. Cornuelle, 2007: Interannual to decadal changes in the ECCO global synthesis. *J. Phys. Oceanogr.*, **37** (2), 313–337. [174](#)
- Krupitsky, A. and M. a. Cane, 1997: A Two-Layer Wind-Driven Ocean Model in a Multiply Connected Domain with Bottom Topography. *J. Phys. Oceanogr.*, **27** (11), 2395–2404. [10](#)
- Krupitsky, A., V. M. Kamenkovich, N. Naik, and M. A. Cane, 1996: A linear equivalent barotropic model of the Antarctic Circumpolar Current with realistic coastlines and bottom topography. *J. Phys. Oceanogr.*, **26** (9), 1803–1824. [11](#)
- LaCasce, J. and P. Isachsen, 2010: The linear models of the acc. *Progress in Oceanography*, **84** (3), 139–157. [11](#)
- LaCasce, J. H., 2008: Statistics from Lagrangian observations. *Prog. Oceanogr.*, **77** (1), 1–29. [135](#)
- LaCasce, J. H. and K. H. Brink, 2000: Geostrophic turbulence over a slope. *J. Phys. Oceanogr.*, **30** (6), 1305–1324. [33](#), [69](#)
- Le Quéré, C., et al., 2007: Saturation of the southern ocean CO₂ sink due to recent climate change. *Science*, **316** (5832), 1735–8. [2](#), [68](#)
- Ledwell, J., L. St. Laurent, J. Girton, and J. Toole, 2011: Diapycnal mixing in the antarctic circumpolar current. *J. Phys. Oceanogr.*, **41** (1), 241–246. [178](#), [180](#)
- Ledwell, J. R., A. J. Watson, and C. S. Law, 1998: Mixing of a tracer in the pycnocline. *J. Geophys. Res.: Oceans (1978–2012)*, **103** (C10), 21 499–21 529. [177](#)
- Lee, M. M. and A. Coward, 2003: Eddy mass transport for the Southern Ocean in an eddy-permitting global ocean model. *Ocean Modelling*, **5** (3), 249–266. [9](#), [67](#)
- Legras, B., B. Joseph, and F. Lefevre, 2003: Vertical diffusivity in the lower stratosphere from Lagrangian back-trajectory reconstructions of ozone profiles. *J. Geophys. Res.*, **108** (D18), 4562. [199](#), [211](#), [219](#)
- Liu, C., A. Köhl, and D. Stammer, 2012: Adjoint-based estimation of eddy-induced tracer mixing parameters in the global ocean. *J. Phys. Oceanogr.*, **42** (7), 1186–1206. [174](#)
- Losch, M. and P. Heimbach, 2007: Adjoint Sensitivity of an Ocean General Circulation Model to Bottom Topography. *J. Phys. Oceanogr.*, **37** (2), 377–393. [10](#)

- Lu, J. and K. Speer, 2010: Topography, jets, and eddy mixing in the Southern Ocean. *J. Mar. Res.*, **68**, 479–503. [67](#)
- Maltrud, M. and G. Vallis, 1991: Energy spectra and coherent structures in forced two-dimensional and beta-plane turbulence. *J. Fluid Mech.*, **228**, 321–342. [43](#)
- Manfroi, A. and W. Young, 1999: Slow evolution of zonal jets on the beta plane. *J. Atmos. Sci.*, **56** (5), 784–800. [17](#)
- Marshall, D., 1995: Topographic Steering of the Antarctic Circumpolar Current. *J. Phys. Oceanogr.*, **25** (7), 1636–1650. [68](#)
- Marshall, J., D. Olbers, H. Ross, and D. Wolfgladrow, 1993: Potential Vorticity Constraints on the Dynamics and Hydrography of the Southern-Ocean. *J. Phys. Oceanogr.*, **23** (3), 465–487. [78](#)
- Marshall, J., E. Shuckburgh, H. Jones, and C. Hill, 2006: Estimates and implications of surface eddy diffusivity in the Southern Ocean derived from tracer transport. *J. Phys. Oceanogr.*, **36** (9), 1806–1821. [8](#), [67](#), [135](#), [137](#), [148](#), [174](#)
- Marshall, J. and K. Speer, 2012: Closure of the meridional overturning circulation through Southern Ocean upwelling. *Nature Geoscience*, **5** (3), 171–180. [1](#), [2](#)
- Mason, P., 1975: Baroclinic Waves in a Container with Sloping End Walls. *Proc. Roy. Soc. A.*, **278** (1284), 397–445. [69](#)
- Maximenko, N., B. Bang, and H. Sasaki, 2005: Observational evidence of alternating zonal jets in the world ocean. *Geophys. Res. Lett.*, **32** (12). [67](#)
- McElroy, M. B., 2012: The contemporary and historical budget of atmospheric CO₂. *Canadian Journal of Physics*, **90** (8), 10. [1](#)
- McIntyre, M. E., 1982: How well do we understand the dynamics of stratospheric warmings? *J. Meteor. Soc. Japan*, **60** (1), 37–65. [19](#)
- McKeague, I. W., G. Nicholls, K. Speer, and R. Herbei, 2005: Statistical inversion of south atlantic circulation in an abyssal neutral density layer. *J. Mar. Res.*, **63** (4), 683–704. [212](#)

- Meredith, M. P. and A. M. Hogg, 2006: Circumpolar response of southern ocean eddy activity to a change in the southern annular mode. *Geophys. Res. Lett.*, **33** (16). [172](#), [176](#)
- Morrison, A. K. and A. McC. Hogg, 2013: On the relationship between southern ocean overturning and acc transport. *J. Phys. Oceanogr.*, **43** (1), 140–148. [6](#)
- Morrow, R., M. L. Ward, A. M. Hogg, and S. Pasquet, 2010: Eddy response to southern ocean climate modes. *J. Geophys. Res.-Oceans*, **115** (C10). [170](#), [172](#), [176](#)
- Müller, R., 1992: The performance of classical versus modern finite-volume advection schemes for atmospheric modeling in a one-dimensional test-bed. *Mon. Wea. Rev.*, **120** (7), 1407–1415. [185](#)
- Munday, D. R., L. C. Allison, H. L. Johnson, and D. P. Marshall, 2011: Remote forcing of the Antarctic Circumpolar Current by diapycnal mixing. *Geophys. Res. Lett.*, **38** (8), L08609. [6](#)
- Munday, D. R., H. L. Johnson, and D. P. Marshall, 2013: Eddy saturation of equilibrated circumpolar currents. *J. Phys. Oceanogr.*, **43** (3), 507–532. [6](#)
- Munk, W. H., 1966: Abyssal recipes. *Deep Sea Research and Oceanographic Abstracts*, **13** (4), 707–730. [3](#)
- Nakamura, N., 1996: Two-dimensional mixing, edge formation, and permeability diagnosed in an area coordinate. *J. Atmos. Sci.*, **53** (11), 1524–1537. [93](#), [135](#)
- Nikurashin, M. and G. Vallis, 2011: A Theory of Deep Stratification and Overturning Circulation in the Ocean. *J. Phys. Oceanogr.* [3](#)
- Orsi, A. H., S. S. Jacobs, A. L. Gordon, and M. Visbeck, 2001: Cooling and ventilating the abyssal ocean. *Geophys. Res. Lett.*, **28** (15), 2923–2926. [68](#)
- Panetta, R. L., 1993: Zonal Jets in Wide Baroclinically Unstable Regions - Persistence and Scale Selection. *J. Atmos. Sci.*, **50** (14), 2073–2106. [68](#), [75](#), [84](#)
- Pedlosky, J., 1987: *Geophysical Fluid Dynamics*. Springer, 710 pp. [18](#), [89](#)
- Phillips, H. and S. Rintoul, 2000: Eddy variability and energetics from direct current measurements in the Antarctic Circumpolar Current south of Australia. *J. Phys. Oceanogr.*, **30** (12), 3050–3076. [182](#)

- Phillips, O., 1972: Turbulence in a strongly stratified fluid – is it unstable? *Deep Sea Res Ocean. Abs.*, Elsevier, Vol. 19, 79–81. [7](#)
- Prandtl, L., 1925: A report on testing for built-up turbulence. *Z. Angew. Math. Mech.*, **5**, 136–139. [134](#)
- Prather, M., 1986: Numerical advection by conservation of second-order moments. *J. Geophys. Res.*, **91 (6)**, 6671–6681. [185](#)
- Rhines, P., 1975: Waves and Turbulence on a Beta-Plane. *J. Fluid Mech.*, **69**, 417–443. [15](#), [22](#), [43](#), [63](#), [213](#)
- Rhines, P., 1994: Jets. *Chaos*, **4 (2)**, 313–339. [7](#)
- Rhines, P. B., 1977: *The Sea*, Vol. 6: Marine Modeling, chap. 7: The dynamics of unsteady currents, 189–318. [16](#)
- Sabine, C. L., et al., 2004: The oceanic sink for anthropogenic CO₂. *Science*, **305 (5682)**, 367–71. [1](#)
- Sallée, J. B., K. Speer, R. Morrow, and R. Lumpkin, 2008: An estimate of Lagrangian eddy statistics and diffusion in the mixed layer of the Southern Ocean. *J. Mar. Res.*, **66 (4)**, 441–463. [135](#), [174](#), [176](#)
- Salmon, R., 1978: Two-layer quasi-geostrophic turbulence in a simple special case. *Geophys. & Astrophys. Fluid Dynamics*, **10**, 25–52. [42](#)
- Salmon, R., 1980: Baroclinic instability and geostrophic turbulence. *Geophysical & Astrophysical Fluid Dynamics*, **15 (1)**, 167–211. [41](#)
- Samelson, R., 1992: Surface-Intensified Rossby Waves over Rough Topography. *J. Mar. Res.*, **50 (3)**, 367–384. [19](#)
- Shuckburgh, E. and P. Haynes, 2003: Diagnosing transport and mixing using a tracer-based coordinate system. *Phys. Fluids*, **15 (11)**, 3342–3357. [93](#), [95](#)
- Shuckburgh, E., H. Jones, J. Marshall, and C. Hill, 2009a: Robustness of an Effective Diffusivity Diagnostic in Oceanic Flows. *J. Phys. Oceanogr.*, **39 (9)**, 1993–2009. [67](#), [135](#), [137](#), [138](#), [141](#), [145](#), [154](#), [155](#), [156](#), [157](#), [166](#), [174](#), [218](#)

- Shuckburgh, E., H. Jones, J. Marshall, and C. Hill, 2009b: Understanding the Regional Variability of Eddy Diffusivity in the Pacific Sector of the Southern Ocean. *J. Phys. Oceanogr.*, **39** (9), 2011–2023. [67](#), [135](#), [137](#), [138](#)
- Sigman, D. M. and E. A. Boyle, 2000: Glacial/interglacial variations in atmospheric carbon dioxide. *Nature*, **407** (6806), 859–69. [2](#)
- Smith, K. S., 2004: A Local Model for Planetary Atmospheres Forced by Small-Scale Convection. *J. Atmos. Sci.*, **61** (12), 1420–1433. [22](#)
- Smith, K. S., 2007: Eddy amplitudes in baroclinic turbulence driven by nonzonal mean flow: Shear dispersion of potential vorticity. *J. Phys. Oceanogr.*, **37** (4), 1037–1050. [68](#), [69](#), [70](#), [72](#), [87](#), [96](#), [130](#), [131](#), [216](#)
- Smith, K. S., G. Boccaletti, C. C. Henning, I. Marinov, C. Y. Tam, I. M. Held, and G. K. Vallis, 2002: Turbulent diffusion in the geostrophic inverse cascade. *J. Fluid Mech.*, **469**, 13–48. [16](#), [17](#), [28](#), [41](#), [43](#), [52](#), [56](#), [57](#), [215](#)
- Smith, K. S. and R. Ferrari, 2009: The production and dissipation of compensated thermohaline variance by mesoscale stirring. *J. Phys. Oceanogr.*, **39** (10), 2477–2501. [177](#)
- Sokolov, S. and S. R. Rintoul, 2007: Multiple jets of the Antarctic circumpolar current South of Australia. *J. Phys. Oceanogr.*, **37** (5), 1394–1412. [8](#), [67](#)
- Spall, M. A., 2000: Generation of strong mesoscale eddies by weak ocean gyres. *J. Mar. Res.*, **58** (1), 97–116. [68](#)
- Srinivasan, K. and W. R. Young, 2012: Zonostrophic Instability. *J. Atmos. Sci.*, **69**, 1633–1656. [17](#), [18](#), [42](#), [63](#), [66](#), [213](#), [215](#), [216](#)
- St Laurent, L., A. C. Naveira Garabato, J. R. Ledwell, A. M. Thurnherr, and J. M. Toole, 2012: Turbulence and diapycnal mixing in Drake Passage. submitted. [180](#)
- Stammer, D., 1998: On eddy characteristics, eddy transports, and mean flow properties. *J. Phys. Oceanogr.*, **28** (4), 727–739. [134](#)
- Steinsaltz, D., 1987: Instability of Baroclinic Waves with Bottom Slope. *J. Phys. Oceanogr.*, **17** (12), 2343–2350. [69](#)
- Stephens, B. and R. Keeling, 2000: The influence of Antarctic sea ice on glacial-interglacial CO₂ variations. *Nature*, **404** (6774), 171–4. [3](#)

Stocker, T. F., 1998: Climate Change: The Seesaw Effect. *Science*, **282** (5386), 61–62.
[3](#)

Straub, D., 1994: Dispersive Effects of Zonally Varying Topography on Quasigeostrophic Rossby Waves. *Geophysical and Astrophysical Fluid Dynamics*, **75** (2-4), 107–130. [19](#)

Sukoriansky, S., N. Dikovskaya, and B. Galperin, 2007: On the Arrest of Inverse Energy Cascade and the Rhines Scale. *J. Atmos. Sci.*, **64** (9), 3312–3327. [28](#), [42](#), [57](#)

Tailleux, R. and J. McWilliams, 2000: Acceleration, creation, and depletion of wind-driven, baroclinic Rossby waves over an ocean ridge. *J. Phys. Oceanogr.*, **30** (9), 2186–2213. [19](#)

Tamaki, K. and K. Ukaji, 2003: An experimental study of wave dispersion in a differentially heated rotating fluid annulus with a radially sloping bottom. *J. Meteor. Soc. Japan*, **81** (5), 951–962. [69](#)

Taylor, G. I., 1921: Diffusion by continuous movements. *Proceedings of the London Mathematical Society*, **20**, 196–211. [193](#)

Thompson, A. F., 2008: The atmospheric ocean: eddies and jets in the Antarctic Circumpolar Current. *Philos. Trans. Roy. Soc. London A*, **366** (1885), 4529–41. [5](#), [9](#)

Thompson, A. F., 2010: Jet Formation and Evolution in Baroclinic Turbulence with Simple Topography. *J. Phys. Oceanogr.*, **40** (2), 257–278. [68](#), [69](#), [84](#), [103](#), [132](#)

Thompson, A. F., P. H. Haynes, C. Wilson, and K. J. Richards, 2010: Rapid Southern Ocean front transitions in an eddy-resolving ocean GCM. *Geophys. Res. Lett.*, **37**. [78](#)

Thompson, A. F. and K. J. Richards, 2011: Low frequency variability of Southern Ocean jets. *J. Geophys. Res.*, **116** (C9), C09022. [93](#)

Thompson, A. F. and J.-B. Sallée, 2012: Jets and Topography: Jet Transitions and the Impact on Transport in the Antarctic Circumpolar Current. *J. Phys. Oceanogr.*, **42** (6), 956–972. [5](#), [216](#)

Thompson, A. F. and W. R. Young, 2007: Two-layer baroclinic eddy heat fluxes: Zonal flows and energy balance. *J. Atmos. Sci.*, **64** (9), 3214–3231. [87](#)

- Thompson, D. W. J., S. Solomon, P. J. Kushner, M. H. England, K. M. Grise, and D. J. Karoly, 2011: Signatures of the Antarctic ozone hole in Southern Hemisphere surface climate change. *Nature Geoscience*, **4** (11), 741–749. [2](#)
- Toggweiler, J. R., J. L. Russell, and S. R. Carson, 2006: Midlatitude westerlies, atmospheric CO₂, and climate change during the ice ages. *Paleoceanography*, **21** (2), PA2005. [3](#)
- Treguier, A. M. and J. C. McWilliams, 1990: Topographic Influences on Wind-Driven, Stratified Flow in a Beta-Plane Channel - An Idealized Model for the Antarctic Circumpolar Current. *J. Phys. Oceanogr.*, **20** (3), 321–343. [10](#), [68](#)
- Treguier, A. M. and R. L. Panetta, 1994: Multiple Zonal Jets in a Quasi-Geostrophic Model of the Antarctic Circumpolar Current. *J. Phys. Oceanogr.*, **24** (11), 2263–2277. [10](#), [68](#)
- Tulloch, R., J. Marshall, C. Hill, and K. S. Smith, 2011: Scales, Growth Rates, and Spectral Fluxes of Baroclinic Instability in the Ocean. *J. Phys. Oceanogr.*, **41** (6), 1057–1076. [103](#), [131](#)
- Vallis, G. K., 2006: *Atmospheric and Ocean Fluid Dynamics*. Cambridge University Press, 745 pp. [15](#), [42](#), [43](#), [58](#)
- Vallis, G. K. and M. E. Maltrud, 1993: Generation of mean flows and jets on a beta plane and over topography. *J. Phys. Oceanogr.*, **23**, 1346–1362. [16](#), [56](#), [63](#), [68](#), [213](#), [214](#), [215](#)
- Venaille, A., G. K. Vallis, and K. S. Smith, 2011: Baroclinic Turbulence in the Ocean: Analysis with Primitive Equation and Quasigeostrophic Simulations. *J. Phys. Oceanogr.*, **41** (9), 1605–1623. [10](#)
- Visbeck, M., J. Marshall, T. Haine, and M. Spall, 1997: Specification of Eddy Transfer Coefficients in Coarse-Resolution Ocean Circulation Models. *J. Phys. Oceanogr.*, **27** (3), 381–402. [6](#)
- Watson, A. J. and A. C. N. Garabato, 2006: The role of Southern Ocean mixing and upwelling in glacial-interglacial atmospheric CO₂ change. *Tellus B*, **58** (1). [3](#)
- Webb, D., 1993: A simple model of the effect of the kerguelen plateau on the strength of the antarctic circumpolar current. *Geophys. Astrophys. Fluid Dyn.*, **70** (1-4), 57–84. [11](#)

- Whitehead, J., M. Stern, G. Flierl, and B. Klinger, 1990: Experimental Observations of Baroclinic Eddies on a Sloping Bottom. *J. Geophys. Res.*, **95** (C6), 9585–9610. [69](#)
- Williams, R., C. Wilson, and C. Hughes, 2007: Ocean and atmosphere storm tracks: The role of eddy vorticity forcing. *J. Phys. Oceanogr.*, **37** (9), 2267–2289. [5](#), [9](#)
- Witter, D. L. and D. B. Chelton, 1998: Eddy-mean flow interaction in zonal oceanic jet flow along zonal ridge topography. *J. Phys. Oceanogr.*, **28**, 2019–2039. [10](#), [68](#), [132](#)
- Wolff, J. O., E. Maierreimer, and D. J. Olbers, 1991: Wind-Driven Flow over Topography in a Zonal Beta-Plane Channel - A Quasi-Geostrophic Model of the Antarctic Circumpolar Current. *J. Phys. Oceanogr.*, **21** (2), 236–264. [10](#), [68](#), [132](#)
- Wordsworth, R. D., P. L. Read, and Y. H. Yamazaki, 2008: Turbulence, waves, and jets in a differentially heated rotating annulus experiment. *Phys. Fluids*, **20** (12). [69](#)
- Zika, J. D., B. M. Sloyan, and T. J. McDougall, 2009: Diagnosing the southern ocean overturning from tracer fields. *J. Phys. Oceanogr.*, **39** (11), 2926–2940. [177](#), [212](#)
- Zurita-Gotor, P. and G. K. Vallis, 2010: Equilibration of Baroclinic Turbulence in Primitive Equations and Quasigeostrophic Models. *J. Atmos. Sci.*, **66**, 837–863. [41](#)